Universidade de Brasília
Instituto de Geociências
Programa de Pós-graduação em Geologia

Geological and morphostructural analysis of the Araguainha impact structure, Brazil

RENATO BORGES BERNARDES

Tese de Doutorado Nº 223

Orientador: Prof. Dr. Wolf Uwe Reimold
Coorientador: Prof. Dr. Roger L. Gibson

Brasília, 27 de outubro de 2025

Universidade de Brasília
Instituto de Geociências
Programa de Pós-graduação em Geologia

Geological and morphostructural analysis of the Araguainha impact structure, Brazil

Análise geológica e morfoestrutural da estrutura de impacto Araguainha, Brasil

RENATO BORGES BERNARDES

Tese apresentada ao Programa de Pós-graduação em Geologia – Instituto de Geociências – IG da Universidade de Brasília – UnB como requisito parcial obrigatório para a obtenção do título de Doutor em Geologia.

Área de concentração: Geologia Regional

Orientador: Prof. Dr. Wolf Uwe Reimold

Coorientador: Prof. Dr. Roger L. Gibson

Comissão Examinadora:

Prof. Dr. Elton L. Dantas (Instituto de Geociências, Universidade de Brasília)
Prof. Dr. John G. Spray (University of New Brunswick, Canadá)
Prof. Dr. Lutz Hecht (Museum für Naturkunde Berlin, Alemanha)

Bernardes, Renato Borges
B522g Geological and morphostructural analysis of the Araguainha impact structure, Brazil / Renato Borges Bernardes; orientador Wolf Uwe Reimold; co-orientador Roger Lawrence Gibson. Brasília, 2025.
193 p.

Tese(Doutorado em Geologia) Universidade de Brasília, 2025.

1. Impact cratering. 2. Structural geology. 3. Central uplift. 4. Asymmetry. I. Reimold, Wolf Uwe, orient. II. Gibson, Roger Lawrence, co-orient. III. Título.

ACKNOWLEDGMENTS

This study was financed in part by the Coordenação de Aperfeiçoamento de Pessoal de Nível Superior – Brasil (CAPES) – Finance Code 001.

I am grateful to:

My wife, Cássia; my parents, Carlos and Cleony; and my brothers, Eduardo and André, for never giving up on me.

My supervisor, Wolf Uwe Reimold; co-supervisor, Roger L. Gibson; and unofficial co-supervisor, Natalia Hauser, for their teaching and tremendous patience with how my neurodivergent brain works.

The *Barringer Family Fund for Meteorite Impact Research*, for providing me with funding to conduct this research.

My immediate work supervisor, Professor Adriana C. Carmelo, and the Director of the Institute of Geosciences at the University of Brasilia, Professor Welitom R. Borges, for allowing me to take a sabbatical leave to complete this project.

The colleagues, technicians, and some professors at the Institute of Geosciences at the University of Brasilia, for their support and encouragement throughout this journey.

The citizens of Araguainha and Ponte Branca, for their hospitality.

The team of physiotherapists at *Lettieri*, for preventing my muscles from collapsing during this journey, which required me to remain seated for long hours.

My childhood friends, Felipe Alves and Flávio Henrique, who doubted that I would complete this project. That definitely motivated me to finish it.

The examining committee of this thesis, for their valuable comments and insights.

And, most importantly, myself, for never giving up the meaningful battles.

ABSTRACT

The Araguainha impact structure (AIS) is the ~40-km-wide erosional remnant of South America's largest confirmed impact structure. It was formed in a mixed crystalline-sedimentary target in the north-northwest part of the Paraná Basin, Central-West Brazil, at 259–252 Ma. Geological and structural mapping, especially the analysis of new, extensive exposures from roadworks on the MT-100 state road in and around the AIS, has been conducted. Combined with a multi-methodological investigation using airborne geophysics, remote sensing, lineament analysis, and modeling of the (apparent) crater rim trace shape, this has provided an updated geological map, expanded the structural inventory, and allowed the investigation of the influence of the preexisting regional structural framework on the development of the first-order morphostructure of the AIS. The formation of the most prominent morphological and structural features in the different sections – i.e., outer rim region, intermediate section, and central uplift – of the AIS is associated with the excavation and modification stages of cratering. Large, fault-bounded blocks dominate the outer domains of the AIS, with the Passa Dois Group Blocks (PDGBs) in the outer rim region resembling gravity-driven complex slumps. The AIS is unlikely to be of the peak-ring type, as previously suggested. The northern core of the central uplift can be divided into a structurally diverse megablock zone, with rare injections of impact melt rock and occurrences of at least three types of impact breccia (suevite and polymict lithic breccia), which in turn overlies a seemingly coherent but folded and faulted crater floor formed by (meta)sedimentary basement. The AIS and its central uplift, the latter of which may be up to ~20 km wide, are (structurally) asymmetric features. The development of the structure's morphostructural asymmetry was fundamentally controlled by the pre-impact anisotropy of the target. A contribution from oblique impact to the observed asymmetry, however, cannot be ruled out. The preexisting structural fabric of the target is primarily characterized by lineaments prominently trending in the NE-SW and NW-SE directions, which can be linked principally to structures related to the Paraguay Belt and, to a lesser extent, the Transbrasiliano Lineament beneath the NNW Paraná Basin. This pre-impact structuration of the target yielded an apparent rim trace shape that is not circular, but best represented by an irregular nine-sided polygon (enneagon). Therefore, the AIS is recognized as the eroded remnant of a polygonal impact crater. These results highlight new aspects of the intricate processes involved in the formation of large, complex impact structures in heterogeneous targets, including the importance of the target's anisotropic features – including layering and/or fractures and faults – in shaping the main morphostructural aspects of these structures.

Keywords: Impact cratering; Structural geology; Central uplift; Asymmetry.

RESUMO

A estrutura de impacto Araguainha (AIS) é o remanescente erosivo de ~40 km de diâmetro da maior estrutura de impacto confirmada da América do Sul. A AIS foi formada em um alvo misto cristalino-sedimentar na porção norte-noroeste da Bacia do Paraná, Centro-Oeste do Brasil, entre 259–252 Ma. Foi realizado mapeamento geológico-estrutural, com especial destaque para a análise de novos e extensos afloramentos expostos por obras na rodovia estadual MT-100, dentro e ao redor da AIS. Combinado com uma investigação multimetodológica que empregou geofísica aerotransportada, sensoriamento remoto, análise de lineamentos e modelagem da forma aparente do traçado do contorno da estrutura, isso proporcionou um mapa geológico atualizado, ampliou o inventário estrutural e permitiu a investigação da influência do arcabouço estrutural regional preexistente no desenvolvimento da morfoestrutura de primeira ordem da AIS. A formação das feições morfológicas e estruturais mais proeminentes nas diferentes seções – região da borda externa, seção intermediária e soerguimento central – da AIS está associada aos estágios de escavação e de modificação do processo de crateração. Grandes blocos delimitados por falhas dominam os domínios externos da AIS, com os Blocos do Grupo Passa Dois (PDGBs) na região da borda externa se assemelhando a deslizamentos complexos mobilizados pela gravidade. É improvável que a AIS seja uma estrutura do tipo peak-ring, como sugerido anteriormente. O núcleo norte do soerguimento central pode ser dividido em uma zona de megablocos estruturalmente diversa, com raras injeções de rocha de fusão por impacto e ocorrências de pelo menos três tipos de brechas de impacto, incluindo suevito e brecha lítica polimítica, que por sua vez recobrem um piso de cratera aparentemente coerente, porém dobrado e falhado, formado por embasamento (meta)sedimentar. A AIS e seu soerguimento central, este último podendo atingir cerca de 20 km de largura, são feições (estruturalmente) assimétricas. O desenvolvimento da assimetria morfoestrutural da estrutura foi fundamentalmente controlado pela anisotropia pré-impacto do alvo. No entanto, não se pode excluir uma contribuição de impacto oblíquo para a assimetria observada. O arcabouço estrutural pré-existente do alvo é caracterizado principalmente por lineamentos proeminentes com orientação NE–SW e NW–SE, que podem ser vinculados, sobretudo, a estruturas relacionadas à Faixa Paraguai e, em menor grau, ao Lineamento Transbrasiliano na porção NNW da Bacia do Paraná. Essa estruturação pré-impacto do alvo resultou em um traçado aparente da borda da estrutura que não é circular, sendo esse melhor representado por um eneágono irregular. Portanto, a AIS é reconhecida como o remanescente erosivo de uma cratera de impacto poligonal. Esses resultados destacam novos aspectos dos intrincados processos envolvidos na formação de grandes estruturas de impacto complexas em alvos heterogêneos, como a importância das feições anisotrópicas do alvo – incluindo estratificação e/ou fraturas e falhas – no condicionamento dos principais aspectos morfoestruturais dessas estruturas.

Palavras-chave: Crateramento por impacto; Geologia estrutural; Soerguimento central; Assimetria.

CONTENTS

CHAPTER 1
INTRODUCTION

CHAPTER 1 – INTRODUCTION

Impact cratering (e.g., Melosh, 1989; Osinski and Pierazzo, 2012) is a highly dynamic and complex process of widespread planetary importance. Impact cratering has fundamentally shaped all solid planetary surfaces in the Solar System. From the stage of planetary accretion onward, impact cratering has played a decisive role in our planet's history. This process occurs when an interplanetary object (i.e., a projectile such as an asteroid or comet) strikes a planetary surface, resulting in the formation of an impact crater (*sensu lato*). More specifically, if a projectile possesses enough kinetic energy to produce a shock wave – and, consequently, shock metamorphism – upon impact, a crater structure may be created, referred to as a hypervelocity impact crater (see Osinski et al., 2022, for a discussion on this matter).

At least one large impact event is widely recognized to have significantly influenced the evolution of life on Earth. The Chicxulub impact event has been linked to the Cretaceous–Paleogene boundary mass extinction (see, e.g., Alvarez et al., 1980; Schulte et al., 2010). This event serves as a reminder of the importance of impact cratering as a geologic process of great planetary and scientific significance.

Although the terrestrial impact record already documents about 210 confirmed impact structures (see Gottwald et al., 2020; Schmieder and Kring, 2020; Kenkmann, 2021; Osinski et al., 2022), it is likely still incomplete – especially regarding small impact structures (Hergarten and Kenkmann, 2015) and possibly others formed offshore. Continued state-of-the-art multidisciplinary analysis is essential to discover more impact structures and to develop a comprehensive understanding of the unique processes involved in this hypervelocity impact phenomenon and ultradynamic impact crater development.

However, detailed mapping of impact-generated structural inventories and high-quality, meticulous structural analysis of impact structures remain rare. Additionally, only a few terrestrial impact structures are easily accessible and suitable for detailed ground-based studies, which enable the investigation of deformational structures and the related formation processes. These field investigations are crucial because they can reveal structural complexities hidden from remote sensing observations and serve as the foundation for understanding the kinematics and ultra-high-strain dynamics of crater formation (see, e.g., Kenkmann et al., 2014).

While some fairly comprehensive hypotheses exist for the structural evolution of complex impact craters (see Kenkmann et al., 2014), they still rely on relatively few, and sometimes limited, field studies of structures that are often at least partially eroded. The validity of current structural hypotheses needs to be tested with additional evidence, especially from large complex impact structures (>30 km in diameter). The different stress fields during initial impact compression, excavation, collapse of the transient cavity, and the subsequent modification stage of cratering produce distinct deformation styles at multiple scales, making it challenging to distinguish the effects generated in these stages.

In this context, the Araguainha impact structure (AIS) – South America's largest and relatively well-preserved impact structure – has strong potential to contribute (Fig. 1.1). Formed around 259–252 Ma (Tohver et al., 2012; Erickson et al., 2017; Hauser et al., 2019), Araguainha is an example of a large (~40 km diameter), complex impact structure in a mixed crystalline-sedimentary target that, despite some limited erosion (see Lana et al., 2007), still retains a substantial impact inventory (see, e.g., Lana et al., 2008; Crósta et al., 2019; Souza et al., 2024). This inventory is also quite accessible, making the AIS a unique field analog for planetary exploration (Lambert and Reimold, 2023). Further geological and structural studies of this structure could provide valuable new insights into the structural geology of impact craters and the impact cratering process as a whole.

Although some aspects of geological and geomorphological features have been studied in detail (see Crósta et al., 2019; Souza et al., 2024, and references therein for an overview), no comprehensive mapping of the macro-, meso-, and microscale deformation or detailed structural analysis have been conducted on the AIS to this day. First-order structural observations have been published by Lana et al. (2006, 2007, 2008), and a locally focused study by Hippertt et al. (2014) exists. Additionally, staff and students from the Institute of Geosciences, University of Brasilia (UnB-IG, 2012, unpublished 5th-year field camp report), produced a litho-geological map of the Araguainha impact structure, but this work contains limited structural information. A more recent fieldwork study (Hauser et al., 2021) suggests that this map requires a systematic review, completion, and revision in certain aspects and sectors.

Figure 1.1. The eight confirmed (red dots) and two suspected (not confirmed – green dots) impact structures in Brazil (as of September 2025) (modified from the Impact Earth database; Osinski et al., 2022). The São Miguel do Tapuio structure location was manually added. Note the highlighted location of the Araguinha impact structure in Central-West Brazil.

In recent years, extensive roadworks along the entire length of the MT-100 state road – which completely crosses the AIS along a basically NE-SW transect (see below) – have revealed new rock exposures (Fig. 1.2). Therefore, the AIS now provides a unique opportunity to document the structural effects associated with various stages of complex crater formation at different scales, aiding our understanding of the kinematics of crater formation and impact-induced strain patterns.

Figure 1.2. Roadworks in the southwestern part of the Araguainha impact structure, on the outer rim region, along the MT-100 state road (adapted from the SINFRA-MT – Secretaria de Estado de Infraestrutura e Logística de Mato Grosso; website: sinfra.mt.gov.br).

1.1. Geographic location and historical background of the study region

The Araguainha impact structure (AIS), located at 52.99151°W, 16.81544°S, is also known as the *Araguainha Dome*. It spans the border between the states of Mato Grosso and Goiás in Central-West Brazil, about 560 km west-southwest of Brasilia (Distrito Federal). Situated in the northern-northwestern part of the Phanerozoic Paraná Basin, the AIS is crossed by the Araguaia River and the recently paved MT-100 state road, both roughly aligned in a NE-SW direction. The small town of Araguainha lies to the southwest of the structure's center, whereas Ponte Branca is located just inward of the perceived NE outer rim (Fig. 1.3).

Since the first mention of the Araguainha Dome by Northfleet et al. (1969), there have been two main hypotheses about how this circular structure formed. These earliest authors believed that the Araguainha structure was of igneous origin and resulted from a syenite intrusion. Similarly, Silveira Filho and Ribeiro (1971, as cited in Crósta et al., 1981) and CPRM (1972) believed the dome had a cryptovolcanic origin. Dietz and French (1973) were the first to suggest and provide initial evidence for an impact origin of the Araguainha Dome. This impact hypothesis was later supported by independent reports on shatter cones by Theilen-Willige (1981) and Crósta et al. (1981), who also provided additional impact-related observations.

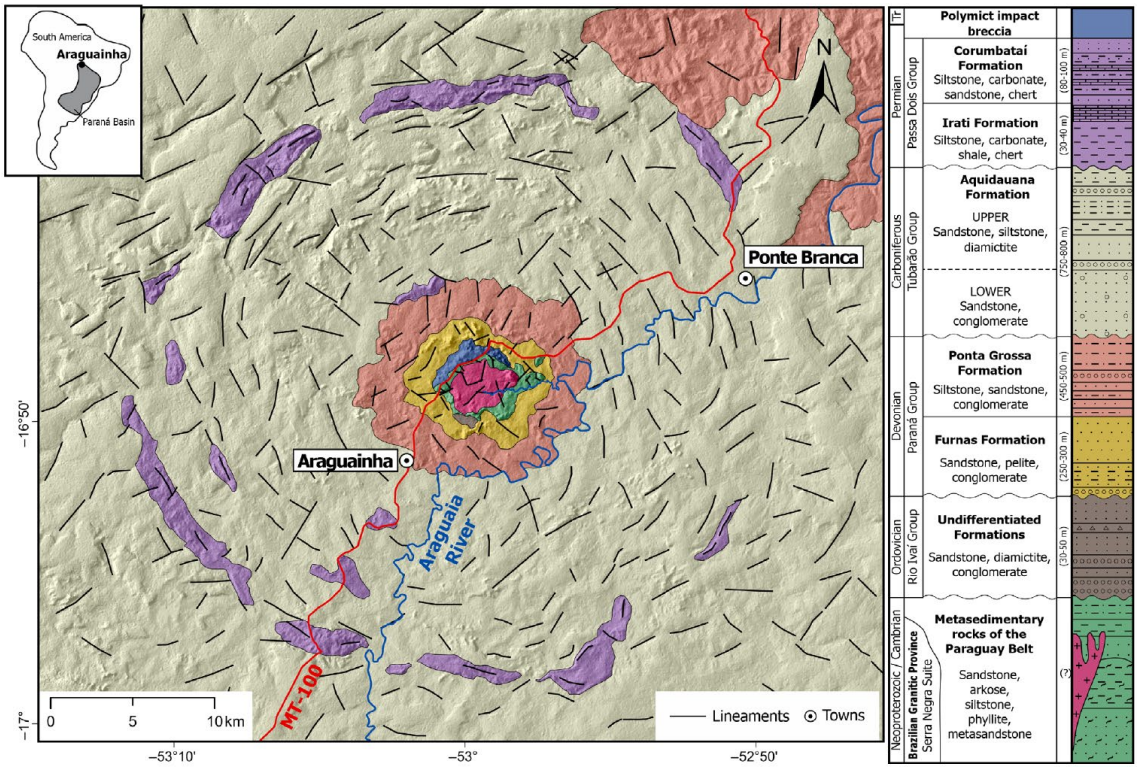

Figure 1.3. The latest geological map of the Araguainha impact structure (Souza et al., 2024). The towns of Araguainha and Ponte Branca, along with the MT-100 state road (red line), are highlighted. The inset map in the upper-left corner shows the location of the AIS within the Paraná Basin and South America. On the right, a stratigraphic column of the geological units related to the map is displayed.

From that point onward, the impact origin was broadly accepted, and subsequent research focused on many other aspects of the AIS – for example, impact age dating (e.g., Deutsch et al., 1992; Hammerschmidt and von Engelhardt, 1995; Tohver et al., 2012; Hauser et al., 2019), geological and/or structural mapping (e.g., von Engelhardt et al., 1992; Lana et al., 2006, 2007, 2008; Hippertt et al., 2014; Tohver et al., 2018; Souza et al., 2024), petrology and geochemistry (e.g., Machado et al., 2009; Silva et al., 2016), and geophysics (e.g., Masero et al., 1994, 1997; Schnegg and Fontes, 2002; Vasconcelos, 2007; Tong et al., 2010; Jovane et al., 2011; Yokoyama et al., 2012; Miyazaki et al., 2021; Leite et al., 2022).

1.2. Objectives

The main objectives of this project were to, with support from fieldwork and remote sensing data, produce an updated geological map and expand the structural inventory of the Araguainha impact structure and its surroundings. In particular, emphasis was placed on the highly complex deformation structures of the central uplift and the

outer rim region of the structure. This new information then provided a foundation for answering some outstanding questions about the Araguainha impact structure (see below) and for improving the broader understanding of how large, complex impact craters form, especially those in mixed, crystalline-sedimentary targets.

The main questions addressed here are:

- Is the currently accepted diameter of 40 km for the Araguainha impact structure accurate? What is the radial extent of the central uplift of the AIS? In recent years, there has been widespread discussion on these topics (including at the Large Meteorite Impacts conference, LMI VI, at the University of Brasilia, in 2019).
- What are the specific types of deformation (such as melting, brittle, or ductile), their spatial distribution, and the lithological factors that influenced these aspects in the different morphostructural sectors of the AIS?
- Is it possible to associate certain recognized styles of deformation with pre- and post-impact tectonics, whereas others are related to different stages of impact cratering (i.e., contact and compression; excavation [extensional]; and modification and collapse – specifically, central uplift formation and collapse, as well as rim terracing – [extensional/compressional], see Melosh, 1989; Kenkmann et al., 2014)?
- What was the paleoenvironment of the Araguainha region just before the impact event? Did this paleoenvironment play a significant role in the formation of the AIS?
- Is the deformation at the Araguainha impact structure symmetrical, or could the structure result from a relatively low-angle oblique impact?

1.3. How is this thesis structured?

The current chapter introduces the subject and study area, providing information on the main research objectives. For a more detailed description of the regional geology of the Araguainha impact structure, the reader should refer to chapters 4 and 5 (see below).

Chapter 2 briefly summarizes the broader topic of impact cratering, including types of impact craters, the stages of cratering, and the overall first-order morphostructure of complex craters.

Chapter 3 presents the materials and methods used in this research. For a more detailed explanation of these materials and methods, refer to the methodology sections in the research articles given in chapters 4 and 5 (see next).

Chapters 4 and *5* contain the full texts of research articles 1 and 2, respectively. Both articles explore the geology, morphology, and structure of the Araguainha impact structure. Article 1 focuses on fieldwork and structural analysis, aiming to provide new insights into the geology and formation of the AIS. Article 2 is based on results from geophysical and remote sensing analyses that were conducted to determine whether the AIS is a remnant of a polygonal impact crater. The cited references and the Supplemental Material (or Supporting Information) for each article are included at the end of its respective chapter.

Chapter 6 provides a brief overview of current knowledge and gaps in understanding the first-order evolution of the AIS's central uplift – mainly its core – focusing on its formation and potential weakening mechanisms that might have influenced its evolution.

Chapter 7 explores aspects of a possible oblique impact that may have contributed to the formation of the AIS, potentially causing asymmetrical features in the structure, particularly in its rim and central uplift.

Chapter 8 offers a summary and the key conclusions from this research project. The reference list for all chapters except chapters 4 and 5 is provided at the end of this chapter.

The core team of this research project includes Professor W.U. Reimold (Universidade de Brasília), the Ph.D. project supervisor; Professor R.L. Gibson (University of the Witwatersrand), the Ph.D. project co-supervisor; Professor N. Hauser (Universidade de Brasília); visiting researcher P. Pavanetto (Universidade Federal do Amazonas); Professor J.B. Curto Ma (Universidade de Brasília); and geophysicist and geosciences researcher A.B. Silva (Serviço Geológico do Brasil). W.U. Reimold contributed by securing funding and resources, providing conceptual guidance, overseeing methodology, offering methodological advice, participating in some field trips, and critically reviewing and editing thesis drafts. The other team members contributed by taking part in some field trips, processing geophysical data (J.B. Curto Ma and A.B. Silva), assisting with data analysis, and critically reviewing the drafts of research articles 1 and 2 and the thesis (in the case of co-supervisor R.L. Gibson).

CHAPTER 2

IMPACT CRATERING: AN OVERVIEW

CHAPTER 2 – IMPACT CRATERING: AN OVERVIEW

2.1. Crater types

Crater morphology varies with crater size, target rock material, planetary conditions, and crater age and degradation (Melosh, 1989). In a first-order approach, crater size–morphology progression is mainly controlled by the target body's surface gravity and strength (Kenkmann et al., 2012). In this context, two main crater morphologies can be distinguished: simple, bowl-shaped craters and complex impact craters, which eventually grade into multi-ring basin structures. As the transition from simple to complex crater morphologies is gradual, it is important to note that so-called *transitional impact craters* have also been proposed (Osinski et al., 2019, 2022). However, these transitional structures are not the focus of this work and will therefore not be further discussed. It should be noted that the term *impact crater* is used for fresh craters, whereas *impact structure* is a broader term that should describe eroded or buried features (see Osinski, 2012; Reimold and Koeberl, 2014).

Simple craters are the classic, well-known bowl-shaped formations with nearly parabolic profiles (Melosh, 1989). A prime example of this is Meteor (Barringer) Crater in Arizona (e.g., Poelchau et al., 2009; Kring, 2017). Pristine, simple craters typically feature a circular raised rim, a steep interior slope near the rim that gradually decreases toward the crater interior, and lack a central flat floor (Melosh, 1989) (Fig. 2.1A). Regarding their morphological ratios, this type of crater typically has a rim-to-floor depth of approximately one-fifth of its rim-to-rim diameter, with the rim height reaching around 4% of the diameter (Melosh, 1989).

The transition diameter from simple to complex crater morphology is inversely related to the surface gravity of the target body (Pike, 1980). This change in morphology is also influenced by the strength of the target material (e.g., crystalline vs. sedimentary vs. icy vs. mixed targets; see Kenkmann et al., 2012). On Earth (9.81 m/s^2 surface gravity), a shift from a simple, bowl-shaped crater to a complex structure generally occurs at crater diameters between 2 and 4 km for sedimentary versus crystalline targets, respectively (Dence, 1972; Melosh, 1989). In comparison, on Mars (with a surface gravity of 3.69 m/s^2), craters with simple morphology can be as large as 8 km in diameter (Kenkmann et al., 2012).

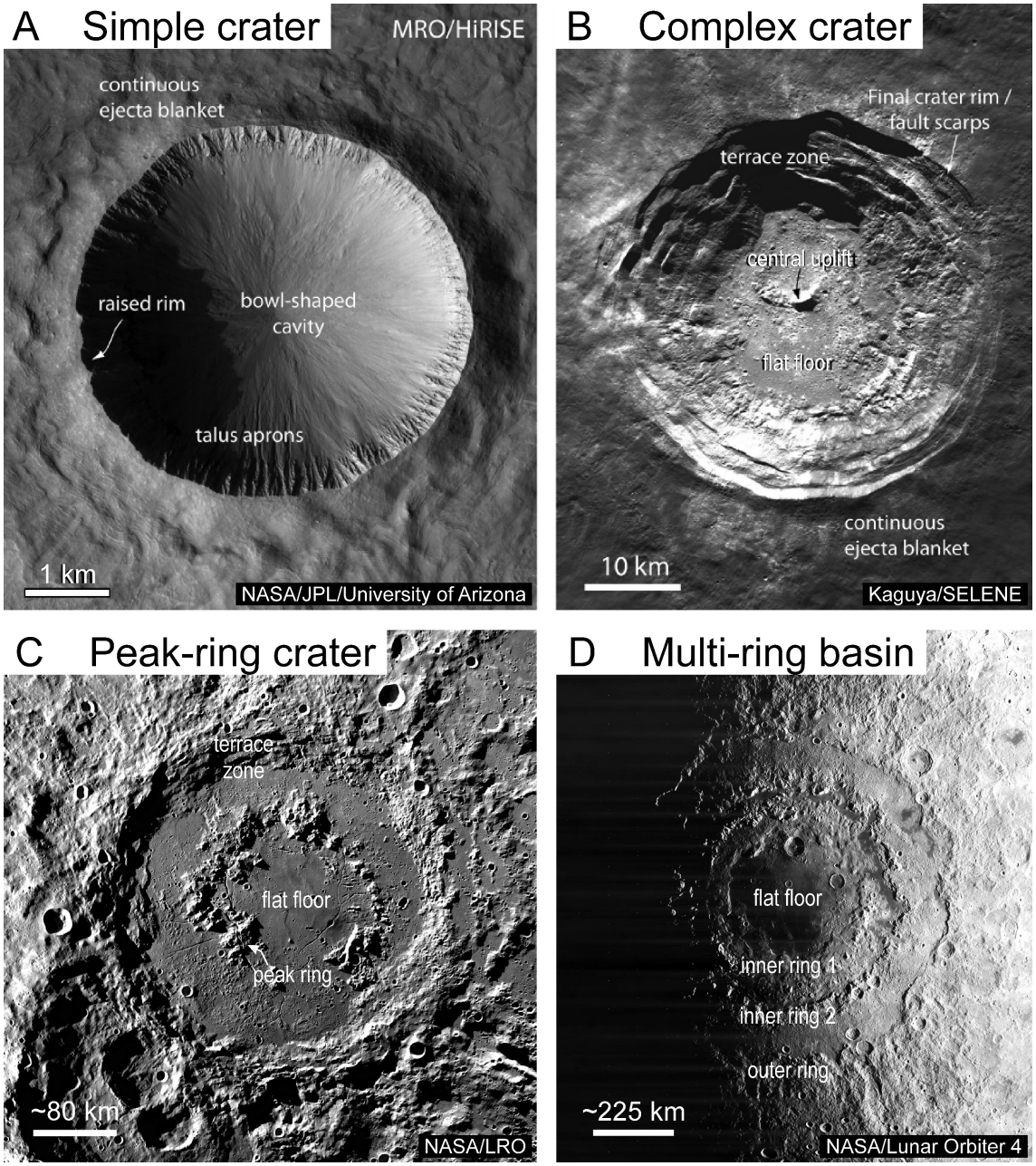

Figure 2.1. Comparison of different crater morphologies (modified from Kenkmann et al., 2014). A) An approximately 4.5-km-wide unnamed simple crater on Mars (Image: NASA/JPL/University of Arizona). B) The 40-km-wide, complex impact crater Aristarchus on the Moon (Image: Kaguya/SELENE). C) The 312-km-wide, peak-ring impact crater Schrödinger on the Moon (Image: NASA/LRO). D) The ~930-km-wide, multi-ring impact basin Mare Orientale, also on the Moon (Image: NASA/Lunar Orbiter 4). Note the different morphological features and scale bars shown in the images.

Complex craters have larger dimensions and a smaller depth-to-diameter ratio than simple craters (Kenkmann et al., 2012). In general, complex craters exhibit slump terraces on their inner walls and a relatively flat interior floor, with a structurally uplifted central region that may form a peak or cluster of peaks (Melosh, 1989) (Fig. 2.1B). The central peak of a complex crater is generally lower in height than the rim crest (Melosh,

1989). Larger complex craters tend to develop, instead of a well-defined central peak, an inner concentric ring of peaks of roughly half the rim-to-rim diameter; these craters are termed *peak-ring craters* (Melosh, 1989) (Fig. 2.1C). Lastly, the largest known impact structures in the solar system are the so-called *multi-ring impact basins* (Fig. 2.1D; Spudis, 1993), whose origin is still vigorously debated.

The target impact structure for the current project, Araguainha, is currently regarded as an example of a peak-ring, complex impact structure (see Lana et al., 2007).

2.2. The cratering stages

The formation of impact craters is a continuous and ultra-rapid process. The traditional subdivision of the impact cratering process into three stages – (1) contact and compression, (2) excavation, and (3) modification (Fig. 2.2; also see, e.g., Melosh, 1989) – provides a practical and educational way to understand the different physical phenomena that happen in sequence and dominate in each stage, as they transition into one another. A brief overview of each cratering stage, primarily based on Melosh (1989), is provided below.

2.2.1. Contact and compression stage

The first and shortest cratering stage begins when the projectile strikes the target surface and ends after the high shock pressure has dissipated from the projectile, i.e., when compression ceases (Fig. 2.2A, B). During this stage, the target material is compressed, heated, and accelerated. Simultaneously, the projectile is decelerated by the target's resistance to penetration. Shock waves form at the projectile–target (contact) interface and propagate both into the target rocks and back into the projectile, creating shock pressures that far surpass the yield strengths of both. Additionally, a rarefaction (or tensional) wave is generated at the “free” upper surface of the projectile because of the shock wave reflection at this interface. This rarefaction wave travels back into the projectile and then into the target, relieving it from the high shock pressures.

The primary outcome of the contact and compression stage is the transference of the major part of the projectile's kinetic energy to the target material. As a result, this initial stage features high pressures, temperatures, and particle velocities – all confined to a volume related to the size of the projectile.

2.2.2. Excavation stage

The excavation stage – which lasts much longer than the previous contact and compression stage – begins immediately after the latter is finished, i.e., once the high shock pressure has been released from the projectile. During this stage, an approximately hemispherical shock wave (and the subsequent rarefaction wave) expands, initiating a subsonic excavation flow field that forms a bowl-shaped crater cavity, called the *transient cavity*. This cavity is typically many times larger than the diameter of the associated projectile. Another key feature formed during the excavation stage is the ejecta curtain, which blankets the area around the final crater (Fig. 2.2C, D, G, H).

2.2.3. Modification stage

The modification stage is the final and longest stage of cratering. It marks a transition from the excavation stage, meaning that some processes related to both the excavation and modification stages may overlap (for example, the initial formation of the central uplift). Therefore, defining the start of the modification stage can be a complex task. Generally, it is considered to begin when the transient cavity reaches its maximum radial extent at the target surface level (Kenkmann et al., 2012).

During the modification stage, the walls of the transient cavity collapse under the influence of gravity, which is the primary driving force of this stage. For small craters (i.e., simple craters), this collapse may cause loose material (debris) to slide down the steep interior walls of the crater (Fig. 2.2E, F). Conversely, for larger (complex) craters, there will be a central rebound of the most strongly compressed part of the target volume, along with the development of slumped, fault-bounded terraces on the crater walls (Fig. 2.2I, J).

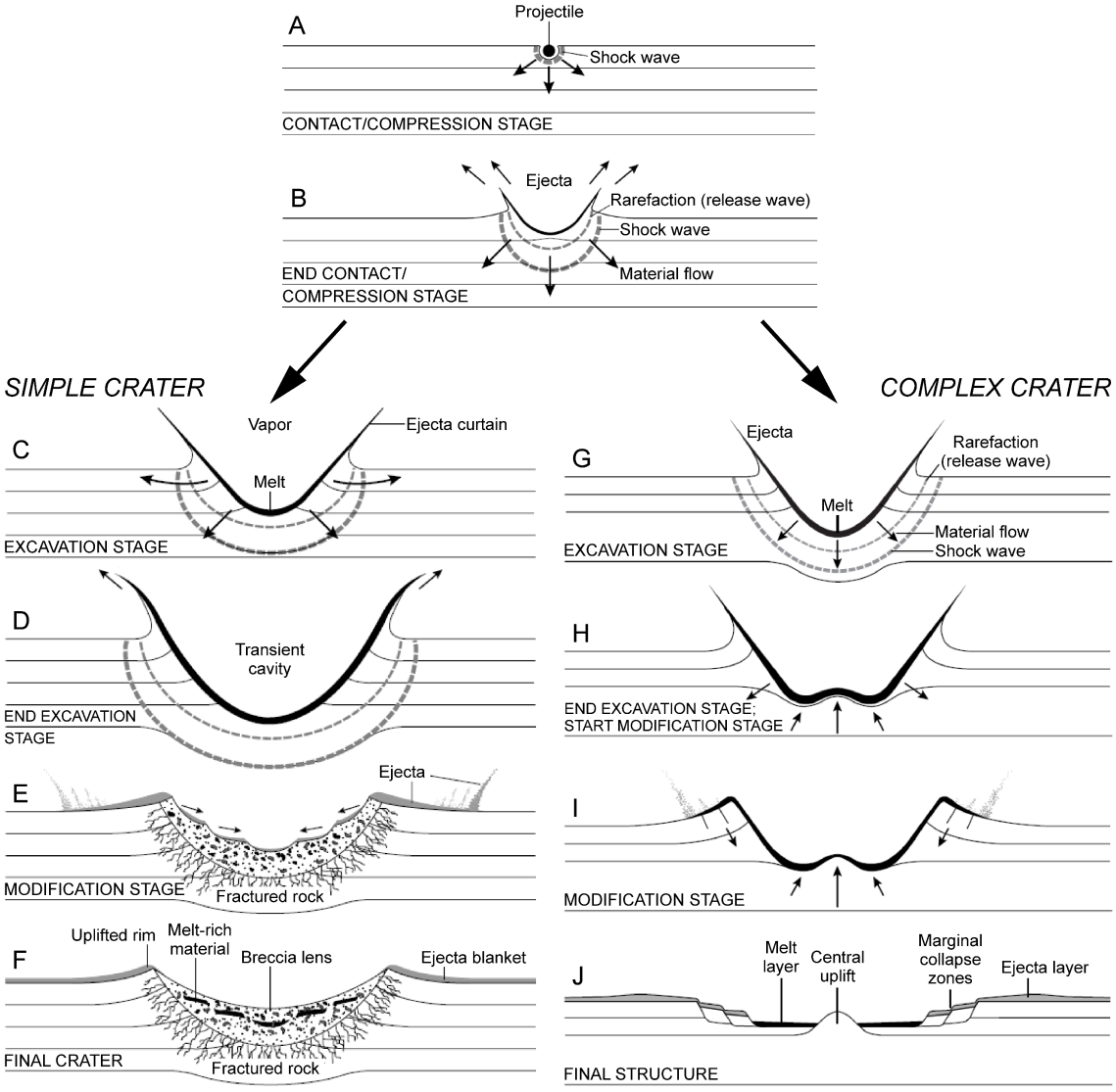

Figure 2.2. The progression of the three stages of crater formation (i.e., contact and compression; excavation; and modification) for simple and complex impact craters (modified from French, 1998). Refer to the text for an overview of each frame (A–J).

2.3. Morphostructural compartmentalization of complex impact craters

Comprehensive morphological and structural research on impact craters – on Earth and beyond – has been essential for advancing our understanding of how these features form and are classified, as well as for exploring the geological processes involved in each stage of cratering (see Kenkmann et al., 2014). Simple and complex impact craters exhibit notable morphological and structural differences (see Section 2.1 and references therein). These differences arise from their formation processes. They are mainly generated during the modification stage, which is particularly prominent in the case of complex impact craters and is influenced by several parameters and conditions, primarily the geology and rheology of the target (see Section 2.2 and references therein).

However, almost all impact structures on Earth are – to some degree – eroded, making it challenging to compare impact structures, especially between terrestrial ones and those from other planetary bodies, such as the Moon. On the other hand, erosion also provides opportunities for direct observations of the subsurface in deeply eroded terrestrial impact structures (see Kenkmann et al., 2014). In this context, variably eroded impact structures must be described using specific morphological and morphometric terms and definitions, as their structural features often do not represent the pristine morphological and morphometric characteristics of fresh (non-eroded) impact craters (see, e.g., Turtle et al., 2005).

Below, the first-order morphostructural domains (i.e., crater rim region, ring syncline, and central uplift or peak ring) and some of their associated structural inventories are described (Fig. 2.3), along with the recommended terms and definitions for properly describing the morphological and morphometric features and parameters of complex impact structures.

2.3.1. Crater rim region

The crater diameter is a key morphometric parameter closely related to the crater rim. For complex impact craters, the crater diameter is defined as "*the diameter of the topographic rim that rises above the outermost slump block not concealed by ejecta.*" (Osinski, 2012, p. 307). However, due to transient cavity collapse and the gradual cessation of deformation at the outer rim region of a crater, accurately defining the final rim of complex craters can be complicated (Kenkmann et al., 2012).

On most planetary bodies with low erosion rates (e.g., the Moon), crater diameter is fairly easy to determine; however, because of Earth's significant erosion rates and tectonic activity, defining crater diameter for terrestrial impact craters is more difficult (Turtle et al., 2005). Thus, the term *apparent crater diameter* was introduced and should be used (ibid). Osinski et al. (2022, p. 30) slightly revised this term's definition to "*the diameter of the outermost ring of (semi-)continuous concentric normal faults at the present-day erosional surface.*" These concentric normal faults commonly go through free-surface dip-slip toward the center of the structure, resulting in a slump terrace zone along the crater rim (Kenkmann et al., 2012) (see Fig. 2.3).

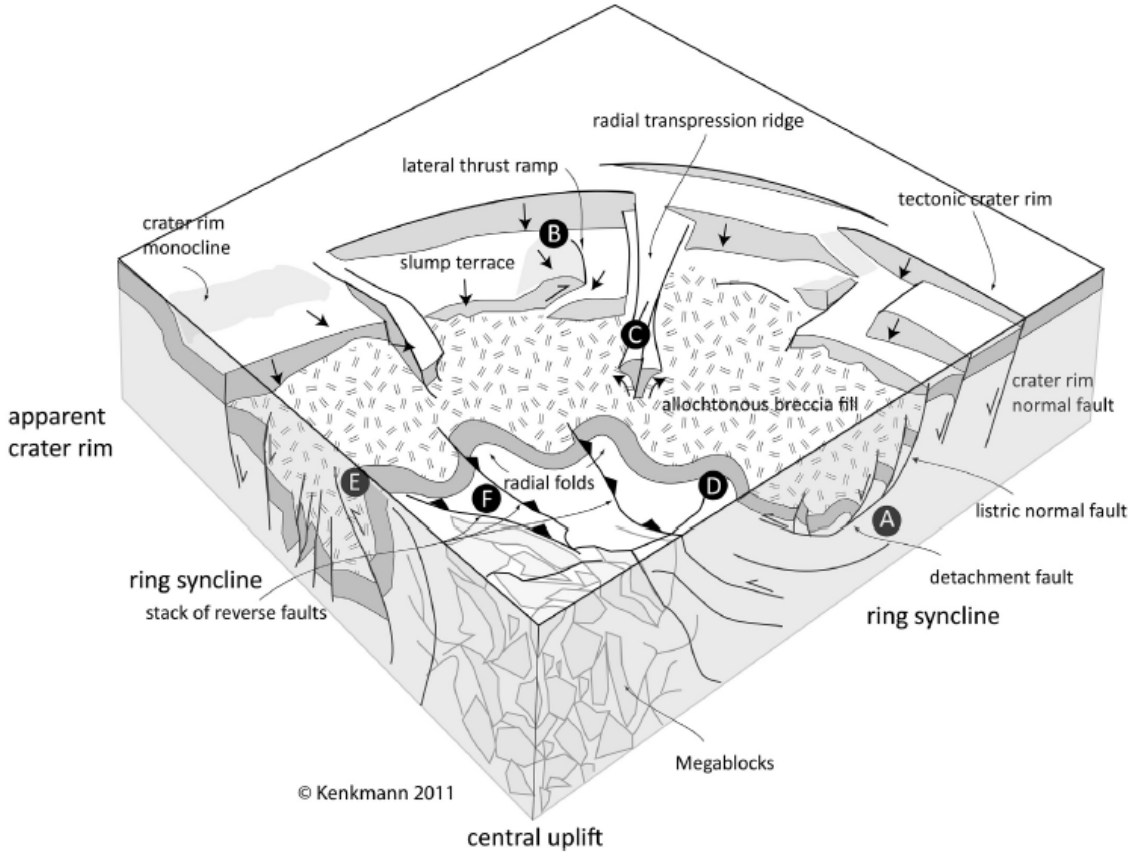

Figure 2.3. Schematic block diagram illustrating some structural features related to different first-order morphostructural domains (i.e., crater rim region, ring syncline, and central uplift) in a complex impact crater (after Kenkmann et al., 2014). Regions and structures in the diagram: A – Low-angle normal fault and detachment within the ring syncline; B – Lateral thrust ramps; C – Radial transpression ridge/positive flower structure; D – Radial folding with outward plunging fold hinges; E – Radial syncline with vertical to overturned plunging fold axis within the central uplift; and F – Imbrication of blocks thrust onto each other in the core of the central uplift. This current project aimed to identify this structural inventory, among other structures, in the different sections of the Araguainha impact structure.

However, one potential problem arises from this definition. Specifically, when there is no evidence of these outermost, concentric normal faults, how can the structure's apparent diameter be determined? Fortunately, alternative techniques can be employed to address this issue (see, e.g., Brenner et al., 2025). These authors used shatter cone apex orientation patterns and their radial distances from the apparent center of the structure to estimate – based on scaling laws (Osinski and Ferrière, 2016) – the ~16 km diameter of the recently discovered Miralga impact structure in Australia.

2.3.2. Ring syncline

Also called an *annular basin/trough* or *crater moat* in the literature, the ring syncline is the wide depression between the crater rim and the central uplift. Ring

synclines in terrestrial complex impact structures are rarely simple synforms; instead, in cross-sections, they commonly show asymmetry, with a steeply dipping – or even overturned – inner limb that transitions to the central uplift (Kenkmann et al., 2012) (see Fig. 2.3).

Within the ring syncline, the inward and downward movement of material is usually indicated by the displacement of structural features associated with the modification stage of crater formation (ibid). Therefore, ring synclines may consist of several fault-bounded segments or blocks, with normal faults of nearly concentric strikes often appearing between the crater rim and the axis of the ring syncline. These concentric normal faults usually turn crater-ward into a listric geometry, merging into low-angle detachment faults at depth in stratified target rocks, with the sedimentary bedding surfaces often serving as glide planes. This helps compensate for the inward-directed material movement during crater collapse (Kenkmann et al., 2012) (see region A in Fig. 2.3).

Due to the quasi-concurrent formation of the central uplift and the collapsing rock volumes moving toward the center of the structure from the outer rim region, the amount of constriction – and thus the structural complexity within the ring syncline – increases toward the center of the structure (Kenkmann et al., 2012). The resulting inward-directed movement of large rock volumes creates a space problem that, in turn, can be compensated either by the transformation of low-angle detachments into outward-dipping reverse faults along the inner limb of the ring syncline (Jahn and Riller, 2009), development of radial transpression ridges (Kenkmann and von Dalwigk, 2000), through tight folding, or by plastic flow (Kenkmann et al., 2012).

2.3.3. Central uplift

The central uplift refers to the target rocks near the center of a complex impact crater that are raised above their pre-impact stratigraphic level (Osinski, 2012). The term *central uplift* is the appropriate term when describing most impact structures on Earth, as it does not depict the surface morphology of a pristine impact crater; in contrast, the term *central peak* should be used only if the central uplift appears as a single peak or a closely grouped set of peaks that emerge from the surrounding allochthonous crater-fill impactites (Osinski, 2012).

Therefore, the term *central peak* is probably not adequate to describe the central uplift of most terrestrial complex impact structures, as these are commonly eroded to

some degree, and as the collapse of the initial central uplift may give rise to a structurally and morphologically complex mountainous terrain (ibid). Furthermore, it is worth noting that the central uplifts of Earth's complex impact structures may never have looked like those of pristine lunar complex craters, as the former – despite being eroded – also seem to have originally had a more subdued morphology and form because of the higher gravity on our planet (Osinski et al., 2022).

Within central uplift structures, the most significant deformation occurs during the modification stage (Kenkmann et al., 2012). There are clear differences between the uplift of crystalline and sedimentary target rocks; in the former, there is a dominance of faulting due to the competence of the material, whereas in the latter, folding may be the prevailing deformation mechanism (ibid). However, due to space limitations toward the crater's center, sedimentary rock-dominated central uplift structures may show a gradual increase in fold tightness, the development of reverse faults within the fold cores, and smaller fault blocks toward the center (Kenkmann et al., 2012, and references therein).

The gravitational collapse of an oversteepened central uplift may lead to the formation of several other deformation features, such as (1) overturning of strata in the central uplift periphery (e.g., Lana et al., 2003; Wieland et al., 2005; Gibson and Reimold, 2008; Jahn and Riller, 2009; Manzi et al., 2021); (2) normal shear zones in the central volume that dip outward and offset uplifted strata (e.g., Osinski and Spray, 2005); (3) radial transtension troughs (e.g., Kenkmann and von Dalwigk, 2000); and (4) outward kinking and buckle folding of uplifted strata (Kenkmann et al., 2012) (see Fig. 2.3).

A useful morphometric parameter associated with a central uplift is the so-called *stratigraphic uplift* (SU), which is defined as "*the observed amount of uplift undergone by the deepest marker horizon now exposed in the center of a complex structure.*" (Grieve et al., 1981, p. 43). In a recent analysis of 53 terrestrial complex impact structures, Osinski et al. (2022) proposed a new relationship to calculate the stratigraphic uplift: $SU = 0.0945D^{0.6862}$, where D represents the crater diameter. As these authors note, this new value is slightly lower than previously published estimates (e.g., Grieve et al., 1981; Grieve and Pilkington, 1996; Kenkmann, 2021) due to more accurate diameter estimates and the variable effects of erosion. Additionally, it is worth noting that the perceived stratigraphic uplift decreases with increased erosion (Kenkmann et al., 2012). In contrast, the ratio of the central uplift diameter to the apparent crater diameter increases with erosion (Kurta et al., 2009).

2.3.4. Peak ring

A peak ring (also called an *inner ring*; Hartmann and Wood, 1971) is a commonly discontinuous ring of mountains located between, and concentric with, the crater center and rim (Turtle et al., 2005). Peak-ring structures are part of a morphological transition that occurs as crater diameter increases, evolving from complex craters with a central peak to multi-ring basins (see Fig. 2.1B–D). This transition passes through the so-called *protobasins*, which are transitional craters featuring a small peak ring surrounding a central peak (see, e.g., Baker et al., 2016). The topographic profiles of peak rings generally display similar inward- and outward-facing slopes (Turtle et al., 2005).

Peak ring formation is a highly debated topic (e.g., Baker et al., 2016, and references therein). There are two main models for their formation: (1) the hydrodynamic collapse of an unstable central uplift (e.g., Melosh, 1989) and (2) the modification and collapse of a nested impact melt cavity (e.g., Cintala and Grieve, 1998). It is worth noting that the former model is commonly invoked to explain peak rings in terrestrial impact structures, such as for the Chicxulub impact structure (e.g., Morgan et al., 2016).

CHAPTER 3

MATERIALS AND METHODS

CHAPTER 3 – MATERIALS AND METHODS

Figure 3.1 summarizes the main data types used, techniques applied, and their outputs in this project. For details, the reader should refer to the "Materials and Methods" sections of research articles 1 and 2, found in chapters 4 and 5 of this thesis.

The main objectives and questions for this project were refined in conjunction with the literature review and data compilation (see the first row of panels in Fig. 3.1). Three main types of data – i.e., geological fieldwork, remote sensing, and geophysical – were collected and/or prepared (see the second row of panels in Fig. 3.1). For each dataset, different products, including spreadsheets, imagery, and maps, were created (see the third row of panels in Fig. 3.1). These products were then integrated and analyzed, yielding various outputs, including a geological map and geological-structural profiles of the AIS, stereograms, and rose diagrams of lineaments and structural data (see the fourth row of panels in Fig. 3.1). Additionally, the shape extraction, analysis, and results of the (apparent) rim trace for the AIS were conducted through an integrated study of the geology and remote sensing products and results (see dashed arrows in Fig. 3.1).

The geological results, and part of the remote sensing results, were first interpreted and discussed, culminating in Research Article 1 (Chapter 4) of this project. The information and knowledge gained from Research Article 1 were combined with additional remote sensing and geophysical results, as well as the AIS rim trace shape results, to produce Research Article 2 (Chapter 5). Insights from both articles were then used to briefly discuss the Araguainha impact structure as potentially resulting from an oblique impact, and its implications (Chapter 6). Finally, the main outputs and final remarks of this project were summarized in Chapter 7 (see the bottom part of Fig. 3.1).

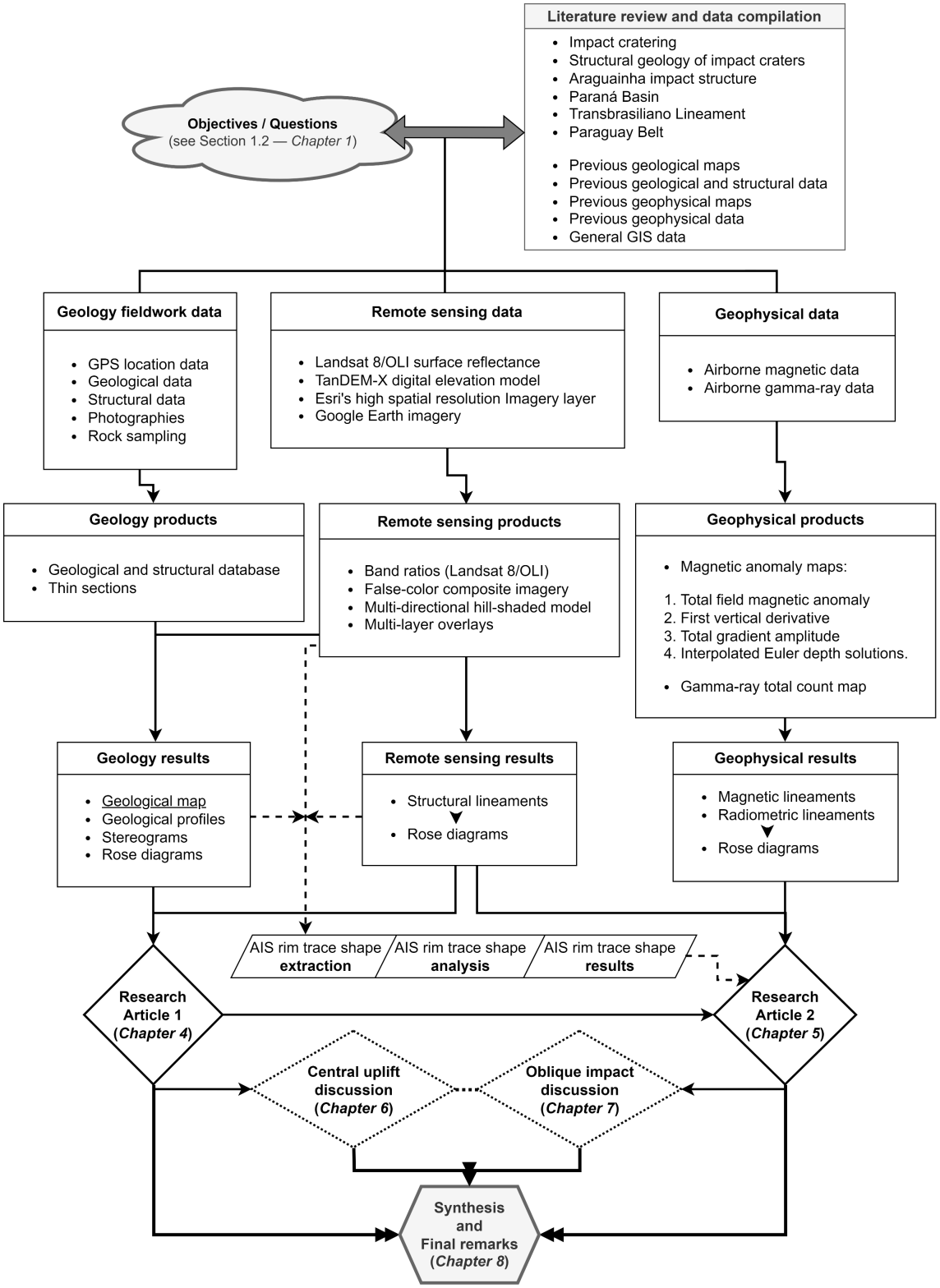

Figure 3.1. Flowchart of the data and techniques used to achieve the objectives of this project. See text for details.

CHAPTER 4

RESEARCH ARTICLE 1

CHAPTER 4 – RESEARCH ARTICLE 1

This manuscript was initially published online in the journal "GSA Bulletin" in 2025:

Bernardes, R.B., Reimold, W.U., Gibson, R.L., Hauser, N., and Pavanetto, P., 2025, New insights into the geology and formation of the Araguainha impact structure, Brazil, from morphological and structural analysis: Geological Society of America Bulletin, 29 p., doi:10.1130/B38443.1.

New insights into the geology and formation of the Araguainha impact structure, Brazil, from morphological and structural analysis

R.B. Bernardes[1*], W.U. Reimold[1], R.L. Gibson[2], N. Hauser[1], and P. Pavanetto[3]

[1]University of Brasilia, Institute of Geosciences, Postgraduate Program in Geology, Campus Universitário Darcy Ribeiro, Brasilia, DF 70910-900, Brazil

[2]School of Geosciences, University of the Witwatersrand, Johannesburg 2050, South Africa

[3]Universidade Federal do Amazonas, Departamento de Geociências, Programa de Pós-graduação em Geociências, Manaus, AM 69077-000, Brazil

[*]Corresponding author (renato.bernardes@unb.br)

Abstract

Recent roadworks across the 40-km-wide Araguainha impact structure (AIS) provided new, extensive exposures for mapping and structural analysis. We present an updated geological map of the AIS, highlighting Passa Dois Group Blocks (PDGBs) and the central uplift geology. Mapping indicates that faults outside the AIS likely result from pre-impact regional tectonics. The most prominent structural features in the AIS are primarily linked to the excavation and modification stages of cratering, with strain likely accommodated through detachments along interfaces between lithologic units with different rheologies. The outer rim and intermediate sections of the structure exhibit similar structural frameworks, where large, fault-bounded blocks dominate. PDGBs generally have quasi-centripetal structural vergences. In the outer rim region, PDGBs resemble gravity-driven complex slumps. There is no consistent evidence for the previously referred kilometer-scale concentric rings in the outer parts of the AIS, which had been surmised as evidence for a peak-ring configuration. PDGBs occur only between 10 km and 20 km from the structure's center, as a result of concurrent central uplift

formation and crater rim collapse. The central uplift diameter is estimated at up to 20 km, and there is evidence for its asymmetric collapse. Besides rare injections of impact melt rock, the northern core comprises three types of impact breccia (suevite and polymict lithic breccia). The core can be divided into a structurally diverse megablock zone that overlies a seemingly coherent but folded and faulted crater floor of (meta)sedimentary basement. The AIS exhibits structural asymmetry that may be controlled, in part, by pre-impact anisotropy of the target.

INTRODUCTION

Impact cratering is a highly dynamic process of ubiquitous planetary importance (e.g., Melosh, 1989; Osinski and Pierazzo, 2012; Kenkmann, 2021). Geological-structural mapping of terrestrial impact structures is crucial for advancing our understanding of the impact cratering process. Comprehensively mapped terrestrial impact sites are also essential because they are the only available field analogs for planetary impact studies (Lambert and Reimold, 2023). Mapping of terrestrial impact structures typically involves field-based geological observations and interpretation, representative rock sampling, and sample analysis, all conducted in conjunction with multi-sensor image analysis (e.g., Kenkmann et al., 2014). However, detailed mapping studies of large (>30 km diameter), complex impact structures are relatively rare. Their outcomes may provide significant insights into the deformation mechanisms and kinematics that operate during the different stages (i.e., contact and compression, excavation, and modification; see Melosh, 1989) of the cratering process at various scales.

The Araguainha impact structure (AIS) (Fig. 1), centered at 52.99151°W, 16.81544°S, in Central-West Brazil, is the erosional remnant of the largest impact structure known in South America. A recent overview of the structure is found in Crósta et al. (2019). Evidence of impact comprises ample occurrences of shatter cones (Crósta et al., 1981) and varied shock metamorphic evidence, including in quartz and zircon (e.g., Hauser et al., 2019). The ~40-km-wide structure was formed at ca. 259–252 Ma (Tohver et al., 2012; Erickson et al., 2017; Hauser et al., 2019) in the NNW part of the intracontinental Paraná Basin (inset, Fig. 1). The AIS has been geologically and structurally investigated since the early 1980s (e.g., Crósta et al., 1981; Theilen-Willige, 1981; von Engelhardt et al., 1992; Lana et al. 2006, 2007, 2008; Machado et al., 2009; UnB-IG, 2012; Hippertt et al., 2014; Silva et al., 2016; Souza et al., 2024).

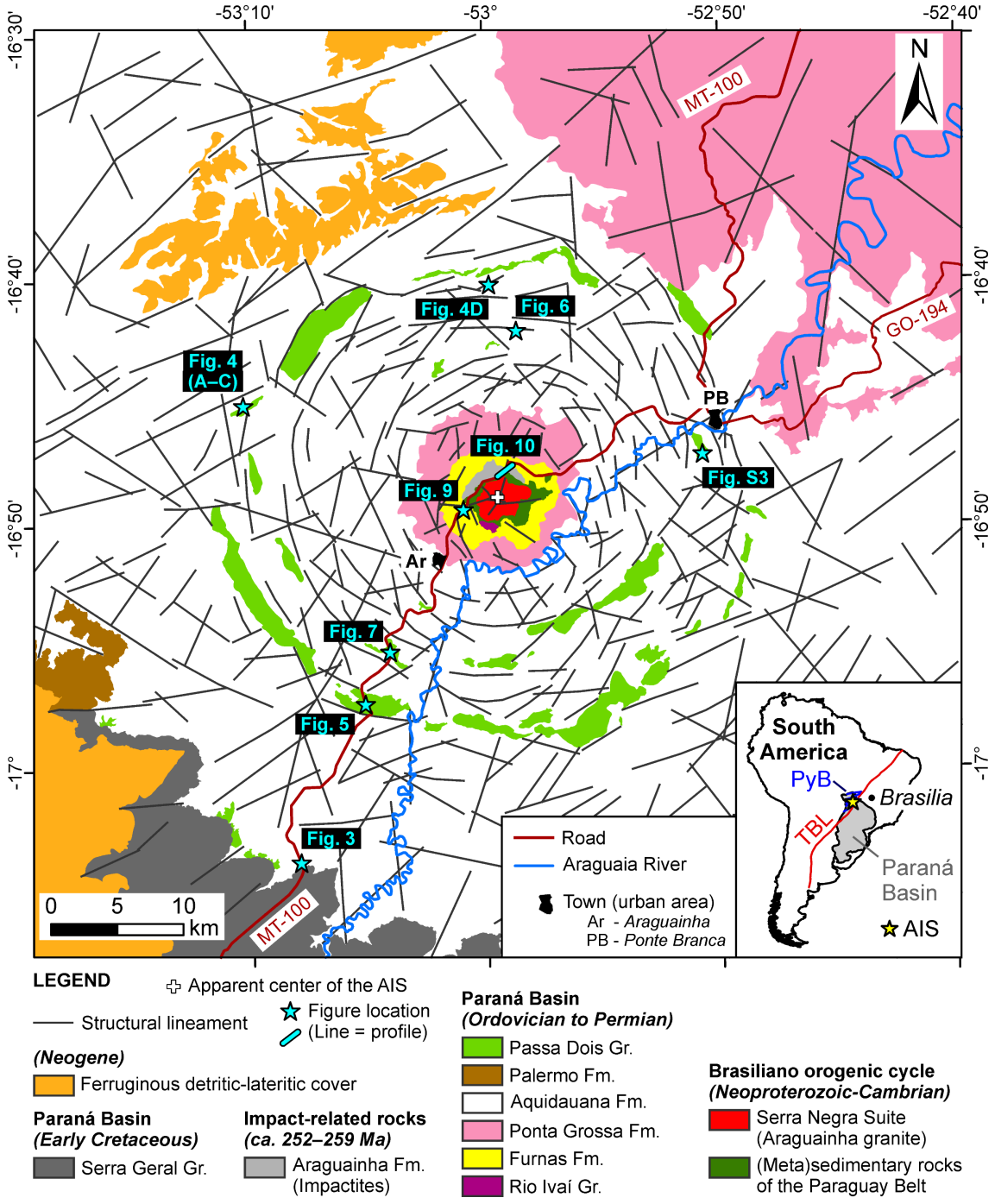

Figure 1. Updated geological map of the Araguainha impact structure (AIS) and environs in the NNW Paraná Basin (based on maps of: CPRM, 1981; Lana et al., 2007, 2008; UnB-IG, 2012; Thomé Filho et al., 2012; Horn et al., 2022; Souza et al., 2024; as well as own field-based data and remote sensing analysis). Map coordinate system: WGS84. See Fig. 2 for details on the stratigraphic units. The AIS is intersected by the MT-100 state road and the Araguaia River. Note the location of Araguainha and Ponte Branca towns. Inset (bottom right): Location of the AIS in the NNW Paraná Basin (base map from Cordani et al., 2016). TBL – Transbrasiliano Lineament. PyB – Paraguay Belt.

Previous works have contributed many observations on the various parts of the AIS, and at different scales. However, most of these studies were hampered by a lack of

continuous and well-preserved exposures that would have allowed the identification of wider structural and impact-related features. This problem, in part, arises from the tropical weathering conditions typical of this region, especially forceful rainy seasons characterized by high humidity and high temperatures, and consequently widespread dense vegetation. The current geological-structural knowledge of the AIS generally relies on small and dispersed outcrops that are commonly located kilometers apart throughout the structure. This has significantly hindered the development of more detailed models for this impact structure, relating, for example, to topics such as the sizes of both the central uplift and the impact structure itself, the nature of the ring syncline, verification of the existence of concentric rings, and the mechanisms of formation of the prominent Passa Dois Group "blocks".

Between 2020 and 2022, however, comprehensive roadworks along the MT-100 state road that transects the entire impact structure from SW to NE generated extensive new outcrops. These new exposures have provided a new perspective on pre- and post-impact geology and impact-related deformation, particularly along the northern part of the central uplift, which displays a markedly complex geology. Souza et al. (2024) were the first to report on some of these new outcrops.

Here, we present the results of our extensive geological-structural mapping within and outside the AIS. We document the still relatively new exposures, ensuring the preservation of their geological record before they become irreversibly altered by human activity and the rapid degradation from tropical weathering. We have built upon the central uplift geological map of the AIS by Souza et al. (2024), notably further refining the mapping of the geology beyond the central uplift area.

We have identified several key topics of discussion, such as the nature of the structures outside the AIS, the structural frameworks of the outer rim region and ring syncline, the existence of the alleged (see Lana et al., 2007) concentric rings in the interior of the structure, the complex nature of the Passa Dois Group Blocks, and the size and deformation of the central uplift. We conclude that the AIS is a structurally asymmetric impact structure and that this asymmetry may, in part, be related to the pre-impact geological anisotropy of the target region.

BACKGROUND

Regional Geology

The Araguainha impact structure (AIS) straddles the border between Mato Grosso and Goiás states in Central-West Brazil (Fig. 1). The AIS formed in the lithosequences of the NNW part of the cratonic, Phanerozoic Paraná Basin (e.g., Zalán et al., 1990; Horn et al., 2022). These strata overlie the basement of the basin, which has been recently related to the Neoproterozoic–Cambrian Paraguay Belt (Souza et al., 2024, and references therein).

The Paraná Basin fill comprises a sedimentary-magmatic sequence with a maximum thickness of ~7 km in the basin center, of which almost 2 km are basaltic flows and intrusions (Milani et al., 2007) of the ca. 134 Ma (Gomes and Vasconcelos, 2021) Serra Geral Group (Gr.; see Rossetti et al., 2018). The stratigraphic record of the basin sequence has been divided into six supersequences that are delimited by unconformities: Rio Ivaí (Ordovician–Silurian), Paraná (Devonian), Gondwana I (Carboniferous–Early Triassic), Gondwana II (Middle to Late Triassic), Gondwana III (Late Jurassic–Early Cretaceous), and Bauru (Late Cretaceous) (see Milani et al., 2007). Some authors consider the topmost Late Cretaceous supersequence as the fill of a separate basin – the Bauru Basin (e.g., Menegazzo et al., 2016).

Besides the Early Cretaceous Serra Geral Gr., only the oldest three supersequences of the Paraná Basin are present in the immediate AIS region (see the up-to-date map of the basin by Horn et al., 2022). This is also supported by a Petrobras drill core (2-AG-1-MT) obtained approximately 50 km WSW of the center of the AIS, in the Alto Garças region of Mato Grosso state (Thomé Filho et al., 2012). Figure 2 summarizes the general stratigraphic framework of the rock units identified within the AIS.

The Rio Ivaí supersequence (Rio Ivaí Gr.) comprises three lithostratigraphic units (Assine et al., 1994): the Alto Garças, Iapó, and Vila Maria formations. This group's occurrence within the AIS is restricted to some patches in the central region of the structure, as mapped by students and staff of the University of Brasilia, Brazil (UnB-IG, 2012). They identified conglomerate, diamictite, sandstones, and siltstones associated with this group, which may comprise a sedimentary pile of estimated 50 m thickness.

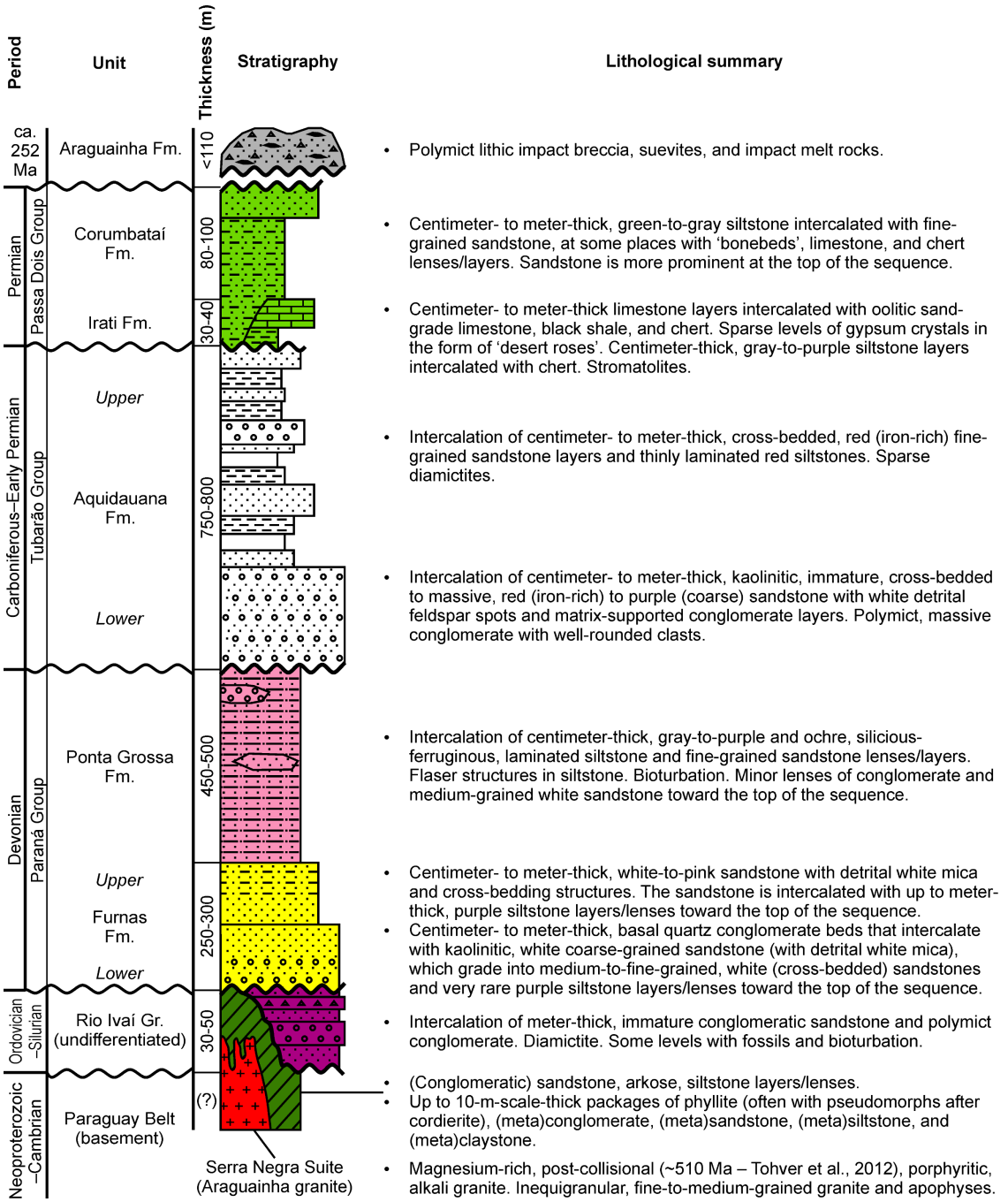

Figure 2. Schematic stratigraphic column and lithological summary of the geological units in the Araguainha impact structure (based on Lana et al., 2007; Tohver et al., 2012; UnB-IG, 2012; Silva et al., 2016; Souza et al., 2024; and own observations). The color codes correspond to those of Fig. 1. Wavy, thick black lines indicate regional unconformities in the Paraná Basin sequence (see Milani et al., 2007).

The Paraná supersequence (Paraná Gr.) generally overlies the Rio Ivaí Gr. strata but is also found in direct contact with the basement of the basin (Milani et al., 2007). The Paraná Gr. is divided into the lower, sand-dominated Furnas Formation (Fm.) and the upper, mud-dominated Ponta Grossa Formation. The Furnas Fm. is predominantly composed of white, medium to coarse, quartz-rich, kaolinitic sandstones with different

types of cross-stratification (Milani et al., 2007). The topmost portion of the Furnas Fm. shows evidence of a gradual transition toward the mainly pelitic Ponta Grossa Formation. This latter formation is subdivided, from bottom to top, into three members (Lange and Petri, 1967): the Jaguariaíva Member, a shale package with fine psammite lenses; the psammitic to pelitic Tibagi Member; and the São Domingos Member, which is mainly composed of pelites. Furnas and Ponta Grossa formations are prominent in the outer section of the central uplift of the AIS (compare Fig. 1).

The Gondwana I supersequence encompasses the thickest sedimentary pile within the Paraná Basin. Deposition started in a marine environment with prominent glacially influenced sedimentation in the Carboniferous, followed by an arid continental interior already in the Early Triassic (Milani et al., 2007). In the AIS region, this supersequence is primarily represented by the Aquidauana Fm., remnants of the Palermo Fm., and some overlying units of the Passa Dois Gr.

The Aquidauana Fm. mainly consists of red sandstones with different textures, diamictites, siltstones, claystones, and rhythmites (Gesicki et al., 2002; Barros et al., 2021), with more pelitic units predominant in the upper parts of the formation (Fig. 2). The Palermo Fm. is not found within the AIS but occurs in a local plateau at ~9.5 km outside the WSW part of the outer rim of the AIS (Fig. 1; see Horn et al., 2022). This formation consists of bioturbated, gray to ochre (sandy) siltstones, fine-grained sandstones with hummocky cross-stratification, and dark gray shales (Milani et al., 2007).

The Passa Dois Gr. is a Paraná Basin-wide unit encompassing several formations, with a maximum thickness of ~1700 m (Milani et al., 2007). In the AIS region, this group has an estimated thickness of only some tens of meters (based on the stratigraphy of the 2-AG-1-MT drill core), with only two recognized formations: the basal Irati Fm. and the overlying Corumbataí Formation. The entire Irati Fm. has a thickness of no more than 70 m in the basin (Milani et al., 2007). It is divided into: (1) a lower, siliciclastic unit – the Taquaral Member, which consists of dark gray non-bituminous shale, siltstones, and sandstones; and (2) an upper, carbonate-bearing unit – the Assistência Member, which mainly consists of black bituminous shales interlayered with carbonates and evaporites (Holz et al., 2010; Callefo et al., 2018; Cagliari et al., 2022). The Assistência Member includes a bentonitic volcanic ash level that has been dated to 280–276 Ma (Santos et al., 2006; Rocha-Campos et al., 2019; Bastos et al., 2021; Cagliari et al., 2022).

The Corumbataí Fm., the northern lateral equivalent to the Teresina Fm. of the basin (e.g., Milani et al., 2007; Warren et al., 2015), indicates the establishment of continental depositional systems in the Paraná Basin during the Late Permian (e.g., Milani et al., 2007; Montibeller et al., 2020). Far southeast of the study region, this formation has a mean estimated thickness of about 90 m (Warren et al., 2015). It is essentially composed of red-brown to purple, pink, and gray varieties of mudstones (mainly siltstones) intercalated with subordinate layers of very-fine-grained sandstones and carbonates (Warren et al., 2015; Zanardo et al., 2016; Montibeller et al., 2020).

Estimates for the depositional age of the Corumbataí Fm. are not as constrained as those for the Irati Fm. and are mainly based on biostratigraphy, besides detrital zircon and dual-polarity remanent magnetization dating. Overall, depositional ages less than 265 Ma have been indicated for the Corumbataí Fm. (see Tohver et al., 2018). Kern et al. (2021) provided a detrital zircon U-Pb maximum depositional age of 254 ± 2.58 Ma for the Teresina Formation. Furthermore, U-Pb dating of zircons of allegedly volcanogenic ash of syn-depositional origin yielded an age of 257.5 ± 2.2 Ma for the uppermost Corumbataí Fm. (Fernandes, 2007). In the N part of the Paraná Basin, the Corumbataí Fm. directly overlies the Irati Fm. (Tohver et al., 2018) and represents the topmost basin unit currently recognized within the AIS (i.e., the uppermost unit directly affected by the impact event; Lana et al., 2007).

Lana et al. (2008) and UnB-IG (2012) reported the occurrence of chert in the Passa Dois Gr. within the AIS, and stromatolitic growths have been identified in association with this chert (UnB-IG, 2012; Souza et al., 2024). Attempts have been made to map the Irati and Corumbataí formations within the AIS separately (e.g., geological maps of CPRM, 1981; Thomé Filho et al., 2012). However, these units are commonly too strongly deformed (i.e., folded, faulted, and brecciated) and weathered (Lana et al., 2008; this work).

The total thickness of the Paraná Basin sedimentary pile in the area of the AIS is poorly constrained. The most comprehensive thickness data come from the 2-AG-1-MT borehole, some 50 km WSW of the center of the AIS. This drill core provided the following thicknesses: Rio Ivaí Gr. (241 m), Furnas Fm. (254 m), Ponta Grossa Fm. (467 m), Aquidauana Fm. (804 m), Irati Fm. (61 m), and Corumbataí Fm. (>96 m) (Thomé Filho et al., 2012). Together, these units form an ~1920-m-thick sedimentary pile that overlies the basement in the AIS region.

Besides the sedimentary units of the Paraná Basin, the AIS also exposes rocks from the basement of the basin (Souza et al., 2024). In the innermost part of the central uplift, a granitic body (see below) that intruded (meta)sedimentary rocks occurs. (Meta)sedimentary rocks (phyllites, [meta]arkoses, and [meta]sandstones) of likely pre-Furnas Fm. age were first reported in this region by Swietlik (1989). In recent decades, these rocks have been assigned to the Cuiabá Gr. of the Paraguay Belt (Sánchez, 2006; Yokoyama et al., 2012; UnB-IG, 2012; Souza et al., 2024). However, Souza et al. (2024) suggest the existence of a second, unmetamorphosed sedimentary sequence of psammites and pelites within the central uplift of the AIS. These authors argue that this sequence could alternatively belong to the topmost (youngest), unmetamorphosed section of the Paraguay Belt or to the basal units of the Paraná Basin (i.e., Rio Ivaí Gr. and/or Furnas Fm.). In this work, we will use the term *(meta)sedimentary basement* to collectively refer to the (meta)sedimentary rocks presented in this paragraph.

The Paraguay Belt is a Brasiliano/Pan-African fold-and-thrust belt exposed along the SE border of the Amazon Craton and the NW margin of the Paraná Basin (inset, Fig. 1). The belt had a protracted depositional and deformational evolution during Neoproterozoic–Cambrian times (e.g., Alvarenga and Trompette, 1993; McGee et al., 2015; D'el-Rey Silva et al., 2016; Frugis et al., 2024).

Intruded into the (meta)sedimentary basement is a Late Cambrian (509.5 ± 12.0 Ma; Tohver et al., 2012), Mg-rich, post-collisional alkali granite (Silva et al., 2016) that is locally known as the Araguainha granite. It forms the predominant lithology within the core of the central uplift. However, extensive and well-preserved exposures of the granite are scarce in this largely agricultural terrain. The granite is porphyritic, with K-feldspar megacrysts up to 6 cm in length, quartz, albitic plagioclase, biotite, and muscovite as major mineral constituents, and Fe-Ti oxides, zircon, monazite, and locally tourmaline as accessory minerals (Crósta et al., 1981; von Engelhardt et al., 1992; Machado et al., 2009; Silva et al., 2016). Due to its location, age, and geochemistry, the Araguainha granite has been commonly assigned to the Serra Negra suite (Lacerda Filho et al., 2004), which encompasses several post-collisional, high-K granitic rocks related to the Goiás Magmatic Arc in Central-West Brazil (e.g., Pimentel et al., 1996).

Impact-related Rocks

Substantial exposures of impactites occur mainly in a swath from the W to the NE around the central granitic core, whereas such deposits are much sparser in the southern part (Souza et al., 2024; compare Fig. 1). The recent study by Souza et al. (2024) updated the geology of the central uplift of the AIS. The work focused on impact-related rocks, such as polymict impact breccia and impact melt rocks, and their relationships with the crater floor and the underlying basement of the basin. The micro- and macroclasts in the polymict impact breccia package are likely derived from the lowermost sequences of the Paraná Basin and, to a large proportion, from the (meta)sedimentary rocks of the basement. Granite clasts in the polymict impact breccia are scarce and may only represent material from more fine-grained apophyses that extend into the (meta)sedimentary basement (Souza et al., 2024).

Historically, *polymict impact breccias* have been described from the AIS (e.g., von Engelhardt et al., 1992). A distinction between melt-bearing suevite and lithic impact breccias (Stöffler and Grieve, 2007) has generally not been attempted. Souza et al. (2024), however, identified polymict impact breccia with melt rock clasts and, thus, reported the presence of suevite in a breccia column with an integrated height of up to 110 m in the northern outer part of the core of the central uplift. These authors also identified three types of impact melt rock (IMR): (1) IMR Type-I, formed from alkali granite and likely representing a pseudotachylitic breccia, possibly formed by decompression melting during uplift in the modification stage (see, e.g., Reimold et al., 2016, 2017); (2) IMR Type-II, formed from (meta)sandstone of the lowermost Paraná Basin formations and the basement that underwent shock melting (partial or total); and (3) IMR Type-III, a silicic melt rock probably derived by shock melting of conglomeratic rocks and sandstone of the lowermost basin strata.

Von Engelhardt et al. (1992) described an extensive occurrence of monomict impact breccia, derived from quartz sandstones, along the S to SE sectors of the core of the central uplift. However, subsequent works did not confirm the occurrence of this unit (Yokoyama et al., 2012; Hauser et al., 2019; Souza et al., 2024). Souza et al. (2024) reclassified this area as (meta)sedimentary basement. Machado et al. (2009) proposed the existence of a "melt sheet" above the granitic core of the central uplift, a concept that was disputed by Souza et al. (2024). These latter authors classify this material as “transitional granite” (after Fischer, 2015) or “part-melted” granite, suggesting it could have formed

due to a thermal overprint on the Araguainha granite from an originally overlying, hot impact melt rock.

Several types of shock metamorphic features – i.e., shatter cones, extensive development of kink bands in biotite (by themselves, not impact diagnostic), planar fractures, planar deformation features in quartz, planar deformation features in feldspar, and shock features in zircon, including the presence of FRIGN (former reidite in granular neoblastic) zircon – have been described in different rocks of the central uplift (see Crósta et al., 1981, 2019; von Engelhardt et al., 1992; Machado et al., 2009; Hauser et al., 2019; Souza et al., 2024). Shock microdeformation features in quartz from the Araguainha granite have been interpreted to indicate peak shock pressures of up to 20–25 GPa (von Engelhardt et al., 1992; Souza et al., 2024). An earlier study reported a shock pressure of 27 ± 1 GPa for quartz and a maximum shock pressure of <32 GPa for albite from brecciated alkali granite at the center of the AIS (Martinez et al., 1991). Multiple sets of planar shock deformation features in zircon and the presence of FRIGN zircon in IMR Type-III indicate a shock pressure of at least 30 GPa (Hauser et al., 2019).

Previous Morphostructural Geological Studies in the Araguainha Impact Structure

Lana et al. (2006, 2007, 2008) provided the most extensive discussions of morphology and structure available to date for the AIS. Despite an estimated differential erosion of about 250–350 m from the original post-impact surface, based on stratigraphic and structural observations (Lana et al., 2007), the structure still displays an apparent outer morphological rim and a topographically elevated central region. The major morphological features of the AIS can still be derived from a combination of remote sensing and field geological observations.

The currently most invoked (e.g., Crósta et al., 2019) morphostructural compartmentalization for the AIS, after Lana et al. (2007), postulates a 40-km-diameter, peak-ring structure with: (1) a 10–12-km-diameter central uplift; (2) a 5-km-wide annular basin around the central uplift; and (3) a not-formally-named “outer region” comprising two concentric ring structures. The apparent outer rim occurs at ~20–22 km from the center of the structure.

However, some workers have considered that the central uplift may be wider (see Lana et al., 2008; Miyazaki et al., 2021). Based on gravity data, Miyazaki et al. (2021) proposed an ~16-km-wide central uplift. This implies that some basal portion of the

Aquidauana Fm. – which outcrops from ~6 km of the center of the structure (compare Fig. 1) – could also be part of the central uplift (see also Lana et al., 2008).

The apparent outer rim is marked by several kilometer-scale, concentrically and radially faulted blocks of the upper Aquidauana Fm., which are locally juxtaposed with Passa Dois Gr. rocks (Crósta et al., 1981; von Engelhardt et al., 1992; Lana et al., 2007, 2008). The gentle folds or shallowly dipping monoclines observed in this outermost region are interpreted to have formed during crater excavation or as a result of the modification stage of cratering. Following the initial formation of these structures, kilometer-scale fault-bounded blocks were created during the collapse of the transient cavity when lateral inward-directed movement took place (Lana et al., 2008). No evidence of low-angle detachment faults that might be associated with such blocks (see Kenkmann et al., 2000) has been found at the present erosion level (Lana et al., 2008).

Bedding orientation data for the Aquidauana Fm. in the apparent outer rim region revealed that the strata are buckled, with shallow (5°–10°) dips inward or outward (Lana et al., 2006, 2008). Generally, the Passa Dois Gr. strata dip shallowly toward the crater rim (Lana et al., 2008). Lana et al. (2008) maintained that the overall fold geometry of the Aquidauana Fm. and Passa Dois Gr. strata along the apparent outer rim is compatible with large-scale, layer-parallel shortening of these units during the inward collapse of the fault-bounded blocks. However, outcrop-scale folds and small-scale intrafolial folds revealed more complexities (Lana et al., 2008). The outcrop-scale folds exhibit an open-to-tight recumbent geometry, with shallowly plunging fold hinges that are obliquely to tangentially oriented with respect to the orientation of the apparent crater rim. Meanwhile, the intrafolial folds are compatible with non-coaxial deformation due to the differential movement of the Passa Dois Gr. rocks toward the center of the structure. Shifts from a mainly concentric bedding direction emerge locally near radial faults, where Passa Dois Gr. bedding dips parallel to the fault surface (Lana et al., 2008).

Lana et al. (2007) proposed two concentric rings in the Aquidauana Fm. rocks at distances of 18–14 km (outer ring) and 12–10 km (inner ring) from the center of the structure. According to these authors, structural data indicated that the outer ring consists of a kilometer-scale inward-verging antiform with a horizontal to shallowly plunging hinge. The overall geometry of this antiform is defined by a shallowly dipping outer limb and a relatively steeply dipping inner limb (Lana et al., 2008). Conversely, bedding in the inner ring exhibits steep dips inward or outward, defining a large, upright, tight antiform

or a steeply dipping monocline (ibid). Both rings were influenced by radial (or oblique) faults, with the outer ring exhibiting lateral directional displacements of 0.5–2.0 km, and the inner one showing merely minor displacements (Lana et al., 2008).

Lana et al. (2007, 2008) identified the relatively flat topographic depression surrounding the central peak up to the inner limit of the inner ring as an annular basin. The basin exposes deformed rocks of the Ponta Grossa and Aquidauana formations and lies within a zone of extensive excavation within what was considered the transient cavity (Lana et al., 2007). The AIS transient cavity was modeled with a diameter of 20–25 km (von Engelhardt et al., 1992; Lana et al., 2006). Lana et al. (2007) raised the question of whether the interpreted annular basin is genuinely an original structure of a peak-ring crater or an artifact of differential erosion.

In general, bedding in the Ponta Grossa Fm. along the annular basin dips concentrically outward at moderate angles (Lana et al., 2008); however, steep to vertical outward or inward dips were also reported (see Lana et al., 2007). In some areas, these strata exhibited upright, concentric, open folds, and recumbent folds, as well as outcrop-scale faults (Lana et al., 2007, 2008). Deviations to oblique dip orientations, recumbent to isoclinal radial folds, and some randomly oriented fold hinges were also observed in the Ponta Grossa Fm. in this domain (Lana et al., 2008). Locally, in the Ponta Grossa Fm., concentrically arranged, centimeter-scale intrafolial asymmetric folds occur. These folds suggested an outward vergence toward the crater rim and, although restricted, were considered direct evidence of the collapse of the central uplift (Lana et al., 2008; more on that below). As for the Aquidauana Fm. within the annular basin, bedding is arranged concentrically, and dips are shallow to steep inward (Lana et al., 2007). In addition, fractures and Aquidauana Fm. breccias are commonplace when Aquidauana Fm. is in contact with the Ponta Grossa Fm. (Lana et al., 2008).

The central uplift of the AIS is not equivalent to its central peak (Lana et al., 2007, 2008). The central uplift is a broader structural feature. In contrast, the central peak is a topographically high morphological feature that consists of a 4–5-km-diameter, granitic and (meta)sedimentary basement core (see Souza et al., 2024) surrounded by a 1–2-km-wide elevated collar of upright to overturned and thickened Furnas Fm. sandstones (Lana et al., 2008). The central peak has a polygonal geometry that is not centered on its focal point (Lana et al., 2008), with folded and faulted blocks and megablocks of Furnas Fm. strata asymmetrically distributed around it (Lana et al., 2008; Hippertt et al., 2014).

Overall, in the central uplift, there is structural evidence for upward and inward movements, apparently followed by outward movements, of the target rocks (Lana et al., 2008). The crystalline-(meta)sedimentary basement was affected by kilometer-scale upward movement from its original position on the transient cavity floor (von Engelhardt et al., 1992). In contrast, lateral, inward-directed movements mainly originated from the sedimentary rock volume detached from the cavity walls. This inward movement was responsible for the folding, imbrication, constriction, and rotation of sedimentary strata blocks – mainly of the Furnas Fm. – observed in the collar of the central uplift, which ultimately led to the thickening of the sedimentary sequences in this region (Lana et al., 2007, 2008).

Structural data in the Furnas Fm. collar showed a complex framework with contrasting structural domains (Lana et al., 2008). Furnas Fm. beds are concentrically arranged, commonly showing upturned to slightly overturned or steep dips (Lana et al., 2007, 2008). However, locally, due to meter-scale folds and strata imbrication, bedding orientations are highly variable, ranging from horizontal to vertical (Lana et al., 2007). Lastly, outward movement of the sedimentary target rocks was inferred in the outer parts of the central uplift (i.e., in the Ponta Grossa Fm. rocks). This was linked to the collapse of the central uplift in the final stage of crater modification (Lana et al., 2008).

In summary, the current structural interpretation of the AIS is that the concentric rings, annular basin, and central peak are features that remained from the differential erosion of a peak-ring structure (Lana et al., 2007). The most prominent structures in the AIS resulted from the collapse of the transient cavity, which promoted a centripetal movement of the target rock volume (Lana et al., 2008). The two proposed concentric rings (see Lana et al., 2007, 2008) are interpreted to have been produced as such: the kilometer-scale outer ring antiform as a product of the slumping of the transient cavity walls, and the inner ring as the result of the interaction between the centrifugal flow field – due to the outward collapse of the central uplift – and the centripetal flow field caused by inward collapse of the transient cavity walls.

MATERIALS AND METHODS

In total, two months of geological-structural mapping campaigns were conducted in the AIS region between 2021 and 2024. Data were collected at 416 GPS-referenced stations within and beyond the limits of the AIS (see Fig. S1). The GPS

(Garmin/GPSMAP® 64X) used has an accuracy of 5–10 m under normal conditions. Virtually all accessible outcrops along the MT-100 and GO-194 roads to a radial distance of ~34 km to both SW and NE from the assumed center of the structure were lithologically and structurally mapped. Structural measurements of bedding planes, fold hinges, axial planes, foliations, and fractures were recorded using a Clar-type geological compass. The magnetic declination correction of the compass was −20° W, and the measured data have an estimated accuracy of ±5°. In addition to the data along these two main roads, complementary data were also acquired along secondary dirt roads and local profiles in the NW, N, E, and SE sectors of the AIS (see Fig. S1).

Many newly excavated roadcuts – e.g., along the MT-100 in the ENE sector – were examined before they became inaccessible. A suite of roadcuts, ranging in extent from tens to hundreds of meters, allowed continuous observation of different lithologies and structures in the various morphostructural compartments. We collected samples from various lithological units within and outside the AIS, primarily from relatively fresh materials that had been recently exposed. Polished thin sections of selected samples were produced and analyzed using polarized light microscopes at the Institute of Geosciences, University of Brasilia. The thin sections were used to verify lithologies and microstructures.

Stereonet (version 11) software (Allmendinger et al., 2012; Cardozo and Allmendinger, 2013) was used for stereogram preparation and structural analysis. The stereograms shown here are in the Lambert azimuthal equal-area lower hemisphere projection (Schmidt net). Notations indicating the orientation of structures (e.g., planes, lines) are presented in the *dip direction/dip* form for planar features (e.g., 030°/45°) and *plunge/plunge azimuth* for linear features (e.g., 45°/030°).

Esri's ArcGIS Pro software was used for spatial data processing and integration, and geological mapping. Available geological maps of the AIS and its environs (CPRM, 1981; Lana et al., 2007, 2008; UnB-IG, 2012; Thomé Filho et al., 2012; Horn et al., 2022; Souza et al., 2024) – together with remote sensing data and GIS techniques (see next) – were integrated to help with regional surveying and to derive a geological map (Fig. 1). More specifically, we used a 30-m-pixel-size, surface reflectance scene (Landsat 8/OLI, Collection 2 Level-2 Science Products, product ID: LC08_L2SP_225071_20200829_20200906_02_T1; courtesy of the U.S. Geological Survey) to generate false-color composite images of spectral band ratios, mineral indexes,

and for principal component analysis. In addition, Esri's high spatial resolution World Imagery layer map service (credits: Esri, Maxar, Earthstar Geographics, and the GIS User Community) and the 12-m-pixel-size, TanDEM-X digital elevation model (Rizzoli et al., 2017) of the AIS and its environs (see Gottwald et al., 2020; courtesy of Manfred Gottwald, formerly of the German Aerospace Center – DLR) were also employed in the map-making process and for the morphological and structural analysis.

Structural lineaments shown in the geological map (Fig. 1) were extracted from Esri's high-spatial-resolution World Imagery layer, overlain with a partially transparent, multidirectional, hill-shaded image of the TanDEM-X digital elevation model with a 5:1 vertical exaggeration applied to emphasize the relief features and facilitate lineament extraction (see Fig. S2). To maintain consistency, only one person (R.B. Bernardes) manually extracted the lineaments at the 1:250,000 scale and during a single-day work session. Local placement refinements were made to some of the lineaments during this process.

The geographical coordinates indicated in the text are in the WGS84 coordinate system. The notation *R* indicates the *radial distance* of a given point of interest (e.g., station, outcrop, feature) from the assumed apparent mean center of the AIS (52.99151°W, 16.81544°S, based on our Fig. 1 map). To avoid extensive repetition in the following sections, the terms *inward*, *outward*, *concentric*, *radial*, *tangential*, and *oblique* will always refer to the orientation or vergence of a given structural feature with respect to the assumed apparent center of the AIS. For instance, the term *tangential* is used to describe features, such as lineaments, fractures, or faults, that intersect a given concentric line around the AIS center at a single point. This term also applies to the dip direction of beds with radial strike relative to the AIS center. In a complementary way, the term *oblique* refers to features whose orientation is neither concentric nor tangential nor radial with respect to the AIS center, i.e., their orientation lies between these reference orientations.

RESULTS

Following the historic first-order morphostructural segmentation of the AIS, we have separated the study region into four sections: (1) terrains beyond the impact structure (R >~20 km); (2) outer rim region (R ~ 20–15 km, analogous to Lana et al., 2006); (3) intermediate section (R ~ 15–8 km); and (4) central uplift ($R \leq 8$ km from the center of the

structure; in agreement with Miyazaki et al., 2021). The results for the central uplift study are further divided into *collar* and *core* subsections to distinguish the supracrustal from the granitic and (meta)sedimentary basement components, respectively.

Beyond the Impact Structure (*R* >~20 km)

The SW and NE regions outside the AIS were primarily mapped along the MT-100 road, between the city of Alto Araguaia and Ribeirãozinho town (both located beyond the area shown in Fig. 1), and the GO-194 road, from Ponte Branca town toward Ribeirãozinho. Along both roads, we made detailed observations extending up to 14 km beyond the apparent SW and NE outer rim locations (*R* >~20 km) (see data stations in Fig. S1), as well as at some isolated outcrops farther outward.

Outcrops surrounding the AIS mainly comprise red sandstones of the Aquidauana Fm. (Fig. 1) with (sub)horizontal (≤15° dip) bedding. Rare beds with moderate dips up to 30° but without a preferred dip direction are observed. No consistent regional folding pattern was observed, and the moderately dipping beds are confined to the vicinity of normal and reverse faults with various orientations.

Purple or ochre siltstones or fine-grained sandstones of the Ponta Grossa Fm. only crop out close to the apparent rim of the AIS to the NE of the structure (Fig. 1). Most exposures show weathered rock in flat pavements of limited extent. In contrast to the Aquidauana Fm., quite diverse bedding dips are noted in Ponta Grossa Fm., from horizontal to moderate (<50°). Dip directions are varied, but are more commonly toward the SW. No folding was observed. Normal and reverse faults that displace and/or tilt the strata up to a few meters are relatively common. Dips of such faults are generally steep, and their strike is typically to NE-SW or NW-SE. Fault planes are, in general, very narrow (mm-wide), with no obvious evidence of either cataclasis or brecciation.

Beyond the apparent SW rim of the AIS, the contact between (sub)horizontally bedded (chert-siltstone-sandstone) Corumbataí Fm. (Passa Dois Gr.) and cross-bedded pink to red sandstone of the Aquidauana Fm. is well-exposed in an ~400-m-long outcrop along the MT-100 road (locally known as “Serra Colorada”; station P-002, *R* ~ 31.3 km, at: 53.13283°W, 17.06358°S). This exposure reveals brittle(-ductile) deformation of the strata.

Two sets of fractures (termed α and β) consistently cut through this outcrop (Fig. 3A). The α fractures have strikes between N10°–45°W and are more penetrative than β

fractures, which mainly strike to N60°–80°E (Fig. 3B). Both sets include normal and reverse faults with apparent displacements of tens of centimeters. However, reverse β faults with meter-scale displacements do occur, and a prominent one of these juxtaposes Aquidauana and Corumbataí formations strata at this location (Fig. 3C). No breccia zones occur along the faulted contact between the two formations in this region outside the AIS. Up to 25-centimeter-wide shear bands with cataclasite (Fig. 3D) occur more commonly associated with the β faults. No evidence was found of displacement of either fault set by the other.

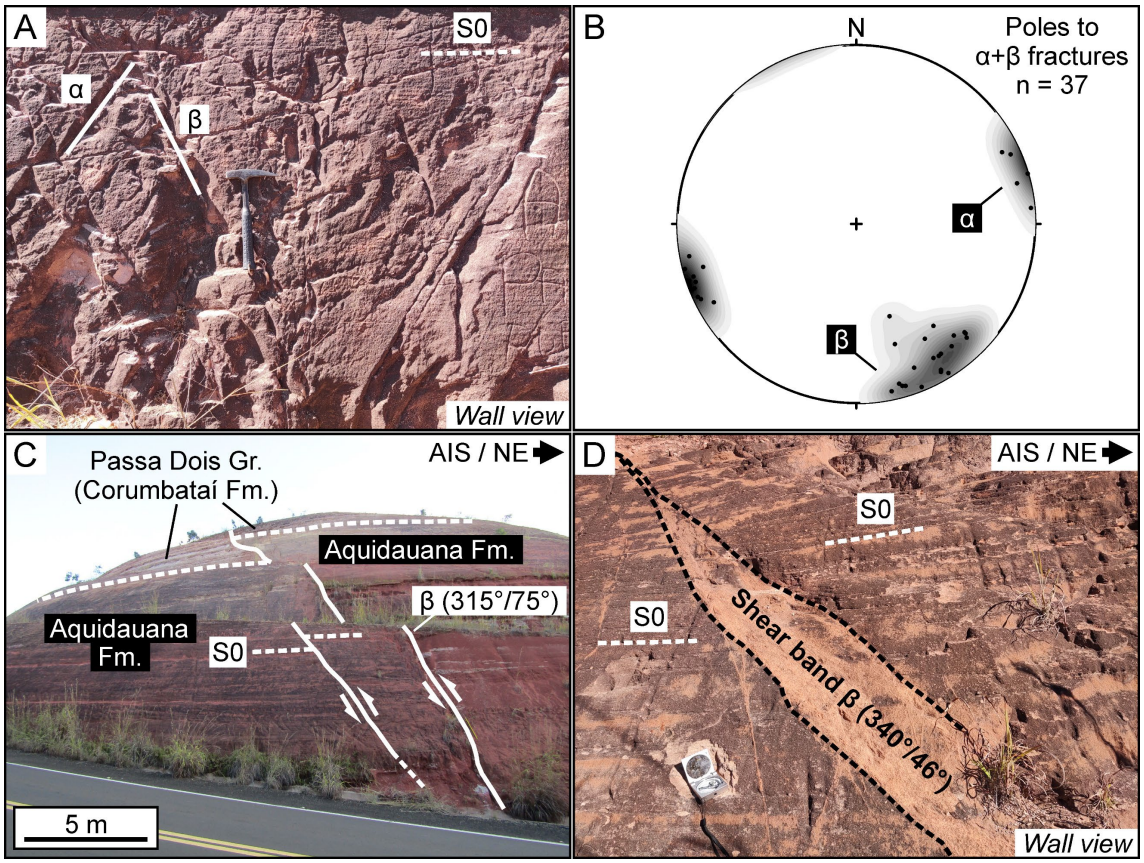

Figure 3. Structural data and observations outside the Araguainha impact structure (AIS), made on an extensive roadcut of strata of the Corumbataí and Aquidauana formations, at ~31.3 km SW of the center of the impact structure (station P-002, 53.13283°W, 17.06358°S). A) Fracture/fault sets α (NW-SE strikes) and β (NE-SW strikes); refer to the text for details. Note fracture orientations with respect to the (sub)horizontal bedding (S0). Hammer for scale is 33 cm long. B) Stereogram of poles to α and β fractures/faults (n = 37). C) Reverse faults related to set β, with the fault on the right showing an apparent displacement of ~5 meters, juxtaposing the younger Corumbataí Fm. (Passa Dois Gr.) against the older Aquidauana Fm. (at the top of the hill). Black arrow at the top right indicates the direction toward the apparent center of the AIS and the respective (inter)cardinal direction. D) Up to 25-cm-wide shear band with cataclasite related to fracture set β in Aquidauana Fm. sandstone. It was not possible to obtain the sense of shear related to this structure. Compass for scale is 15 cm long.

In an ~150-m-long outcrop farther southwestward from the AIS, at *R* ~ 56 km along the MT-100 road and relatively close to Alto Araguaia city (station P-001; 53.30111°W, 17.22300°S; beyond the area in Fig. 1), Corumbataí Fm. strata show intense brittle-ductile deformation. Bedding dips vary from horizontal to vertical, but (sub)horizontal and moderate (≤40°) dips toward the ENE and WSW predominate, locally defining meter-scale, gentle, upright to steeply inclined, asymmetric folds with shallowly NW- or SE-plunging hinges. These folds commonly have their limbs or hinge zones displaced by reverse faults, with local drag folds emerging along fault planes.

Despite a significant part of the outcrop exhibiting flat-lying strata, the reverse faults repeatedly separate meter-wide domains of tilted and/or folded strata from others with flat attitudes. These reverse faults show displacements up to tens of centimeters and generally strike NNW-SSE, similar to the α fractures noted at the Serra Colorada site. The faults show moderate to steep (>25°) ENE or WSW, to vertical, dips, with steeper dips being more common. No brecciation or cataclasis was noted along fault planes. However, due to the weathered state of the exposure, it was not possible to determine if a narrow fault gouge was originally present along the fault planes. Slickenlines with a down-dip plunge were found on the fault plane of two moderately WSW-dipping reverse faults. Together, these structures and folds indicate that the main structural vergence in this outcrop area is toward ENE (to ~080° azimuth). The absence of β fractures at station P-001 may be because the direction of the roadcut is subparallel to their strike.

Outer Rim Region (*R* ~ 20–15 km)

The outer limit of this region is defined by prominent, approximately concentric outermost rim faults, several of which are still associated with topographic scarps (e.g., in the SW, NW, and N sectors). The inner limit of this region is located where Lana et al. (2006) defined kilometer-scale, downfaulted blocks of Passa Dois Gr. strata at *R* ~ 15 km, meaning that this region also comprises most of Lana et al.'s (2007) outer ring (*R* = 18–14 km).

The outer rim region predominantly consists of generally massive, red to purple, coarse-grained sandstones of the Aquidauana Formation. Along the Aquidauana escarpments, as well as in sectors that do not show escarpments at similar radial distances, bedding is (sub)horizontal.

In contrast, farther inward in the AIS (R = 20–18 km), Aquidauana Fm. bedding orientations and dips are variable and primarily inclined. Outward-dipping beds with moderate to steep dips (25°–65°) predominate, but subhorizontal beds may also occur. Close to the apparent rim in the NW and N sectors, outcrop-scale normal faults with steep (60°–70°) inward dips occur (Fig. 4A, B), some of which preserve down-dip slickenlines in fault gouge (Fig. 4C). The magnitude of the displacements on these normal faults could not be estimated accurately due to a lack of adequate markers in the generally massive sandstone, but throws appear to be of the order of meters.

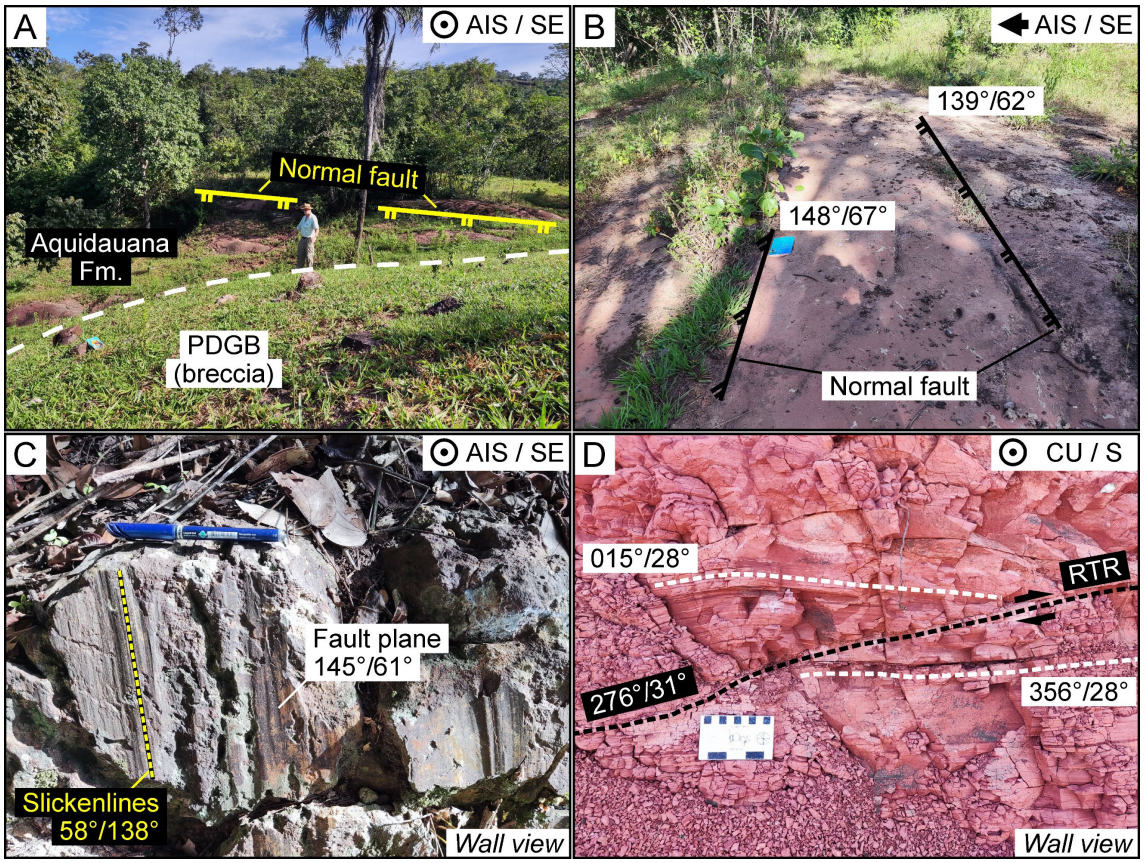

Figure 4. Structures in the Aquidauana Fm. in different sectors of the outer rim region. Black arrow at the top right of each figure indicates the direction toward the Araguainha impact structure (AIS), the central uplift (CU), and the respective (inter)cardinal direction. A) Normal-faulted region within the Aquidauana Fm., close to a Passa Dois Gr. Block (PDGB) breccia hill in the NW sector (station P-258; R ~ 20.4 km; 53.17082°W, 16.75191°S). Person for scale is ~2 m tall. B) Meter-spaced, steep (~60°–70°), inward-dipping normal faults in the Aquidauana Fm. in the vicinity of Fig. 4A. Notebook for scale is ~20 cm long. C) Inward-dipping, normal fault plane with down-dip slickenlines in the Aquidauana Fm., also near the location shown in Fig. 4A. No steps were observed on the fault plane. Pen for scale is ~15 cm long. D) A (structural) radial transpression ridge (RTR) as a lateral thrust ramp (see Kenkmann and von Dalwigk, 2000) in laminated red sandstone of the Aquidauana Fm. in the N sector of the AIS (station P-230; R ~ 16 km; 52.99628°W, 16.67024°S). White dashed lines indicate bedding traces. The scale is 10 cm long.

In the inner part of the outer rim region, at R = 18–15 km, bedding is subhorizontal to obliquely dipping and moderately inclined (<40°) with either inward or outward dips. In certain places, tangentially dipping beds are observed in the outer rim region and may locally predominate in some outcrops. Bedding generally becomes more shallowly dipping inward – although this is not systematic, and local deviations occur. For example, bedding dip angles are quite variable in the ENE sector along the MT-100. A few 10-cm-scale (structural) radial transpression ridges (Kenkmann and von Dalwigk, 2000) were observed in the outer rim region. They display lateral thrust ramps and occur in laminated Aquidauana Fm. sandstone of the SW and N sectors (Fig. 4D).

Overall, steep (>50°), inward-, tangentially, or obliquely dipping beds are of subordinate importance but occur disseminated throughout the outer rim region. These beds are closely associated with fractures/faults, with the strikes of the former commonly parallel to the strikes of the latter. With high-resolution remote sensing imagery, we noted that these faults are typically spatially related to sets of more significant structural lineaments (see Fig. 1; see also "Intermediate Section of the AIS (R ~ 15 –8 km)" section). Near such faults, Aquidauana Fm. rocks are also commonly fractured or cataclastically brecciated in centimeter- to meter-wide zones that are usually subparallel to bedding or fault planes. Fractured or brecciated Aquidauana Fm. rocks are also common in up to meter-wide zones along the faulted contacts with the Passa Dois Gr. in the outer rim region.

Besides localized 10-cm-scale gentle undulations of some laminated and more pelitic Aquidauana Fm. strata, outcrop-scale folds are rare in the outer rim region. Only a meter-sized, open, upright, asymmetric, antiformal fold with one of its limbs shallowly dipping obliquely inward and the other moderately dipping quasi-tangentially was observed in the NW sector.

Passa Dois Group Blocks (PDGBs) of the Outer Rim Region

The most notable map-scale features in the outer rim region are large, primarily concentrically arranged domains of deformed Passa Dois Gr. strata (see Fig. 1). In plan view, these strata are generally juxtaposed against the Aquidauana Fm. by faults that strike concentrically/tangentially, radially, or obliquely. The Passa Dois Gr. contact with the underlying Aquidauana Fm. may be tectonized (detached). However, in some places, the contact exposed by erosion appears to be conformable. Following Lana et al. (2008),

who noted some of them, we term these features *Passa Dois Group Blocks* (PDGBs). PDGBs occur in most sectors of the outer rim region and are generally found at elevations between ~450 m and 750 m, with their relative elevation decreasing inward into the AIS. Their dimensions range up to >2 km in radial width and >8 km in concentric length. Each PDGB is distinct in terms of lithology and geological structures, but an overall framework can be identified.

The PDGBs primarily consist of centimeter- to meter-thick, variegated mudstone sequences interspersed with up to tens-of-centimeters-thick chert and comparatively sparse, fine-grained sandstone layers. Stromatolites are commonly associated with the chert of some PDGBs (e.g., in the SW and SE sectors) and relate the strata to the basal Irati Formation. Fossil fragments of bivalve shells and rare clastic dikes are observed in the NE PDGB along the MT-100 road to the north of Ponte Branca (Fig. 1), indicating that this part of the PDGB represents Corumbataí Fm. of the uppermost Passa Dois Group. Breccia zones commonly mark the high-angle, distal, normal-fault-bounded contacts between Passa Dois Gr. and Aquidauana Fm. (Fig. 4A). These zones can reach several meters in width. Many breccia occurrences are entirely composed of chert, with or without stromatolite fragments, but some brecciated siltstones also occur.

In the distal domain of a PDGB along a dirt road (GO-542) in the ENE sector, close to and SW of Ponte Branca town, a new outcrop was exposed by recent roadworks. This PDGB is oriented quasi-concentrically and stretches from the outer rim region to almost the intermediate section (R ~ 16.4–15.3 km). Within the PDGB, at station P-304 (52.84600°W, 16.78651°S), a breccia of gray-to-purple, thinly laminated mudstone and fine-grained sandstone fragments is embedded in a red, pelitic-to-psammitic matrix (Fig. S3A). The lithic fragments are mostly millimeter- to centimeter-sized but can reach lengths up to a couple of meters. Some lithic fragments are angular and deformed in a brittle manner (Fig. S3B), others are boudinaged and quasi-ductile (Fig. S3C). Gray and purple, thinly laminated fragments reveal millimeter- to centimeter-scale folds and faults with millimeter-scale displacements (Fig. S3D).

Where the Passa Dois Gr. sedimentary package is not brecciated, it is folded, faulted, and/or tilted. However, advanced weathering generally hampers detailed structural analysis. Bedding dips range from subhorizontal to subvertical, commonly with shallow to moderate (~10°–45°) inward- or outward-directed dips dominating but locally rotating to tangential or oblique directions. Centimeter- to meter-scale folds are mostly

asymmetric, with gentle to isoclinal recumbent forms. Locally, in some more pelitic strata of the SW and NE PDGBs, centimeter-thick domains with disharmonic and incoherent small-scale (mm to cm) folds occur, which are commonly dismembered and rootless.

The vergence of the folds within the PDGBs depends on the location of those folds within a block. Inward-verging, recumbent to shallowly inclined, asymmetric folds predominate in the proximal domains of the PDGBs. These inward vergences are not always truly centripetal. Outward- and tangentially verging folds also occur and, in general, are spatially related to the distal and lateral (i.e., tangential) domains of the PDGBs, respectively. Folds with oblique vergences do occur at various sites, but are subordinate.

Deviations in bedding strike and dip along the margins of the PDGBs are generally related to proximity to fractures/faults, which, in turn, are spatially related to structural lineaments (Fig. 1). Bedding directions at the margins of the blocks are generally parallel to fault strikes, and dip angles are commonly high (≥40°). Moreover, Passa Dois Gr. bedding orientations tend to be similar to those of the Aquidauana Fm. rocks near the PDGBs. Normal and reverse faults in some PDGBs have displaced the strata by millimeters to meters. Locally, at the distal margin of the SE PDGB, meter-spaced extensional faults have rotated the hanging wall Passa Dois Gr. bedding to outward dips.

The southwest PDGB. This block is remarkable for its extensive exposures in several-meter-high roadcuts along the MT-100 road ($R \sim 19.1–17.8$ km), with exceptional perspectives into the complex deformation experienced by these rocks (Fig. 5A). Folds vary in scale from centimeters to multiple meters. Meter-scale folds are predominant, and smaller ones are parasitic, isoclinal or chaotic folds that occur in the most strongly deformed pelitic cores of large folds. Fold tightness ranges from gentle to isoclinal recumbent, with the prevalence of tight, asymmetric folds that commonly have overturned limbs.

Although the overall structural vergence in this PDGB is toward the interior of the AIS, the local deformation style and fold vergence vary along the road profile. At the SW distal domain of the block, in an area known as “Matinha hill,” breccias and asymmetric folds with an overall outward vergence are typical (Fig. 5B). In the proximal domain of the block, the fold vergence is predominantly inward-directed, toward NNE (Fig. 5C, D). Although radial folds have not been observed along this PDGB, the poles to bedding stereograms (Fig. 5B, C) suggest either non-cylindrical folds or superposition of a radial

folding pattern onto the quasi-concentric one. Fold axes plunge mainly at moderate angles (~30°) to WNW; however, some axes may also have been rotated due to the radial folding superposition (Fig. 5D).

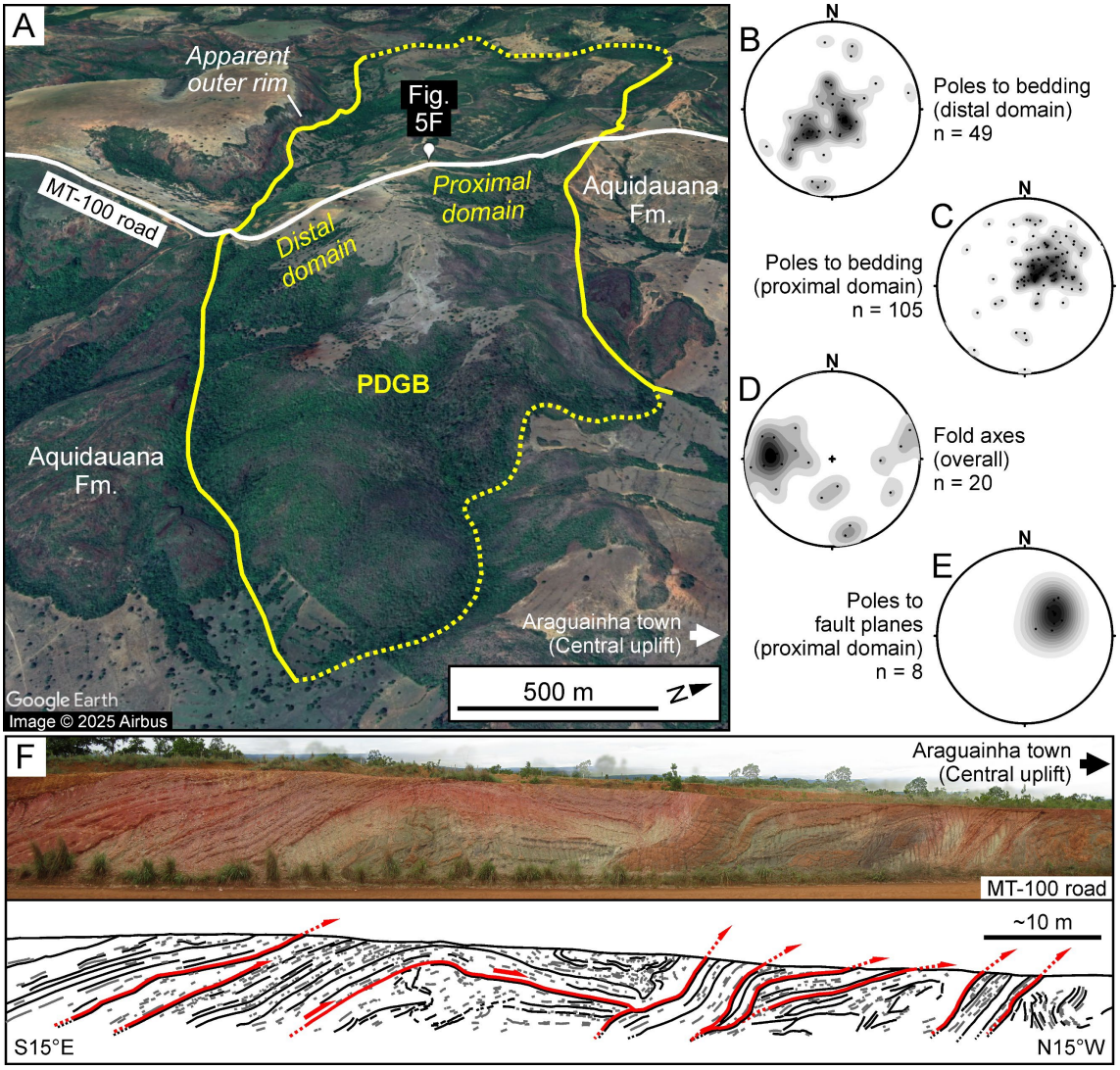

Figure 5. Structures in the Passa Dois Gr. Block (PDGB) in the SW sector of the outer rim region (*R* ~ 19.1–17.8 km; 53.08621°W, 16.95593°S). A) Oblique aerial view of the whole block and its environs (see attribution in the figure). B) Poles to bedding (n = 49) for the distal domain of the PDGB. Beds dip mainly inward in this zone, and folds verge outward. Note the pole distribution, which suggests the occurrence of a superimposed radial-to-oblique folding pattern. C) Poles to bedding (n = 105) for the proximal domain, where beds dip mainly outward, and the general fold vergence is inward (see text for details). A superimposed, quasi-radial (or non-cylindrical) folding pattern can be inferred. D) Overall WNW-plunging fold axes (n = 20) measured throughout this PDGB. Deviations from this trend likely emerge from the superposition of the radial folding pattern (e.g., the ESE-plunging axes). E) Poles to fault planes (n = 8) from the proximal domain of the PDGB, within the area of Fig. 5F. F) Composite panorama (above) and its interpretation (below) showing an imbricate fan-like geometry for the Passa Dois Gr. profile along a prominent roadcut through the proximal domain of the PDGB (see Fig. 5A for location). Thick red lines with arrows in the interpreted roadcut profile indicate thrust fault traces (see data in Fig. 5E). Regretfully, this panoramic composition, based on a series of individual photographs, suffers from some parallax artifacts in the background.

Within the proximal domain of this PDGB, shallowly to moderately (~10°–50°) outward-dipping reverse faults with tangential to oblique strikes (Fig. 5E) are associated with previously unreported, prominent inward-verging folds. These structures resemble an imbricated fan (Fig. 5F). Varied rheologies of the strata appear to have controlled the development of the folds and faults in this domain. The most competent sandstone layers usually accommodated strain by reverse faulting along fold hinges and at the contacts with pelitic packages. Total displacements on the faults are generally difficult to estimate due to weathering, erosion, and restrictions on outcrop height, but approach ~4 m on a reverse fault. A single set of slickenlines (35°/230°) on one of the fault planes (248°/38°) supports the folded bedding data that suggest that structural vergence is not truly centripetal.

Some meter-wide exposures of massive, although heavily fractured, Aquidauana Fm. sandstone are noted beneath the folded and fractured Passa Dois Gr. rocks in the roadcuts. Up to 1-m-wide red sandstone blocks of Aquidauana Fm. are locally entrained and enclosed in the basal part of the Passa Dois Gr. volume.

Intermediate Section of the AIS (*R* ~ 15–8 km)

The intermediate section of the AIS follows directly inward from the outer rim region and extends to the central uplift, and also comprises Aquidauana Fm. and Passa Dois Gr. rocks. While the spatial distribution of our structural data in the intermediate section is not azimuthally comprehensive (see Fig. S1), it still allows a general perspective on this domain.

The character of Aquidauana Fm. in this area is, overall, similar to that in the outer rim region. Bedding is generally poorly defined due to the massive nature of the sandstones, weathering overprint, and local extensive cataclasis and/or brecciation. Bedding predominantly dips subhorizontally to moderately (≤50°) inward or outward, but tangentially or obliquely dipping beds also occur throughout the section. However, no outcrop-scale folds were observed. Steep (>50°) inward or outward, tangential, or oblique bedding dips are found at a few sites at various radial distances. Remote sensing analysis shows these steeply dipping beds generally occur close to, and with strikes parallel to, structural lineaments with respective tangential, radial, or oblique trends (see Figs. 1, S1, and S2). A systematic steepening of bedding dips from the outer to the inner parts of the

intermediate section is not observed, except at $R \sim 10–8$ km in the SW sector along the MT-100 road, in relatively close proximity to the central uplift.

Two exceptions to this general Aquidauana Fm. framework are noted in the N and NNE sectors. The first, at $R \sim 12.7$ km in the N sector (station P-246; 52.97724°W, 16.70187°S), is an intercalation of fine-grained sandstone with thinly laminated, meter-thick siltstone strata that host folds >100 m to 1 km in wavelength and that are visible in remote sensing imagery. These large fold structures can be observed along a swath from the NNW to the NNE sectors at $R \sim 13.5–12$ km. A fold pair, which forms an asymmetric "S"-shaped structure in plan view, was analyzed in detail (Fig. 6). The more northerly fold is a gentle synform with a subhorizontal, ENE-trending hinge line, whereas the more southerly fold is an open antiform with a moderately (~30°) ENE-plunging hinge. Progressive steepening of the fold limbs occurs from the N (from 15° to 40° dips) to the S (from 40° to vertical dips) in this folded domain. To the south, a 100-m-scale domain of more massive, coarse-grained, subhorizontal (not folded) Aquidauana Fm. sandstones occur at the inward limit of the folded domain.

The second notable exception to the general bedding orientation in this section, at $R \sim 13$ km of the NNE sector, occurs along an NW-SE-trending dirt road (station P-245; 52.93828°W, 16.70813°S). Along an almost 2-km-long, continuous exposure at the road level, fine-grained red sandstone and siltstone of the Aquidauana Fm., with millimeter- to centimeter-thick lamination, form steeply dipping (60°–90°) beds that dip inward or outward. Importantly, our data here were acquired close to and along a prominent structural lineament that trends NW-SE (see Fig. S1). Locally, steeply dipping fractures/faults cut obliquely across the strata and separate meter-scale domains of massive, relatively coarse-grained, and fractured red sandstone from meter-wide zones of 10-cm-scale chaotically folded, well-laminated, fine-grained red sandstone and siltstone that are commonly cataclastically deformed.

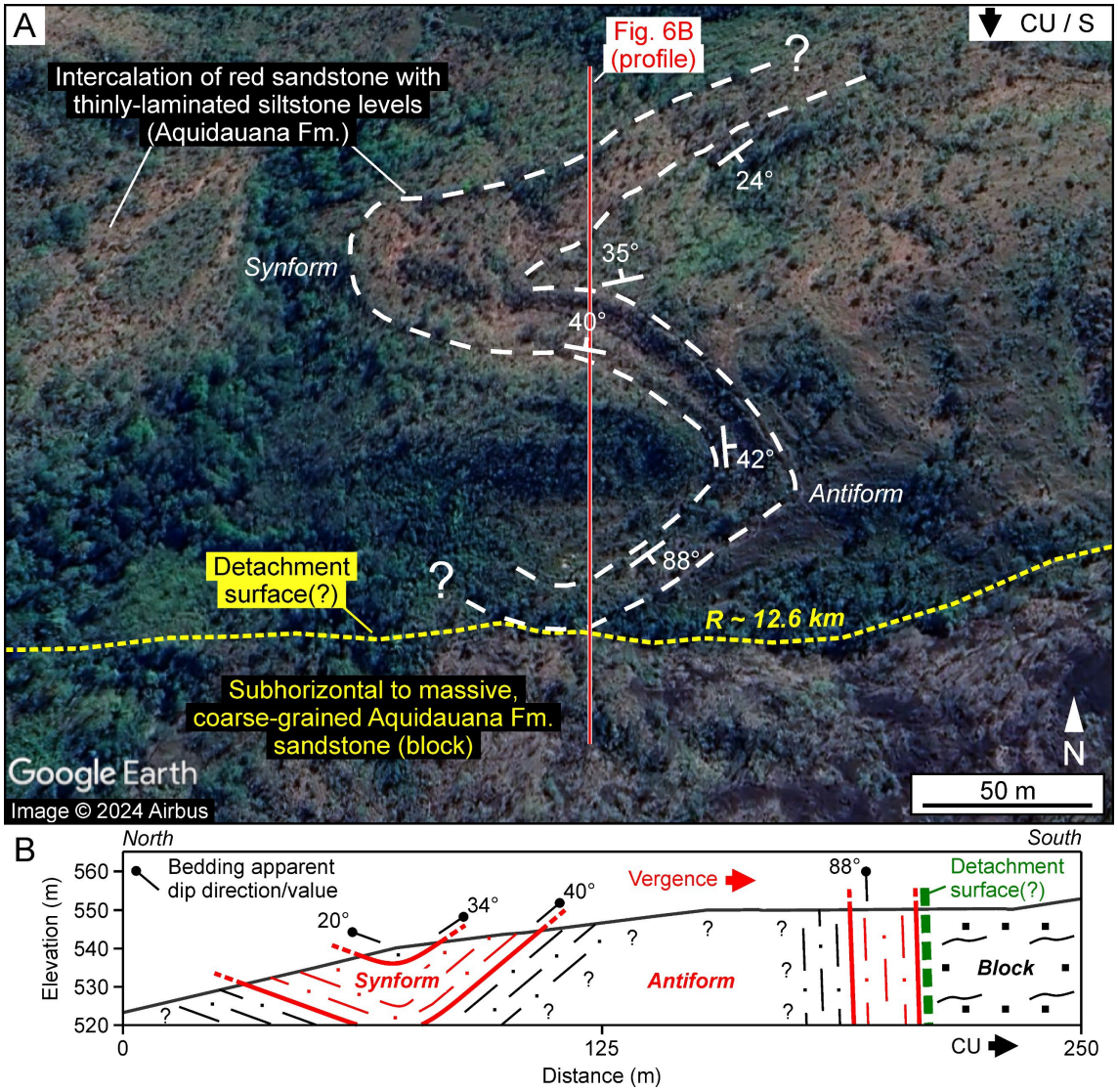

Figure 6. A) An ~200-m-wide fold structure in a more pelitic level of the Aquidauana Fm. in the N sector of the intermediate section (station P-246; *R* ~ 12.6 km; 52.97724°W, 16.70187°S; see attribution in the figure). Black arrow at the top right points to the south, toward the central uplift (CU). Bedding directions and dips along the fold structure are given (white symbols). A detachment surface is inferred between the fold structure and the comparatively coarser-grained block. B) Structural profile along the fold structure in Fig. 6A. The profile is presented without vertical exaggeration. The structure begins in the north with a gentle, asymmetric synform, which transitions into an open, asymmetric antiform to the south (see text for details). Note the steepening of bedding toward the south, from shallow to vertical. The folds have an overall inward-directed vergence (i.e., toward the south; see red arrow). These observations imply radial, inward shortening of the strata.

Passa Dois Group Blocks (PDGBs) of the Intermediate Section

These PDGBs generally occur at lower elevations (between ~450 m and ~650 m) than their outer rim counterparts. Our map (Fig. 1) shows that the blocks in the intermediate section are generally smaller than those in the outer rim region. They also tend to have more distinct shapes: e.g., the middle PDGB, at *R* ~ 15.0–13.5 km in the SW

sector along the MT-100 road, has a "horseshoe" shape (see Figs. 1 and 7). The innermost PDGBs identified to date occur in the intermediate section at $R \sim 10$ km (compare Fig. 1).

Structural data were acquired for PDGBs in the SW, N, and SE sectors (see stations in Fig. S1). The Passa Dois Gr. lithotypes in these blocks are identical to those of the blocks in the outer rim region. Stromatolites in the chert domains are abundant in some areas and are common as fragments in brecciated zones near the distal limits of the PDGBs.

Bedding dip directions are variably inward, outward, or tangential, with generally moderate to steep (30°–85°) dips. Inward-dipping beds tend to occur more commonly along the distal limits of the PDGBs. Obliquely dipping beds occur subordinately throughout the blocks. In the horseshoe-shaped PDGB in the SW sector that was mentioned above, a recurring bedding dip pattern features inward- and outward-dipping beds, which are more commonly observed in the central part of the block. In contrast, tangentially dipping beds prevail along the tangential sides of the block (see Fig. 7). Overall, Passa Dois Gr. bedding orientations at the limits of the PDGBs are similar to those in Aquidauana Fm. rocks in their environs. Moreover, Aquidauana Fm. rocks also crop out within some of the PDGBs, suggesting that the thickness of the Passa Dois Gr. occurrences may not be substantial.

Compared to the deformation in the PDGBs of the outer rim region, folds and faults are less common in the PDGBs of the intermediate section. Fold wavelengths are up to a couple of meters, and folds are asymmetric and locally isoclinal recumbent. Fold vergence in the middle PDGB in the SW sector is inward (Fig. 7). A concentric-radial folding interference pattern seems to apply to the folds in the SW (see Fig. 7) and SE intermediate PDGBs. In the SE PDGB, a centimeter-thick chert layer locally forms a meter-scale, upright to gently plunging, gentle fold. Both limbs of the fold have moderate (35°–40°) dips. One of the limbs is dipping radially to obliquely inward, whereas the other is dipping tangentially to obliquely. A mineral-stretching lineation (slickenlines) oriented at 26°/268° occurs on the upper surface of this latter limb. These observations are consistent with inter-strata movement in the W–E direction, oblique to the apparent center of the AIS. Due to the weathered state of the exposures of the SE PDGB, no consistent folding patterns could be identified (see stations in Fig. S1).

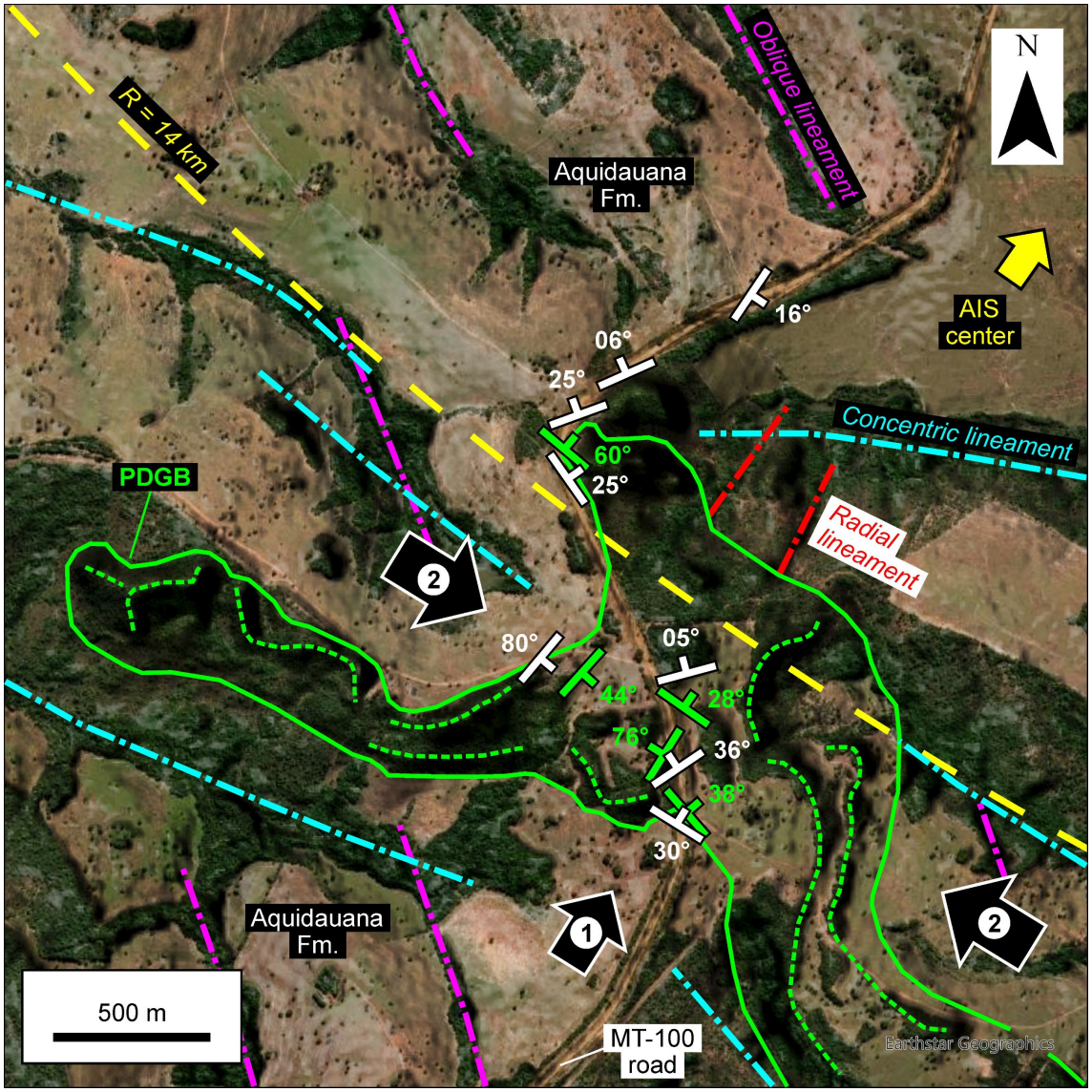

Figure 7. Structural data and interpretation of an inner Passa Dois Gr. Block (PDGB) (green line) and its vicinity within the intermediate region (R ~ 15.0–13.5 km; 53.06850°W, 16.92043°S) in the SW sector of the Araguainha impact structure (AIS). The image is from Esri's World Imagery layer map service (Credits: Esri, Maxar, Earthstar Geographics, and the GIS User Community). It has been overlain with a TanDEM-X digital elevation model with some transparency (see Materials and Methods section). Within the PDGB, some small patches of Aquidauana Fm. rocks crop out due to the thinning in parts of the PDGB. White symbols represent the orientation of bedding in Aquidauana Fm. psammites, whereas green symbols represent bedding in Passa Dois Gr. rocks. Green dashed lines are interpreted as major fold traces in the PDGB. Note the "horseshoe" shape of the PDGB. Also, note the bedding's radial, tangential, or oblique orientations with respect to the apparent center of the AIS (yellow arrow). Cyan, magenta, and red dashed-dotted lines are interpreted as different (concentric/tangential, oblique, and radial, respectively) sets of structural lineaments. The yellow dashed line marks the inner limit (at R = 14 km) of the alleged concentric outer ring after Lana et al. (2007). Black arrows indicate the interpreted succession of deformation events that imprinted this "horseshoe" shape to the PDGB: (1) inward movement of the rock volume, likely related to the inward-directed collapse of the transient cavity walls; and (2) tangential constriction of the migrating rock volume due to reduction of available space between the crater rim and the emerging central uplift (see text for details).

The contacts between the PDGBs and the Aquidauana Fm. were studied in small exposures in the SW and N sectors. The central part of the SW horseshoe-shaped PDGB at the MT-100 road is only a couple of meters thick and allows the observation of the contact between this unit and the Aquidauana Fm. (see Fig. 7). The contact is undulating and dips at shallow angles. Ten-centimeter-scale folds or slightly sinuous Passa Dois Gr. strata follow the contact and overlie commonly fractured, massive, red, or purple, locally conglomeratic Aquidauana Fm. sandstone, indicating a significant competence contrast between the two units. In the N sector, along a dirt road (station P-248; R ~ 11.6 km; 52.99009°W, 16.71085°S), the contact between a relatively small PDGB and Aquidauana Fm. sandstone occurs with moderate to steep (>35°) dips to either SW or NNW, i.e., obliquely inward or outward. This contact area is also significantly fractured, with up to 1-m-sized blocks of red sandstone incorporated into the PDGB close to the contact with the Aquidauana Formation.

Central Uplift ($R \leq 8$ km)

Here, we first present results obtained in the collar of the SW and ENE sectors of the central uplift, mainly along the MT-100 road (see Fig. S1). Then follow results from the northern portion of the core of the central uplift, also along the road, which encompasses (meta)sedimentary basement rocks, Araguainha granite with granitic apophyses, and impact breccias (see Figs. 1 and 2; also see Souza et al., 2024).

SW Collar of the Central Uplift

Structural data for the SW collar could be obtained at R = 7.1 to 2.6 km. The studied strata belong to the Aquidauana, Ponta Grossa, and Furnas formations. Most strata dip moderately to steeply (~30°–60°) outward, toward the SW. However, each formation shows local structural features (see Fig. 8A–C). Deviations from radial dips (i.e., tangential or oblique bedding dips) do occur, but are generally restricted to a few outcrops or only parts of an outcrop. The lack of continuous exposure and the weathered conditions in this collar region preclude a more thorough observation of the complete structural framework.

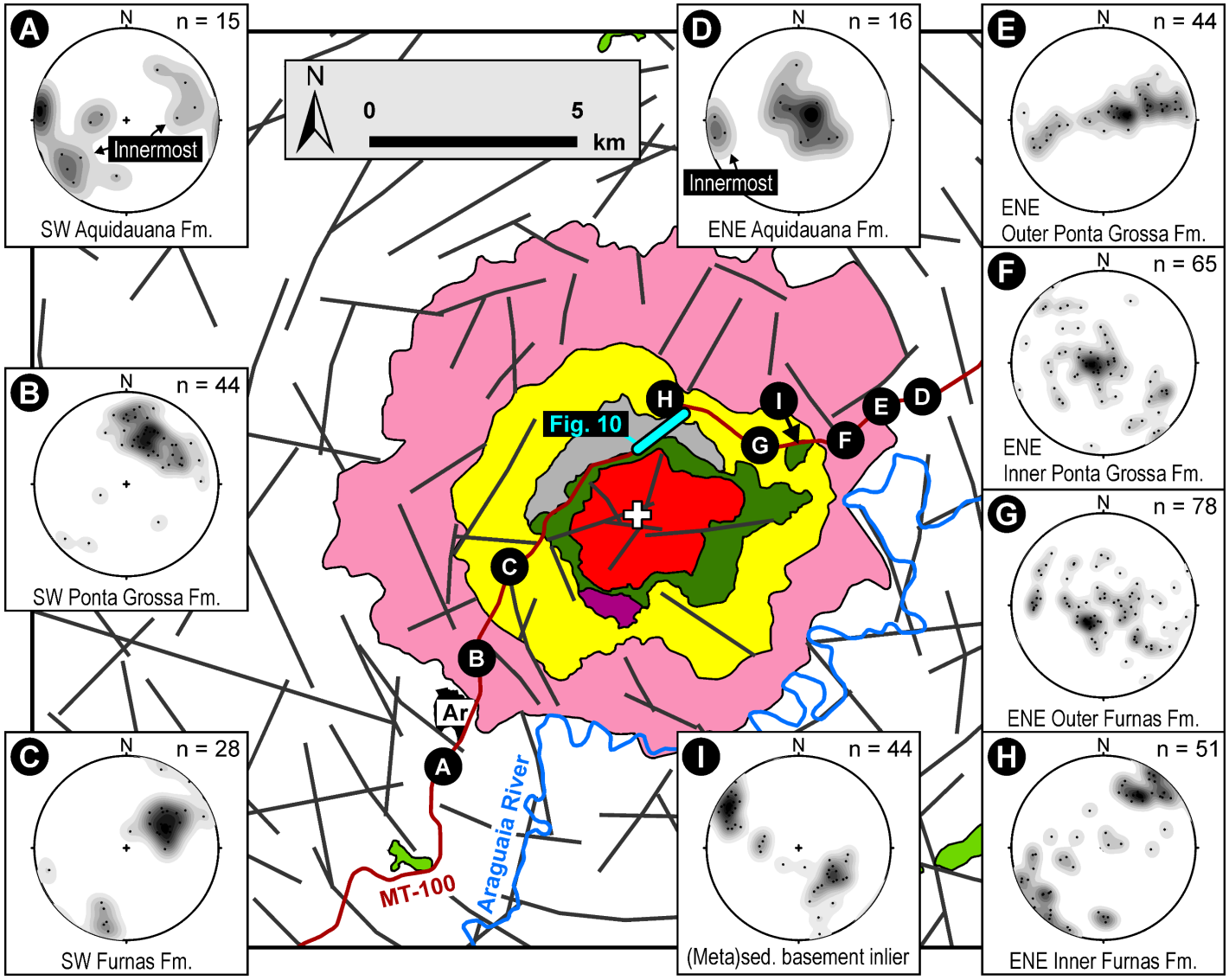

Figure 8. Structural data (poles to bedding) in the SW (A–C) and ENE (D–I) collar of the central uplift, extending up to $R \sim 8$ km, and mainly obtained from newly exposed outcrops along the MT-100 road. The symbols and colors of the geological units are the same as those in the geological map (Fig. 1). The white cross marks the apparent center of the Araguainha impact structure. Ar – Araguainha town. The thick cyan line indicates the location of the profile in Fig. 10. Note the structural differences between the SW and ENE collar. The SW collar has a more homogeneous structural framework, primarily related to the central uplift formation, characterized by a prevalence of outward-dipping beds and asymmetric folds with an overall inward-directed vergence (see A–C). In contrast, the ENE collar has a more complex structural framework. Here, overturning and decoupling of the innermost Furnas Fm. collar (see H) from the rest of the collar of the central uplift can be inferred. Moreover, the outer collar (i.e., the transition from Aquidauana to Ponta Grossa; D and E) shows evidence for outward-directed collapse.

In the outer portions of the collar, the Aquidauana Fm. comprises laminated sandstone beds with consistently steep (>75°) tangential to oblique dips. No folds were observed in this region. Near the presumed contact between the Aquidauana and Ponta Grossa formations (at R ~ 6.2 km), the Aquidauana Fm. strata exhibit moderate to steep (~20°–80°), inward- and outward-directed dips. Here, tight, inclined, asymmetric, meter-scale folds with horizontal tangentially trending fold axes occur in poorly stratified red sandstone. This folding pattern indicates an inward-directed vergence of the innermost Aquidauana Fm. strata (see "Innermost" label in Fig. 8A).

Within Ponta Grossa Fm., bedding dips are mainly outward-directed, at moderate to steep (25°–80°) angles (Fig. 8B). Faults strike parallel to the steeper-dipping bedding. However, due to the weathered state of the rocks, the sense and magnitude of displacements could not be constrained. Folds are rarely observed. They vary in scale from centimeters to meters, are slightly asymmetric, and range from upright to steeply inclined, with interlimb angles that are variably open to tight. Bedding and fold data indicate an overall inward vergence. However, a minor component of radial folding – indicating tangential constriction – can also be inferred (Fig. 8B).

In a Ponta Grossa Fm. exposure close to the presumed contact with Furnas Fm. (station P-104; R ~ 4.6 km; 53.02656°W, 16.84030°S), a prominent fracture cleavage occurs throughout the outcrop but is better developed in pelitic strata. Where the rock is laminated, bedding is cross-cut by the cleavage in an anastomosing pattern with an ~10-cm-wide spacing. The cleavage planes dip horizontally to moderately (<35°) toward SW and NW. On a single cleavage plane dipping NW (338°/24°), a very fine mineral lineation (14°/286°) was recorded. This direction is quasi-tangential to the SW limit of the core of the central uplift.

The Furnas Fm. defines the inner collar at R = 4.3–2.3 km (along the MT-100). The Furnas Fm. has an essentially flat relief in this area. From close to the contact with the Ponta Grossa Fm. up to R ~ 3.4 km, small, weathered outcrops of Furnas Fm. beds of white to purplish sandstone with purple siltstone lenses occur. These beds have mostly outward-directed, rather steep dips (>55° to subvertical) (Fig. 8C). Due to the discontinuous and weathered state of the outcrops, no outcrop-scale folds or faults could be observed. Also, due to the limited size of the exposures, it was not possible to determine whether this Furnas Fm. terrain in the SW collar is part of the so-called "megablock zone" (after Lana et al., 2008).

Close to the core of the structure, at *R* ~ 2.6 km in the SW, an extensive Furnas Fm. outcrop (station P-107; 53.01562°W; 16.82379°S) reveals multiple meter-scale folds and meter-wide imbricated slices of white to pink sandstone. The sandy strata mostly dip moderately to steeply (~30°–65°) outward (Fig. 8C). Inward-dipping strata are not common but, together with the outward-dipping strata, may form 10-cm- to 1-m-scale asymmetric folds that verge toward the core of the central uplift.

However, these folds are not the dominant structures in this area. Instead, millimeter-to-centimeter-wide, dark gray or dark red bands of pelitic material rich in iron oxide demarcate shear bands separating meter-wide thrust slices of Furnas Fm. sandstone (Fig. 9A). These imbricated thrust slices (and associated shear bands) are curviplanar and generally dip at 30°–50° outward. No slickenlines were observed on the shear bands. This geometry indicates an inward vergence of the hanging wall (Fig. 9A).

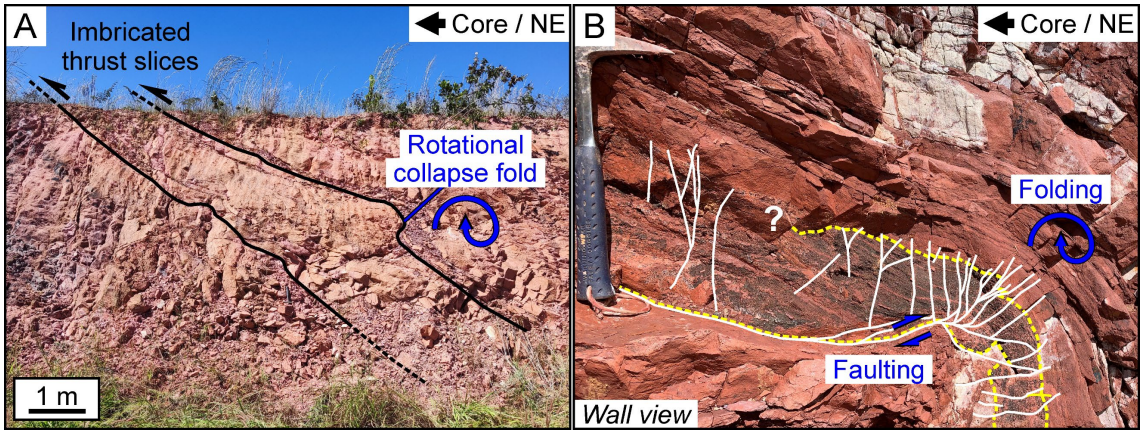

Figure 9. Prominent Furnas Fm. outcrop in the SW collar of the central uplift at the MT-100 road (station P-107; *R* ~ 2.6 km; 53.01562°W, 16.82379°S). This outcrop is located <500 m SW of the outer limit of the core of the central uplift. Black arrow at the top right of each panel indicates the direction toward the core of the central uplift and the respective (inter)cardinal direction. A) Up to centimeter-wide, dark gray/red bands of pelitic material rich in iron oxide demarcate shear bands that separate meter-wide imbricated thrust slices of Furnas Fm. sandstone. We interpret that this overall geometry was generated due to the inward-directed vergence of the hanging wall during central uplift formation. Later, open folds related to rotational (ramp-parallel) collapse developed locally along some of the imbricated thrust slices and are interpreted as evidence of a minor collapse of this SW part of the collar. B) Within one of the thrust slices, an up to 20-cm-thick, dark gray pelitic band shows evidence of a connection between folding and faulting. We interpret these structures as having been generated during the minor, outward-directed, gravitational collapse of this part of the collar (see text for details). Hammer for scale is 33 cm long.

Rotational collapse (ramp-parallel) related open folds (formed due to outward-directed drag and back-rotation between the shear bands) are observed in some of the imbricated thrust slices (Fig. 9A, B). The apparent plastic behavior that promoted these

folds was, at least in part, due to brittle deformation fostered by millimeter-to-centimeter-spaced – and mostly reverse – faults forming a network of local displacements mainly in fold hinge zones (Fig. 9B; see Kenkmann, 2002). Locally, there are also radial, steeply dipping (e.g., 324°/80°), small-scale strike-slip faults that dextrally displace the strata in a domino-like pattern by a few millimeters each. However, the relationship and timing between these structures and the thrust slices could not be constrained.

ENE Collar of the Central Uplift

Our data reveal a more complex structural framework between R = 7.2 to 2.5 km in this sector than in its SW counterpart (compare Fig. 8A–C and Fig. 8D–I). Aquidauana Fm. beds in the ENE collar generally have inward, outward, or tangential, shallow to moderate (10°–50°) dips (Fig. 8D); however, no outcrop-scale folds were observed. This pattern is much like that in the Aquidauana Fm. rocks in the intermediate section. Close to the inferred contact with the Ponta Grossa Fm., at R ~ 6.4 km (station P-275; 52.93617°W, 16.79206°S), a more than 20-m-long section of locally brecciated, laminated, red Aquidauana Fm. sandstone, with centimeter-scale intercalations of planar- and cross-bedding, consistently dips steeply (~70°–80°) inward (see "Innermost" label in Fig. 8D).

In the outermost Ponta Grossa Fm. at R ~ 6.2 km (station P-008; 52.93777°W, 16.79362°S), a >100-m-long exposure with silicified and ferruginous strata exhibited bedding that dipped inward and up to meter-scale, highly asymmetric to overturned folds that consistently verge outward (Fig. 8E). Sparse moderately inward-dipping fault planes were oriented parallel to some of the inward-dipping fold limbs. One of these fault planes showed slickenlines that plunged down-dip, supporting an outward vergence. In the course of further roadworks, this unique outcrop was unfortunately destroyed.

The Ponta Grossa Fm. beds at R ~ 6.0–4.7 km show highly variable bedding dips that range from subhorizontal to vertical. Dip directions are quaquaversal, with a slight predominance of quasi-tangential to oblique dip orientations (Fig. 8F). The weathered state of exposures hinders identification of any folds and faults that might exist. Where observable, folds display wavelengths and amplitudes of tens of centimeters and are upright, tight, slightly asymmetric, and oriented radially to obliquely. Shallowly dipping, gently undulating, ferruginous beds occur repeatedly in this inner part of the Ponta Grossa Formation. These beds exhibit gently warped surfaces with wavelengths of tens of

centimeters to ~1 m, and quaquaversal, up to slightly moderate (≤25°), bedding dips (Fig. 8F).

We identified that the Furnas Fm. collar in this sector can be divided into two distinct structural domains – an outer Furnas domain, at R >2.6 km, characterized by flat terrain, and an inner Furnas domain, at R ≤2.6 km, comprising in the studied area (see stations in Fig. S1) a 250–350-m-wide zone of prominent hills that are elevated up to 70 m above road level, immediately adjacent to the core of the central uplift.

The kaolinitic sandstone in the outer Furnas Fm. structural domain is commonly severely weathered and crumbly, making it challenging to observe folds and faults. Purple siltstone layers/lenses occur locally. Bedding dips range from subhorizontal to vertical, but most dips scatter around shallow to moderate (<50°) angles. Dip directions are mainly tangential to oblique but locally also radially outward (Fig. 8G). In some places, bedding forms 10-cm-scale, gentle undulations or tight, moderately inclined radial folds, some of which have overturned limbs.

Bedding in this outer Furnas Fm. domain is, in places, disrupted by faults. The few faults we could study have quasi-tangential or radial-to-oblique strikes. Faults are generally parallel to the contacts between white sandstone layers and up to meter-thick purple siltstone layers/lenses. The tangentially striking fault planes have shallow to steep (20°–75°) outward dips, commonly subparallel to the NE-dipping beds in their vicinity. Slickenlines associated with these fault planes generally show down-dip plunges. However, one steep, outward-dipping fault plane displays slickenlines with a shallow tangential plunge (24°/120°). We did not observe features that could indicate a sense of movement related to these two lineation sets. The radial faults have moderate to steep, locally vertical, dips (generally >55°). One of the radial faults indicates sinistral displacement of at least a few meters, with an associated meter-scale drag fold within a purple siltstone layer. Another, but more radial-to-oblique, steeply dipping fault plane shows down-dip plunging slickenlines (58°/280°), indicative of dip-slip movement.

In contrast, the inner Furnas Fm. structural domain, at R ≤2.6 km, comprises comparatively more competent, laminated, white/beige sandstone (notably purple siltstone layers/lenses are absent). Here, bedding dips are highly variable, ranging from subhorizontal to vertical, with steep (>60°), inward- or outward-dipping beds being more abundant (Fig. 8H). Folds and faults are comparatively more readily observable in this domain. Folds are common at the meter to multi-meter scale, with open, asymmetric

forms or overturned limbs. In some places, parasitic, 10-cm-scale folds can be observed. Overall, the folds in the ENE inner Furnas Fm. domain verge outward. In some areas, a secondary (in scale and timing) folding pattern is noted as well. It has gently and quasi-radially re-folded the already folded bedding.

Different fault sets occur in the inner Furnas Fm. domain. A set of fault planes that dip subparallel to oblique to the NE-dipping limbs, i.e., with outward dips (at 40°–85° toward 045°–075°), is most prominent. Slickenlines with both down-dip (radial) or strike-parallel (26°/131°; i.e., tangential) orientations are observed along some of these fault planes. No relationships between these two sets, nor any further kinematic indicators, could be constrained in this area.

The (meta)sedimentary basement inlier in the ENE collar of the central uplift. In the outer Furnas Fm. structural domain, close to the contact with the Ponta Grossa Fm., at $R \sim 4.6–3.8$ km, the MT-100 transects an ~340-m-long, continuously exposed (meta)sedimentary basement inlier, at 52.95561°W, 16.80036°S (see Figs. 1 and 8). From E to W, the sequence comprises (1) dark gray to dark purple phyllite, followed by (2) gray to purple, matrix-supported (meta)conglomerate containing elongated, well-rounded quartz pebbles measuring from 1 cm to 6 cm in length. These clasts do not show any macroscopic shear fractures of the type discussed as shock-related by King et al. (2025). The matrix of the (meta)conglomerate primarily consists of coarse quartz sand, but 1–2-mm-sized flakes of dark mica are also noted. From the contact with the phyllite and toward the W, the (meta)conglomerate grades into a gritty (meta)sandstone, and again – abruptly – into (meta)conglomerate, which finally grades into a red (meta)sandstone with lenses and layers of purple (meta)siltstone. Locally in the (meta)conglomerate, some tabular, 10-cm-wide, heavily weathered, granitic intercalations occur with lengths of up to tens of centimeters. These are oriented subparallel to the stratification of the (meta)sedimentary host and are segmented by a local, steep fault set. The sequence ends in the W with (3) a white to pink (meta)sandstone containing muscovite.

This entire (meta)sedimentary basement inlier forms a 100-m-scale, asymmetric radial fold, the limbs of which dip quasi-tangentially (NW–SE) with respect to the NE limit of the core of the central uplift (Fig. 8I). In the phyllite of the eastern part of the outcrop, foliation consistently dips ≥65° tangentially to the SE. Foliation dip gradually changes to subhorizontal in the hinge zone of this large fold, which is exposed in the

central part of the roadcut. The contact between phyllite and (meta)conglomerate is folded, and the phyllite foliation truncates the contact at a shallow oblique angle. Farther W, this contact steepens and dips to the NW. Still farther W, the contacts between the different (meta)sedimentary packages dip at 40°–50° to the NW, and even steeper dips occur toward the W end of the exposure. Here, centimeter-spaced fractures dip subhorizontally to moderately (~10°–30°) to the SW, i.e., quasi-inward with regard to the NE limit of the core of the central uplift. No kinematic indicators could be observed on these fractures.

The Northern Domain of the Core of the Central Uplift

New outcrops along the MT-100 road occur from the W edge of the core to its NE limit (see Fig. S1). At the westernmost limit of the core, close to the contact with the Furnas Fm., lies the phyllite basement outcrop that has long been known for its abundant, up to 15-cm-long shatter cones (station P-005, R ~ 2.3 km, 53.01253°W, 16.81873°S). Roadworks severely damaged this outcrop by removing volumes of accessible phyllite with shatter cones, so that the best observational level is now ~3 m above the new road surface. The phyllitic foliation in this area dips consistently steeply (60°–75°) outward, and no folds are observed. Reverse faults in the phyllite exhibit an inward movement of their hanging walls, but the magnitude of the displacement could not be measured owing to a lack of reliable markers. Some steeply dipping reverse faults have juxtaposed phyllite and polymict impact breccia packages of several meters in thickness. Also, up to meter-thick, purplish-gray, polymict lithic impact breccia dikes occur at several places in the phyllite.

Following the MT-100 northeastward, fractured basement phyllite gives way to further prominent exposures of polymict impact breccia, discussed by Souza et al. (2024), although the actual contact is not exposed.

The MT-100 roadcuts provide an ~1400-m-long SW-NE transect through the NE region of the core and innermost collar of the central uplift (Fig. 10; see Figs. 1 and 8 for profile location). Phyllite, fine- to medium-grained granite, different impact breccia types, and blocks of (meta)sedimentary and/or lowermost Paraná Basin sequence lithologies, up to tens of meters in width, are exposed along this profile.

Phyllite occurs as up to 10-m-scale blocks, as well as wider, seemingly coherent exposures that may represent the crater floor (also Souza et al., 2024). Such coherent

phyllite has foliation that generally dips moderately (40°–50°) to the SW (i.e., obliquely inward). Both shallower and steeper dips have also been observed, and together, this evidence may relate to segments of asymmetric folds with wavelengths of meters to tens of meters (see Fig. 10). Alternatively, this may indicate block-faulting, as steeply dipping faults, seemingly perpendicular to oblique to the road extension, interrupt this folding pattern in some places. However, the weathered strata and crumbly conditions of the phyllite outcrops precluded more systematic fault analysis. In addition, some up to 50-cm-wide and almost vertical pegmatite dikes cut across the phyllite (Fig. 10). Local reverse faults striking perpendicular or oblique to the road trend have displaced some of these dikes.

Granite is exposed over a 110-m-long roadcut section (Fig. 10). It is white to pink, characterized by an inequigranular, fine- to medium-grained (crystal sizes ≤5 mm) texture, and lacks the large, centimeter-sized K-feldspar phenocrysts that are typical of the main Araguainha alkali granite phase of the inner core. Instead, this roadcut granite is similar to the fine- to medium-grained granite described from a nearby area by Souza et al. (2024).

This fine- to medium-grained granite is intrusive into the phyllite and primarily consists of plagioclase, K-feldspar, quartz, biotite and muscovite as minor phases, and accessory Fe-Ti oxides. In the vicinity of these granite occurrences, the phyllite exhibits disseminated, lozenge-shaped, dark green phyllosilicate spots up to 1 cm in diameter. These clots have been interpreted as pseudomorphs after cordierite formed due to contact metamorphism. Locally, cataclasite marks the interfaces between the granite and the phyllite (see Fig. 10). At one of these interfaces (station P-108; $R \sim 1.9$ km; 52.98738°W, 16.79909°S), an almost vertical, meter-wide fracture zone filled with polymict impact breccia (red polymict lithic breccia and light green suevite; details below) with ample phyllite fragments occurs (Fig. 11).

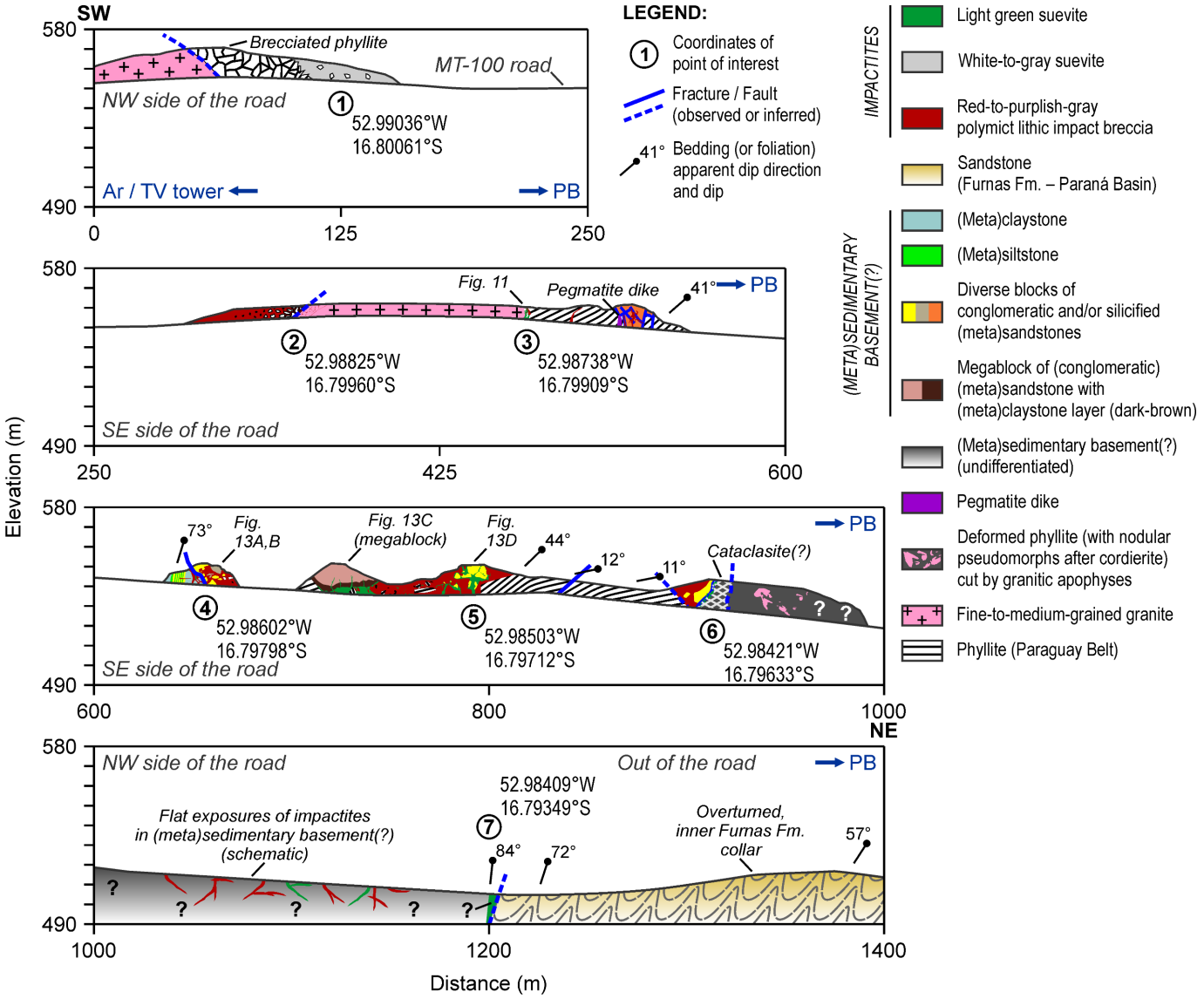

Figure 10. A 1,400-m-long, SW-NE composite profile across the NNE region of the core and part of the inner collar of the central uplift, mainly along the MT-100 road. See Figs. 1 and 8 for profile location. The profile has no vertical exaggeration. It summarizes a quasi-continuous exposure of the main features of this area. Note that the composite profile shows roadcuts from both sides of the road and beyond. Blue arrows in the profile point to the direction of specific spatial references. Ar – Araguainha town; PB – Ponte Branca town. Coordinates of some points of interest and the location of other figures are indicated.

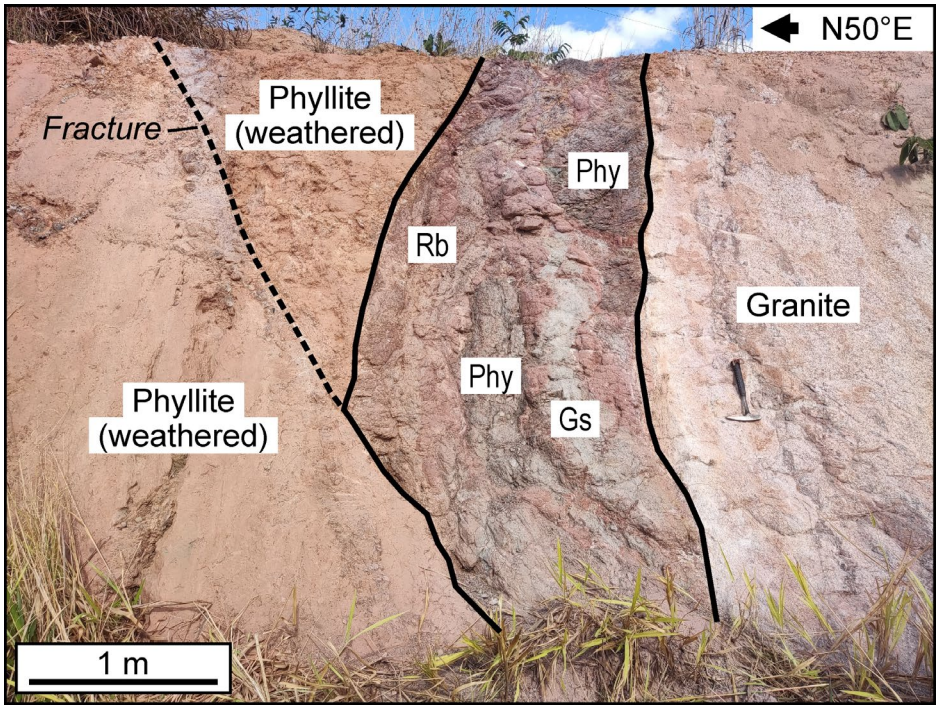

Figure 11. The interface between basement phyllite and fine- to medium-grained granite along the MT-100 road (station P-108; *R* ~ 1.9 km; 52.98738°W, 16.79909°S). This interface features an up to 1.3-m-wide fracture zone, filled with red polymict lithic impact breccia (Rb), light green suevite (Gs), and phyllite (Phy) fragments. Black arrow at the top right points to the (inter)cardinal direction.

At least three types of polymict impact breccia occur in the N part of the core of the central uplift (see also Souza et al., 2024, for more detail on these breccias): (1) white-to-gray suevite that carries up to meter-sized clasts of highly silicic impact melt rock; this corresponds to impact melt rock Type-II of Souza et al. (2024), who interpreted it as derived mainly from the Furnas Fm. (Fig. 12A); (2) a red (locally purplish-gray) polymict lithic impact breccia (Fig. 12B); and (3) a light green suevite with a fluidal-textured matrix and clasts of dark gray impact melt rock (Fig. 12C). The relative proportions of the different breccia types are highly variable across the studied section (Fig. 10; see also Souza et al., 2024). However, the red polymict lithic breccia appears to be the dominant type.

The white-to-gray suevite (Fig. 12A) was observed in a single roadcut along the MT-100 (station P-045; *R* ~ 1.6 km; 52.99036°W, 16.80061°S; also described by Souza et al., 2024). Its volume in this outcrop is considerable. This road section shows sharp and discordant lateral transitions (to NE) from fine- to medium-grained granite into brecciated phyllite and, finally, suevite (see Fig. 10). No other structural-spatial relationship was

observed between this white-to-gray suevite and the other impact breccia types or target rocks.

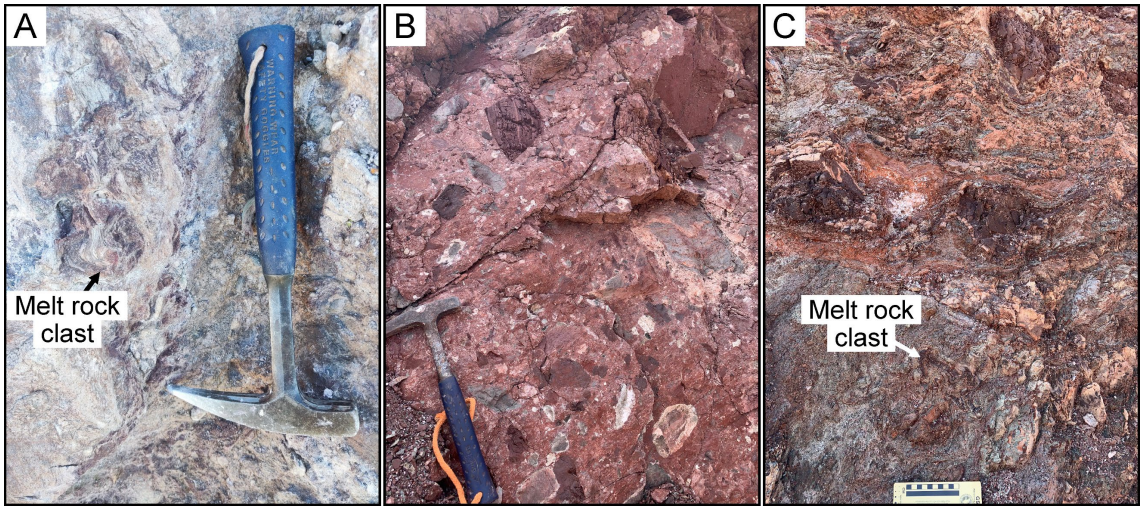

Figure 12. General appearance of the different impact breccia types identified in this work in the northern region of the core of the central uplift (see text for details). Hammer for scale is 33 cm long. A) White-to-gray suevite containing up to 1-m-sized impact melt rock clasts of highly silicic composition (impact melt rock Type-II of Souza et al., 2024). B) Red, locally purplish-gray, polymict lithic impact breccia. C) Light green suevite with a fluidal-textured matrix and micro- to mesoscopic, dark gray impact melt rock clasts. The scale at the base of the image is 10 cm wide.

The red polymict lithic impact breccia (Fig. 12B) is commonly found enclosing tens-of-meters-wide zones of brecciated phyllite and up to meter-scale (meta)sedimentary blocks, or as up to tens-of-centimeters-wide dike injections into phyllite or other (meta)sedimentary rocks. These dikes appear to be randomly oriented. This breccia also occurs as up to meter-sized blocks in the light green suevite (see Fig. 13). The major components of the red impact breccia are derived from (meta)pelites and (meta)psammites of the basement of the Paraná Basin and, to a lesser degree, from the basal sequences of the basin (see also Souza et al., 2024).

The light green suevite (Fig. 12C) commonly occurs as centimeter- to meter-wide dikes – with a fluidal-textured matrix surrounding mineral and lithic clasts – that cut through red polymict lithic breccia and the (meta)sedimentary basement (Fig. 10; see Fig. 13). This suevite can be a prominent phase in some exposures (see examples in Fig. 13 and below); however, it is commonly highly weathered. From field observations, the main lithic components of the light green suevite are phyllite, (meta)sandstone, blocks of the red polymict lithic breccia, minor granite clasts, and abundant clasts of impact melt rock – sometimes occurring as vitroclasts.

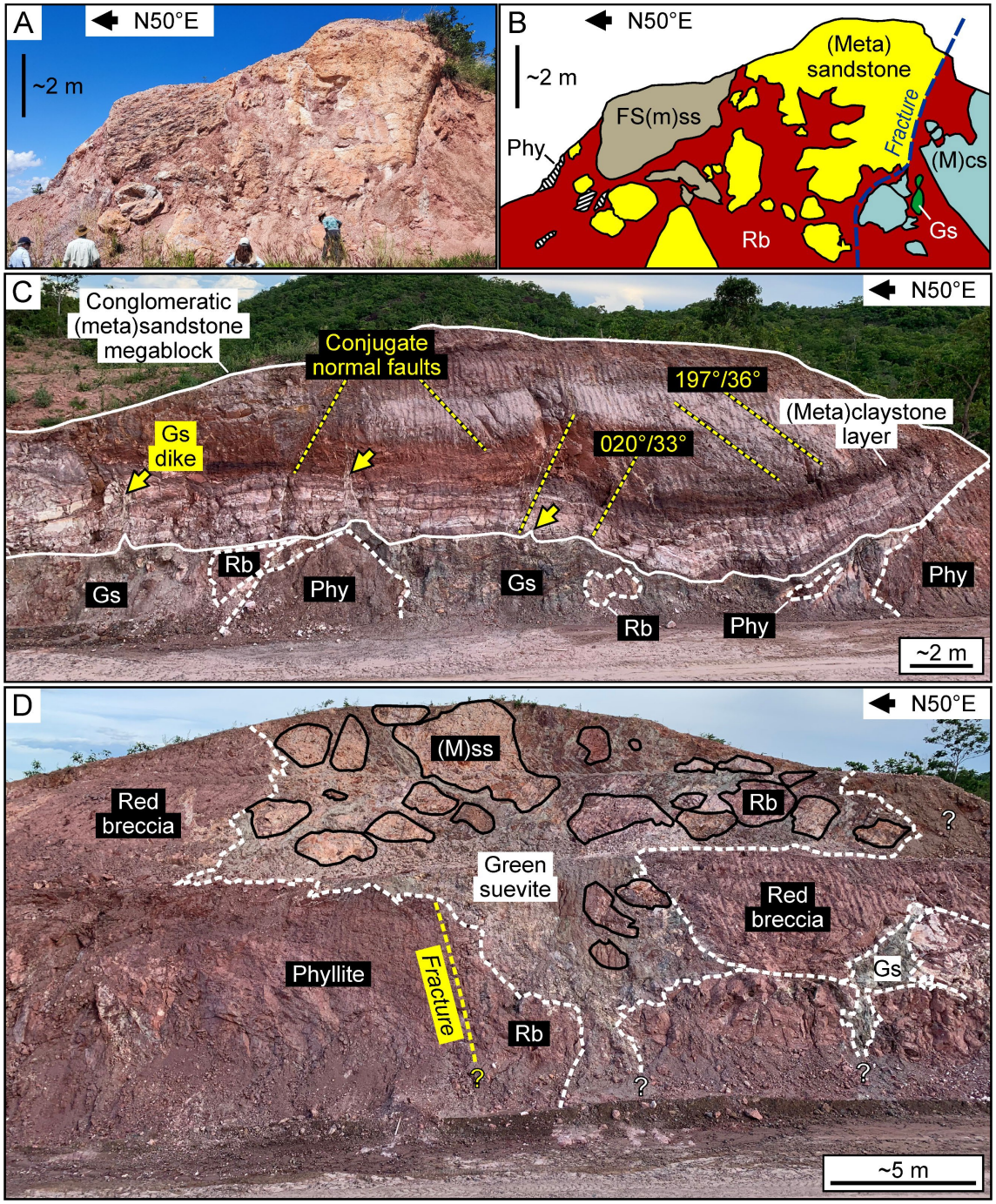

Figure 13. Selected new exposures in the northern region of the core of the central uplift along the MT-100 road profile shown in Fig. 10. Black arrow at the top of each panel points to the (inter)cardinal direction. A) Photo of and B) drawing of an outcrop (station P-321; *R* ~ 2.0 km; 52.98602°W, 16.79798°S) showing the relationship between up to meter-sized blocks of different target lithologies, red polymict lithic impact breccia (Rb), and a local occurrence of light green suevite (Gs). Vertical black bar for scale is ~2 m long. The block lithologies are mainly (meta)sandstone (yellow), fractured and silicified (meta)sandstone [FS(m)ss – beige], (meta)claystone [(M)cs – light blue], and phyllite (Phy – zebra stripe pattern). The blue dashed line indicates a fracture trace. Color codes are the same as in Fig. 10. C) A large (10-m-scale) megablock of conglomeratic (meta)sandstone along the MT-100 road (station P-014; *R* ~ 2.1 km; 52.98553°W, 16.79756°S). This megablock rests above a wide occurrence of light green suevite (Gs), which contains blocks of other brecciated materials (e.g., Phy – monomict phyllite breccia, Rb – red polymict lithic impact breccia). Yellow arrows show injections of light green suevite. Radially dipping,

penetrative conjugate normal faults (yellow dashed lines) cross-cut the entire megablock. Note that the whole outcrop wall also displays quasi-vertical excavator bucket tooth marks. D) An ~15-m-high roadcut at *R* ~ 2.1 km (52.98503°W, 16.79712°S) that reveals the structural-spatial relationships between some impactites and the (meta)sedimentary basement lithologies. A fracture (yellow dashed line) has juxtaposed phyllite with red polymict lithic impact breccia (Rb). A prominent volume of light green suevite (Gs) cuts through phyllite and red polymict lithic impact breccia. Up to meter-sized blocks of the red breccia, (meta)sandstone – (M)ss, and other materials occur in the light green suevite.

Along the different roadcut exposures in the northern core, up to 10-m-scale blocks of (meta)claystone, (meta)siltstone, (meta)sandstone intercalated with (meta)siltstone, conglomeratic (meta)sandstone, (meta)conglomerate, and phyllite occur. These blocks are separated by faults with highly varied orientations, or they are embedded in polymict impact breccia (Figs. 10, 13A, and 13B). (Meta)conglomerate blocks are particularly prominent. They are matrix-supported and characterized by vein quartz or quartzite pebbles/cobbles measuring up to 10 cm in size in a white, kaolinitic, sandy matrix. These clasts have low sphericity, are subrounded to rounded, and consistently display transverse shear fractures (like the fractures discussed by King et al., 2025).

Two high roadcut exposures reveal the main structural and spatial aspects between the light green suevite and the other lithologies. The first (station P-014; *R* ~ 2.1 km; 52.98553°W, 16.79756°S) shows an ~35-m-long and ~8-m-high allochthonous megablock of stratified, mostly conglomeratic (meta)sandstone that overlies a light green suevite horizon (Fig. 13C). Within this horizon, there are up to meter-sized blocks of phyllite and red polymict lithic breccia. Locally, immediately beneath the megablock, the light green suevite has a shear foliation that dips shallowly to moderately outward. A penetrative conjugate pair of moderately dipping normal faults cross-cuts the megablock and has boudinaged some parts of it (Fig. 13C). These conjugate faults dip radially. Subvertical, upward-thinning, decimeter-wide light green suevite dikes intrude the megablock (see yellow arrows in Fig. 13C).

The second exposure is an ~15-m-high roadcut (Fig. 13D) located ~70 m NE of the previous station, at 52.98503°W, 16.79712°S. Here, light green suevite emerges from a meter-wide dike that cuts red polymict lithic breccia and widens upward, encompassing meter-sized blocks of, *inter alia*, (meta)sandstone, phyllite, and red polymict lithic breccia.

It should be noted that Souza et al. (2024) could provide lithological and structural observations on a 350-m-long transect where the MT-100 originally curved through the "Serra da Arnica" megablock zone. They identified block faulting of the

(meta)sedimentary basement, injections of granitic phases, and an extensive occurrence of impact melt rock Type-I. This is the only such impact melt rock occurrence along the entire profile through the northern core of the central uplift. Unfortunately, this roadcut transect was partially destroyed by further roadworks.

DISCUSSION

The Updated Araguainha Geology in Comparison to Previous Morphostructural Understanding

A new suite of large, fresh exposures created in recent roadworks, combined with other newly described outcrops throughout the structure and the higher-resolution remote sensing imagery used here, have allowed the creation of an improved geological map of the AIS and its environs (Fig.1). Our observations have also contributed to a refined perspective on the morphology and structure of the AIS (see Fig. 14). In the following, we discuss our results consecutively from the environs of the impact structure toward its central uplift area.

The Nature of the Structures Outside the AIS: What is the Size of the Impact Structure?

Previous geological fieldwork in the AIS (e.g., Crósta et al., 1981; Theilen-Willige, 1981; Lana et al., 2008) did not significantly explore the structural framework in the environs of the outer rim region (R >~20 km). Furthermore, early mapping in the area of the structure (e.g., CPRM, 1981) did not consider the structural implications of impact cratering. Others, such as Lacerda Filho et al. (2004) and Tohver et al. (2018), worked on a wider regional scale. Notably, Tohver et al. (2018) proposed the occurrence of soft-sediment deformation features (interpreted as seismites) in the uppermost strata of the Passa Dois Gr. (i.e., the Corumbataí Fm.) over a region from 50 km to 1000 km from the center of the AIS. They related these features to the effects of the Araguainha impact event.

Our field observations, which extend for ~14 km beyond the SW and NE apparent outer rim sections (see data stations in Fig. S1), did not reveal evidence requiring revision of the currently accepted ~40 km apparent diameter for the AIS. However, the structural variability observed beyond the outer rim of the structure is more prominent than previously reported. Structural data do not show widespread, steeply dipping beds and

significant folding at *R* >~20 km, although faulting and very limited (up to meter-scale) folding do occur locally.

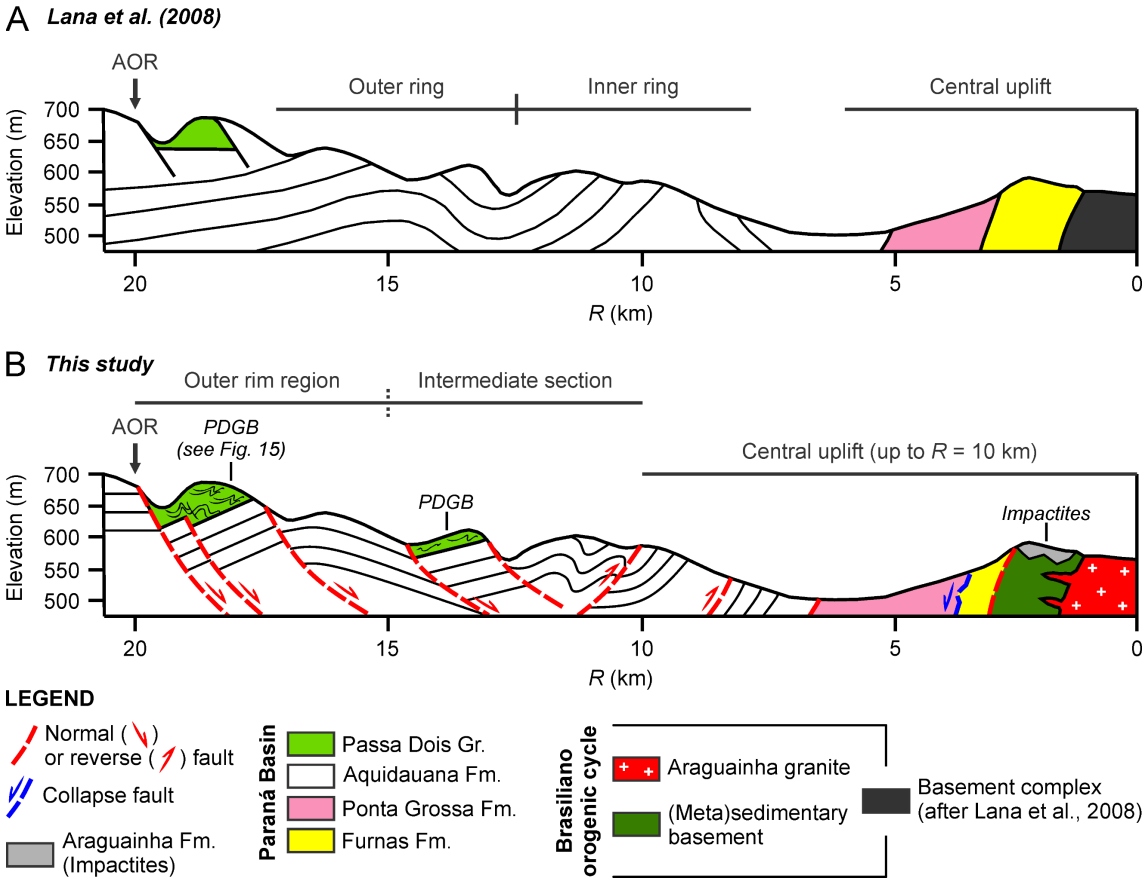

Figure 14. Schematic, and vertically exaggerated, radial cross-sections showing contrasting morphostructural models for the Araguainha impact structure (AIS). The models only depict first-order morphological and structural features. A) This model, after Lana et al. (2008), proposes the existence of kilometer-scale, antiformal outer and inner concentric rings in the Aquidauana Formation. B) Our model utilizes the same topographic profile for ready comparison. It favors: large-scale, tilted and/or rotated, fault-bounded blocks; different morphology of, and structure in, the Passa Dois Gr. Blocks (PDGBs; see Fig. 15 for more detail); no concentric rings; and a comparatively wider central uplift. *R* – radial distance from the apparent center of the AIS. AOR – apparent outer rim. See text for details.

Outside the AIS, (1) the Ponta Grossa Fm. beds overall dip shallowly to moderately to the SW; no outcrop-scale folding is in evidence, but beds are commonly tilted by faults; (2) Aquidauana Fm. strata are oriented (sub)horizontally and not folded; and (3) Passa Dois Gr. beds are generally horizontal but are locally faulted and folded on the meter scale. The structural lineaments mapped with remote sensing imagery are seen within all these geological units (see Figs. 1 and S2).

We highlight the existence of a well-acknowledged (Zalán et al., 1990; Gesicki et al., 2002; Milani et al., 2007; Horn et al., 2022) regional unconformity between the

Devonian Ponta Grossa Fm. and the Carboniferous–Early Permian Aquidauana Fm. (see Fig. 2). This unconformity has been related to a significant amount of erosion and a long hiatus in the depositional record of the Paraná Basin (Milani et al., 2007). As the end-Permian (ca. 259–252 Ma) Araguainha impact event postdates the deposition of these formations, the observed bedding orientation contrast between these units in the environs of the AIS cannot be attributed to the impact event. Thus, we consider this structural contrast to be associated with the pre-impact evolution of the NNW Paraná Basin during the Paleozoic, when a mainly brittle (faulting-related) tectonic event fractured and tilted the Devonian strata before the deposition of the flat-lying Aquidauana Formation. The only significant tectonic event(s) we can associate this with are possible movements along the broad deformation zone of the Transbrasiliano Lineament (Schobbenhaus et al., 1975; see inset in Fig. 1), which is known for its repeated reactivations throughout the Phanerozoic and its structural influence in the crustal framework and evolution of the NNW Paraná Basin (see Curto et al., 2014, 2015, and references therein).

Despite the existence of an unconformity between the Aquidauana Fm. and the overlying Passa Dois Gr. in the NNW Paraná Basin (Milani et al., 2007; see Fig. 2), beyond the SW quadrant of the AIS, the bedding of the Aquidauana Fm. and the upper Passa Dois Gr. (Corumbataí Fm.), as well as the contact between them, are primarily (sub)horizontal. However, these formations show local evidence of brittle-ductile deformation: (1) they may be juxtaposed along reverse faults (at station P-002; $R \sim 31.3$ km; Fig. 3C); and (2) the Corumbataí Fm. is locally faulted and folded at the meter-scale (e.g., at station P-001; $R \sim 56$ km; also along the MT-100). As both these units were deposited before the impact, it is likely that these locally observed deformation structures also developed as a result of the same regional reactivations of the Transbrasiliano Lineament and related structures in the NNW Paraná Basin. The relatively more common evidence of folds in the Passa Dois Gr. – relative to the more massive, psammitic Aquidauana Fm. – may stem from the Passa Dois Gr.'s heterolithic, pelite-dominated character.

The overall strike of the fractures/faults beyond the AIS ($R >\sim 20$ km) and their parallelism with the structural lineaments in the AIS environs (see Figs. 1 and S2) also suggest that the impact event did not generate these structures. The strike of faults outside the AIS (e.g., the α and β fractures of Fig. 3B) relates well to the NE-SW and NW-SE lineament trends that characterize the wider NNW Paraná Basin and that can be associated

with the older and continental-scale structures of the Transbrasiliano Lineament and the Paraguay Belt underlying and adjacent to the basin (compare with Curto et al., 2014, 2015).

The folding in the Corumbataí Fm. outcrop at $R \sim 56$ km (station P-001) is seemingly controlled by such faults. The vergence of these folds is conditioned by the orientation of the earlier faults and clearly does not indicate centripetal or centrifugal movement that could be directly related to the impact.

Notwithstanding the observation that the structural framework beyond the AIS can be explained by regional pre-impact tectonics, it should be considered that pre-existing structures might have undergone reactivation during the Araguainha impact event. A basic simulation of the Araguainha impact event using the Earth Impact Effects Program (Collins et al., 2005) – with the input of typical impact parameters as listed in Table S1 – yields a possible projectile diameter of 3.2 km, an amount of energy of 7.44 x 10^{21} joules for the meteoritic projectile before it entered the atmosphere, a final crater diameter of 40.3 km, and an 8.8 magnitude seismic event resulting from the impact. This projectile diameter is similar to the 3 km impactor proposed by Miyazaki et al. (2021) from iSALE-2D modeling of the Araguainha impact. Also, the resulting seismic magnitude is within the 8.6–10 range for impactogenic seismicity calculated for the Araguainha impact by Tohver et al. (2013).

At $R \sim 56$ km – i.e., the radial distance of the farthest Passa Dois Gr. (Corumbataí Fm.) outcrop with limited folding that we could observe, and which is within Tohver et al.'s (2018) proposed range for impact-related seismite development in the Corumbataí Fm. – this hypothetical seismic event would have generated a seismic wave with sufficient energy equivalent to the intensities X and XI on the Modified Mercalli Intensity scale (out of a total of 12 intensities; see Collins et al., 2005). These intensities would have been sufficient to cause, *inter alia*, large landslides and, thus, could have caused some liquefaction and localized remobilization (folding?) of the topmost Corumbataí Fm. as a direct consequence of the impact at such a distance.

How much of the AIS diameter has been lost to erosion? A first-order loss to erosion from the original Araguainha crater diameter can be estimated with a simple trigonometric approximation, explained graphically in Fig. S4. Assuming 60° as the minimum normal fault dip angle for the outermost rim faults, as observed in this work

(see Fig. 4A–C), and by accepting the 250–350 m depth of erosion in the AIS proposed by Lana et al. (2007) based on regional stratigraphic and elevation associations, a range of 290–400 m of loss of diameter for the AIS since its formation is obtained.

A relative degree of erosion of 6 (on their scale of 7 degrees) was assigned by Osinski et al. (2022) as a measure of preservation for the AIS. By their definition, this degree indicates that the ejecta blanket and the pristine crater rim are eroded, but remnants of crater-fill impactites are still preserved. Based on our observations, this suggested level of preservation seems adequate for the AIS. Indeed, remnants of crater-fill breccia are observed predominantly along a swath from the W to the NE around and within the core of the central uplift (also Souza et al., 2024). However, the original crater rim is differentially eroded across the various azimuthal sectors of the AIS (e.g., the apparent outer rim still exhibits a prominent topographic scarp in the SW, NW, and N sectors but not in the E and SE sectors; Fig. S2). Thus, our limited estimate for the loss of diameter (290–400 m), which represents ~1% of the apparent diameter of the structure (40 km), should be taken as a first-order average estimate across the different sectors.

Our field observations and inductive reasoning for a minimum 60° dip for the outer rim normal faults do not disallow the existence of outer rim faults with lesser dip values. Such normal faults with lesser dips would yield larger values of lost diameter. In this sense, we should also consider the 290–400 m range for the AIS diameter lost to erosion with caution and as a possible minimum estimate. Either way, these values are dwarfed by the up to 2 km offset of the apparent crater rim along radial-to-oblique faults, which have distorted the circular geometry of the structure (Lana et al., 2008).

Structures of the Outer Rim Region and Intermediate Section

The outer rim and intermediate domains have structural frameworks that are more complex than previously proposed by Lana et al. (2006, 2007, 2008). Nevertheless, despite some local peculiarities unique to either of these domains, the overall structural framework for the $R \sim 20–8$ km section is remarkably consistent across both domains. The prevalence of inward and outward, radially dipping beds in both domains suggests that (sub)horizontal inward-directed, centripetal compression related to the collapse of the structure during the modification stage of cratering was the primary driving mechanism of deformation in these domains (see also Lana et al., 2006, 2008).

We could not identify any systematic, gradual steepening of bedding dips from the outermost rim region into the intermediate section. One notable exception occurs in the innermost intermediate section in the SW sector, at $R \sim 10–8$ km along the MT-100, where a progressive steepening of the dips of Aquidauana Fm. bedding occurs toward the center of the structure. The reasons for and implications of this deviance appear to be related to central uplift formation and collapse and will be discussed below.

The otherwise rather consistent framework calls for a single, impact-related deformation mechanism involving these outer and intermediate domains. Firstly, continuous, outcrop-scale folding is not standard in these domains. Secondly, moderately to steeply dipping beds that dip tangentially or obliquely are much more common than previously acknowledged. These observations, combined with the fact that bedding direction is commonly parallel to the strikes of fault sets (akin to the structural lineaments of Figs. 1 and S2) throughout both domains, allow us to propose a new model to explain the structure of these sections.

A model of tilted (from the horizontal) and/or rotated fault-bounded blocks (of Aquidauana Fm.) can adequately explain the first-order structural framework in the outer rim region and intermediate section. The blocks appear to vary in size on the 100–1000 m scale and are delimited by an intersecting system of concentric/tangential, radial, and oblique faults that we attribute to a combination of reactivated regional pre-impact faults and new, impact-created, faults (Figs. 1 and S2).

Thus, our model departs from the relatively continuous and concentric folding-dominated model previously proposed by Lana et al. (2008) for these domains (compare Fig. 14A, B). In our view, the fault-bounded blocks would constrain the folding to individual blocks, allowing local structural peculiarities to develop within and between blocks. This scenario accounts for the variability in structural observations across different sectors.

The major structural peculiarities of each domain are: (1) 100- to 1000-m-scale, generally concentrically arranged, fault-bounded blocks that resemble terraces of pristine craters, particularly in the NW and N sectors at $R \sim 20–16$ km (outer rim region); and (2) 100-m-scale folded or steeply dipping zones of rather well-laminated Aquidauana Fm. sandstones intercalated with coarser-grained, generally massive, commonly brecciated sandstone blocks in the N and NNE sectors of the intermediate section at $R \sim 13.5–12$ km (Fig. 6). These features in the Aquidauana Fm. are specific to certain azimuthal sectors

and radial distances and, thus, suggest a structural asymmetry in the AIS (which will be discussed in the last part of this Discussion section).

The first-order differences between the outer rim region and the intermediate section revolve around the size of the resulting major structures present in each domain. For example, the fault-bounded Aquidauana Fm. blocks and the PDGBs tend to be more prominent in size in the outer rim region, where the lineament density seems lower when compared to the inner parts. Although we cannot rule out that differential erosion might be responsible, to some degree, for these differences, the difference in size between the features of these domains is more likely a consequence of the "space problem" related to the inward collapse of the transient crater walls, compounded by the simultaneous rise of the central uplift during the modification stage. This space problem leads to complex 3-D deformation patterns (e.g., Kenkmann and von Dalwigk, 2000; Kenkmann et al., 2014).

The rare radial-to-oblique folding and radial transpressional features in the outer rim region (Fig. 4D) attest to some degree of tangential constriction of the Aquidauana Fm. in the outer rim domain. Due to the space problem, however, this tangential constriction was even more prominent throughout the intermediate section – as, for example, evidenced by the occurrence of the horseshoe-shaped PDGB at $R \sim 15.0–13.5$ km of the SW sector (Fig. 7).

The rheological contrast between the laminated, more pelitic upper Aquidauana Fm. and the more massive and, in large part, psammitic, lower Aquidauana Fm. (see Fig. 2) likely also played a significant role in the development of different structural styles in the strata now exposed in the various sectors and at different radial distances. Thus, the development of detachment (displacement) surfaces should have been facilitated locally along rheologically contrasting interfaces to accommodate the increase in inward-directed strain (as suggested in Fig. 6).

Conversely, and in agreement with Lana et al. (2008), we found no direct evidence of low-angle detachment faults within the Aquidauana Fm. in the outer rim and intermediate domains. Low-angle detachment faults are expected from structural models of some impact structures, as they may serve as a mechanism to accommodate the inward movement of terraced blocks along the outer rim–ring syncline transition (Kenkmann et al., 2000, 2014). A possibility is that low-angle detachment faults may occur along the contact between the basal Aquidauana Fm. and the top of the Ponta Grossa Fm., where a prominent rheological contrast is present (see Fig. 2).

The Passa Dois Group Blocks (PDGBs)

The combination of remote sensing analysis and mapping of newly exposed outcrops has revealed new PDGBs and refined the mapped extent of previously identified blocks. Our observations indicate that the PDGBs are primarily erosional remnants of the hanging wall blocks of faults (mainly concentric) with overall crater-inward downthrow. Seemingly, no PDGBs occur inside R <10 km (see Fig. 1). However, the geological maps of UnB-IG (2012) and Souza et al. (2024) show a PDGB against Ponta Grossa Fm. in the NW sector of the outer central uplift, at R ~ 7–6 km. In contrast, our remote sensing analysis suggests that this region in the outer collar actually represents Ponta Grossa Formation. Unfortunately, it was not possible to ground truth in this area, as the landowner did not grant permission to access the property.

The Passa Dois Gr. is the uppermost and youngest, pre-impact stratigraphic unit in the AIS region (Fig. 2). Overall, within the AIS, the relative elevations of the PDGBs decrease inward, from ~750 m down to ~450 m. Excluding the large and quasi-concentrically arranged outermost PDGBs in the NW, N, and NE outer rim region, there is a lack of other prominent blocks in the intermediate section of these sectors, in stark contrast to the southern part of the AIS, where PDGBs are abundant (see Fig. 1). This difference could be due to the pre-impact geological configuration of the target region (i.e., lack of widespread Passa Dois Gr. deposition in the northernmost region of the Paraná Basin; see Zalán et al., 1990), differential pre- or post-impact erosion between the N and S parts of the target region, or a possible consequence of oblique impact. However, the fact that the N intermediate section lacks major PDGBs coincides with the observation that this region is the least eroded (i.e., it is more elevated and exhibits the more pelitic, upper Aquidauana Fm.; see Fig. 2). This is a strong argument against the differential erosion hypothesis. This same observation favors either: (1) that the occurrence of the Passa Dois Gr. was possibly enhanced in the southern part of the target region at the time of the Araguainha impact event; and/or (2) that the Passa Dois Gr. rocks were pushed even higher on the downrange (northern) side of an oblique impact and thus were locally more susceptible to erosion.

Lana et al. (2007, 2008) stated that most of the strata in the PDGBs in the outer rim region dip shallowly outward. Lana et al. (2008) also recognized that local structural bedding variations occur in some PDGBs. These local features include meter-scale, gentle to isoclinal, asymmetric folds, and recumbent folds; shallowly plunging fold hinges with

fold axes trending obliquely to tangentially to the center of the structure; small-scale intrafolial folds; and local bedding orientation changes due to radially striking faults. We have observed all these structural features within the PDGBs, especially in the large, outermost block in the SW (Fig. 1) along an MT-100 transect (Fig. 5). We emphasize, however, that the strata of the PDGBs are significantly more disturbed than previously described. This deformation is heterogeneous between the individual PDGBs and is also heterogeneously distributed within them.

The principal, newly registered structural features in the PDGBs include: (1) meter-spaced, extensional faults at the distal margins indicating back-rotation of Passa Dois Gr. strata in the hanging wall to outward dips; (2) inward-dipping beds that form asymmetric, outward-verging folds at the distal domain (Fig. 5B); (3) meter-scale, asymmetric folds, in certain places with overturned limbs (Fig. 5C), or with an imbricated fan geometry that may occur in the proximal domain (Fig. 5F); and (4) significant volumes of brecciated and/or brittle(-ductile)-deformed Passa Dois Gr. rocks at the faulted, distal margins (Figs. 4A and S3). Furthermore, (5) there are up to 1-m-wide red sandstone blocks of Aquidauana Fm. within basal Passa Dois Gr. material. The existence of these blocks indicates different rheological behaviors and substantial scraping – possibly by detachment drag – of materials along the contact between these two units.

The available data allow several first-order observations about the strain evolution of the PDGBs: (1) most of the structures observed in the PDGBs are consistent with an overall inward-directed movement (non-coaxial shear; see black arrow “1” in Fig. 7) and penecontemporaneous tangential constriction (see black arrows “2” in Fig. 7) of the Passa Dois Gr. rock volumes, which would be in agreement with the consequences of crater wall collapse during the modification stage (see Kenkmann et al., 2014, and references therein); (2) faults with concentric/tangential, radial, or oblique strikes influenced the structural evolution of the PDGBs. This strengthens our fault-and-block-dominated model for the structure, outlined above (Fig. 14B); and (3) the first-order structural style of PDGBs in the outer rim region seems to differ from that of the blocks in the intermediate section (see below).

We report subordinate folds that show different (oblique) vergences from the general folding pattern in the PDGBs. The result of the inward collapse and simultaneous constriction manifests as complex internal structural patterns and deviation of the vergence of internal folds from a true centripetal orientation. Structural analysis failed to

establish clear overprinting relationships between concentric inward-verging folds and radial/oblique folds. However, reactivation of pre-existing radial and oblique faults may also have played a major role in the observed complex fold patterns.

Considering the general differences in size, shape, structures, and radial distance between PDGBs, we propose that the structural style of the outermost (outer rim region; $R \sim 20–15$ km) PDGBs of the AIS resembles "complex slumps" promoted by an inward-directed, and mostly coherent, gravity-driven mass transport of the Passa Dois Gr. volumes triggered by the collapse of the crater walls (compare with Fig. 15). Complex slumps occur along curved or irregular sliding surfaces (i.e., detachments), giving rise to more internal deformation features (e.g., normal and reverse faults, folds; see, e.g., Fossen, 2025). This structural interpretation for the PDGBs of the outer rim region significantly differs from Lana et al.'s (2008) graben-like structure (compare Fig. 14A, B).

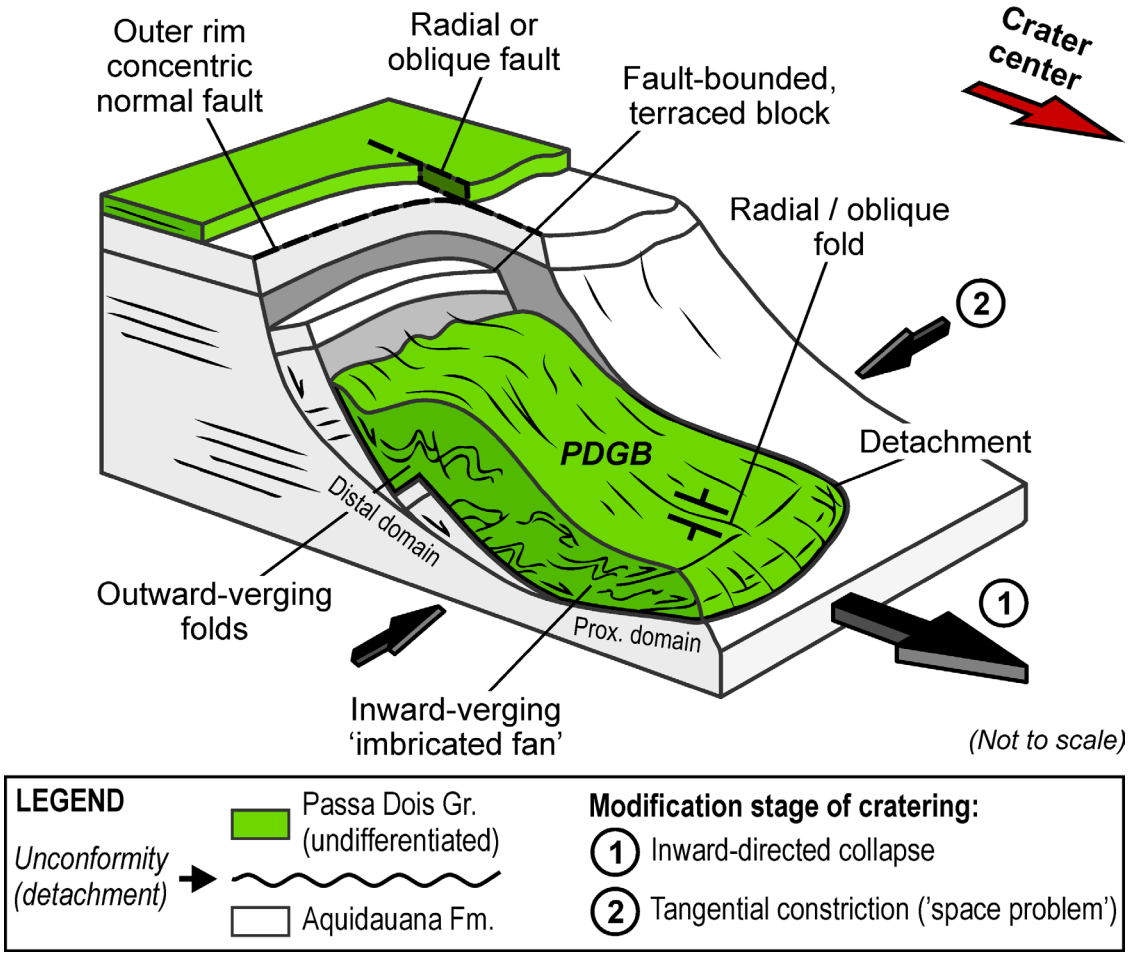

Figure 15. Schematic, unscaled (both vertically and horizontally) block diagram (adapted from Fossen, 2025, p. 3) of a typical outermost Passa Dois Gr. Block (PDGB) in the outer rim region of the Araguainha impact structure. The structural style of these outermost PDGBs resembles complex slumps generated by inward-directed gravity-driven mass transport of the Passa Dois Gr. volume triggered by the collapse of the transient crater wall. See text for further information.

The formation of the inner (intermediate section) PDGBs is somewhat different. Here, inward-directed collapse and tangential constriction also occurred. However, the latter process seems to have been more prominent due to the significant reduction of available space toward the interior of the structure (Fig. 7).

Was the Passa Dois Gr. extensively lithified before the Araguainha impact event? The current knowledge about the stratigraphy in the area of the AIS indicates that the Corumbataí Fm. was the youngest Paraná Basin unit that occurred regionally and was targeted by the bolide. Earlier works suggested that the impact target could have been a shallow marine environment (Crósta et al., 1981; Theilen-Willige, 1981; von Engelhardt et al., 1992). More recent observations proposed a lagoonal to shallow marine environment (Tohver et al., 2012) or even a brackish-to-freshwater, very shallow lacustrine environment (Lana et al., 2007). Little attention has been paid to the lithification state of the Passa Dois Gr. units of the uppermost target and its possible influence on impact effects.

Compared to the relatively well-constrained depositional age of 280–276 Ma for the Irati Fm. (lower Passa Dois Gr.; Santos et al., 2006; Rocha-Campos et al., 2019; Bastos et al., 2021; Cagliari et al., 2022), the estimate of the depositional age of the Corumbataí Fm. is more uncertain (less than 265 Ma; maximum depositional age of less than ca. 254 Ma; Fernandes, 2007; Tohver et al., 2018; Kern et al., 2021). These age estimates overlap, within uncertainties, with the current estimates for the timing of the Araguainha impact (ca. 259–252 Ma; Tohver et al., 2012; Erickson et al., 2017; Hauser et al., 2019).

Based on our geological-structural observations from the Passa Dois Gr. rocks in the AIS and environs, we can draw some inferences about the rheological state of the Passa Dois Gr. during the impact event. First, there is evidence to suggest that the lower sequence (Irati Fm.) was already lithified, primarily because it commonly occurs in a brittle-deformed (brecciated) state in the AIS, especially along the distal fault-bounded contacts of PDGBs against Aquidauana Fm. (Fig. 4A). This prominent brecciation must be related to the impact event, as it is not observed beyond the AIS. Second, the upper Passa Dois Gr. exhibits evidence of deformation of coherent beds (folding), both beyond and more commonly within the AIS. However, some structures in this unit resemble soft-sediment deformation features, possibly generated by liquefaction of target material (e.g.,

disharmonic and incoherent, small-scale folds locally observed in the outermost SW and NE PDGBs and, also, clastic dikes in the NE block). This may imply one of the following scenarios: (1) at least the uppermost level of the Corumbataí Fm. was still being deposited and/or undergoing lithification at the time of impact; or (2) the Corumbataí Fm. was already lithified prior to the impact event and was, to some extent, affected by an additional condition.

For example, a groundwater-saturated phreatic level related to this uppermost Passa Dois Gr. unit may have played a role in supporting more ductile-plastic behavior of the sediments/sedimentary rocks due to high pore pressure at a time shortly after impact. Thus, it is possible that some form of localized liquefaction of this material may have facilitated the development of the observed ductile-plastic deformation in the uppermost Passa Dois Group. Impact liquefaction of fluid-saturated sedimentary rocks has been proposed as an effective mechanism for accommodating strain in the Furnas Fm. sandstone collar of the central uplift (Hippertt et al., 2014). This scenario, however, does not disallow the possibility that the rheological behavior of Passa Dois Gr. materials located beyond the AIS might have been caused by fault reactivations unrelated to the impact event (e.g., regional earthquakes in the NNW Paraná Basin; see Curto et al., 2014). Nonetheless, a marine impact target is not needed to explain the deformation observed in the Passa Dois Gr. rocks.

The Alleged Outer and Inner Concentric Rings: Evidence for a Peak-Ring Impact Structure?

Lana et al. (2006, 2007, 2008) indicated that kilometer-scale upright folds – without observable fold hinges – occurred in the Aquidauana Fm. at radial distances equivalent to the outer rim region and intermediate section (see Fig. 14A). Lana et al. (2007, 2008) associated these alleged fold structures with large outer (R = 18–14 km) and inner (R = 12–10 km) antiformal "concentric rings," postulating that the AIS is a peak-ring structure (see Lana et al., 2007).

Our field data and remote sensing analysis did not show any evidence of continuous, kilometer-scale concentric fold structures within the Aquidauana Fm. in the outer rim and intermediate sections. Moreover, our conceptual model of tilted and/or rotated fault-bounded blocks in these zones precludes the existence of such continuous, long-wavelength fold structures. Meter- to 100-m-scale folds occur in the Aquidauana

Fm. along these domains; however, they are not widespread and are restricted to some azimuthal sectors over limited radial distances. We suggest that these folds are subordinate features formed within, and limited to, individual fault-bounded blocks or at interfaces between some of them (see Fig. 14B). We have observed 100-m-scale folds adjacent to a massive fault block in the Aquidauana Fm. of the N sector at $R \sim 12.6$ km (Fig. 6). This structural pattern occurs in a broader zone ($R \sim 13.5$–12 km) between Lana et al.'s (2007) two alleged concentric rings. Notably, Lana et al. (2008) reported difficulty in characterizing this zone and suggested the existence of a single kilometer-scale, relatively tight synform. Our data, based on the evaluation of structures in this zone (see Fig. 6), do not support this.

Although inward- and outward-dipping beds are significant, their orientations are not consistently the only ones at the radial distances where the concentric rings were proposed. In the zone alleged to contain the outer ring ($R = 18$–14 km), our structural data and remote sensing observations support instead the idea of an outer terraced zone at $R \sim$ 20–16 km. We also have structural evidence that, in some sectors, this terraced zone transitions inward to a large, gently inward-dipping, fault-bounded monocline around R = 16 km (see Fig. 14B). This scenario is particularly applicable to the less eroded SW, NW, and N sectors of the outer rim region. This transition is not observed in the SE and ENE sectors, possibly due to enhanced erosion or structural asymmetry between different sectors. Regarding the region allegedly containing the inner ring (R = 12–10 km), our data favor that it has the same overall structural framework as found elsewhere in the intermediate section. Thus, the current structural inventory of the AIS does not support the interpretation of the structure as the remnant of a peak-ring crater.

The Central Uplift

The central uplift of the AIS is now much better exposed in extensive new roadcuts along the MT-100 road than before. Our observations advance the discussions of: (1) whether the central uplift is an asymmetric feature; (2) whether it may extend up to $R \sim 10$ km; and (3) whether its core is a unique field laboratory for the study of at least three types of impact breccias and other impact-related features.

Asymmetry of the central uplift. Some previous work has already highlighted the existence of asymmetry within the Furnas Fm. collar of the central uplift (see Lana et al.,

2007, 2008) and provided limited evidence of central uplift collapse from the Ponta Grossa Fm. (Lana et al., 2008). Here, we show that evidence for structural asymmetry and outward-directed collapse of the central uplift along different sectors of the AIS is more prevalent than previously acknowledged. The asymmetry extends throughout the Ponta Grossa and Aquidauana formations around the central uplift. We also show that the outward collapse of the central uplift affected the outermost collar region (Aquidauana Fm.) in the ENE sector (see Fig. 8) and, to a much lesser extent, the Furnas Fm. in the SW sector (see Fig. 9).

The structural data from the SW collar area indicate a predominance of moderately and steeply outward-dipping beds, with evidence of subtle tangential constriction (especially noted in the Ponta Grossa Fm.; see Fig. 8B). Overall, our SW collar observations align with the four sequential, progressive deformation stages that were described for the collar strata by Lana et al. (2008): (1) outcrop-scale folding due to differential inter-strata slip movement; (2) imbrication of sheets of Furnas Fm.; (3) lateral constriction of the units; and (4) additional rotation of bedding due to the uplift. However, we identified a further step (5) in part of the SW collar, namely that an innermost Furnas Fm. outcrop at <500 m SW of the collar-core contact at the MT-100 road (station P-107; 53.01562°W, 16.82379°S) likely indicates minor outward collapse (see Fig. 9). Farther inward, at the W margin of the core of the central uplift, reverse faults in phyllite (station P-005; $R \sim 2.3$ km; 53.01253°W, 16.81873°S) show an inward movement of the hanging walls, which suggests that this core region did not participate in this collapse of the collar. Together, these observations indicate that a minor decoupling between the collar and core domains of the SW sector of the central uplift might have occurred during the modification stage.

On the other hand, the ENE collar exhibits a much more complex structural framework, with distinct structural domains displaying evidence of considerable outward collapse and tangential-to-oblique constriction of the strata along the sedimentary collar (Fig. 8D–I). In the innermost Furnas Fm. domain and along the transition between outermost Ponta Grossa and innermost Aquidauana formations, the outward-directed collapse of the collar is prominent, as evidenced by overturned, inward-dipping limbs and outward-verging folds (see Fig. 8D, E, and H). Extensional structures (tangentially striking conjugate normal faults) in the (meta)sedimentary basement megablock in the NE core region (see Fig. 13C) suggest that this region also underwent some extensional

collapse. In contrast, in the outer Furnas Fm. domain – including the (meta)sedimentary basement inlier within it – and throughout most of the Ponta Grossa Fm., beds with tangential-to-oblique dips predominate (see Fig. 8F, G, and I). Altogether, these observations suggest significant decoupling of the different collar and core units.

The outcrop-scale faults with variable orientations in the ENE Furnas Fm. collar are primarily interpreted here as resulting from impact. Outward-dipping fault planes, which are (sub)parallel to the uplifted bedding and show down-dip slickenlines, are most prominent within the inner and outer Furnas Fm. domains. These fault planes may have originated from the initial rise and/or outward collapse of the central uplift. Currently, this distinction cannot be made, as no kinematic indicators were found. In addition, on some of these fault planes, some slickenline sets plunge moderately (~25°) tangentially to the NE region of the core. This suggests a significant lateral (tangential to the core) displacement of the rock volume within this part of the collar. However, we do not have sufficient directional data to support a robust interpretation of rock movement direction(s). It is also not clear whether all observed slickensides relate to the same deformation stage in the evolution of the central uplift.

The main conclusion from this comparison between the SW and ENE collar sectors is that the AIS central uplift is an asymmetric structural feature. For example, we have shown that in the SW collar, moderately and steeply outward-dipping beds predominate and, locally, minor collapse folds occur. In contrast, in the ENE collar, beds have more complex arrangements with, e.g., the occurrence of inward-dipping beds (overturned limbs) and outward-verging folds. Moreover, we propose that the morphological and structural differences observed between inner and outer Furnas Fm. domains in the ENE collar sector may, in part, result from the lithological (rheological) contrast between the lower (i.e., sand-dominated) and upper (i.e., with pelitic layers/lenses) Furnas Fm. (see Fig. 2).

The debate about the diameter of the central uplift. Lana et al. (2008) already recognized that the basal Aquidauana Fm. at $R \sim 6$ km was uplifted by hundreds of meters, and they consequently suggested a diameter of 12 km for the central uplift. Schnegg and Fontes (2002) reassessed magnetotelluric and geomagnetic deep sounding data from Masero et al. (1994) in an effort to improve the available, first-order, magnetotelluric model of the AIS. Their new magnetotelluric model suggested that, from the center of the

AIS outward, the interface between the Paraná Basin sequence and the (meta)sedimentary basement continuously deepens to $R \sim 11$ km, where it reaches a maximum depth >3 km. We suggest that this radial distance marks the inflection point from downward-sloping central uplift into the intermediate section (ring syncline) of the AIS. Furthermore, the more recent gravity anomaly inversion and hydrocode modeling by Miyazaki et al. (2021) suggested that the central uplift could be 16 km in diameter.

Our observations suggest that the AIS central uplift may be wider than this, more in agreement with the geophysical model of Schnegg and Fontes (2002), and likely extending up to $R \sim 10$ km. This is mainly supported by: (1) no PDGBs occur at $R < 10$ km; and (2) in the SW sector, we have abundant evidence of consistent moderate to subvertical (40°–85°) outward-directed dips in Aquidauana Fm. at $R \leq 10$ km. This suggests that Aquidauana Fm. rocks up to $R \sim 10$ km were uplifted and are part of the outermost collar of the central uplift.

A diameter of ~20 km for the central uplift would fall within the lower range of proposed diameters for the AIS transient cavity (20–25 km; see von Engelhardt et al., 1992; Lana et al., 2006). This aligns with cratering models for complex craters, in which the collapse of the transient cavity at the beginning of the modification stage causes the excavated rock volume to migrate inward and upward, culminating in the buildup of the central uplift (Melosh, 1989). Hence, we argue that a transient cavity of ~20 km in diameter is a suitable estimate for the AIS.

We suggest that a central uplift diameter of up to ~20 km and the absence of PDGBs at $R < 10$ km are related. In our model, central uplift formation was responsible for uplifting and rotating the Aquidauana Fm. strata up to $R \sim 10$ km. This uplift likely started at the end of the excavation stage, i.e., before the inward-verging movement of the PDGBs. When the inward-directed collapse movement began at the modification stage, the Aquidauana Fm. volume in the outermost collar, at $R \sim 10$ km, had already been partially uplifted, thus acting as an increasing physical barrier to the inward-moving PDGBs, preventing their migration to $R < 10$ km.

However, this general idea does not explain the different structural patterns observed in the other radial sectors at $R < 10$ km. For example, the radial extent of the uplifted Aquidauana Fm. is <8 km in the W sector and, in the ENE sector along the MT-100 road (see data stations in Fig. S1), it is difficult to define as it blends with the structural framework of the intermediate section ($R = 15–8$ km). In any case, these varied

observations may imply any combination of the following: (1) pre-existing target anisotropy caused an asymmetric central uplift; (2) central uplift asymmetry was caused by oblique impact; and/or (3) a sector-dependent (asymmetric) collapse of the central uplift.

The SW collar sector shows very limited evidence of collapse (Fig. 9) in contrast to the more pronounced collapse features in the ENE sector (Fig. 8E). This alone allows us to propose an asymmetric (sector-dependent) collapse for the central uplift. However, the study of the full extent of this asymmetric collapse and its possible causes (oblique impact and/or target anisotropy) is beyond the scope of this work and requires further extensive field analysis and numerical modeling.

The core of the central uplift and the various impactite types. Souza et al. (2024) have provided, to date, the most comprehensive overview of the geology of the core of the central uplift of the AIS. Our northern core transect along the new exposures of the MT-100 road (Fig. 10) complements their work. Moreover, our transect represents a significant improvement over the ~500-m-long structural profile of Lana et al. (2008), which was surveyed in a similar, but poorly exposed, road section. Their transect has since been obliterated by the recent roadworks. The new exposures along the MT-100 provide opportunities to study the relationship between impact-generated and impact-deformed materials along an almost continuous, kilometer-long section.

We report new, extensive exposures of fine- to medium-grained granite in situ along the MT-100 (see Fig. 10). We interpret this granite as the outer limit and apophyses of the Araguainha granite stock. This conclusion was also drawn by Souza et al. (2024), though from other sections. Detailed compositional and structural analyses of this fine- to medium-grained granite have yet to be conducted. However, a general conclusion can be drawn: the alkali granite and marginal phases related to it have been uplifted together with the enveloping (meta)sedimentary basement lithologies, as part of the central uplift of the AIS (see also Souza et al., 2024).

The road section consists of two main structural domains: (1) the most prominent one, with blocks of various (meta)sedimentary lithologies from meters to tens of meters (megablocks) in size, interspersed with polymict lithic impact breccia and suevite; and (2) seemingly coherent, and at places folded and faulted (at the 10-m-scale),

(meta)sedimentary basement, locally intruded by granitic apophyses and impactites, and likely representing the crater floor.

The vast majority of blocks exposed in the northern core section along the MT-100 (Fig. 10) appear to be randomly oriented, with mostly steeply dipping contacts against blocks of other lithologies and apparent injections (dikes) of impact breccia. Orientations of bedding within the (meta)sandstone, (meta)conglomerate, and phyllite blocks are also random. The coherent exposures of phyllite display 10-m-scale, asymmetric folds, some of which are segmented by steeply dipping faults with strikes perpendicular or oblique to the SW-NE-trending road. This structural framework suggests a NE-directed vergence of the phyllite volume in this area (see Fig. 10). This could be associated with an outward collapse of this part of the core of the central uplift. However, as the road section only provides an essentially two-dimensional perspective that is also variably affected by weathering and locally dense vegetation, it is challenging to investigate the true juxtapositions of the blocks, variability of crater floor lithologies, and orientations of fractures/faults.

At least three impact breccia types, each with different clast populations and matrix types, can be distinguished in this domain (see also Souza et al., 2024): (1) a white-to-gray suevite; (2) a red/purplish-gray polymict lithic impact breccia; and (3) a light green suevite (Fig. 12). Only a single occurrence of this white-to-gray suevite, which carries melt rock clasts up to ~1 m in size, is known. Due to this singular occurrence (see Fig. 10), the structural relationship between the white-to-gray suevite and the other impact breccias remains unresolved. We also demonstrate that the light green suevite is intrusive into, and carries fragments of, the red polymict lithic impact breccia (Fig. 13C, D).

However, with the current data available, we cannot propose a comprehensive formation model for the impact breccias of the AIS. Souza et al. (2024) devoted part of their discussion to these aspects. Still, due to its overall complexity and widespread lack of off-road mapping, the core of the AIS requires further detailed lithological and structural studies.

A Possible Origin for the Morphostructural Asymmetry of the AIS

We have highlighted evidence of morphological and structural asymmetry throughout the AIS: (1) the irregular distribution, sizes, shapes, and structural vergences of the PDGBs; and (2) the different bedding orientations and structures throughout the

various sectors of the AIS, especially in the Aquidauana Fm. and in the central uplift with its contrasting SW and ENE collar sections (e.g., Fig. 8).

Terrestrial complex impact structures exhibiting structural asymmetry are known – for example, the 23-km-diameter Haughton impact structure in Canada (Osinski and Spray, 2005). This structure, which is significantly smaller and younger than the AIS (ca. 31 Ma; see Erickson et al., 2021; compared to ca. 259–252 Ma), was also formed in a mixed, sedimentary-crystalline target with a sedimentary pile of ~1880 m thickness (Osinski and Spray, 2005), similar to the AIS's estimated sedimentary target thickness.

The leading cause of asymmetry in impact structures is widely considered an oblique impact (see Kenkmann et al., 2014). However, anisotropy (heterogeneity) in the pre-impact target may also lead to some degree of asymmetry in a structure (e.g., the Serra da Cangalha complex impact structure, Brazil; Kenkmann et al., 2011) or even to the formation of a polygonal impact crater (see Öhman et al., 2010). Lana et al. (2008) speculated that the asymmetry observed in the Furnas Fm. collar of the central uplift of the AIS could be related to either of these mechanisms.

We have shown that although inward- and outward-dipping beds predominate in the AIS, there are also tangentially and obliquely dipping beds that are more common than previously considered. Furthermore, we have found that many of these beds are controlled by fractures/faults (Fig. 3) that can be spatially related to 100- to 1000-m-scale structural lineaments (Figs. 1 and S2). An analysis of these lineaments outside the apparent outer rim of the AIS indicates that their trends relate well to the overall trends of the Transbrasiliano Lineament (~N30°E) and the underlying Paraguay Belt (mainly N60°–70°E) regional structures throughout the wider NNW Paraná Basin (see inset in Fig. 1; also, Curto et al., 2014). The fractures and faults related to these tectono-structural features are pre-impact in age but may have been reactivated before, after, and likely during the impact event. Ultimately, rheological contrasts due to the alternation of different sedimentary layers (e.g., sandstone vs. mudstone) in the stratigraphic column for the AIS (Fig. 2) probably also played a role in controlling the development of some of the observed deformation structures in the AIS.

With these findings in mind, we propose that at least part of the perceived morphostructural asymmetry of the AIS is a consequence of a pre-impact, laterally and vertically anisotropic target volume in the NNW Paraná Basin. The lateral anisotropy would mainly originate from the fractures/faults (structural lineaments) presumed to be

related to the Transbrasiliano Lineament and the Paraguay Belt regional structural trends. This could also suggest that Araguainha may be the eroded remnant of a polygonal impact crater. However, further studies focused on this hypothesis are needed. In a complementary manner, the vertically varied anisotropy would result from rheological layering contrasts along the AIS stratigraphic column. Numerical modeling has shown that a layered target with material anisotropy can influence the resulting morphology of complex craters (e.g., Hopkins et al., 2019).

SUMMARY AND CONCLUSIONS

Recent roadworks across and beyond the Araguainha impact structure (AIS) resulted in extensive new exposures. We used these exposures for geological mapping and structural analysis before tropical weathering and further anthropogenic action could cause more degradation. With these observations and their integration with up-to-date remote sensing imagery, we have improved the geological map of the AIS and its immediate environs (Fig. 1). The main contributions of our new map are the more realistic distribution, sizes, and shapes of the Passa Dois Gr. Blocks (PDGBs) and of the units in the central uplift, as well as the expansion of the structural inventory of the AIS.

The main results and findings of this study are:

- The commonly accepted 40 km apparent diameter for the structure still holds. We estimate that the AIS has undergone a loss of 290–400 m in diameter since its formation, which is equivalent to no more than 1% of the apparent diameter.
- The main, widespread regional fracture/fault sets in the environs of the AIS pre-date the impact. They are likely related to the Transbrasiliano Lineament and Paraguay Belt structural trends and, to some extent, may have influenced deformation (e.g., folds) in the region. Whether the deformation structures (folds) outside the AIS are solely related to tectonic reactivation of these pre-impact fractures/faults during the Phanerozoic or are, at least in part, a consequence of the impact event remains unresolved.
- The majority of the structural features in the AIS appear to be related to the end of the excavation stage and ensuing modification stage of the impact event. Accommodation of strain throughout the AIS likely occurred through detachments along interfaces between or within units with different rheologies

(e.g., Passa Dois Gr.–Aquidauana Fm., Furnas Fm. collar–Crystalline-(meta)sedimentary core of the central uplift).

- The structural frameworks of the outer rim region and intermediate section domains are similar. Despite inward- and outward-dipping beds being the norm, tangentially and obliquely dipping beds are more common than previously acknowledged. Fractures/faults also played a more significant role than previously considered in conditioning the orientation of bedding and other structures in these domains during the modification stage.
- Rather than a continuous, large-scale, concentric folding model, as previously proposed for the outer rim and intermediate domains, we favor a model of large, tilted, and/or rotated fault-bounded blocks to explain the first-order structural framework in these domains. We attribute their main structural differences to the "space problem" that arises from the inward movement of rock volumes during crater collapse, as well as to rheological contrasts in the sedimentary target sequence.
- The PDGBs are more deformed and exhibit a greater variety of structures than previously known. The structural vergences in some PDGBs are approximately centripetal. However, other blocks show inward-directed vergences of structures that diverge from a truly centripetal direction, i.e., they are oblique with respect to the apparent center of the AIS.
- The structural style of the outer rim region PDGBs resembles "complex slumps" related to gravity-driven mass transport and results from the collapse of the transient crater.
- The bottom part of the Passa Dois Gr. (Irati Fm.) was seemingly already lithified pre-impact. The uppermost Passa Dois Gr. (Corumbataí Fm.) shows mixed evidence regarding possible lithification. We suggest that a shallow groundwater-saturated phreatic level likely played a role in conditioning the more ductile-plastic behavior of these uppermost materials immediately after impact or due to earthquake activation.
- There is no consistent evidence for kilometer-scale, antiformal outer (R = 18–14 km) and inner (R = 12–10 km) concentric rings in the AIS, as previously proposed.

- PDGBs occur between radial distances of around 10 to 20 km. We propose that this inner limit (~10 km) was controlled by the formation of the central uplift, which included the uplift of Aquidauana Fm. at R ~ 10 km to form a barrier against inward-moving Passa Dois Gr. volumes. In addition, the collapse of the crater rim during the modification stage set the outer limit (~20 km) of occurrence of PDGBs.
- Dips in the Aquidauana Fm. in the SW sector and the inner limit of occurrence of PDGBs support a central uplift diameter of up to 20 km, although it might be slightly less in different sectors. The SW collar sector exhibits evidence of minor outward-directed collapse, in contrast to the more prominent collapse features in the ENE sector. Thus, we propose that an asymmetric, sector-dependent collapse occurred in the central uplift.
- The northern core of the central uplift along the MT-100 road depicts a structurally and lithologically highly diverse megablock zone, with litho-blocks of up to tens of meters in size, and locally larger, overlying a seemingly coherent but folded and faulted crater floor.
- Araguainha is a (structurally) asymmetric impact structure. It exhibits noticeable directional variability in terms of morphology and orientation of its structural features across different sectors and at varied radial distances. Whether this structural asymmetry results from an oblique impact and/or pre-impact structural anisotropy remains equivocal. Our observations favor the second option, whereby asymmetry has, at least partially, emerged from lateral and vertical anisotropies generated by pre-impact fracture/fault sets in the target crust and by rheological contrasts in the sedimentary stratigraphic pile, respectively.

There remains a significant opportunity for further research on the AIS, such as a comprehensive survey of the Araguaia River profile across the structure, now informed by the new perspectives resulting from the present study. Further, detailed structural mapping and in-depth analysis of: (1) the different PDGBs in all sectors of the AIS will shed more light on the processes and mechanisms involved in their formation and on the first-order asymmetry of the crater; and (2) the “Serra da Arnica” region, located within the mountainous megablock zone of the northern Furnas Fm. collar, as well as of the more

chaotically deformed southern Furnas Fm. collar, could provide further insights into the structural evolution – including the collapse and asymmetry – of the central uplift.

Acknowledgments

This work is part of R.B. Bernardes' Ph.D. project in the Postgraduate Program in Geology at the Institute of Geosciences, University of Brasilia (IG–UnB). This study was financed in part by the Coordenação de Aperfeiçoamento de Pessoal de Nível Superior – Brasil (CAPES) – Finance Code 001. The authors thank the University of Brasilia and the Institute of Geosciences for providing part of the infrastructure and conditions required to conduct and complete this research, including an Esri ArcGIS Pro academic user license and a sabbatical research leave to Bernardes. We also thank Manfred Gottwald and the German Aerospace Center (DLR) for providing access to the TanDEM-X digital elevation model of the Araguainha impact structure. Bernardes acknowledges financial support through a research grant from the Barringer Family Fund for Meteorite Impact Research. He also thanks C. A. Bernardes, P. B. Macedo, D. A. Guerrero, C. S. M. Souza, and W. H. López for joining and supporting him during some of the fieldwork. Bernardes is grateful to professors A. C. Carmelo, E. I. N. Peixoto, and L. J. H. D'el-Rey Silva, IG–UnB, for their support during this work. Reimold and Hauser have been supported by the Brazilian National Council for Scientific and Technological Development (CNPq) through fellowship grants (Nos. 305761/2019-6 and 309878/2019-5, and 307109/2023-2, respectively). Gibson acknowledges the National Research Foundation of South Africa (Grant No. SRUG200503519568). Associate Editor Christian Koeberl is thanked for his swift editorial handling and constructive evaluation of this work. Reviewers David Baratoux and John Spray made many valuable comments that led to significant improvements to the original manuscript.

REFERENCES CITED

Allmendinger, R.W., Cardozo, N., and Fisher, D.M., 2012, Structural Geology Algorithms: Vectors and Tensors: New York, Cambridge University Press, 302 p.

Alvarenga, C.J.S., and Trompette, R., 1993, Evolução tectônica Brasiliana da Faixa Paraguai: A estruturação da região de Cuiabá: Revista Brasileira de Geociências, v. 23, p. 18–30, doi:10.25249/0375-7536.19932311830.

Assine, M.L., Soares, P.C., and Milani, E.J., 1994, Sequências tectono-sedimentares mesopaleozóicas da Bacia do Paraná, Sul do Brasil: Revista Brasileira de Geociências, v. 24, p. 77–89, doi:10.25249/0375-7536.19947789.

Barros, G.E.B., Becker-Kerber, B., Sedorko, D., Lima, J.H.D., and Pacheco, M.L.A.F., 2021, Ichnological aspects of the Aquidauana Formation (Upper Carboniferous, Itararé Group, Brazil): An arthropod-colonized glacial setting: Palaeogeography, Palaeoclimatology, Palaeoecology, v. 578, p. 110575, doi:10.1016/j.palaeo.2021.110575.

Bastos, L.P.H., Rodrigues, R., Pereira, E., Bergamaschi, S., Alferes, C.L.F., Augland, L.E., Domeier, M., Planke, S., and Svensen, H.H., 2021, The birth and demise of the vast epicontinental Permian Irati-Whitehill sea: Evidence from organic geochemistry, geochronology, and paleogeography: Palaeogeography, Palaeoclimatology, Palaeoecology, v. 562, p. 110103, doi:10.1016/j.palaeo.2020.110103.

Cagliari, J., Serratt, H., Cassel, M.C., Schmitz, M.D., and Chemale Jr., F., 2022, New high-precision U-Pb zircon age of the Irati Formation (Paraná Basin) and implications for the timing of the Kungurian anoxic events recorded in southern Gondwana: Gondwana Research, v. 107, p. 134–145, doi:10.1016/j.gr.2022.03.004.

Callefo, F., Arduin, D.H., Ricardi-Branco, F., Galante, D., Rodrigues, F., and Branco, F.C., 2018, The giant stromatolite field at Santa Rosa de Viterbo, Brazil (Paraná Basin) – A new paleoenvironmental overview and the consequences of the Irati Sea closure in the Permian: Journal of South American Earth Sciences, v. 84, p. 299–314, doi:10.1016/j.jsames.2018.04.008.

Cardozo, N., and Allmendinger, R.W., 2013, Spherical projections with OSXStereonet: Computers & Geosciences, v. 51, p. 193–205, doi:10.1016/j.cageo.2012.07.021.

Collins, G.S., Melosh, H.J., and Marcus, R.A., 2005, Earth Impact Effects Program: A Web-based computer program for calculating the regional environmental consequences of a meteoroid impact on Earth: Meteoritics & Planetary Science, v. 40, p. 817–840, doi:10.1111/j.1945-5100.2005.tb00157.x.

Cordani, U.G., Ramos, V.A., Fraga, L.M., Cegarra, M., Delgado, I., Souza, K.G., Gomes, F.E.M., and Schobbenhaus, C., 2016, Tectonic Map of South America, Second edition: CCGM/CGMW (Commission of the Geological Map of the World), scale 1:5,000,000, 12 p., doi:10.14682/2016TEMSA.

CPRM (Companhia de Pesquisa de Recursos Minerais), 1981, Projeto prospecção de carvão energético nas bordas norte e oeste da Bacia do Paraná – Áreas I, II e III: Companhia de Pesquisa de Recursos Minerais, Final technical report 1106, 167 p., http://rigeo.sgb.gov.br/handle/doc/4262 (accessed November 2024).

Crósta, A.P., Gaspar, J.C., and Cândia, M.A.F., 1981, Feições de metamorfismo de impacto no Domo de Araguainha: Revista Brasileira de Geociências, v. 11, p. 139–146.

Crósta, A.P., Reimold, W.U., Vasconcelos, M.A.R., Hauser, N., Oliveira, G.J.G., Maziviero, M.V., and Góes, A.M., 2019, Impact cratering: The South American record – Part 1: Geochemistry, v. 79, p. 1–61, doi:10.1016/j.chemer.2018.06.001.

Curto, J.B., Vidotti, R.M., Blakely, R.J., and Fuck, R.A., 2015, Crustal framework of the northwest Paraná Basin, Brazil: Insights from joint modeling of magnetic and gravity data: Tectonophysics, v. 655, p. 58–72, doi:10.1016/j.tecto.2015.05.011.

Curto, J.B., Vidotti, R.M., Fuck, R.A., Blakely, R.J., Alvarenga, C.J.S., and Dantas, E.L., 2014, The tectonic evolution of the Transbrasiliano Lineament in northern Paraná Basin, Brazil, as inferred from aeromagnetic data: Journal of Geophysical Research: Solid Earth, v. 119, p. 1544–1562, doi:10.1002/2013JB010593.

D'el-Rey Silva, L.J.H., Walde, D.H.-G., and Saldanha, D.O., 2016, The Neoproterozoic–Cambrian Paraguay Belt, central Brazil: Part I — New structural data and a new approach on the regional implications: Tectonophysics, v. 676, p. 20–41, doi:10.1016/j.tecto.2016.03.019.

von Engelhardt, W., Matthäi, S.K., and Walzebuck, J., 1992, Araguainha impact crater, Brazil. I. The interior part of the uplift: Meteoritics, v. 27, p. 442–457, doi:10.1111/j.1945-5100.1992.tb00226.x.

Erickson, T.M., Kirkland, C.L., Jourdan, F., Schmieder, M., Hartnady, M.I.H., Cox, M.A., and Timms, N.E., 2021, Resolving the age of the Haughton impact structure using coupled 40Ar/39Ar and U-Pb geochronology: Geochimica et Cosmochimica Acta, v. 304, p. 68–82, doi:10.1016/j.gca.2021.04.008.

Erickson, T.M., Timms, N.E., Kirkland, C.L., Tohver, E., Cavosie, A.J., Pearce, M.A., and Reddy, S.M., 2017, Shocked monazite chronometry: integrating microstructural and in situ isotopic age data for determining precise impact ages: Contributions to Mineralogy and Petrology, v. 172, p. 11, doi:10.1007/s00410-017-1328-2.

Fernandes, M.T., 2007, Ocorrências de material vulcanoclástico na Formação Corumbataí (Neopaleozóico), Bacia do Paraná [B.Sc. monograph]: São Paulo, Universidade de São Paulo, 39 p. [in Portuguese].

Fischer, S., 2015, Ein Beitrag über die Impaktgesteine der Araguainha Impaktstruktur (Brasilien) [Master's thesis]: Berlin, Freie Universität, 101 p. [in German].

Fossen, H., 2025, Fault crest collapse and gravity sliding in the late Jurassic northern North Sea rift: Journal of Structural Geology, v. 192, p. 105345, doi:10.1016/j.jsg.2025.105345.

Frugis, G.L., Campos Neto, M.C., Westin, A., and Fanning, C.M., 2024, New perspectives on the tectonic evolution of the eastern Paraguay Belt revealed through zircon U-Pb-Hf-O systematics of the inner units: Precambrian Research, v. 411, p. 107529, doi:10.1016/j.precamres.2024.107529.

Gesicki, A.L.D., Riccomini, C., and Boggiani, P.C., 2002, Ice flow direction during late Paleozoic glaciation in western Paraná Basin, Brazil: Journal of South American Earth Sciences, v. 14, p. 933–939, doi:10.1016/S0895-9811(01)00076-1.

Gomes, A.S., and Vasconcelos, P.M., 2021, Geochronology of the Paraná-Etendeka large igneous province: Earth-Science Reviews, v. 220, p. 103716, doi:10.1016/j.earscirev.2021.103716.

Gottwald, M., Kenkmann, T., and Reimold, W.U., 2020, Terrestrial Impact Structures: The TanDEM-X Atlas: Munich, Verlag Dr. Friedrich Pfeil, 608 p.

Hauser, N., Reimold, W.U., Cavosie, A.J., Crósta, A.P., Schwarz, W.H., Trieloff, M., Souza, C.S.M., Pereira, L.A., Rodrigues, E.N., and Brown, M., 2019, Linking shock textures revealed by BSE, CL, and EBSD with U-Pb data (LA-ICP-MS and SIMS) from zircon from the Araguainha impact structure, Brazil: Meteoritics & Planetary Science, v. 54, p. 2286–2311, doi:10.1111/maps.13371.

Hippertt, J.P., Lana, C., Weinberg, R.F., Tohver, E., Schmieder, M., Scholz, R., Gonçalves, L., and Hippertt, J.F., 2014, Liquefaction of sedimentary rocks during impact crater development: Earth and Planetary Science Letters, v. 408, p. 285–295, doi:10.1016/j.epsl.2014.09.045.

Holz, M., França, A.B., Souza, P.A., Iannuzzi, R., and Rohn, R., 2010, A stratigraphic chart of the Late Carboniferous/Permian succession of the eastern border of the Paraná Basin, Brazil, South America: Journal of South American Earth Sciences, v. 29, p. 381–399, doi:10.1016/j.jsames.2009.04.004.

Hopkins, R.T., Osinski, G.R., and Collins, G.S., 2019, Formation of Complex Craters in Layered Targets With Material Anisotropy: Journal of Geophysical Research: Planets, v. 124, p. 349–373, doi:10.1029/2018JE005819.

Horn, B.L.D., Oliveira, A.A., Simões, M.S., Besser, M.L., and Araújo, L.L., 2022, Mapa geológico da Bacia do Paraná: SGB (Serviço Geológico do Brasil)/CPRM (Companhia de Pesquisa de Recursos Minerais), Projeto Geologia e Potencial Mineral da Bacia do Paraná, scale 1:1,000,000, http://rigeo.sgb.gov.br/handle/doc/23037 (accessed November 2024).

Kenkmann, T., 2002, Folding within seconds: Geology, v. 30, p. 231–234, doi:10.1130/0091-7613(2002)030<0231:FWS>2.0.CO;2.

Kenkmann, T., 2021, The terrestrial impact crater record: A statistical analysis of morphologies, structures, ages, lithologies, and more: Meteoritics & Planetary Science, v. 56, p. 1024–1070, doi:10.1111/maps.13657.

Kenkmann, T., and von Dalwigk, I., 2000, Radial transpression ridges: A new structural feature of complex impact craters: Meteoritics & Planetary Science, v. 35, p. 1189–1201, doi:10.1111/j.1945-5100.2000.tb01508.x.

Kenkmann, T., Ivanov, B.A., and Stöffler, D., 2000, Identification of ancient impact structures: Low-angle faults and related geological features of crater basements, *in* Gilmour, I., and Koeberl, C., eds., Impacts and the Early Earth: Berlin, Heidelberg, Springer, Lecture Notes in Earth Sciences, v. 91, p. 279–307, doi:10.1007/BFb0027764.

Kenkmann, T., Vasconcelos, M.A.R., Crósta, A.P., and Reimold, W.U., 2011, The complex impact structure Serra da Cangalha, Tocantins State, Brazil: Meteoritics & Planetary Science, v. 46, p. 875–889, doi:10.1111/j.1945-5100.2011.01199.x.

Kenkmann, T., Poelchau, M.H., and Wulf, G., 2014, Structural geology of impact craters: Journal of Structural Geology, v. 62, p. 156–182, doi:10.1016/j.jsg.2014.01.015.

Kern, H.P., Lavina, E.L.C., Paim, P.S.G., Girelli, T.J., and Lana, C., 2021, Paleogeographic evolution of the southern Paraná Basin during the Late Permian and its relation to the Gondwanides: Sedimentary Geology, v. 415, p. 105808, doi:10.1016/j.sedgeo.2020.105808.

King Jr., D.T., Rampino, M.R., and Petruny, L.W., 2025, Shocked quartzite clasts with transverse fractures from Araguainha impact structure, Brazil: Meteoritics & Planetary Science, v. 60, p. 124–132, doi:10.1111/maps.14290.

Lacerda Filho, J.V., Abreu Filho, W., Valente, C.R., Oliveira, C.C., and Albuquerque, M.C., 2004, Geologia e recursos minerais do estado de Mato Grosso: CPRM (Companhia de Pesquisa de Recursos Minerais); SICME-MT (Secretaria de Estado de Indústria, Comércio, Minas e Energia do Estado de Mato Grosso), Programa Integração, Atualização e Difusão de Dados da Geologia do Brasil technical report, 235 p., http://rigeo.sgb.gov.br/handle/doc/4871 (accessed November 2024).

Lambert, P., and Reimold, W.U., 2023, Terrestrial impact sites as field analogs for planetary exploration: Frontiers in Astronomy and Space Sciences, v. 10, p. 1186173, doi:10.3389/fspas.2023.1186173.

Lana, C., Romano, R., Reimold, U., and Hippertt, J., 2006, Collapse of large complex impact craters: Implications from the Araguainha impact structure, central Brazil: Geology, v. 34, p. 9, doi:10.1130/G21952.1.

Lana, C., Souza Filho, C.R., Marangoni, Y.R., Yokoyama, E., Trindade, R.I.F., Tohver, E., and Reimold, W.U., 2007, Insights into the morphology, geometry, and post-impact erosion of the Araguainha peak-ring structure, central Brazil: Geological Society of America Bulletin, v. 119, p. 1135–1150, doi:10.1130/B26142.1.

Lana, C., Souza Filho, C.R., Marangoni, Y.R., Yokoyama, E., Trindade, R.I.F., Tohver, E., and Reimold, W.U., 2008, Structural evolution of the 40 km wide Araguainha impact structure, central Brazil: Meteoritics & Planetary Science, v. 43, p. 701–716, doi:10.1111/j.1945-5100.2008.tb00679.x.

Lange, F.W., and Petri, S., 1967, The Devonian of the Paraná Basin, *in* Bigarella, J.J., ed., Problems in Brazilian Devonian Geology: Curitiba, Universidade Federal do Paraná, Boletim Paranaense de Geociências 21/22, p. 5–55, https://repositorio.usp.br/item/002241599 (accessed September 2023).

Machado, R., Lana, C., Stevens, G., Souza Filho, C.R., Reimold, W.U., and McDonald, I., 2009, Generation, mobilization and crystallization of impact-induced alkali-rich melts in granitic target rocks: Evidence from the Araguainha impact structure, central Brazil: Geochimica et Cosmochimica Acta, v. 73, p. 7183–7201, doi:10.1016/j.gca.2009.08.029.

Martinez, I., Schärer, U., and Deutsch, A., 1991, Determination of shock-wave peak pressure and Rb-Sr isotope systematics in a granite from the Araguainha impact crater (Brasil): Houston, March 18-22, Lunar and Planetary Institute, Lunar and Planetary Science Conference XXII, abstract #1427, p. 857–858.

Masero, W., Schnegg, P.-A., and Fontes, S.L., 1994, A magnetotelluric investigation of the Araguainha impact structure in Mato Grosso-Goiás, central Brazil: Geophysical Journal International, v. 116, p. 366–376, doi:10.1111/j.1365-246X.1994.tb01803.x.

McGee, B., Collins, A.S., Trindade, R.I.F., and Payne, J., 2015, Age and provenance of the Cryogenian to Cambrian passive margin to foreland basin sequence of the northern Paraguay Belt, Brazil: GSA Bulletin, v. 127, p. 76–86, doi:10.1130/B30842.1.

Melosh, H.J., 1989, Impact Cratering: A Geologic Process: New York, Oxford University Press, Oxford monographs on geology and geophysics 11, 245 p.

Menegazzo, M.C., Catuneanu, O., and Chang, H.K., 2016, The South American retroarc foreland system: The development of the Bauru Basin in the back-bulge province: Marine and Petroleum Geology, v. 73, p. 131–156, doi:10.1016/j.marpetgeo.2016.02.027.

Milani, E.J., Melo, J.H.G., Souza, P.A., Fernandes, L.A., and França, A.B., 2007, Bacia do Paraná: Boletim de Geociências da Petrobras, v. 15, p. 265–287.

Miyazaki, M.R., Leite, E.P., Vasconcelos, M.A.R., Wünnemann, K., and Crósta, A.P., 2021, Bouguer anomaly inversion and hydrocode modeling of the central uplift of the Araguainha impact structure: Anais da Academia Brasileira de Ciências, v. 93, p. e20210081, doi:10.1590/0001-3765202120210081.

Montibeller, C.C., Navarro, G.R.B., Zanardo, A., Rohn, R., Roveri, C.D., Rocha, R.R., and Conceição, F.T., 2020, Geochemistry of siltstones from the Permian Corumbataí Formation from the Paraná Basin (State of São Paulo, Brazil): Insights of provenance, tectonic and climatic settings: Journal of South American Earth Sciences, v. 102, p. 102582, doi:10.1016/j.jsames.2020.102582.

Öhman, T., Aittola, M., Korteniemi, J., Kostama, V.-P., and Raitala, J., 2010, Polygonal impact craters in the solar system: Observations and implications, *in* Gibson, R.L., and Reimold, W.U., eds., Large Meteorite Impacts and Planetary Evolution IV: Boulder, Geological Society of America, Geological Society of America Special Paper 465, p. 51–65, doi:10.1130/2010.2465(04).

Osinski, G.R., Grieve, R.A.F., Ferrière, L., Losiak, A., Pickersgill, A.E., Cavosie, A.J., Hibbard, S.M., Hill, P.J.A., Bermudez, J.J., Marion, C.L., Newman, J.D., and Simpson, S.L., 2022, Impact Earth: A review of the terrestrial impact record: Earth-Science Reviews, v. 232, p. 104112, doi:10.1016/j.earscirev.2022.104112.

Osinski, G.R., and Pierazzo, E., eds., 2012, Impact Cratering: Processes and Products: Oxford, Wiley-Blackwell, 336 p.

Osinski, G.R., and Spray, J.G., 2005, Tectonics of complex crater formation as revealed by the Haughton impact structure, Devon Island, Canadian High Arctic: Meteoritics & Planetary Science, v. 40, p. 1813–1834, doi:10.1111/j.1945-5100.2005.tb00148.x.

Pimentel, M.M., Fuck, R.A., and Alvarenga, C.J., 1996, Post-Brasiliano (Pan-African) high-K granitic magmatism in Central Brazil: the role of late Precambrian-early Palaeozoic extension: Precambrian Research, v. 80, p. 217–238, doi:10.1016/S0301-9268(96)00016-2.

Reimold, W.U., Hauser, N., Hansen, B.T., Thirlwall, M., and Hoffmann, M., 2017, The impact pseudotachylitic breccia controversy: Insights from first isotope analysis of Vredefort impact-generated melt rocks: Geochimica et Cosmochimica Acta, v. 214, p. 266–281, doi:10.1016/j.gca.2017.07.040.

Reimold, W.U., Hoffmann, M., Hauser, N., Schmitt, R.-T., Zaag, P.T., and Mohr-Westerheide, T., 2016, A geochemical contribution to the discussion about the genesis of impact-related pseudotachylitic breccias: Studies of PTB in the Otavi and Kudu Quarries of the Vredefort Dome support the "In Situ Formation" hypothesis: South African Journal of Geology, v. 119, p. 453–472, doi:10.2113/gssajg.119.3.453.

Rizzoli, P., Martone, M., Gonzalez, C., Wecklich, C., Tridon, D.B., Bräutigam, B., Bachmann, M., Schulze, D., Fritz, T., Huber, M., Wessel, B., Krieger, G., Zink, M., and Moreira, A., 2017, Generation and performance assessment of the global TanDEM-X digital elevation model: ISPRS Journal of Photogrammetry and Remote Sensing, v. 132, p. 119–139, doi:10.1016/j.isprsjprs.2017.08.008.

Rocha-Campos, A.C., Basei, M.A.S., Nutman, A.P., Santos, P.R., Passarelli, C.R., Canile, F.M., Rosa, O.C.R., Fernandes, M.T., Santa Ana, H., and Veroslavsky, G., 2019, U-Pb Zircon Dating of Ash Fall Deposits from the Paleozoic Paraná Basin of Brazil and Uruguay: A Reevaluation of the Stratigraphic Correlations: The Journal of Geology, v. 127, p. 167–182, doi:10.1086/701254.

Rossetti, L., Lima, E.F., Waichel, B.L., Hole, M.J., Simões, M.S., and Scherer, C.M.S., 2018, Lithostratigraphy and volcanology of the Serra Geral Group, Paraná-Etendeka Igneous Province in Southern Brazil: Towards a formal stratigraphical framework: Journal of Volcanology and Geothermal Research, v. 355, p. 98–114, doi:10.1016/j.jvolgeores.2017.05.008.

Sánchez, J.P., 2006, Mapeamento 1:25.000 do núcleo do astroblema Domo de Araguainha (MT) e aspectos geoturísticos da região [B.Sc. monograph]: Rio Claro, Universidade Estadual Paulista, 69 p. [in Portuguese].

Santos, R.V., Souza, P.A., Alvarenga, C.J.S., Dantas, E.L., Pimentel, M.M., Oliveira, C.G., and Araújo, L.M., 2006, Shrimp U–Pb zircon dating and palynology of bentonitic layers from the Permian Irati Formation, Paraná Basin, Brazil: Gondwana Research, v. 9, p. 456–463, doi:10.1016/j.gr.2005.12.001.

Schnegg, P.-A., and Fontes, S.L., 2002, Feasibility study of the geoelectric structure of the Araguainha impact, Brazil: Earth, Planets and Space, v. 54, p. 597–606, doi:10.1186/BF03353048.

Schobbenhaus, C., Ribeiro, C.L., Oliva, L.A., Takanohashi, J.T., Lindenmayer, A.G., Vasconcelos, J.C., and Orlandi, V., 1975, Carta Geológica do Brasil ao Milionésimo, Folha Goiás (SC-22): Departamento Nacional de Produção Mineral, map text, p. 99–113.

Silva, D., Lana, C., and Souza Filho, C.R., 2016, Petrographic and geochemical characterization of the granitic rocks of the Araguainha impact crater, Brazil: Meteoritics & Planetary Science, v. 51, p. 443–467, doi:10.1111/maps.12601.

Souza, C.S.M., Hauser, N., Reimold, W.U., Bernardes, R.B., Vieira, L.C., Guimarães, E.M., and Gottwald, M., 2024, Araguainha impact structure, Brazil: New insights into the geology of the central uplift: Meteoritics & Planetary Science, v. 59, p. 2577–2607, doi:10.1111/maps.14236.

Stöffler, D., and Grieve, R.A.F., 2007, Impactites, *in* Fettes, D., and Desmons, J., eds., Metamorphic Rocks: A Classification and Glossary of Terms – Recommendations of the International Union of Geological Sciences: New York, Cambridge University Press, p. 82–92.

Swietlik, R.M., 1989, Zur Geologie des nordöstlichen Araguainha-Doms, Mato Grosso, Brasilien [Diploma thesis]: Münster, University of Münster, 73 p. [in German].

Theilen-Willige, B., 1981, The Araguainha impact structure/Central Brazil: Revista Brasileira de Geociências, v. 11, p. 91–97, doi:10.25249/0375-7536.19819197.

Thomé Filho, J.J., Crósta, A.P., and Paula, T.L.F., 2012, Geoparque Astroblema de Araguainha - Ponte Branca (GO/MT): proposta, *in* Schobbenhaus, C., and Silva, C.R., eds., Geoparques do Brasil: propostas: Rio de Janeiro, CPRM (Companhia de Pesquisa de Recursos Minerais), v. 1, p. 151–182.

Tohver, E., Lana, C., Cawood, P.A., Fletcher, I.R., Jourdan, F., Sherlock, S., Rasmussen, B., Trindade, R.I.F., Yokoyama, E., Souza Filho, C.R., and Marangoni, Y., 2012, Geochronological constraints on the age of a Permo–Triassic impact event: U–Pb and $^{40}Ar/^{39}Ar$ results for the 40 km Araguainha structure of central Brazil: Geochimica et Cosmochimica Acta, v. 86, p. 214–227, doi:10.1016/j.gca.2012.03.005.

Tohver, E., Cawood, P.A., Riccomini, C., Lana, C., and Trindade, R.I.F., 2013, Shaking a methane fizz: Seismicity from the Araguainha impact event and the Permian–Triassic global carbon isotope record: Palaeogeography, Palaeoclimatology, Palaeoecology, v. 387, p. 66–75, doi:10.1016/j.palaeo.2013.07.010.

Tohver, E., Schmieder, M., Lana, C., Mendes, P.S.T., Jourdan, F., Warren, L., and Riccomini, C., 2018, End-Permian impactogenic earthquake and tsunami deposits in the intracratonic Paraná Basin of Brazil: GSA Bulletin, v. 130, p. 1099–1120, doi:10.1130/B31626.1.

UnB-IG (Universidade de Brasília–Instituto de Geociências), 2012, Araguainha Project – Final coursework mapping project by the 2012 geology graduating class: Brasilia, Universidade de Brasília, Instituto de Geociências, unpublished report [in Portuguese].

Warren, L.V., Assine, M.L., Simões, M.G., Riccomini, C., and Anelli, L.E., 2015, A Formação Serra Alta, Permiano, no centro-leste do Estado de São Paulo, Bacia do Paraná, Brasil: Brazilian Journal of Geology, v. 45, p. 109–126, doi:10.1590/23174889201500010008.

Yokoyama, E., Trindade, R.I.F., Lana, C., Souza Filho, C.R., Baratoux, D., Marangoni, Y.R., and Tohver, E., 2012, Magnetic fabric of Araguainha complex impact structure (Central Brazil): Implications for deformation mechanisms and central uplift formation: Earth and Planetary Science Letters, v. 331–332, p. 347–359, doi:10.1016/j.epsl.2012.01.005.

Zalán, P.V., Wolff, S., Astolfi, M.A.M., Vieira, I.S., Conceição, J.C.J., Appi, V.T., Neto, E.V.S., Cerqueira, J.R., and Marques, A., 1990, The Paraná Basin, Brazil, *in* Leighton, M.W., Kolata, D.R., Oltz, D.F., Eidel, J.J., and Coury, A.B., eds., Interior Cratonic Basins: Tulsa, American Association of Petroleum Geologists Memoir, v. 51, p. 681–708, doi:10.1306/M51530C34.

Zanardo, A., Montibeller, C.C., Navarro, G.R.B., Moreno, M.M.T., Rocha, R.R., Roveri, C.D., and Azzi, A.A., 2016, Formação Corumbataí na região de Rio Claro/SP: Petrografia e implicações genéticas: Geosciences = Geociências, v. 35, p. 322–345.

SUPPLEMENTAL MATERIAL

CHAPTER 4 – RESEARCH ARTICLE 1: *New insights into the geology and formation of the Araguainha impact structure, Brazil, from morphological and structural analysis*

CONTENTS (see next pages)

REFERENCES CITED IN THIS SUPPLEMENTAL MATERIAL

Collins, G.S., Melosh, H.J., and Marcus, R.A., 2005, Earth Impact Effects Program: A Web-based computer program for calculating the regional environmental consequences of a meteoroid impact on Earth: Meteoritics & Planetary Science, v. 40, p. 817–840, doi:10.1111/j.1945-5100.2005.tb00157.x.

CPRM, 1981, Projeto prospecção de carvão energético nas bordas norte e oeste da Bacia do Paraná – Áreas I, II e III: Companhia de Pesquisa de Recursos Minerais, Final technical report 1106, 167 p., http://rigeo.sgb.gov.br/handle/doc/4262 (accessed November 2024).

Horn, B.L.D., Oliveira, A.A., Simões, M.S., Besser, M.L., and Araújo, L.L., 2022, Mapa geológico da Bacia do Paraná: SGB/CPRM, Projeto Geologia e Potencial Mineral da Bacia do Paraná, scale 1:1,000,000, http://rigeo.sgb.gov.br/handle/doc/23037 (accessed November 2024).

Lana, C., Souza Filho, C.R., Marangoni, Y.R., Yokoyama, E., Trindade, R.I.F., Tohver, E., and Reimold, W.U., 2007, Insights into the morphology, geometry, and post-impact erosion of the Araguainha peak-ring structure, central Brazil: Geological Society of America Bulletin, v. 119, p. 1135–1150, doi:10.1130/B26142.1.

Lana, C., Souza Filho, C.R., Marangoni, Y.R., Yokoyama, E., Trindade, R.I.F., Tohver, E., and Reimold, W.U., 2008, Structural evolution of the 40 km wide Araguainha impact structure, central Brazil: Meteoritics & Planetary Science, v. 43, p. 701–716, doi:10.1111/j.1945-5100.2008.tb00679.x.

Souza, C.S.M., Hauser, N., Reimold, W.U., Bernardes, R.B., Vieira, L.C., Guimarães, E.M., and Gottwald, M., 2024, Araguainha impact structure, Brazil: New insights into the geology of the central uplift: Meteoritics & Planetary Science, v. 59, p. 2577–2607, doi:10.1111/maps.14236.

Thomé Filho, J.J., Crósta, Á.P., and Paula, T.L.F., 2012, Geoparque Astroblema de Araguainha - Ponte Branca (GO/MT): proposta, *in* Schobbenhaus, C., and Silva, C.R., eds., Geoparques do Brasil: propostas: Rio de Janeiro, CPRM , v. 1, p. 151–182.

UnB-IG, 2012, Araguainha Project – Final coursework mapping project by the 2012 geology graduating class: Brasilia, Universidade de Brasília, Instituto de Geociências, unpublished report [in Portuguese].

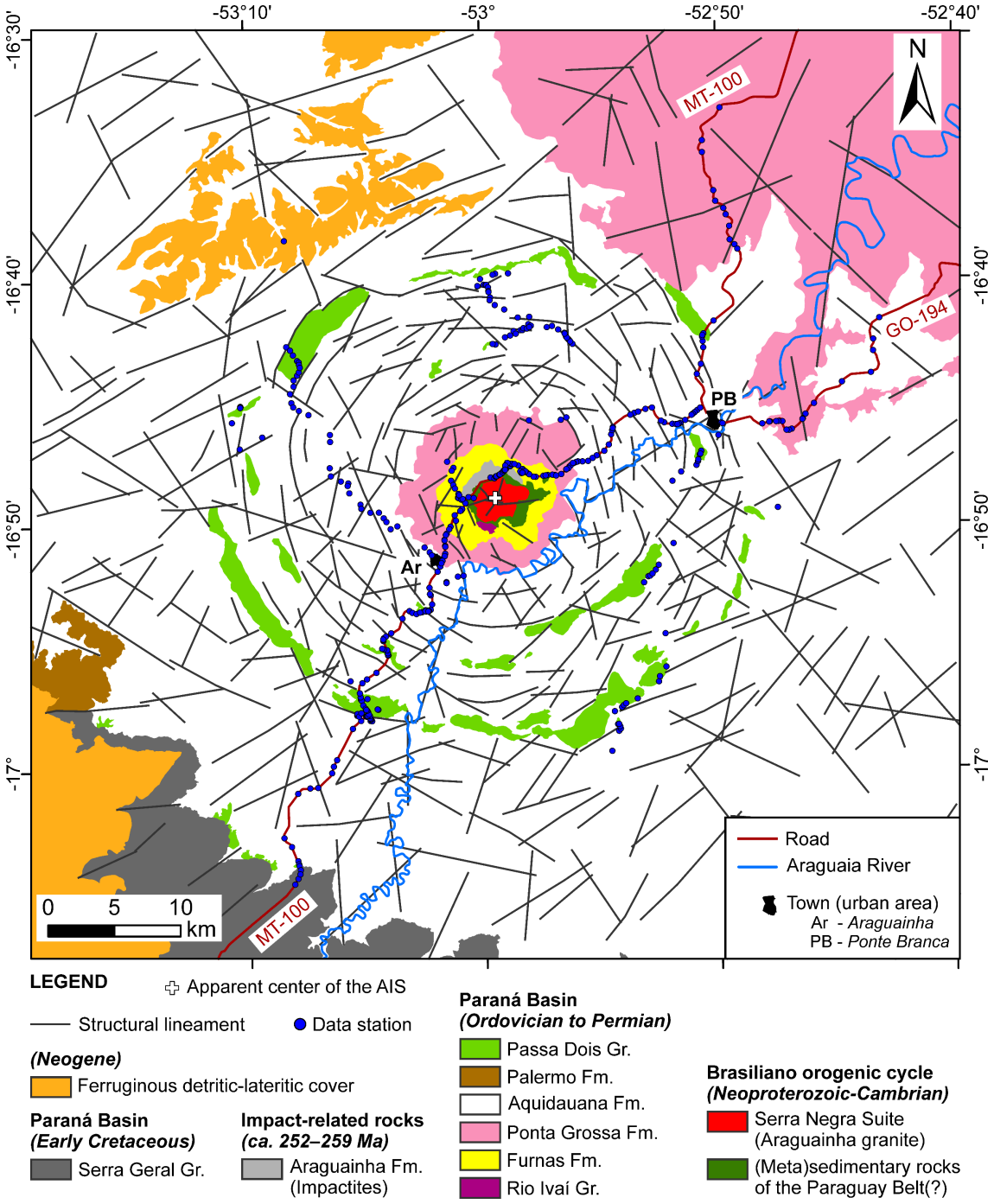

Figure S1. Locations (n = 415 data stations – blue circles) where data were collected during our field campaigns between 2021 and 2024 overlain on our geological map of the Araguainha impact structure and its environs (see Fig. 1). The map is based on maps of CPRM (1981), Lana et al. (2007, 2008), UnB-IG (2012), Thomé Filho et al. (2012), Horn et al. (2022), and Souza et al. (2024), as well as our own field-based data and remote sensing analysis. Map coordinate system: WGS84. Data station P-001 (coordinates: 53.30111°W, 17.22300°S) is not represented here because it is located far beyond the map area, at a radial distance of ~56 km to the SW of the apparent center of the structure, along the MT-100 road (see text).

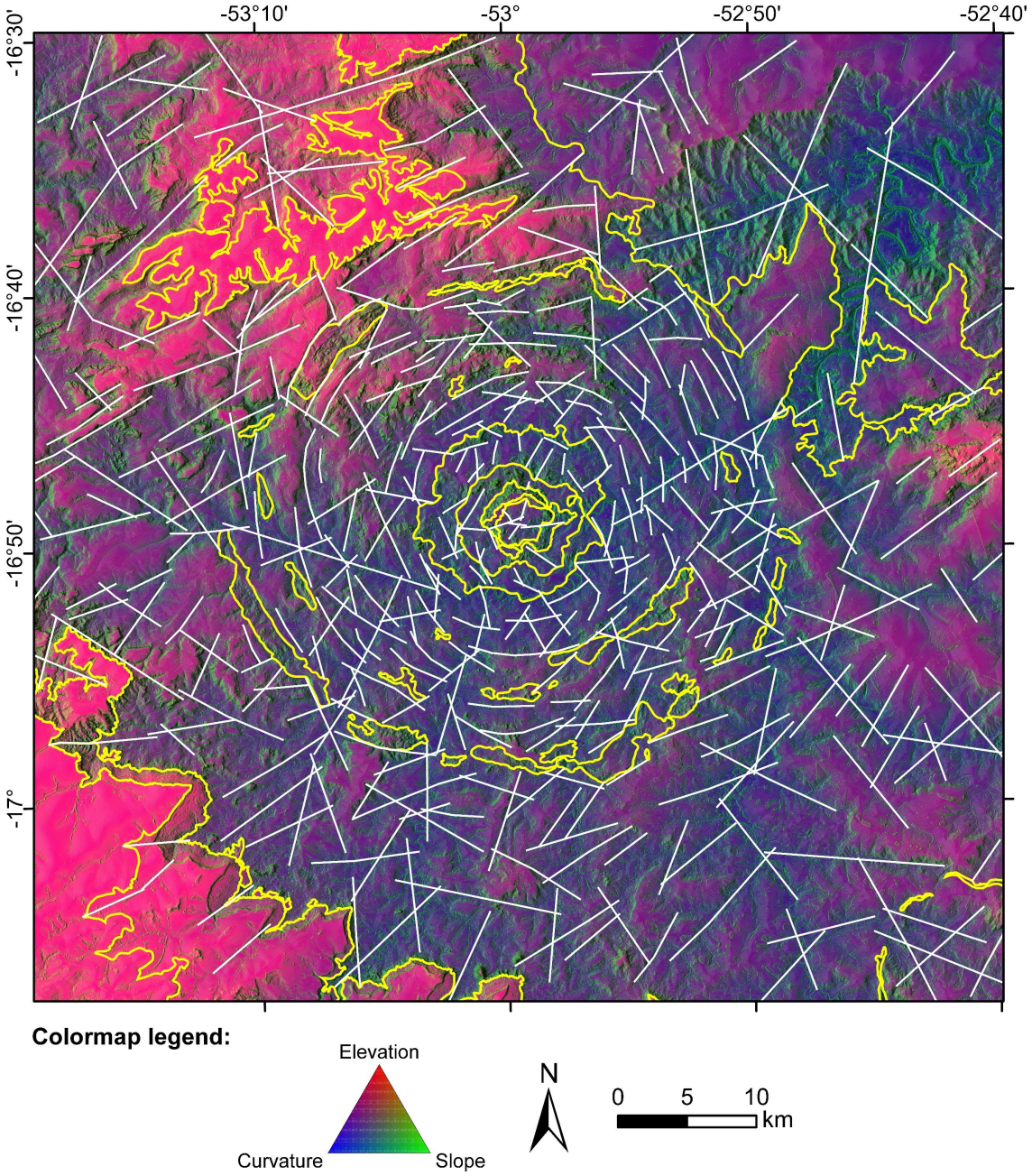

Figure S2. False-color composite image of processed TanDEM-X digital elevation model (DEM) data for the Araguainha impact structure and environs (courtesy of Manfred Gottwald, formerly of the German Aerospace Center – DLR) superimposed by a partially transparent multidirectional, hill-shaded image of the same DEM with a 5:1 vertical exaggeration to emphasize relief features and facilitate appraisal of the extracted structural lineaments. This map shows the same area as Figs. 1 and S1. False-color composite image colormap legend: red channel = elevation (the DEM itself), green channel = DEM slope, and blue channel = DEM curvature. Structural lineaments (white lines; also shown in Figs. 1 and S1) were extracted at the 1:250,00 scale (see Materials and Methods section for details). Yellow contours are the outlines of the mapped geological units (see Figs. 1 and S1). Map coordinate system: WGS84.

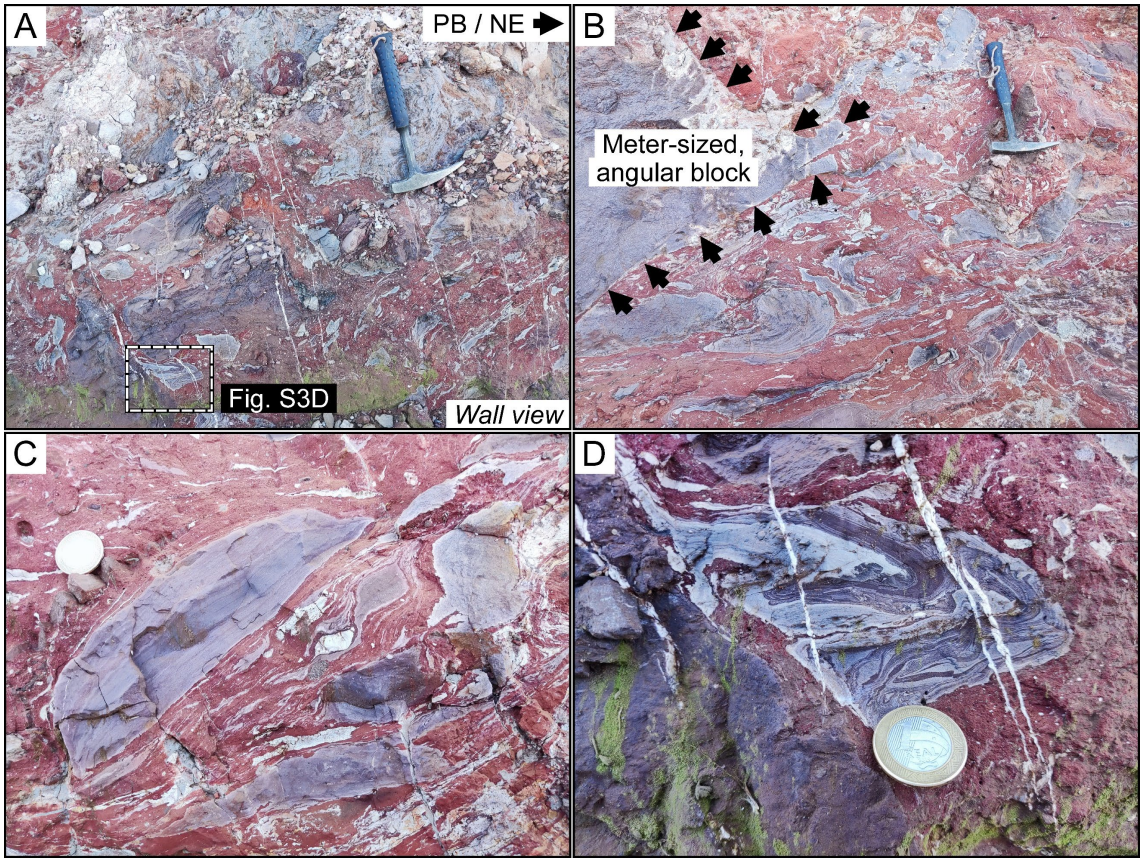

Figure S3. Structures observed in a recently excavated road trench in the outer portion of a Passa Dois Gr. Block (PDGB) in the ENE sector of the Araguainha impact structure (AIS), ~2 km SW of Ponte Branca town. This PDGB almost straddles the transition from the outer rim region into the intermediate section (station P-304, R ~ 15.8 km, 52.84600°W, 16.78651°S). Hammer for scale is 33 cm long. Coin diameter for scale is 2.7 cm. All photos were taken from the same perspective. A) General view of a Passa Dois Gr. breccia, consisting of gray to purple, thinly laminated fragments (mostly of mudstone) embedded in a red, pelitic to psammitic matrix. Black arrow at the top right indicates the direction toward Ponte Branca (PB) and the respective (inter)cardinal direction. B) A meter-sized, angular mudstone block (framed by black arrows) indicative of brittle deformation. C) Lithic fragments showing signs of boudinage and quasi-ductile deformation at contacts with red matrix. D) An internally folded and faulted pelitic fragment. Locally, millimeter-wide fractures filled with a fine, white material (possibly zeolite) cross-cut the entire breccia package (see also Fig. S3A). These fractures are oriented obliquely to the apparent center of the AIS.

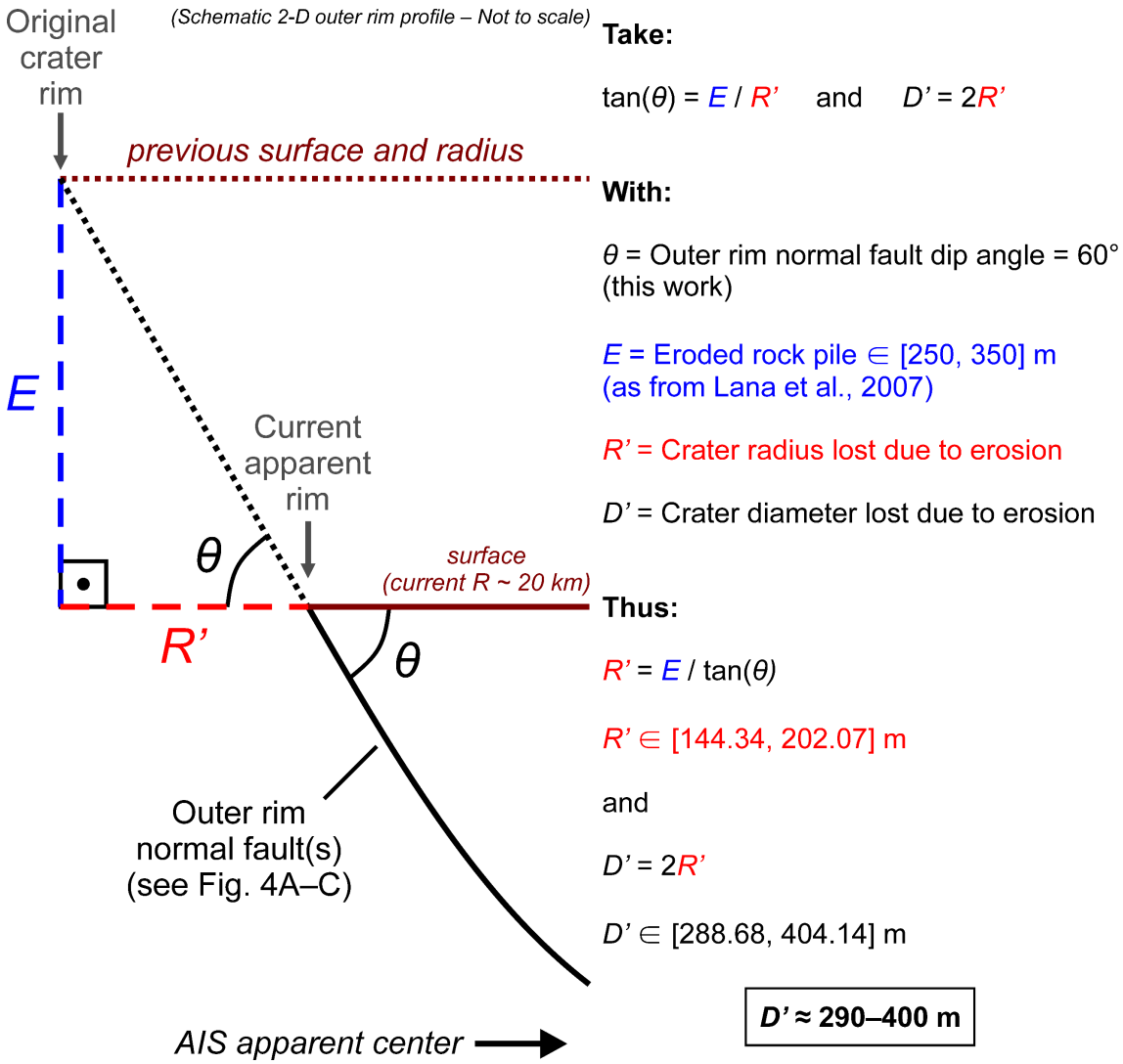

Figure S4. Trigonometric approximation for estimating the diameter loss (*D'*) of the Araguainha impact structure (AIS) based on our structural observations and previously published, estimated (vertical) erosion within the structure (*E*) (see Lana et al., 2007). See text for details.

TABLE S1. INPUT PARAMETERS AND PERTINENT RESULTS OF A BASIC IMPACT SIMULATION OF THE ARAGUAINHA IMPACT EVENT USING THE EARTH IMPACT EFFECTS PROGRAM

Input parameters	
Distance from impact	56.00 km
Projectile diameter	3.20 km
Projectile density	3000 kg/m^3
Impact velocity	17.00 km/s
Impact angle	45°
Target density	2500 kg/m^3
Target type	Sedimentary rock
Main results	
Transient crater diameter	26.2 km
Transient crater depth	9.26 km
Final (complex) crater diameter	40.3 km
Final crater depth	900 m
Volume of melted or vaporized target	46.6 km³
Average melt thickness in the crater	86.6 m

Note: The Earth Impact Effects Program is based on the work of Collins et al. (2005). The program can be accessed at: impact.ese.ic.ac.uk/ImpactEarth/ImpactEffects/

CHAPTER 5

RESEARCH ARTICLE 2

CHAPTER 5 – RESEARCH ARTICLE 2

(This manuscript was submitted for publication to the "Meteoritics & Planetary Science" journal on January 12, 2026)

Araguainha Dome, Brazil: A polygonal impact structure due to a complex pre-impact regional structural framework

R.B. Bernardes[1*], W.U. Reimold[1], R.L. Gibson[2], J.B. Curto Ma[3], A.B. Silva[1,4], and N. Hauser[1]

[1]University of Brasilia, Institute of Geosciences, Postgraduate Program in Geology, Campus Universitário Darcy Ribeiro, Brasilia, DF 70910-900, Brazil

[2]School of Geosciences, University of the Witwatersrand, Johannesburg 2050, South Africa

[3]University of Brasilia, Institute of Geosciences, Postgraduate Program in Applied Geosciences and Geodynamics, Campus Universitário Darcy Ribeiro, Brasilia, DF 70910-900, Brazil

[4]Serviço Geológico do Brasil (SGB-CPRM), Superintendência de Goiânia, Goiânia, GO 74170-110, Brazil

[*]Corresponding author (renato.bernardes@unb.br)

Abstract

We investigated the structural framework of the north-northwestern Paraná Basin in Brazil and its influence on the first-order morphostructure of the Araguainha impact structure (AIS). The AIS – an ~40-km-diameter remnant of the largest confirmed, complex impact structure in South America – was formed ca. 259–252 Ma in a mixed crystalline-sedimentary target. We employed a multi-method approach, including airborne geophysics, remote sensing, lineament analysis, fieldwork, and modeling of the shape of the (apparent) outer rim trace. This approach reveals that prominent NE-SW- and NW-SE-trending lineaments characterize the AIS region. Much of this fabric can be linked to regional structures associated with the Paraguay Belt and, to a lesser extent, the Transbrasiliano Lineament – both of which influenced the NNW Paraná Basin during its pre-impact evolution. We present evidence that this preexisting regional structural framework partially controlled the formation and shape of the AIS. The AIS and its

central uplift are asymmetric features, with the asymmetry of the central uplift evident from the time of its formation. Our results suggest that the shape of the AIS rim trace is consistent with a polygonal structure. At the analyzed scale, the AIS rim trace is best described as an irregular nine-sided polygon. This polygonal shape was likely formed during the modification stage, when crater collapse was influenced by the regional pre-impact structural fabric. Our findings improve understanding of the cratering process in structurally anisotropic targets and provide valuable insights into the target region's subsurface structural framework.

INTRODUCTION

Planetary crater records show that most craters formed on rocky bodies are centro-symmetric, i.e., circular (Melosh, 1989; Öhman et al., 2010; Robbins and Riggs, 2023). Crater non-concentricity is typically attributed to preexisting topography (on many bodies, often due to older impacts) and highly oblique impacts, with angles <20° relative to the target surface seemingly necessary, based on numerical modeling (e.g., Elbeshausen et al., 2013) and physical analog experiments (e.g., Gault and Wedekind, 1978). However, computational capacity generally requires the numerical models to use significantly simplified targets, usually with homogeneous (isotropic) properties (see Collins et al., 2012, and references therein).

On Earth, however, the target crust – especially the longer-lasting continental crust, where most craters are preserved – usually exhibits inherited structural heterogeneity (anisotropy) across various scales, such as joint and fault patterns, layered supracrustal sequences, or intrusions with distinct geometries and orientations. More detailed field structural and GIS-based analyses of preexisting structures (i.e., heterogeneities) in the target crust reveal that, during a meteoritic impact, these features can affect crater formation. A well-studied example of this is the ~1.2-km-wide Meteor (Barringer) Crater, which is a relatively young (ca. 60000 ka; Barrows et al., 2019) and well-preserved, simple impact crater (see Kumar and Kring, 2008; Poelchau et al., 2009). Furthermore, if a thick layer of unconsolidated materials does not cover the target surface and if preexisting structures such as fractures, faults, or joints create sufficient anisotropy and are appropriately spaced relative to the size of the resulting crater, a polygonal impact crater (PIC) may form (see Fulmer and Roberts, 1963). Otherwise, and if the impact

occurs at a sufficiently high angle relative to the target surface, a standard circular impact crater is formed (Melosh, 1989).

A common definition of polygonal impact craters states that their rim trace, when viewed from above, must have at least two adjacent straight segments, indicating a deviation from a typical circular shape (Öhman et al., 2010). However, there is no widespread consensus on a formal definition of PICs yet (see Robbins and Riggs, 2023, for a recent discussion). PICs are present on all solid, cratered bodies in our solar system, including Earth; however, ground-truth data for PICs are limited (Öhman et al., 2010). It has been estimated that PICs might constitute about 10–20% of the current planetary impact crater inventory (Öhman et al., 2010; Robbins and Riggs, 2023).

Polygonal impact craters are believed to form when the cratering process exploits existing structural inhomogeneities, such as fractures, faults, or joints (Öhman et al., 2010). PICs can form as either simple (e.g., Meteor Crater; Poelchau et al., 2009) or complex (e.g., Manicouagan, in Canada; Fobert et al., 2025) impact structures, and on the basis of either extensional (e.g., Eppler et al., 1983; Öhman et al., 2010) or contractional (Beddingfield et al., 2024) structures in the target region. Identifying and studying PICs may provide valuable insights into the subsurface structural framework of a target – especially for structures that are difficult to access – and, more broadly, enhance our understanding of how the cratering process operates on structurally anisotropic targets (see Eppler et al., 1983; Öhman et al., 2010).

The Araguainha impact structure (AIS) is the ~40-km-diameter, somewhat eroded remnant of the largest confirmed such structure in South America (Crósta et al., 2019; Souza et al., 2024; Bernardes et al., 2025). It formed ca. 259–252 Ma (Tohver et al., 2012; Erickson et al., 2017; Hauser et al., 2019) in a mixed crystalline-sedimentary target in the north-northwestern part of the Phanerozoic Paraná Basin (for basin geology, see Zalán et al., 1990; Milani et al., 2007; Horn et al., 2022) (Fig. 1). In this region, the Paraná Basin, whose sedimentary record began in the Ordovician period (Milani et al., 2007), partially overlies Neoproterozoic–Cambrian orogens of the Tocantins (tectonic) Province (Almeida et al., 1981), with the Paraguay Belt being one of these partially concealed orogens (see Curto et al., 2014, 2015).

The Tocantins Province comprises the Araguaia, Brasilia, and Paraguay orogenic belts, which formed during the Brasiliano orogenic event (ca. 800 Ma to ca. 500 Ma) mainly due to the convergence and collision of the Amazonian, São Francisco-Congo,

and the hypothetical Paranapanema paleocontinents, which contributed significantly to the consolidation of the western portion of the Gondwana paleocontinent (see Brito Neves et al., 2014, for a review). This tectonic evolution led to the development of the Transbrasiliano Lineament (TBL; Schobbenhaus et al., 1975), a transcontinental mega-shear zone developed at the early Cambrian (see, e.g., Caxito et al., 2025; inset map in Fig. 1).

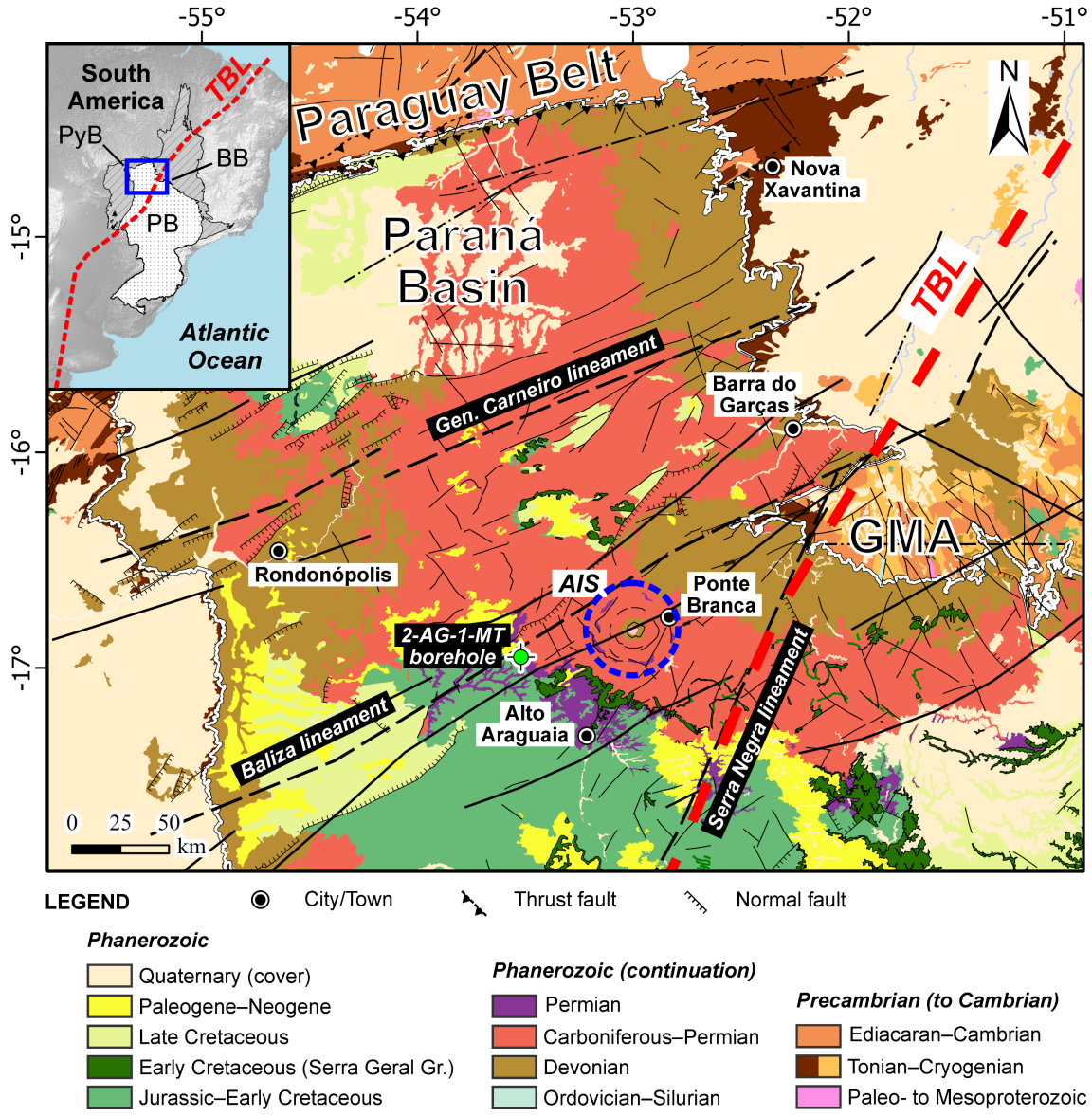

Figure 1. The NNW Paraná Basin (blue outline in the inset map) in the wider tectonic context of the South American platform. PB – Paraná Basin (Phanerozoic); Neoproterozoic belts that are part of the Tocantins Province: PyB – Paraguay Belt, BB – Brasilia Belt; TBL – Transbrasiliano Lineament (see inset map; after Schobbenhaus et al., 2004). The main map displays the regional geology of the NNW Paraná Basin and its surroundings. Note the location of the Araguainha impact structure (AIS – blue dashed circle), the 2-AG-1-MT borehole (green circle), the main trend of the Transbrasiliano Lineament (TBL – red dashed line), the Paraguay Belt, the Goiás Magmatic Arc (GMA; part of the Brasilia Belt), the main magnetics-derived lineaments (Serra Negra, Baliza, and General Carneiro – thick, dashed black lines – after Curto et al., 2014), and other general structural features (e.g., regional or local undifferentiated fractures/faults or lineaments – other diverse black lines/symbols) (modified after Curto et al., 2014, and references therein).

Based on magnetotelluric (Masero et al., 1997) and potential field (Vasconcelos, 2007) data, these authors suggested a possible structural influence of the Transbrasiliano Lineament on the crustal framework in the region of the AIS. However, they did not further develop this idea. Recently, Bernardes et al. (2025) revived this hypothesis, also proposing that the overall structural trend beneath the NNW Paraná Basin – including the Paraguay Belt – had also influenced the first-order morphostructure of the Araguainha impact structure.

Here, we explore two main questions related to the AIS in its regional tectonic setting: What is the nature of the structural framework of the AIS region, and did this framework influence the morphology of the Araguainha impact structure, imparting a polygonal shape to it? To answer these questions, we employ a multi-methodological approach that includes airborne geophysics, remote sensing analysis, fieldwork, and modeling of the (apparent) crater rim trace shape.

BACKGROUND

Araguainha impact structure (AIS): Morphostructure and geology

The most recent morphostructural compartmentalization of the AIS (Fig. 2) by Bernardes et al. (2025) proposes an ~40-km-diameter structure with: (1) an up to 20-km-wide, asymmetric central uplift that may have different widths in different sectors (e.g., relatively more narrow in the ENE sector), likely due to sector-dependent collapse; (2) an intermediate section, starting at the outer limit of the uplifted area at approximately 10 km from the apparent center of the structure, and representing a fault-block-dominated ring syncline region; this section transitions at approximately 15 km radial distance to (3) an ~5-km-wide, outer rim region that extends to the structure's edge. This last compartment resembles a terraced zone similar to that of pristine craters, where large-scale, generally concentric, fault-bounded slump blocks are found. The main structural differences between the outer rim and intermediate sections of Araguainha (see Bernardes et al., 2025) probably stem from inward-increasing radial and tangential constrictions of the inward-slumping rock volumes in these sections, caused by limited space resulting from the inward movement of the crater wall materials during crater collapse in the modification stage (see Melosh, 1989; Kenkmann et al., 2012).

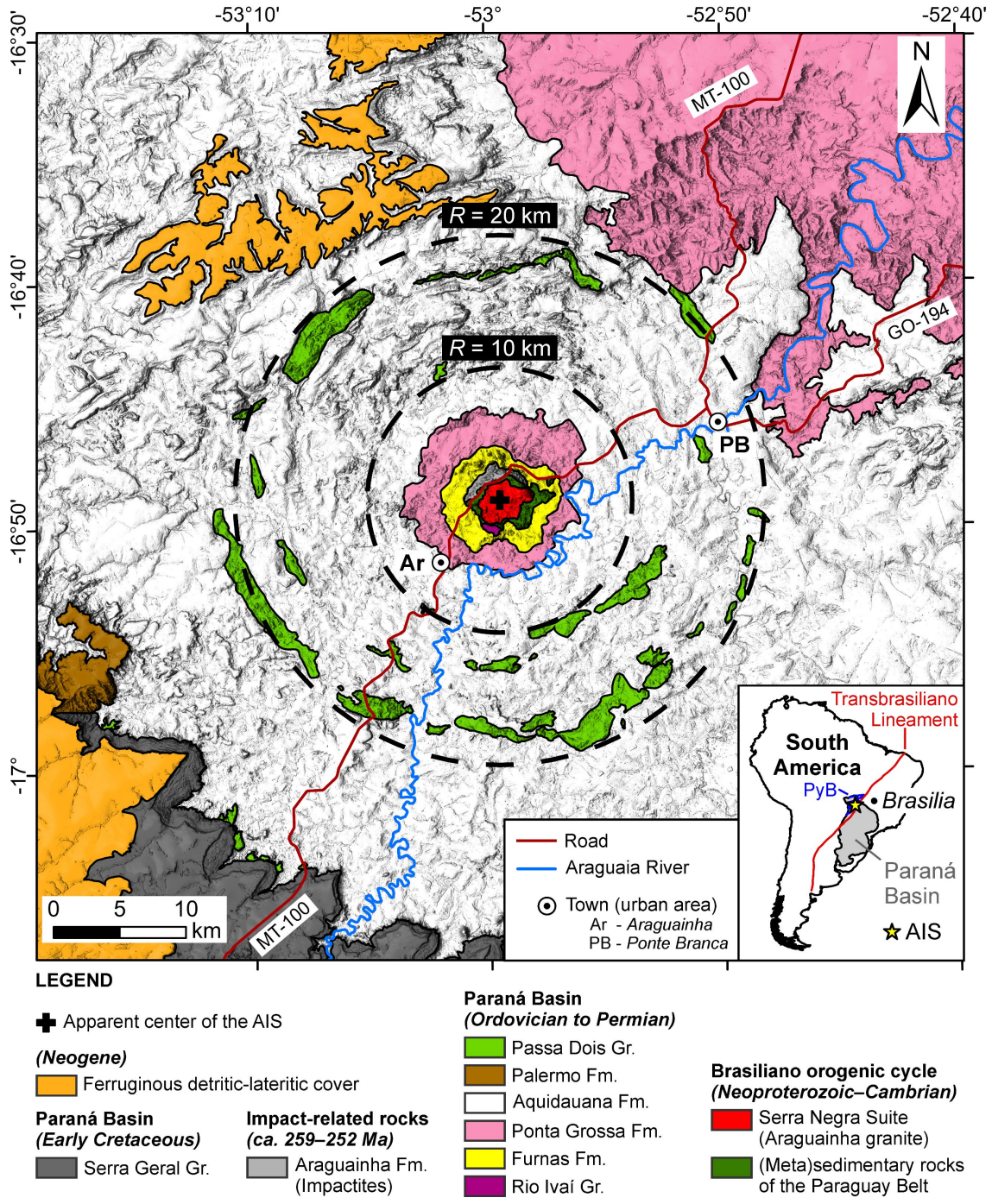

Figure 2. Geological map of the Araguainha impact structure (AIS) and environs in the N-NW part of the Paraná Basin (after Bernardes et al., 2025) superimposed onto TanDEM-X multidirectional digital elevation model with some transparency and vertical exaggeration (5:1). Map coordinate system: WGS84. Thick, black dashed lines represent circles with different radial distances (*R*) from the apparent center of the AIS. The inner circle with *R* = 10 km depicts the proposed maximum extent of the central uplift (after Bernardes et al., 2025). The outer circle with *R* = 20 km approaches the apparent diameter of 40 km of the AIS. Inset (bottom right): Location of the AIS in the NNW Paraná Basin. PyB – Paraguay Belt; TBL – Transbrasiliano Lineament (after Cordani et al., 2016).

The stratigraphic units of the Paraná Basin that are involved in the AIS are arranged in a quasi-concentric, "bull's-eye" pattern. The youngest unit (Passa Dois Group) forms broadly concentric, downfaulted, and internally deformed blocks that outline the outer rim of the impact structure and occur as large patches in the interior (Fig. 2; see also Lana et al., 2008, and Bernardes et al., 2025). In contrast, the older stratigraphic units are exposed sequentially toward the center of the AIS, where units related to the crystalline and (meta)sedimentary basement of the basin emerge in the core of the central uplift.

The (meta)sedimentary basement exposed in the central parts of the AIS comprises phyllites and metasandstones, which have recently been linked to the Cuiabá Group of the Paraguay Belt (see references and discussion in Souza et al., 2024). However, these same authors present evidence for the existence of another, unmetamorphosed sedimentary sequence in the central uplift of the AIS. This second sequence may belong to the uppermost Paraguay Belt or the lowermost Paraná Basin unit (Souza et al., 2024). Notably, the recent work by Frugis et al. (2024) proposes the occurrence of their newly defined "Barra do Garças-Coxim" unit in Paraguay Belt exposures relatively close to the AIS. This unit, comprising immature metasedimentary rocks believed to have been directly derived from erosion of the Goiás Magmatic Arc to the northeast of the AIS, represents part of a collisional foreland basin system within the Paraguay Belt (Frugis et al., 2024).

The Araguainha Granite is the main lithology in the inner core of the central uplift of the AIS (see Fig. 2). It is a post-collisional, porphyritic granite characterized by potassium feldspar megacrysts up to 5 cm in size (Silva et al., 2016). U-Pb isotopic ages from zircon indicated a Cambrian crystallization age of 509.5 ± 12 Ma (Tohver et al., 2012), which may link it to post-Brasiliano/Pan-African, high-K granitic magmatism of the Goiás Magmatic Arc in central Brazil (see Pimentel et al., 1996).

Within the AIS, only the three oldest stratigraphic supersequences of the Paraná Basin (Milani et al., 2007) – specifically, the Rio Ivaí (Ordovician–Silurian), Paraná (Devonian), and Gondwana I (Carboniferous–Early Triassic) – are present. Some tens of kilometers SW and NW of the apparent outer rim of the structure, igneous rocks of the Serra Geral Group (Early Cretaceous; ca. 134 Ma; Gomes and Vasconcelos, 2021) also crop out locally (see the geological maps of Horn et al., 2022, and Bernardes et al., 2025). Approximately 50 km WSW of the center of the AIS, the drill core from Petrobras

borehole 2-AG-1-MT was recovered, indicating a local basin thickness of roughly 1920 meters (Thomé-Filho et al., 2012).

The Rio Ivaí supersequence (Rio Ivaí Group) features a thin (30–50 m thick) and limited occurrence of conglomerate, diamictite, sandstone, and siltstone, as identified in the central part of the AIS (UnB-IG, 2012; Souza et al., 2024). The Paraná supersequence (Paraná Group) generally overlies the Rio Ivaí Group but can also be found in direct contact with the basement of the basin and is divided into two units: the lower, psammite-dominated Furnas Formation, and the upper, pelite-dominated Ponta Grossa Formation (Milani et al., 2007). The Furnas and Ponta Grossa formations make up a significant part of the collar of the central uplift of the AIS (Souza et al., 2024; Bernardes et al., 2025).

In the AIS, the Gondwana I supersequence is represented by the Aquidauana Formation and two units of the Passa Dois Group. The former occurs from the outer part of the collar of the central uplift to beyond the limits of the AIS, whereas the latter is restricted to the outer regions of the structure, beyond the central uplift (Fig. 2; see Bernardes et al., 2025). The Aquidauana Formation mainly consists of red sandstones, conglomerates, and mudstones with various textures (Gesicki et al., 2002; Barros et al., 2021), with pelitic lithotypes more frequently found within the AIS in the upper section of the formation (Lana et al., 2007; UnB-IG, 2012).

The Passa Dois Group in the study area includes the basal Irati Formation and the Corumbataí Formation. The Corumbataí Formation is the uppermost stratigraphic unit affected by the Araguainha impact, and in the vicinity of the AIS, it directly overlies the Irati Formation (Bernardes et al., 2025). The Irati Formation is divided into a lower, siliciclastic unit, known as the Taquaral Member, and an upper, carbonate-rich unit, referred to as the Assistência Member (Holz et al., 2010; Callefo et al., 2018; Cagliari et al., 2022). The Corumbataí Formation consists of red-brown to gray mudstones, with minor intercalations of sandstones and carbonates (Warren et al., 2015; Zanardo et al., 2016; Montibeller et al., 2020). These units form the so-called “Passa Dois Group Blocks” (PDGBs) within the AIS, which also outline the apparent outer rim of the structure (Bernardes et al., 2025; see Fig. 2).

Impact-related rocks (impactites) are mostly found from the west to the northeast around the transition from the core into the topographically elevated sedimentary collar of the central uplift (Souza et al., 2024; Bernardes et al., 2025). There are comparatively fewer and smaller deposits in the southern part of the central uplift (Souza et al., 2024).

The northern part of the core of the central uplift includes a highly diverse (structurally and lithologically) megablock zone that overlies a folded and faulted, yet generally coherent, crater floor (Souza et al., 2024; Bernardes et al., 2025).

Polymict impact breccia in the AIS may contain micro- and macroclasts, likely derived from the lowermost sequences of the Paraná Basin and from the (meta)sedimentary rocks of the basement of the basin (Souza et al., 2024). Granite clasts are uncommon and probably represent material from the fine- to medium-grained border and apophyses of the Araguainha granite stock extending into the (meta)sedimentary basement (Souza et al., 2024; Bernardes et al., 2025). Souza et al. (2024) identified three types of impact melt rock in the AIS. These authors were also the first to report polymict impact breccia with melt rock clasts (suevite) in breccia packages in the northern outer part of the core of the central uplift. Complementary, Bernardes et al. (2025) distinguished three types of polymict impact breccia – a lithic impact breccia and two types of suevite – in the same core region.

Regional structural framework of the NNW Paraná Basin region

Since the end of the Brasiliano orogenic cycle, around 500 Ma (Brito Neves et al., 2014), tectonic activity within the Paraná Basin has been limited to vertical and horizontal movements along preexisting basement fractures, which have been repeatedly reactivated (Zalán et al., 1990). These reactivations shaped the current outline of the northwestern border of the basin, adjacent to the Paraguay Belt (ibid). Statistical analysis of aeromagnetic lineament distribution and fieldwork across the entire Paraná Basin primarily revealed a bimodal structural framework dominated by structures trending N50°–70°E and N45°–65°W, with subordinate lineaments trending N85°–90°W (Zalán et al., 1990).

In the NNW region of the Paraná Basin and adjacent terrains, subsequent, more localized studies have shown that this general structural pattern persists, alongside another prominent lineament direction around N25°–30°E (see Curto et al., 2014, 2015; Pinto and Vidotti, 2019; Dalat de Sousa et al., 2024). These works mainly associated the NE-trending lineaments in this region with the Paraguay Belt (~N50°–70°E) and the Transbrasiliano Lineament (~N25°–30°E) regional structural trends. In contrast, the nature of the NW-SE and E-W lineaments in this region remains less constrained. It is suggested that their origin may be related to the opening of the South Atlantic Ocean

during the Early Cretaceous (Curto et al., 2014) – designated as the Wealdenian reactivation or Meso-Cenozoic tectonic activation (Zalán, 2004) – and/or to a morphostructural regional uplift associated with the intrusion of the Goiás Alkaline Province (Dalat de Sousa et al., 2024).

The Transbrasiliano Lineament (TBL; Schobbenhaus et al., 1975) is one of the most prominent tectono-structural features in the north-northwestern Paraná Basin region (and beyond, within the broader western Gondwana; see Caxito et al., 2025). In the NNW Paraná Basin region, the TBL is mainly concealed by the overlying sedimentary successions, but can be easily identified using geophysical techniques, primarily potential-field methods (e.g., Curto et al., 2014, 2015; Pinto and Vidotti, 2019; see also Dalat de Sousa et al., 2024).

The TBL represents a first-order, transcontinental, polycyclic, NE-SW-trending, tectonic corridor and shear zone system (see Caxito et al., 2025, and references therein). The main tectonic activity (dextral ductile shearing) along this zone began at ca. 510–505 Ma, about 30–60 Ma after the last collisional events associated with the Brasiliano/Pan-African orogenies (Caxito et al., 2025). It has been proposed that the TBL separates the Goiás Magmatic Arc and the Paranapanema Cratonic Block to the east-southeast from the supracrustal rocks of the Paraguay Belt and the Amazon Craton to the west (see Cordani et al., 1984; Curto et al., 2014).

The TBL comprises a series of NE-SW-striking ductile shear zones with (sub)parallel faults (Cordani et al., 2013a) over a 100- to 200-km-wide corridor (Brito Neves et al., 2014), for at least 2700 km across parts of Brazil, Paraguay, and Argentina (inset map in Fig. 1; Schobbenhaus et al., 2004). The TBL shear zone system originally and predominantly had dextral transcurrent kinematics (Pimentel and Fuck, 1992; Caxito et al., 2025). However, diverse tectonic activities – such as brittle-ductile extensional or sinistral reactivations along the corridor – seem to have operated along it throughout the Phanerozoic (see, e.g., Brito Neves et al., 1984; Cordani et al., 2013a, b; Ganade de Araujo et al., 2014; Curto et al., 2014; Amaral et al., 2017).

To date, the works by Curto et al. (2014, 2015) represent the most comprehensive regional analysis of TBL-related structures focused on the NNW Paraná Basin. They identified that the primary trend of the TBL in this region is N30°E, as exemplified by the Serra Negra fault (Fig. 1). Prominent N45°–70°E-trending lineaments, especially related to the major N60°–70°E-trending Baliza and General Carneiro faults (Fig. 1), also

occur in the area (Curto et al., 2014). In contrast, lineaments trending N80°W, N80°E, and N50°W are interpreted to be caused by extensional tectonics and the emplacement of alkaline intrusions during the Cretaceous (Curto et al., 2014). Moreover, these authors suggested that the NW-trending lineaments may have remained active, based on recent nearby earthquake activity, whereby these lineaments also dextrally displaced some of the NE-trending lineaments. Curto et al. (2015) concluded that neotectonic activity associated with older basement structures generally influenced the topography and drainage patterns in the NNW Paraná Basin region.

MATERIALS AND METHODS

Airborne geophysical data

The geophysical data used in this work come from the Alto Garças Airborne Project, which was completed in 1971 (CPRM, 1972). This project involved an airborne survey combining gamma-ray spectrometry and magnetometry. The Geological Survey of Brazil (SGB/CPRM) and the National Nuclear Energy Commission (CNEN) have since made part of this database publicly available in digital format. This survey is regional and was conducted over a relatively large area within central Brazil. We have only processed and analyzed data for the area of the AIS and its surroundings.

The Alto Garças Project had a nominal flight height of 120 meters, with north-south flight lines spaced 1 km apart, and west-east tie lines spaced 20 km apart. Gamma-ray spectrometric data were collected using a four-channel spectrometer fitted with a sodium iodide (NaI) crystal sensor (volume: 6,850 cm^3) that measured gamma rays at a 1-second sampling rate. The magnetometric data were recorded at 1-second intervals using a Fluxgate magnetometer (see CPRM, 1972, for more details).

The final project report includes maps of the anomalous magnetic field (AMF) and gamma-ray total count (TC) (CPRM, 1972). However, only the magnetic data were successfully retrieved and made public in digital format by the SGB/CPRM. The original radioelement data (K, eTh, eU) were lost and, later, only partially recovered (see below). We used two commercial software packages, Oasis Montaj Educational 2024.2 (Seequent) and ArcGIS Pro 3 (Esri), to process the datasets and create the geophysical maps shown here. The geophysical results provide sufficient information for regional studies, including the analysis of anomaly geometries, the definition of structures at various depths, and the assessment of lineament directions.

Processing of airborne magnetic data

Several methodologies are available for the automated and rapid analysis of magnetic anomalies, enabling the estimation of geological source locations and depths over large areas (Li, 2003; Li and Nabighian, 2015; Betts et al., 2024, and references therein). We planned the processing stages of the gridded magnetic data to enable the detection of concealed intrasedimentary and basement structures at depth. Although the final gridded database underwent meticulous processing steps (see below), it is essential to note that the original data contained several types of noise, including instrumental errors and fluctuations in flight height and direction.

To enhance near-surface and intrasedimentary magnetic features, our initial analysis was based on the residual component of the anomalous magnetic field (AMF; Fig. 3A), i.e., the total measured field corrected for diurnal variations, the main geomagnetic field (IGRF), leveling errors, and removal of a regional trend surface (see Betts et al., 2024). The AMF map was generated by applying a bi-grid interpolation with a cell size of 250 m.

The applied techniques rely on horizontal and vertical derivatives of magnetic anomalies (Li and Nabighian, 2015; Betts et al., 2024). Specifically, the first-order vertical derivative (Fig. 3B) was employed to identify shallow magnetic sources that might characterize linear features (e.g., Betts et al., 2024).

Skewness in magnetic anomalies arises from the influence of non-vertical magnetization and ambient field vectors, making their interpretation more complex (Blakely, 1995). This problem is acute in Brazil, where the inclination of Earth´s main field is shallow (ca. −20°), and anomaly amplitudes are low. To overcome these problems and assist with our analysis of magnetic sources, we used the total gradient amplitude of the magnetic anomalies (TGA; see Macleod et al., 1993; Li, 2006; Li and Nabighian, 2015) (Fig. 3C). The TGA is a linear transformation that combines horizontal and vertical derivatives of magnetic anomalies, illuminating spatial distributions of their sources even at low latitudes (Li, 2006; Li and Nabighian, 2015). The depicted anomalies have shapes indicative of the source depth. However, the TGA is attenuated with increasing depth to source, thus hampering interpretations when both shallow and deep sources are present (e.g., Curto et al., 2014).

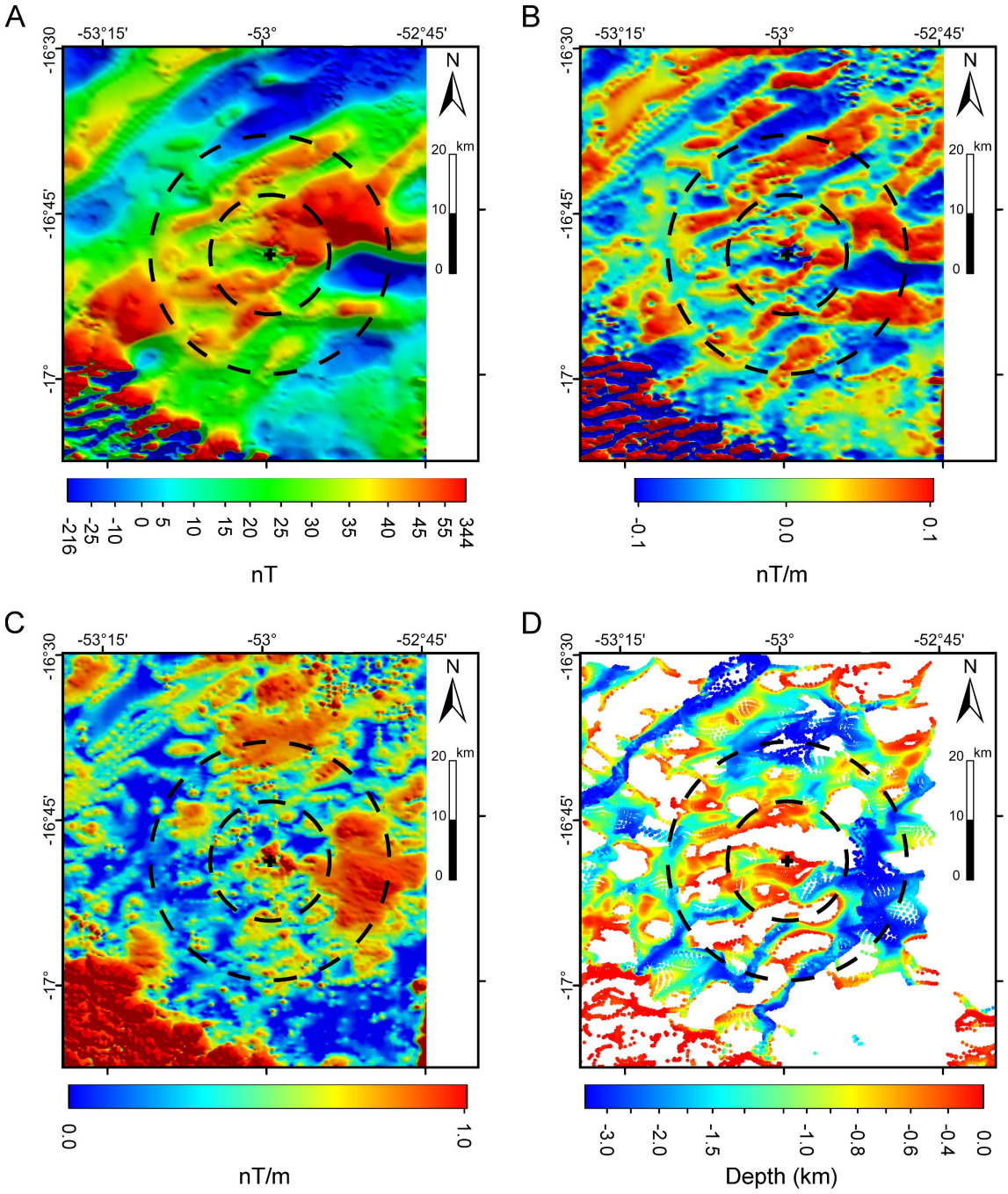

Figure 3. Airborne magnetic anomaly maps of the Araguainha impact structure and environs. The map frames have the same extent as the geological map in Fig. 2. The vertical white stripe in the eastern portion of each map indicates "no data" and originally contained noisy data. These data were removed during processing. In each map, the inner black dashed circle has a radius of 10 km and depicts the proposed maximum extent of the central uplift (after Bernardes et al., 2025). The outer black dashed circle has a radius of 20 km and approaches the 40 km apparent diameter of the AIS. A) Total field magnetic anomaly. B) First vertical derivative. C) Total gradient amplitude (TGA). D) Interpolated Euler depth solutions. (See "Materials and Methods" section for details.)

In addition to the qualitative analysis of magnetic source depths, we applied the Euler Deconvolution (ED) technique, a semi-quantitative method based on Euler's

differential equation, to estimate magnetic source depths (Reid et al., 1990; Li, 2003, and references therein). The ED method requires the assumption of a "structural index," a parameter indicative of the source geometry, yielding a distribution of depth solutions that require further evaluation based on additional constraints (Barbosa et al., 1999; Li, 2003; Betts et al., 2024). In our calculations, we prioritized a structural index of 1, which relates sources to linear and planar geometries, such as shear zones and dikes. The window size selection criterion was a trade-off between minimizing interference from close anomalies generated by distinct sources (smaller window sizes) and ensuring the inclusion of wider anomalies arising from deeper sources (larger window sizes). We thus opted to use a 20 x 20 grid cell window size and a grid interval of 250 meters. The Euler solutions were interpolated using the Inverse Distance Weighted (IDW) algorithm, with a cell size of 100 m, to provide a clearer view of the source geometries. The resulting Euler solution map (Fig. 3D) shows depth solution gaps, where solutions separated by more than 300 m are considered insufficient to allow interpolation.

Processing of airborne gamma-ray spectrometry data

The original analog data files from the airborne gamma-ray spectrometry survey were lost. An attempt to recover part of the Total Count (TC) data was made by Johann Lambert (Universidade Estadual de Campinas, Brazil), who digitized the map from the printed final report of the project (CPRM, 1972). He digitized ~34000 data points from the analog TC contour map of the AIS region (Crósta et al., 2019; Leite et al., 2022). These data points were kindly provided to us by him. With them, we produced a newly processed digital TC map for the area of the Araguainha impact structure (Fig. 4). However, this map is based on legacy data, as it was derived from manually digitized 1970s data without explicit quality control and may contain digitization-related errors.

The main corrections commonly applied to radiometric data (e.g., dead time, background removal, height, Compton effect; Killeen et al., 2015) were employed in this survey. However, the airborne gamma-ray spectrometry databases acquired in the 1970s have not been calibrated, so radioelement concentrations in these surveys are expressed in counts per second (cps). Moreover, several flight-line artifacts are noticeable when such data are interpolated, suggesting that the leveling and microleveling (when applied) were ineffective.

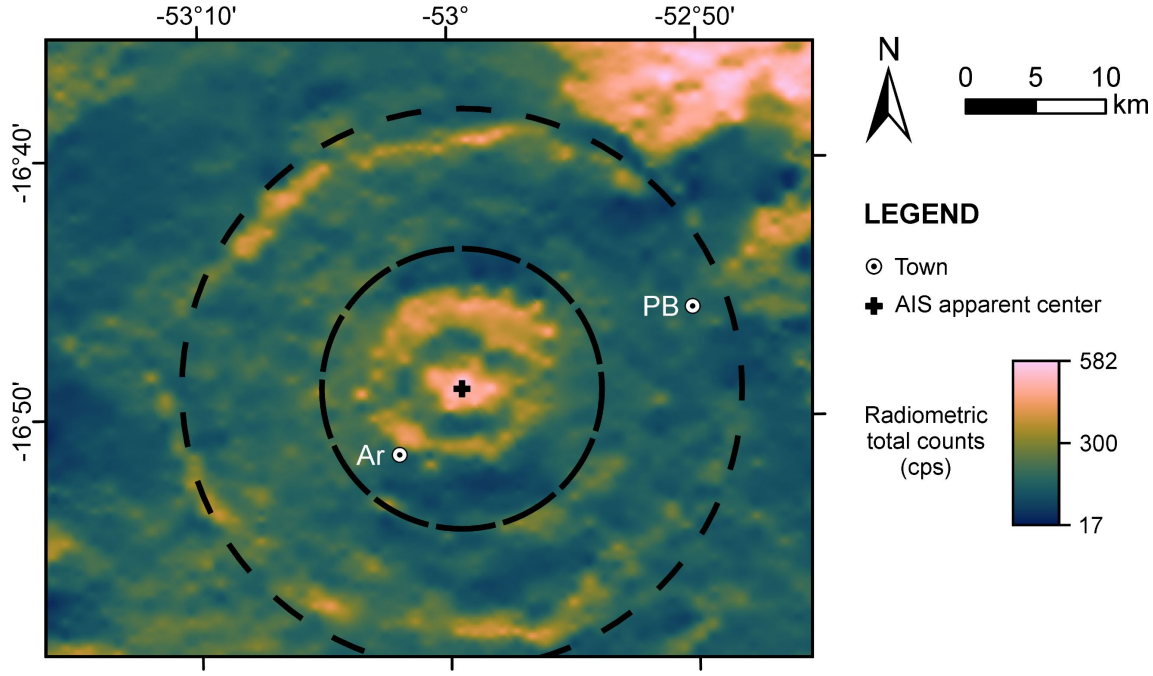

Figure 4. Airborne gamma-ray total count map of the Araguainha impact structure and its surroundings, based on legacy data from the 1970s, reprocessed and georeferenced (see "Materials and Methods" section for details). Data recovered and kindly made available by J. Lambert (University of Campinas, Brazil). Data coverage in the southern outer rim region of the AIS was originally limited. The scientific color map "batlow" (Crameri, 2018) was used to prepare this map. Black dashed circles are the same as in the previous figures. Inner circle has R = 10 km. Outer circle has R = 20 km. Note how the apparent outer rim of the AIS, at R ~ 20 km, is marked by a discontinuous radiometric ring of medium-to-high total counts (cps) and with a concentric but somewhat polygonal shape. Also, note the asymmetric and somewhat polygonal geometry of the central uplift region of the AIS within the black dashed inner circle (see text for details). Towns: Ar – Araguainha; PB – Ponte Branca.

During the first processing step, we observed that the original spatial reference of the TC data points did not align with our survey area, despite several attempts to reproject them. Thus, initially in Oasis Montaj, we interpolated TC data points without a defined georeferenced system. We employed the Inverse Distance Weighted (IDW) method to interpolate the TC data points because it is suitable for interpolating airborne gamma-ray data (e.g., Silva et al., 2023). We selected the interpolation cell size that yielded a smooth grid without data gaps. Second, we applied a directional cosine filter (azimuth = 0 and cosine function degree = 1) and a Hanning filter (three passes) to suppress flight-line artifacts and spurious spikes.

The resulting TC grid was exported to ArcGIS as a TIFF file. We extracted five Ground Control Points (GPCs) from the 12-m-pixel TanDEM-X digital elevation model over the Araguainha impact structure (Gottwald et al., 2020), overlain by the contours of the geological units derived from the most recent and most detailed AIS geological map

available at the time (Souza et al., 2024). Then, the TC map was georeferenced (WGS84 UTM Zone 22S projection) using the five GPCs with a first-order polynomial (resulting root mean square <0.1%). Our interpretations were then conducted on this newly georeferenced gamma-ray spectrometry total count map (Fig. 4).

Remote sensing data

Remote sensing data were derived from two sources: Esri's high-spatial-resolution optical World Imagery layer map service (Credits: Esri, Maxar, Earthstar Geographics, and the GIS User Community) and the TanDEM-X (12 m pixels) digital elevation model (Rizzoli et al., 2017) of the AIS and environs (Gottwald et al., 2020).

The high-spatial-resolution optical image layer was overlain with a partially transparent, processed, multidirectional hill-shaded image of the TanDEM-X digital elevation model, featuring a 5:1 vertical exaggeration. This exaggeration was applied to emphasize the relief features, which, in general, are subdued over the study area (compare Fig. 2). We used this combined overlay to extract the structural lineaments and the apparent rim trace of the AIS (see below).

Field data

Fieldwork in the Araguainha region was conducted from 2021 to 2024 as part of a geological mapping project. Outcrops within and outside the AIS were described and registered, and their structures were measured. The bulk field data from this mapping endeavor are presented and discussed, with a focus on the geological-structural aspects of the AIS, as described by Bernardes et al. (2025).

Here, we discuss some outcrops and specific areas within and outside the impact structure to exemplify and relate the structural data with geophysical and remote sensing observations. Additionally, more regional NNW Paraná Basin structural field observations were reprocessed (after Curto et al., 2014) and incorporated into this work to provide a wider view of this part of the basin.

Lineaments: Definition and extraction procedures

We use the definition of "lineament" after O'Leary et al. (1976, p. 1467): "L. *linea* = line + L. *mentum* = akin to; hence, akin to or like a line. A lineament is a mappable, simple or composite linear feature of a surface, whose parts are aligned in a rectilinear or

slightly curvilinear relationship and which differs distinctly from the patterns of adjacent features and presumably reflects a subsurface phenomenon."

Lineaments were extracted with Esri's ArcGIS Pro software and processed and analyzed with the OpenStereo 2.0b software (Grohmann and Campanha, 2010). Lineament extraction was performed manually by a single person (R.B. Bernardes) at specific scales and across different sessions to ensure consistency and reduce subjectivity. All lineament trends presented in the text are referenced to True North. We use the term *R* to indicate the radial distance of a specific feature of interest from the apparent center of the AIS (Fig. 2; 52.99151°W, 16.81544°S).

We extracted three types of lineaments from the processed imagery: *magnetic*, *radiometric*, and *structural* lineaments. Structural lineaments are those derived from remote sensing imagery. The extracted lineaments were classified as "inside the AIS" or "outside the AIS." This separation was effected at $R = 22$ km. This radius was used as a buffer to account for the variable radial distances of segments of the apparent outer rim trace of the AIS, ensuring that the entire AIS structural domain was included in the "inside the AIS" analysis. Thus, the lineaments that for more than half of their length occur within this circular area were classified as "inside the AIS."

The magnetic lineaments were extracted from the interpolated Euler solution map (Fig. 3D), whereas the radiometric lineaments were extracted from the newly reprocessed total count map (Fig. 4). In both cases, the respective lineaments were extracted at the 1:250,000 scale and in single-day sessions each. In addition, magnetic lineaments from the entire NNW Paraná Basin were reprocessed (after Curto et al., 2014) and incorporated into this work to complement our analysis.

The structural lineaments were extracted from the previously described composite overlay of remote sensing imagery (see "Remote sensing data" section). These lineaments were extracted at the 1:50,000 scale and during limited sessions over a nearly two-week period. As structural lineaments, we considered natural, linear features with a negative topographic break, a length of ≥1 km in any direction, and that were readily observable at the working scale.

Due to the working scale and the relatively large size of the study area, the structural lineaments were systematically extracted from different circular areas, both within and outside the impact structure, to optimize the extraction procedure. The central circular area was the same as the previously defined one for a radius of 22 km and

centered on the AIS. Eight other circular areas, each with a radius of 15 km and centered at 40 km from the AIS center in different (inter)cardinal sectors (e.g., N, NE, etc.), were also defined and considered representative of structural domains "outside the AIS."

The apparent rim trace of the AIS and its shape analysis

The rim trace of a given impact structure can be analyzed to obtain insights into its shape and, consequently, of the target structuration (see Robbins and Riggs, 2023). Araguainha, however, is a degraded impact structure (see Osinski et al., 2022). Its ejecta blanket has been removed entirely (Lana et al., 2007). Still, a sizable volume of crater fill impactites can be observed around the core of the central uplift (Souza et al., 2024; Bernardes et al., 2025). The pristine crater rim is somewhat eroded. However, due to the Passa Dois Group blocks, the (apparent) rim of the AIS is still rather well-marked, and there are some continuous segments of the seemingly terraced outer rim (e.g., in the NW and N sectors; Bernardes et al., 2025; see Fig. 2). Moreover, Lana et al. (2007) suggested that vertical erosion at the structure was not extreme (~250–350 m). This estimated erosion led to a first-order estimated (minimum) loss of crater diameter of no more than 1% (290–400 m) of the 40 km apparent diameter of the AIS (Bernardes et al., 2025). Thus, working with the apparent crater rim trace of the AIS, although not ideal (see Robbins and Riggs, 2023), is justifiable and may still offer insights into crater shape, target structure, and crater formation – such as oblique impact.

We employed the algorithm of Robbins and Riggs (2023) to conduct a rim trace shape analysis of the AIS. This code uses a Monte Carlo approach to return the best-fit rim trace shape of a given impact structure by testing N-dimensional (N being a natural number ≥ 3) polygons with N sides that are represented by either straight lines or arcs, where the number of arcs is $\leq [N \div 2]$. As input, the code only requires a list of latitude and longitude entries representing the vertices of the rim trace of the structure.

For the eroded Araguainha impact structure, we sought to pick a minimum set of vertex points that contained the most indicative morphological and topographic features (see criteria below), and that still preserved a first-order (apparent) rim trace shape at the analyzed scale (1:50,000). This was done to avoid overinterpretation of the apparent rim structure. Moreover, to make the rim trace picking procedure more systematic and objective, we assumed two criteria, according to their relative importance: (1) the outermost juxtaposed (commonly topographic) interfaces between the Aquidauana

Formation and the Passa Dois Group fault-bounded blocks as the best markers for the (apparent) outer rim trace. The geological map of Bernardes et al. (2025) was used for this purpose (see Fig. 2); (2) In the absence of this marker interface, we considered an interplay between the more prominent negative topographic breaks and the occurrence of concentric/tangential (in relation to the apparent center of the AIS) structural lineaments. We note, however, that the identification of the ENE sector apparent rim trace segment (near Ponte Branca town) is a more fragile one, due to its overall subdued morphological features and greater erosion by the Araguaia River (see Fig. 2). Still, we opted to include this segment in the rim trace analysis. We emphasize that this segment should be treated with caution.

Following these guidelines, we traced the apparent outer rim of the AIS using 141 vertex nodes (see Fig. S1 of the Supporting Information) from the same remote sensing dataset used for extracting structural lineaments (see "Remote sensing data" section). Then, the Robbins and Riggs' (2023) code was run for 25 different shape models (i.e., N = 4–9, with 0–[(N ÷ 2)] arcs instead of a straight side; and an additional 10-sided polygon). The 10-sided polygon was included in the analysis because, in our tests, we found that at the scale of our analysis (1:50,000), this geometry is already outside the upper limit of the possibly representative models (see "Results" section).

Each model was run 100 times, and at each time, the algorithm carried out up to 15,000 iterations to try to improve the model by checking for convergence with the reference rim trace. As output parameters, the code primarily provides the residual fits (i.e., the normalized area difference between the shape fit and the rim trace), the resulting shapes, and the azimuths of the straight-line sides for each shape (see Robbins and Riggs, 2023, for further details).

The models obtained were then analyzed to gain insights into the shape of the Araguainha impact structure. The model that provided the best fit without overparameterization (following the "Occam's Razor" principle) was selected as the most representative model for the AIS (see argument in "Results" section). Lineament data were then analyzed in conjunction with regional geological and geophysical knowledge, field observations, and the results of the AIS shape-fitting analysis.

RESULTS

Magnetic anomaly maps

The different magnetic anomaly maps (Figs. 3A–D) essentially highlight two main patterns: 1) high-frequency (shallow) anomalies in the SW of the map area, and 2) lower-frequency, thus deeper located, anomalies generally trending NE-SW. The high-frequency shallow anomaly pattern is spatially related to the occurrences of the Serra Geral Group volcanics (mainly basalts) and intrusive mafic rocks (compare Figs. 2 and 3). In contrast, we attribute the lower-frequency, NE-SW-trending anomalies to the magnetic signatures of the tectono-structural framework beneath the NNW Paraná Basin (see "Discussion" section).

The Euler solution map (Fig. 3D) is crucial because it is the map from which the magnetic lineaments were derived (see next). This map shows Euler depths ranging from near-surface levels to a few hundred meters (≤700 m, in orange to red colors) to depths of several kilometers, even exceeding 3 km (in dark blue). The shallowest (near-surface) Euler solutions, located in the SW of the map area, are associated with the Serra Geral Group igneous rocks, but shallow solutions also appear around the apparent center of the AIS. Deeper Euler solutions (≥1.5 km depth; in cyan to dark blue) are typically expressed as either NE-SW- or NW-SE-trending corridors or as broader, more irregular regions.

Magnetic lineaments

Magnetic lineaments (n = 57) extracted from the interpolated Euler solution map show that the NE-SW magnetic "corridors" correspond to the majority of these lineaments, both outside and inside the AIS domain (see Fig. 5A). However, some differences can be observed between these domains. Outside the AIS, there is less variability in the direction of the magnetic lineaments. Lineaments trending N50°–60°E predominate (Fig. 5B) and can be observed nearly all around the AIS (Fig. 5A). Two other lineament directions are also important, at N80°–90°E and N40°–50°W orientation trends (Fig. 5B).

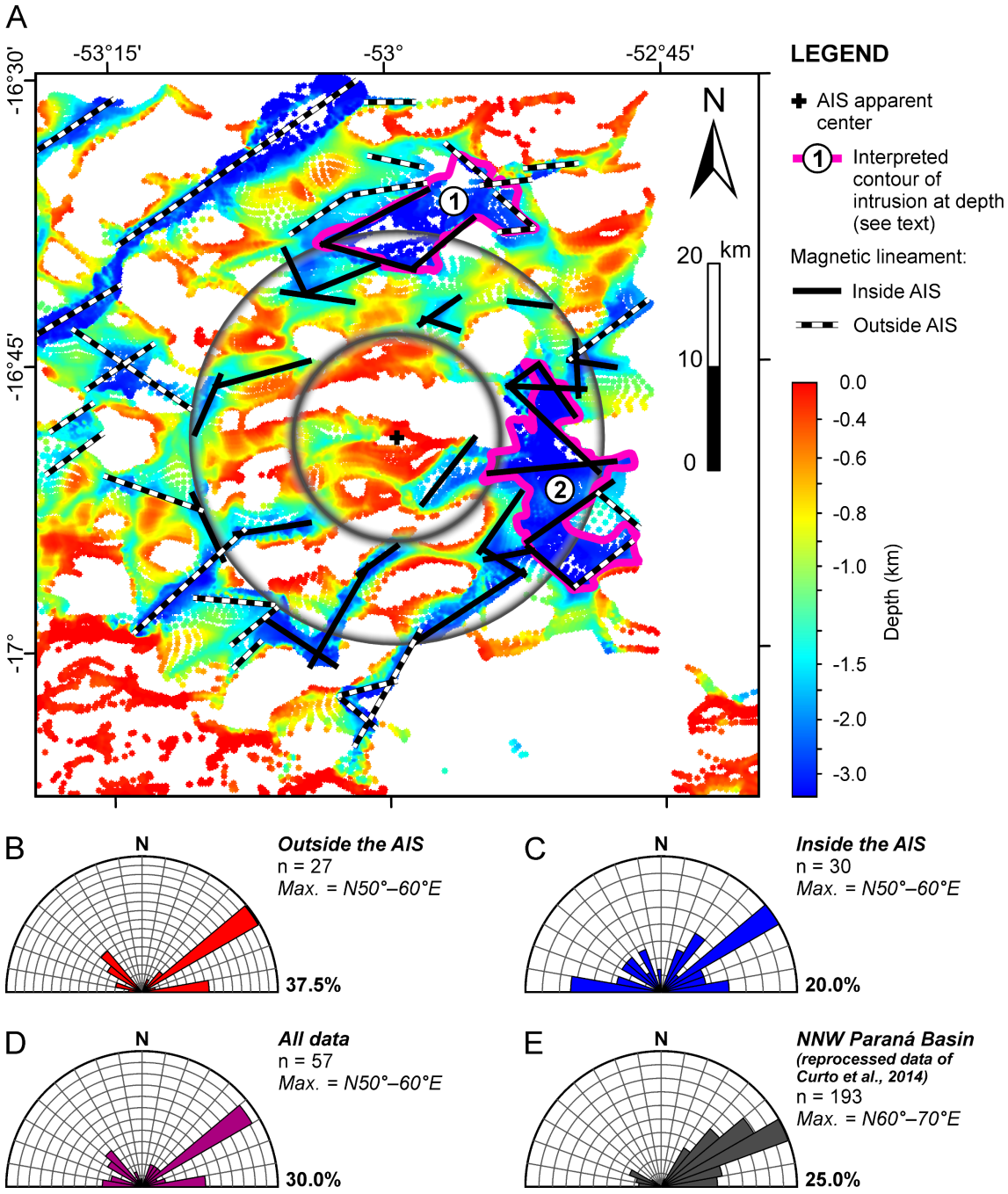

Figure 5. A) Interpreted magnetic lineaments from the interpolated Euler deconvolution map of the Araguainha impact structure and environs. Dark gray circles are the same as the black dashed circles in the previous figures. Inner circle has R = 10 km. Outer circle has R = 20 km. Note the distinction between lineaments inside (black) and outside (black and white dashed) the AIS area. The existence of two intrusions at depth (see tags "1" and "2" and thick magenta lines) is interpreted from this map. See the "Discussion" section for more details. B) Rose diagram for orientations of magnetic lineaments inside the AIS. C) Rose diagram for magnetic lineaments outside the AIS. D) Rose diagram of all (outside + inside) magnetic lineaments in the AIS and surroundings. E) Rose diagram for magnetic lineaments in the wider NNW Paraná Basin (reprocessed data of Curto et al., 2014). The "n" symbol indicates the number of lineaments in each diagram. The percentage (%) indicates the frequency of the outer limit of each diagram. The trend range with maximum frequency is highlighted for each diagram.

Inside the AIS area, there is a greater spread in lineament directions. Yet, the N50°–60°E direction remains predominant, followed by a nearly E-W (i.e., N80°–90°W) trending direction (Fig. 5C). Combined magnetic lineament data from outside and inside the AIS (Fig. 5D) are in overall agreement with the magnetic lineament data for the wider NNW Paraná Basin (reprocessed data of Curto et al., 2014), which indicates a more prominent dispersion of lineaments around N40°–70°E, with a maximum at N60°–70°E (Fig. 5E).

Airborne gamma-ray spectrometry total count map

Our total count (TC) map of the AIS (Fig. 4) improves upon the previously available map (see Leite et al., 2022). Despite both TC maps showing a remarkable concentric pattern, our new map exhibits more uniform, smoother radiometric contours, without the "bull's-eye" artifacts. The previous TC map was built on data interpolated using the minimum curvature method, which commonly generates "bull's-eye" artifacts in airborne gamma-ray spectrometry data acquired in sedimentary basins with low radiometric signals, making the interpretation of gridded data difficult (see Silva et al., 2023). Moreover, the previous TC map shows prominent artifacts along the flight line, probably related to poor leveling and microleveling. Our approach of interpolating the TC data using the inverse distance weighting (IDW) method and applying filters to suppress directional trends and spurious peaks (see "Airborne geophysical data" section) proved effective in producing a map with a distribution of total count measurements that is more consistent with the geology of the Araguainha region (compare with the geological map of Fig. 2).

Concentric radiometric features are observed in airborne gamma-ray spectrometry data of some impact structures (see, e.g., Niang et al., 2021, and references therein). The first-order concentric radiometric patterns observed in the new TC map of the AIS result from the intercalation of low, medium, and high TC values (see Fig. 4). These distinct TC signatures are associated with specific geological units. The lower TC values (<180 cps) are predominantly associated with psammitic rocks (e.g., Aquidauana and Furnas formations), which are primarily composed of quartz and relatively poor in radioelements (Dentith and Mudge, 2014). In contrast, medium to high TC values (up to 450 cps) are generally related to geological units containing pelitic materials (e.g., Passa Dois Group and Ponta Grossa Formation). For example, the highest TC values are found in the

northeast, outside the AIS, where they are related to the regional occurrence of the Ponta Grossa Formation. (Fig. 2 and Fig. 4). As TC values show a positive correlation with clay content and U and Th contents (Taylor et al., 2002), the higher TC signature in these lithotypes is likely associated with the high phyllosilicate contents in these units.

In the outer rim region of the impact structure, the discontinuous concentric aspect of these medium to high TC signatures can be related to up to kilometer-wide, fault-bounded blocks of the Passa Dois Group (PDGBs; see Bernardes et al., 2025). The absence of this concentric TC signature in the eastern outer sector of the AIS ($R \sim 20$ km) makes it challenging to define the outer rim of the structure in this sector. Notably, this discontinuous, medium to high TC, discontinuous "ring" of PDGBs that highlights the apparent rim of the AIS is somewhat polygonal, with some relatively continuous and straight segments, e.g., in the NW, N, and SSE sectors, inter alia (Fig. 4).

In the collar of the central uplift, at R <10 km (inner black, dashed circle in Fig. 4), an inward change from medium-to-high TC to low TC marks the transition from the Ponta Grossa Formation (pelite-dominated) to the Furnas Formation (psammite-dominated) radiometric domains, respectively. Notably, this medium-to-high TC domain, which is related to the Ponta Grossa Formation collar, shows asymmetry. Its northern half is wider than its southern half.

In the core of the central uplift (black cross in Fig. 4), the highest TC values (>500 cps) are related to the Araguainha granite. This granite is rich in K-bearing minerals (K-feldspar megacrysts, biotite) and in U- or Th-bearing accessory minerals (e.g., zircon, oxides, and tourmaline) (von Engelhardt et al. 1992; Silva et al., 2016). Ground-based gamma-ray spectrometry surveys in the Araguainha granite revealed >4% $K_{(total)}$, 10–30 ppm eTh, and 3–10 ppm eU contents (Leite et al., 2022), which corroborates this radiometric-geological association. In addition, when visualizing the TC anomalies of the central region of the AIS (R <10 km), their shape resembles a polygon, with an overall major axis in the WNW-ESE direction (Fig. 4).

We note that it is not straightforward to relate a specific TC signature and shape with the (meta)sedimentary basement and impactite units that are distinguished in the geological map (Fig. 2). This may be due to the interplay between the more regional (i.e., less detailed) resolution of the TC data and the relatively smaller outcrop areas of these units. Moreover, the (meta)sedimentary basement and impactites in the AIS exhibit remarkable lithological variability (see Souza et al., 2024; Bernardes et al., 2025),

suggesting that their TC signatures may also be heterogeneous and blend with those of other geological units.

Radiometric lineaments

The radiometric contrasts observed in the TC map were used to interpret and extract (radiometric) lineaments. These lineaments are thought to be akin to fractures, faults, and/or contacts between different geological units.

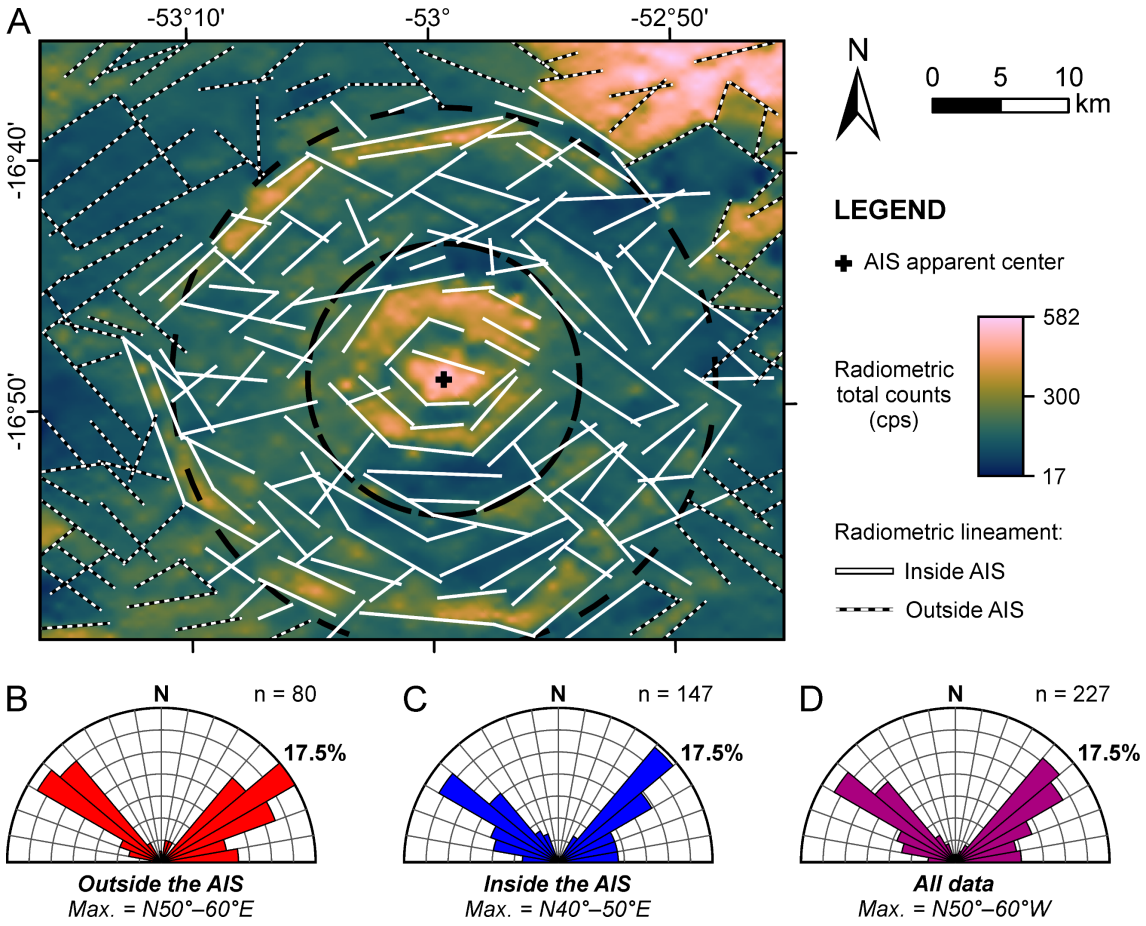

Figure 6. Interpreted radiometric lineaments from the radiometric total count map of the Araguainha impact structure and environs (Fig. 4). Black dashed circles are the same as in the previous figures. Inner circle has R = 10 km. Outer circle has R = 20 km. Note the distinction between lineaments inside (white) and outside (black and white dashed) the AIS area. B) Rose diagram for orientations of radiometric lineaments inside the AIS. C) Rose diagram for radiometric lineaments outside the AIS. D) Rose diagram for all (outside + inside the AIS) radiometric lineaments. The "n" symbol indicates the number of lineaments in each diagram. The percentage (%) indicates the frequency of the outer limit of each diagram. The trend range with maximum frequency is highlighted for each diagram.

Radiometric lineaments (n = 227) extracted from our total count map show a consistent trend, both outside and inside the AIS (Fig. 6A). Outside the AIS, there are two

predominant sets of lineaments: one trending N40°–70°E, with a maximum at N50°–60°E, and the other trending N40°–60°W, with a weak maximum at N50°–60°W (Fig. 6B).

Inside the AIS, there are two similar lineament trends, which, however, show somewhat less spread. One set is constrained at N40°–60°E, with a maximum at N40°–50°E, and the other set trends N40°–60°W, with a maximum at N50°–60°W (Fig. 6C). When combined, the bulk of the radiometric lineament data of the AIS region shows two, quasi-perpendicular major trends at N40°–60°E and N40°–60°W, with an overall maximum at N50°–60°W (Fig. 6D). Notably, there is a lack of any north-trending data, and only a very minor occurrence of radiometric lineaments trending in a roughly E-W direction.

Remote-sensing-derived structural lineaments

A four-interval, Jenks natural breaks classification (performed within ArcGIS Pro 3) of all extracted structural lineaments (n = 3487) from both outside and inside the AIS indicates the existence of quasi-balanced groups of lineaments trending in four standard directions, namely: ENE, NNE, NNW, and WNW (see Fig. 7 and its inset). Overall, structural lineaments outside the AIS have a major NE-SW orientation trend, with a considerable spread in this direction from N20°E to N80°E, and a maximum at N50°–60°E (see the "All sectors outside" rose diagram in Fig. 8). Lineaments trending NW-SE are also relatively common outside the AIS. They also have a substantial spread in orientations, but no distinct maximum. Structural lineaments trending N-S or E-W are not prominent outside the AIS.

However, when the structural lineament data from outside the AIS are analyzed by individual sector, more local trends can be distinguished (see gray-colored diagrams around the "AIS" diagram in Fig. 8). For example, the northern sector shows two distinct sets of lineaments, one trending N30°–40°E and the other N70°–80°E. In the eastern sector, although most common lineaments trend in a swath at N20°–70°E, another, more restricted set trending N20°–50°W is quite strong. In the southeastern sector, in turn, lineaments trending N20°–60°E (with a maximum at N40°–50°E) predominate, but a minor set trending at N40°–50°W also exists. In the southwestern sector, lineaments trending N50°–80°E are the most common, but a subordinate set trending N60°–70°W is also observed. A prominent observation is that the northeastern sector is unique in not

showing any preferred lineament orientation. This observation can be related to the lithologically and structurally distinct Ponta Grossa Formation present in this region (see Fig. 2; also, Bernardes et al., 2025).

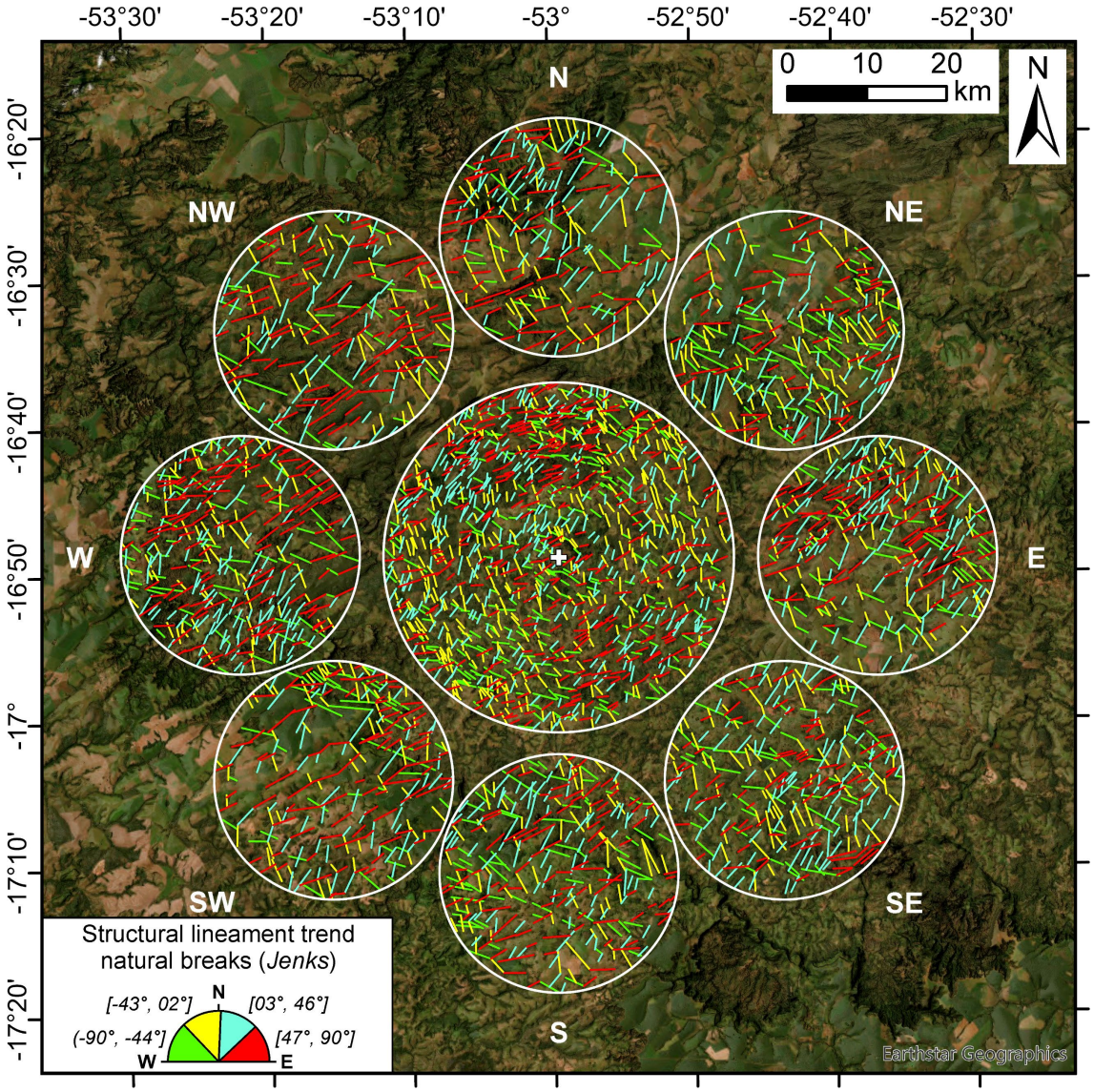

Figure 7. Structural lineaments (n = 3487) extracted from the remote sensing data. Remote sensing data include a TanDEM-X digital elevation model of the AIS region with vertical exaggeration (5:1) and some transparency superimposed onto a segment from Esri's World Imagery layer map service (Credits: Esri, Maxar, Earthstar Geographics, and the GIS User Community). See the "Materials and Methods" section. The inner white circle, with a radius of 22 km, delimits the lineaments extracted from within the Araguainha impact structure area (n = 1278). The white cross in the center of the figure marks the apparent center of the AIS. The eight smaller white circles around the AIS perimeter have a radius of 15 km each. They are distributed in (inter)cardinal directions to capture a comprehensive spatial distribution of lineaments (n = 2209). The structural lineaments are classified according to four natural breaks (Jenks) (see inset). The rose diagrams and statistical analysis of the orientations of the structural lineaments are presented in Fig. 8.

Structural lineaments inside the AIS domain show a wider spread of trends in all directions; however, two orientations are dominant in this large dataset (n = 1278): a broad trend at orientations of N20°–80°E, with a prominent maximum at N60°–70°E, and another trend at N00°–50°W, with a maximum at N20°–30°W (Fig. 8). In addition, structural lineaments trending N-S or E-W are the least common inside the AIS domain, as also observed for outside the AIS.

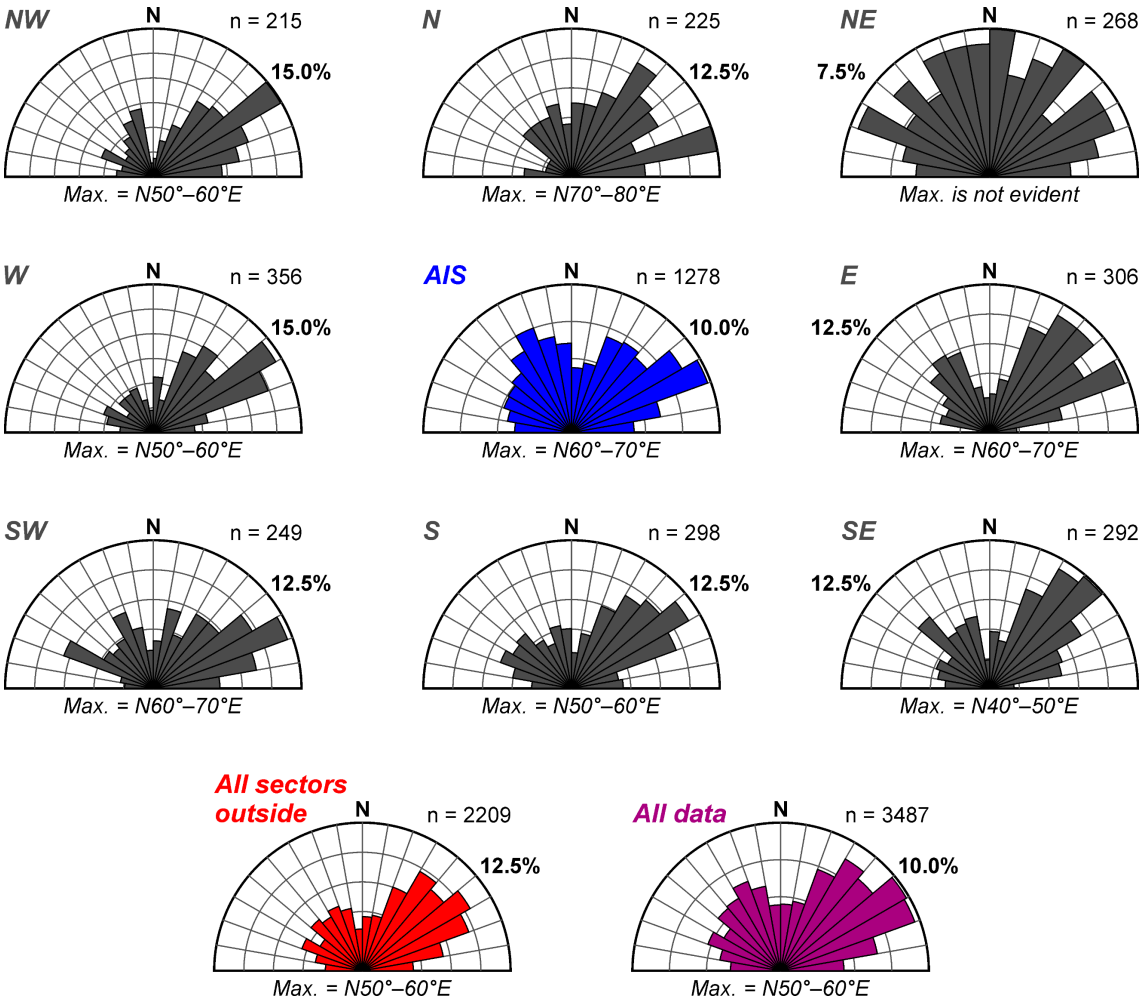

Figure 8. Rose diagrams with the trends of the orientations of remote-sensing-derived structural lineaments shown in Fig. 7. The "n" symbol indicates the number of lineaments in each diagram. The percentage (%) indicates the frequency of the outer limit of each diagram. The trend range with maximum frequency is highlighted for each diagram. The blue diagram in the center represents structural lineaments extracted from within the Araguainha impact structure. The red diagram represents orientations of all structural lineaments outside the AIS. Each dark gray diagram indicates lineaments from a bordering circular area outside the AIS in different (inter)cardinal directions (compare Fig. 7). The purple diagram (bottom right) compiles all the extracted structural lineaments. See text for details.

Structural observations from fieldwork

Structure observations in the geological units of the NNW Paraná Basin, including the environs around the AIS (Bernardes et al., 2025), indicate the occurrence of brittle (e.g., fractures, faults) and brittle-ductile (e.g., folds, shear bands) deformation, but with a predominance of the former (ibid; Curto et al., 2014). These brittle structures exhibit diverse trends, but fractures and faults trending in the NE-SW and NW-SE directions are the most common. In the wider NNW Paraná Basin, field data (n = 128; reprocessed data of Curto et al., 2014) indicate that brittle structures follow four principal trends: N50°–80°E, N20°–30°E, N00°–20°W, and N50°–70°W (see Fig. 9A).

In an extensive outcrop ~12 km outside the SW rim of the AIS (at 53.13283°W, 17.06358°S), at the MT-100 state road, fractures and faults trending NE-SW and NW-SE in red Aquidauana Formation sandstone are also the most prominent deformation features (Fig. 9B). The faults primarily exhibit steep dips, displaying either normal or reverse displacement on the meter scale. One of the reverse faults juxtaposed the Aquidauana Formation with the younger Corumbataí Formation sandstone (Passa Dois Group) (Bernardes et al., 2025). A rose diagram of fractures and faults (n = 58) for this outcrop shows the predominance of two sets of structures with distinct strikes: N60°–80°E and N10°–50°W (inset in Fig. 9B). No cross-cutting relationships could be identified between these fracture/fault sets.

At the NW outer rim of the AIS, also in the Aquidauana Formation, meter-spaced normal faults with steeply dipping planes (60°–70°SE) occur. These faults are interpreted as outer rim faults that were activated during the collapse of the impact structure during the modification stage of cratering (Bernardes et al., 2025). These faults strike approximately N50°–60°E (Fig. 9C). When analyzed in conjunction with remote sensing data, these faults strike (sub)parallel to the structural lineaments and the contact between the downfaulted outer block of the Passa Dois Group of this rim region (Fig. 9D).

Within the AIS, fractures and faults are also widespread. They occur with concentric, tangential, radial, or oblique orientations in relation to the apparent center of the AIS (Bernardes et al., 2025). Moreover, these authors showed that obliquely oriented fractures/faults – i.e., structures that deviate from the concentric and radial directions, which are commonly generated during the impact process – are more common than has been previously acknowledged (e.g., Lana et al., 2008). Fracture and fault data surveyed

in different parts of the AIS indicate that an overall NE-SW strike is most prominent for these structures.

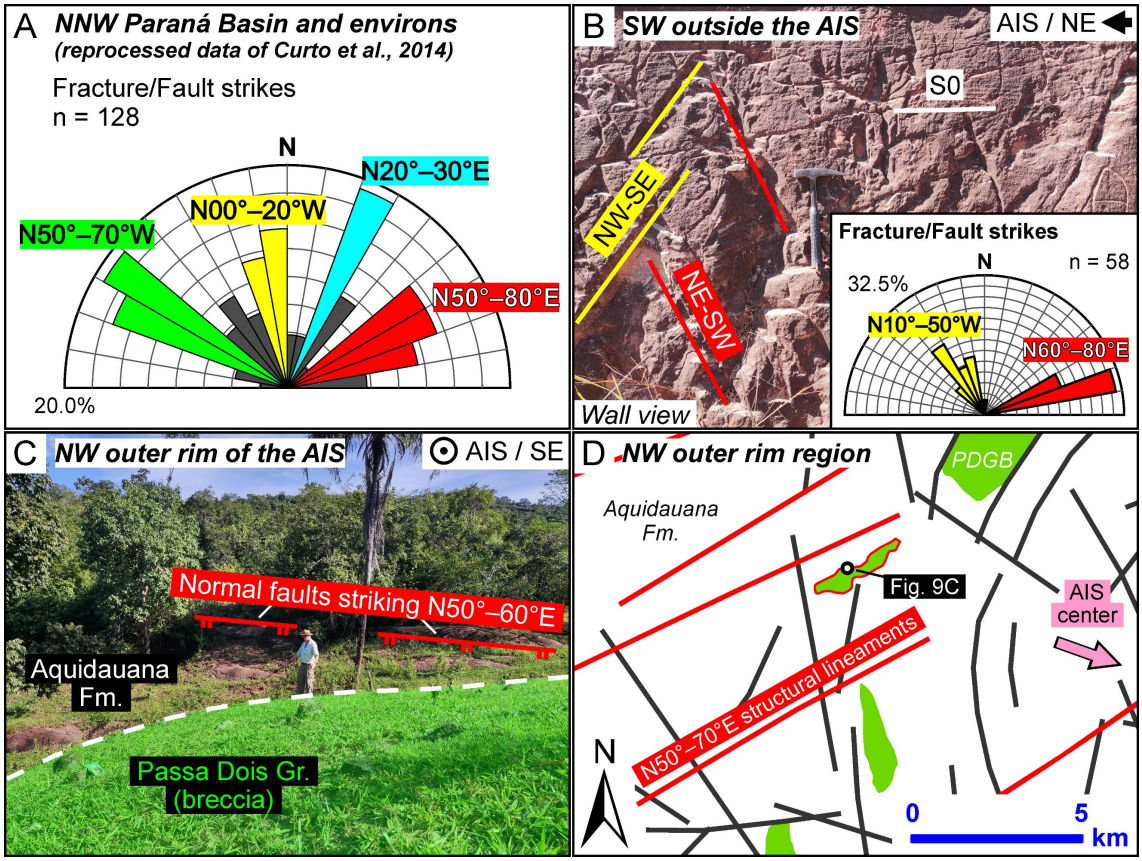

Figure 9. Field structural data for the AIS and its environs. A) Strike orientations for fractures and faults in the wider NNW Paraná Basin (reprocessed data of Curto et al., 2014). Note the four prominent, well-discriminated families of structure orientations. The "n" symbol indicates the number of lineaments in the diagram. The percentage (%) indicates the frequency of the outer limit of the diagram. B) Most prominent fractures/faults in an extensive Aquidauana Formation outcrop southwest of the rim of the AIS, at $R \sim 31.3$ km. Bedding (S_0) here is (sub)horizontal. Hammer for scale is 33 cm long. In the inset: note that the strikes of the two main families of structures occurring in this outcrop (NE-SW – red-colored and NW-SE – yellow-colored) are equivalent to the ones identified in the wider NNW Paraná Basin (compare Fig. 9B inset with 9A). C) An outcrop in the NW apparent outer rim of the AIS, at $R \sim 20.4$ km, depicting the contact between Aquidauana Formation and Passa Dois Group breccia. Person for scale is ~2 meters tall. Near the contact, several meter-spaced normal (rim) faults occur in the Aquidauana Formation. These faults, overall, dip 60°–70° obliquely inward to the AIS and strike N50°–60°E. These strikes are within the same range as the orientations of fractures/faults outside the AIS (see Fig. 9A, B). D) Geological map excerpt of the NW outer rim region of the AIS (after Bernardes et al., 2025; see Fig. 2 for a complete map). Thick, dark gray or red lines are remote-sensing-derived structural lineaments (ibid). The Passa Dois Group Block (PDGB) outlined in red on this map is the same as the one in Fig. 9C. Note how this PDGB orientation diverges from a truly concentric arrangement in relation to the apparent center of the AIS (pink arrow) and the other PDGB. Also note how the structural lineaments highlighted in red in the vicinity of this PDGB control its contacts with the Aquidauana Formation. Finally, note how the trends of these lineaments are equivalent to those for the fractures/faults striking N50°–80°E (red-colored set shown in Fig. 9A–C).

Numerical analysis of the (apparent) rim trace shape of the AIS

Our application of the Robbins and Riggs' (2023) algorithm to resolve the (apparent) rim trace shape of the Araguainha impact structure provided several insights. Notably, solutions that included shapes with any number of arcs to fit the AIS rim trace never converged to a single or a few specific shapes. The shapes with arcs obtained here differed significantly across runs, with the vertex points showing a spread along the entire rim trace in all tested scenarios (see, e.g., model "AIS-6-3" provided in Panel S1 of the Supporting Information). Furthermore, in almost all models that included arcs, straight sides with a rough E-W trend were more commonly placed into the northern and southern rim segments (ibid). But during repeated code runs, these same straight sides were frequently replaced by vertex points that initiated an arc. In summary, no consistent solution emerges from the arc-bearing models.

In contrast, most models with shapes featuring only straight sides (i.e., polygons with $N = 4–10$) tended to converge to a single or, at least, very few preferred solutions (see Panel S1). An exception was the 4-sided model, which did not yield a consistent solution and resulted in poor residual fits of 0.1200–0.1390 (i.e., the code-provided normalized area difference between the shape fit and the rim trace; dimensionless; see Robbins and Riggs, 2023). The 5-sided model is the one that visually yielded the fewest distinct solutions (see model "AIS-5-0" in Panel S1). However, despite showing a significant improvement in the residual fits compared to the 4-sided model, the residual fits of the 5-sided model (0.0653–0.0693) are still significantly larger than those of the 6- to 10-sided models (by at least ~18.1%; see below). Combined with a visual inspection of the resulting polygons (Panel S1), these observations indicate that the 4-sided and 5-sided models do not adequately represent the (apparent) rim trace shape of the AIS at the analyzed scale.

The 6- to 10-sided polygon models, however, exhibit a limited number of distinct solutions, with all cases displaying a preferred shape (see Panel S1). Their residual fits also tend to be sequentially smaller, despite some superposition: 0.0401–0.0535 (for the 6-sided model), 0.0295–0.0390 (7-sided), 0.0234–0.0388 (8-sided), 0.0199–0.0337 (9-sided), and 0.0192–0.0270 (10-sided model). Statistical analysis suggests that these five residual fit distributions are statistically significantly different from one another; thus, they should be treated as distinct solutions. It also shows a clear progression in the central tendency measures of the residual fits from the 6-sided results (highest) to the 10-sided

results (lowest). This indicates a pattern in which the polygon order tends to be inversely proportional to the residual fits.

However, a visual analysis of the 6- to 10-sided resulting polygon models reveals that, despite the 10-sided model showing a significant improvement in the residual fits against the 9-sided model (median improvement of ~13.2%), the preferred 10-sided solutions are virtually the same as those of the 9-sided model (compare models "AIS-9-0" and "AIS-10-0" in Panel S1). That is, one of the iterative vertices of the 10-sided model consistently merges with one of the other nine vertices during successive Monte Carlo iterations. This behavior objectively indicates that the 10-sided model is an overparameterized solution for the studied Araguainha rim trace shape. Moreover, it also suggests that the 9-sided polygon model (AIS-9-0) may be the best solution to this shape-fitting problem. Therefore, we have discarded the 10-sided polygon as a candidate model.

The conundrum now is to objectively determine which polygonal model among the remaining options (i.e., the 6- to 9-sided ones) best represents the rim trace shape of the AIS. If we were to select the optimal solution based solely on the code's residual fits, the enneagon (the 9-sided polygon) would be the preferred choice. However, to comprehensively resolve shape-fitting problems like the one addressed here, ideally, a trade-off between the goodness-of-fit and the need for a sufficient number of free parameters (i.e., the polygon order) should be evaluated (see Robbins and Riggs, 2023). The candidate model that most effectively balances these two features would then represent the "best" rim trace shape for the AIS at the scale of our analysis and input dataset. Unfortunately, Robbins and Riggs' (2023) code does not include an additional tool to make such an assessment, although they discuss the possibilities and implications of this matter in their work.

Here, we independently used an additional metric to evaluate and compare the candidate models quantitatively – the Bayesian Information Criterion (BIC; Schwarz, 1978). The BIC is a model-selection criterion that balances the trade-off between goodness-of-fit and model complexity (i.e., the number of free parameters; see Table 1), while also penalizing more complex models (see Schwarz, 1978; Robbins and Riggs, 2023, and references therein). The lower the BIC score (which can be negative) of a model, the more preferred this model should be.

To maintain an objective approach, we evaluated only a single polygon for each of the (6- to 9-sided) candidate models – specifically, the solution with the lowest code-

provided residual fit among the 100 generated solutions for each model. Table 1 presents the results of the BIC score calculations. It shows that, despite being the highest-order (and thus more complex) polygon among the candidates, the irregular enneagon model (AIS-9-0) is still identified as the best model for describing the AIS (apparent) rim trace in the analyzed scenario (see Fig. 10).

TABLE 1. RESULTS OF STATISTICAL METRICS AND RANK OF EACH CANDIDATE MODEL FOR THE BEST SOLUTION FOR THE ARAGUAINHA IMPACT STRUCTURE (APPARENT) RIM TRACE SHAPE

Polygon model	No. of sides (N)	Residual fit (code-provided)	No. of free parameters ($k = 2 \cdot N + 1$)	BIC (Bayesian Information Criterion)	Model rank
AIS-6-0	6	0.0401	13	-941.6	4th
AIS-7-0	7	0.0295	15	-1006.8	3rd
AIS-8-0	8	0.0234	17	-1071.4	2nd
AIS-9-0	9	0.0199	19	-1081.4	1st

Note: The smaller the BIC score, the more favored the model should be.

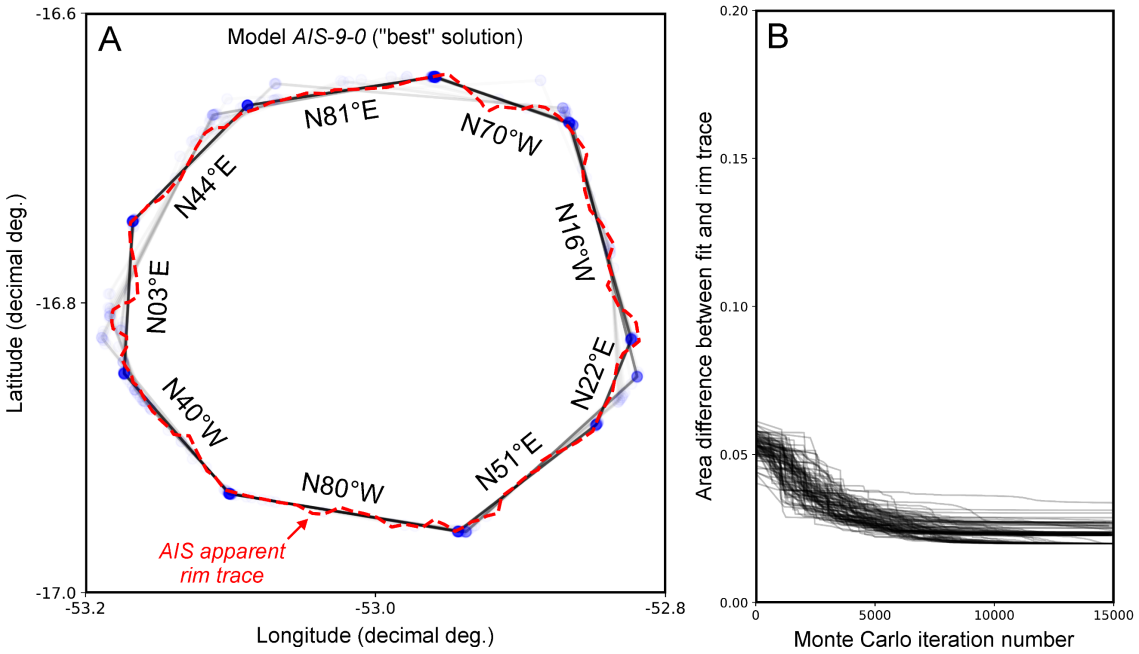

Figure 10. A) The 9-sided polygon (irregular enneagon) model that emerged as the "best" solution (more prominent straight black lines) to represent the apparent rim trace shape (red dashed line) of the Araguainha impact structure on the regional scale of our data analysis (1:50,000). Here, 100 code solutions (black lines) were plotted with some level of transparency. The more common solutions overlap, increasing the visual prominence of the preferred shape. Blue dots represent the minimized locations of the vertex points of the tested 9-sided polygons. The bearing (trend) of each straight side of the irregular enneagon with the least residual fit among the 100 solutions is shown within the polygonal area. B) The resulting minimized residual fits (area difference between fit and rim trace) of the 9-sided polygon model after several successive iterations. See text for details.

DISCUSSION

The nature of lineaments in the Araguainha impact structure (AIS) region

Table 2 summarizes the general orientations of the different lineament sets and structural field data analyzed in this study. This overview shows that lineaments trending NE-SW and NW-SE are the most common in the Araguainha impact structure and its immediate surroundings. Overall, these results agree with previous regional lineament studies in the Paraná Basin (Zalán et al., 1990; Pinto and Vidotti, 2019), especially in the NNW part of the basin (Curto et al., 2014), including the AIS region (Theilen-Willige, 1981).

The AIS is located within the "Bom Jardim" magnetic domain of the NNW Paraná Basin (Curto et al., 2014). These authors describe this domain as a transitional crustal block beneath the NNW Paraná Basin, constrained between the Transbrasiliano Lineament (TBL) and the Baliza lineament (see Fig. 1). This domain incorporates magnetic signatures from both the Paraguay Belt (PyB) and the TBL (Curto et al., 2014).

More detailed observations can be made about the nature of the analyzed lineaments and their relationships with the AIS, as each lineament type (magnetic, radiometric, and structural) provides different information about the depth, scale, and characteristics of the geological features associated with it. Overall, magnetic lineaments reveal the larger, deeper features in our study, whereas radiometric and structural lineaments provide more shallow information about the structural framework of the wider AIS region.

Regional geophysical airborne magnetic matched-filter analysis indicates a depth of 15 km for the deepest magnetic anomalies in the Bom Jardim crustal domain (Curto et al., 2014). These authors also calculated an average depth of 20 km for the top of the deepest level of magnetic anomalies in the entire NNW Paraná Basin, i.e., to the west of the TBL (see Fig. 1). Moho discontinuity depths in this part of the Paraná Basin range from approximately 36 km to 41 km, based on the seismological Moho model by Lima et al. (2024). These observations collectively suggest that the deeper magnetic framework of the NNW Paraná Basin, which includes the AIS region, extends at least throughout the entire upper crustal depth profile.

TABLE 2. SUMMARY OF THE PREDOMINANT DIRECTIONAL DATA TRENDS OBTAINED IN THIS STUDY

Dataset type	n*	Outside the AIS	Inside the AIS	AIS region (outside + inside)	Wider NNW Paraná Basin†
Magnetic lineament	250	N50°–60°E	N50°–60°E	N50°–60°E	N40°–70°E (max. at N60°–70°E)
Radiometric lineament	227	N40°–70°E (max. at N50°–60°E) N40°–60°W (max. at N50°–60°W)	N40°–60°E (max. at N40°–50°E) N40°–60°W (max. at N50°–60°W)	N40°–60°E (max. at N40°–50°E) N40°–60°W (max. at N50°–60°W)	n/a§
Structural lineament (derived from remote sensing)	3487	N20°–80°E (max. at N50°–60°E)	N20°–80°E (max. at N60°–70°E) N00°–50°W (max. at N20°–30°W)	N20°–80°E (max. at N50°–60°E) N10°–50°W (max. at N20°–30°W) N60°–70°W	n/a
Structural field data (fractures and faults)	186	N60°–80°E N10°–50°W	Highly variable: Concentric, tangential, radial, and oblique.# But NE-SW trends predominate.	n/a	N20°–30°E N50°–80°E N00°–20°W N50°–70°W

*n = number of data points.

†Reprocessed data of Curto et al. (2014).

§n/a = not applicable.

#Regarding the AIS apparent center (see Bernardes et al., 2025).

The analysis of the Euler solution map for the AIS region (Fig. 5A) reveals that magnetic lineaments mainly trend NE-SW. The sedimentary pile of the Paraná Basin near the AIS region is probably no thicker than 1.9 km (based on the 2-AG-1-MT borehole data; see Thomé Filho et al., 2012). Moreover, as the sedimentary pile of the basin thins from the borehole toward the northeast, in the direction of the AIS (see Cordani et al., 2016), its thickness is likely <1.5 km, as also suggested by gravity data modeling within the AIS (Vasconcelos, 2007). Thus, we can infer that some magnetic lineaments are located above the basement – i.e., within the basin, at depths <1.5 km –, whereas most extend into the basement, at depths of 1.5 km or more (see Fig. 5A). The magnetic signature of the lineaments is obscured in the SW imaged area by higher-frequency (Fig. 3C), shallow anomalies (Fig. 5A). As previously mentioned, this interference results from the Early Cretaceous Serra Geral Group igneous rocks exposed in the region (see geological map; Fig. 2).

Previous regional geophysical studies have suggested that the overall NE-SW-trending lineaments in the wider NNW Paraná Basin are structures associated with the PyB and the TBL (Curto et al., 2014, 2015; Pinto and Vidotti, 2019). The primary TBL magnetic trend in the NNW Paraná Basin is ~N30°E, whereas the PyB trend is mainly N60°–70°E (Curto et al., 2014). This PyB magnetic trend is corroborated by structural data (e.g., axial planar foliation of isoclinal folds) from the northern Paraguay Belt, which show a dominant N60°E strike direction (e.g., Manzano et al., 2008).

Our results (see Table 2) indicate that magnetic lineaments in the wider NNW Paraná Basin have a notable trend between N40°E and N70°E, with rare instances reaching approximately N30°E, and mainly at N60°–70°E orientations (Fig. 5E; reprocessed data of Curto et al., 2014). More locally, in the AIS region, they dominantly trend at N50°–60°E, both within and outside the AIS (see Fig. 5B–D). These main magnetic trends (ranging from N50°E to N70°E) closely align with the dominant NE-SW radiometric (N40°–60°E; see Fig. 6) and structural (N50°–60°E; see the "All data" diagram in Fig. 8) lineament trends observed in the AIS region, as well as with the strikes of a major fracture/fault set seen regionally along the wider NNW Paraná Basin (see the red-colored set in Fig. 9A), and both outside (red-colored set in Fig. 9B) and within (red-colored set in Fig. 9C, D) the AIS – the overall N50°–80°E trend. From these findings, we infer that these NE-SW-trending lineaments, identified across various sources and at different depths, share a common origin.

We propose that the most prominent and deep magnetic lineaments in the AIS region, i.e., those trending mainly N50°–60°E (Fig. 5A–D), primarily originate from the tectono-structural framework created by the evolution of the Paraguay Belt during the Neoproterozoic–Cambrian orogenic event. This PyB structural framework was then imprinted in the overlying units of the NNW Paraná Basin by regional brittle tectonic reactivations since the early Phanerozoic (Zalán et al., 1990).

As mentioned earlier, in the NNW Paraná Basin, the ~N30°E direction is commonly associated with structures related to the Transbrasiliano Lineament corridor, which is hundreds of kilometers wide (Curto et al., 2014). Although geological features with a roughly N30°E trend appear in the magnetic (Fig. 5E) and fracture/fault (cyan-colored set in Fig. 9A) directional data of the wider NNW Paraná Basin (also Curto et al., 2014), they are generally of lesser significance in the AIS region, neither standing out in the magnetic data (see Fig. 5A–D) nor in the radiometric lineament data (Fig. 6). However, it is notable that structural lineaments trending about N30°E are quite common to the east and southeast of the AIS (see "E" and "SE" diagrams in Fig. 8).

The E and SE sectors in the AIS region are the closest to where the main faults of the TBL occur, approximately 60 km to the E-SE of the AIS (see Fig. 1). Therefore, this may indicate that the tectono-structural framework of the TBL may have only substantially affected the eastern part of the AIS. Moreover, the fact that this TBL directional signature in the AIS region is seemingly only evident in the structural (remote-sensing-derived) lineaments (Figs. 7 and 8) – which were extracted at a more detailed scale (see "Materials and Methods" section), and thus provide higher resolution information from the surface – suggests that the TBL overprint in the AIS region is of a less-spaced (more penetrative) and probably more shallow-natured when compared to the PyB structural signature.

The overall NE-SW-trending structural lineaments display a notably broader directional range (N20°–80°E; see the "All data" diagram in Fig. 8). However, despite being extracted at a more detailed scale, they mainly maintain a trend similar to the magnetic and radiometric maxima in the AIS region (see Table 2), suggesting a strong structural influence from the brittle-reactivated trend of the PyB even within the NNW Paraná Basin. Furthermore, as the AIS area lies within the Bom Jardim magneto-structural crustal domain that is influenced by the major trends related to both the PyB and TBL (Curto et al., 2014), the broader directional spread of the structural lineament

data observed in this area can be attributed to two factors: (1) the higher resolution of the lineament extraction (1:50,000), which (2) reveals a superposition (i.e., an interplay) of the PyB and TBL structural trends present in parts of this domain.

In contrast, the nature of the NW-SE lineaments in the AIS region is less constrained. Regional field data indicate that there are two very distinct sets of overall NW-SE-trending fractures/faults in the wider NNW Paraná Basin: N50°–70°W and N00°–20°W (green- and yellow-colored sets in Fig. 9A, respectively). Curto et al. (2014) suggested that the former set is related to Cretaceous extensional reactivation (expanded below), but these authors do not discuss the nature of the latter (N00°–20°W) set. Some possibilities we suggest are that this latter set may have a conjugate relationship with the main structural trend of the Paraguay Belt, or, alternatively, may be related to regional structures imprinted by the evolution of the Neoproterozoic Goiás Magmatic Arc, which crops out approximately 100 km northeast of the AIS, close to the TBL (see "GMA" in Fig. 1). Notably, and more locally, in the surroundings of the AIS, a spread of strikes (N10°–50°W) between the two sets occurs (see inset in Fig. 9B) and may suggest an interplay between them. However, with the current regional structural inventory, these structural relationships cannot be fully verified.

We note that, in the AIS region, NW-SE lineaments are more typically detected in the shallower (e.g., radiometric; Fig. 6) and more detailed (remote-sensing-derived; Fig. 8) datasets but are somewhat less evident in the magnetic data (Fig. 5A–D). This may indicate a predominantly non-magnetized, shallower nature for the structures related to them, unlike the lineaments that trend NE-SW. The rarer NW-SE magnetic lineaments in the AIS region seemingly reach the same depth range as the NE-SW ones (Fig. 5A). However, we were unable to observe cross-cutting relationships between these sets from our magnetic data of the AIS region. Also, cross-cutting relationships were not observed in the field data with respect to the NE-SW- and NW-SE-striking fractures/faults in the AIS and its environs (e.g., Fig. 9B).

On the other hand, a previous geophysical study in the wider NNW Paraná Basin showed that the NW-SE-trending magnetic lineaments disrupt and displace the NE-SW lineaments (Curto et al., 2014). However, this does not rule out the possibility that both the NE-SW and NW-SE structures are originally cogenetic, meaning both are older than the AIS. That is, the two sets of NW-SE structures may be related to – and as old as – the NE-SW ones (i.e., PyB and TBL), but with at least the N50°–70°W-trending set (see Fig.

9A) being reactivated more recently. This is supported by observations by Curto et al. (2014), who suggested that ongoing seismic activity in the region occurs subparallel to lineaments trending in this NW-SE direction and that these are somewhat aligned with Cretaceous volcanic rocks and alkaline intrusive bodies.

Additionally, we note that the N50°–70°W direction, which appears as fractures and faults in the wider NNW Paraná Basin (Fig. 9A), as well as lineaments in the AIS region (see, e.g., Fig. 6), closely aligns with the general trend of the "125°-Azimuth Lineament." This suggests a possible relationship between these structures. The 125°-Azimuth Lineament is an ~1000-km-long and ~70-km-wide structural feature, comprising an extensive network of NW-SE-oriented, sinistral faults and dikes that occur adjacent to the northern part of the Paraná Basin and cut through various tectonic units of the basin's basement (see Moraes Rocha et al., 2014; and Moraes et al., 2021, for an overview). It is believed that this lineament formed during the Brasiliano orogenic cycle (Neoproterozoic–Cambrian) and was reactivated during Cretaceous times (Moraes Rocha et al., 2014); however, its interplay with the TBL remains poorly understood (Moraes et al., 2021). Thus, its possible influence on the AIS region needs further investigation.

Nonetheless, as the AIS impact event is older (ca. 259–252 Ma; Tohver et al., 2012; Erickson et al., 2017; Hauser et al., 2019) than the Cretaceous period (ca. 143–66 Ma), the observations above may suggest that some of the NW-SE-trending lineaments could have been reactivated after the Araguainha impact event. However, the magnitude and extent of this reactivation, as well as whether it has reached and left any morphostructural imprint on the AIS, remain unresolved. Nevertheless, more multidisciplinary studies are needed to better understand the nature of the NW-SE-oriented structures in the wider NNW Paraná Basin and its surroundings.

Implications from lineament analysis for the first-order morphostructure of the AIS

The overall orientation of the different lineament types remains fairly consistent inside and outside the AIS (see Table 2). However, in the structural lineament dataset (i.e., the more detailed one), the Araguainha impact event seems to have conditioned and balanced the frequency between lineaments trending NE-SW and NW-SE (compare the "AIS" with "All sectors outside" diagrams in Fig. 8). This suggests that NE-SW structures were more reactivated, whereas more NW-SE shallow structures were newly formed within the AIS.

The NE-SW-trending magnetic lineaments, along with the somewhat less prominent NW-SE magnetic lineaments, appear to control the shape of two larger and more irregular magnetic anomalies located beneath the outer parts of the AIS (at $R \geq 10$ km) and at depths ≥3 km, which are related to the basement beneath the Paraná Basin (see tags "1" and "2" in Fig. 5A). These magnetic anomalies can also be associated to the anomalies in the same area of the total gradient amplitude (TGA) of the magnetic anomalies map (see Fig. 3C). We interpret these anomalies as intrusive igneous (likely granitic) bodies associated with the evolution of the regional basement related to the Paraguay Belt. These buried intrusions may represent a lateral extension of the Cambrian Araguainha granite (ca. 510 Ma; Tohver et al., 2012), which crops out in the central part of the structure, or other granitic bodies also associated with the post-orogenic Serra Negra suite (see, e.g., Lacerda Filho et al., 2004). Additionally, at $R > 10$ km from the apparent center of the AIS, these two intrusions were likely not excavated or significantly displaced during the excavation stage of the Araguainha impact event – which has exhumed the basin's basement in the central part of the AIS by removing supracrustal units by no more than ~1.9 km (Souza et al., 2024) within a transient cavity of possibly 20 km diameter (Bernardes et al., 2025).

Our analysis shows that lineament sets in the AIS area influenced the morphological and structural development of the impact structure. At $R \leq 10$ km – i.e., within the region proposed by Bernardes et al. (2025) as the maximum extent of the central uplift region – even the deep, predominantly NE-SW-trending magnetic framework nearly vanishes. In this area (see inner circle in Fig. 5A), the Euler solution map displays very shallow solutions (hot colors), except in the SE sector, where a NE-SW-trending, deep magnetic lineament remains. To explain this framework, we suggest that the formation of the central uplift during the transition from the end of the excavation stage to the modification stage of cratering (see Melosh, 1989) was able to overprint most of the preexisting, first-order NE-SW-trending structural framework related to the PyB and the TBL at a radial distance of up to approximately 10 km from the apparent center of the structure. This interpretation of the Euler solution map for $R \leq 10$ km supports Bernardes et al.'s (2025) morphostructural hypothesis that the central uplift of the AIS likely extends to a maximum of 10 km from the center of the structure.

In addition, the recent work on gravity anomaly modeling of the AIS by Miyazaki et al. (2021), which focused solely on the central uplift area, did not acknowledge or

discuss structural asymmetry in this feature. Our Euler solution map (Fig. 5A), however, indicates that the uplift of the AIS central region is not of a symmetrical circular shape. As we have pointed out, the SE sector at $R \leq 10$ km still exhibits the same deep, NE-SW magnetic lineament trend present at larger radial distances (see Fig. 5A). This finding indicates that the uplift of the central AIS area was asymmetric and might have been, to some extent, influenced by the preexisting structural framework of the target crust.

An asymmetric central uplift for the AIS has been previously proposed based on remote sensing observations and structural field data (Lana et al., 2008; Bernardes et al., 2025); however, it has remained unclear whether the asymmetry was generated during the formation of the central uplift or only during its collapse (see Bernardes et al., 2025). The preservation of the pre-impact structural framework in the SE sector of the central uplift region (Fig. 5A) attests that the structural asymmetry originated with the formation of the central uplift; otherwise, the impact would have erased this deep, NE-SW-trending, preexisting magnetic feature in the SE sector, and a roughly circular, shallow magnetic signature of the central uplift would likely have emerged.

We also note that the western sector of the outer AIS, beyond the central uplift ($10 \text{ km} < R \leq 20 \text{ km}$), lacks deep magnetic lineaments and has relatively shallower Euler solutions compared to most other sectors (see Fig. 5A). Gravity anomaly modeling (Vasconcelos, 2007) across various sectors within the outer AIS shows an asymmetric interface with varied topographies (depths) between the Paraná Basin sequences and the crystalline-(meta)sedimentary basement beneath the basin. Whether the complex topography of this interface results from an oblique impact and/or from a pre-impact configuration of the target remains to be investigated further.

In summary, Bernardes et al. (2025) proposed that at least part of the structural asymmetry of the AIS can be explained by a heterogeneous target whose anisotropy was created before impact and influenced by fracture/fault sets and rheological contrasts within Paraná Basin sequences. Our lineament analysis supports this hypothesis regarding the influence of pre-impact fractures and faults in the impact target (see the first part of the “Discussion” section).

Araguainha impact structure: The remnant of a polygonal impact crater

The results of our numerical shape-fitting analysis indicate that arc segments are not effective in accurately representing the rim trace of the AIS (see the last part of the

"Results" section). This was already, to some extent, visually noticeable when considering a 20-km-radius circle centered at what we estimate as the apparent center of the structure (Fig. 2). We note that a quasi-perpendicular pair of NE-SW and NW-SE trends (Table 2) emerges from the dominant radiometric lineament directions extracted from the TC map (see Fig. 6). This quasi-perpendicular geometry appears to significantly influence the large-scale morphology of the apparent outer rim outline of the AIS and its fault-bounded Passa Dois Groups Blocks (Figs. 2, 6A, and 9D). The eastern sector of the outer rim region, however, is more eroded, lacking prominent Passa Dois Group Blocks (Bernardes et al., 2025). Still, NE-SW and NW-SE radiometric lineaments are commonly observed in this sector of the AIS, indicating that the structural features (i.e., fractures and faults) associated with these lineaments are widespread and somewhat penetrative. It is also notable how this quasi-perpendicular pair of lineament trends also imprints polygonal shapes on the radiometrically contrasting units of the central uplift of the AIS, almost resembling the shape of the apparent outer rim trace of the structure, with a more elongated direction at WNW-ESE (see Fig. 6A).

The best candidate shapes modeled for the AIS involve polygons with six to nine sides (see "Results" section). Our results have shown that, of the tested models, an irregular 9-sided polygon is the best solution to fit the AIS (apparent) rim trace shape at the scale of our analysis (Fig. 10). It must be clear, however, that we are not affirming that the AIS is undoubtedly of enneagon shape. This result must be taken as a scale-dependent, probabilistic finding. In other words, at the scale of our regional analysis (1:50,000), the rim trace of the Araguainha impact structure appears to be best modeled by an irregular enneagon. More local rim trace features, such as the undulating bulges in the W and NNE sectors (see Fig. 10A), may likely be explained by impact-related radial (to oblique) faults that directionally displaced portions of the outer rim during the final stage of crater formation (see Lana et al., 2008; Bernardes et al., 2025).

Furthermore, it is mathematically intuitive to think that any higher-order (N >9) shape with only straight sides would also achieve a more improved fit than any of its predecessors, implying that the higher the polygon order, the better. However, this is not objectively practical, as rim trace shape fitting is a physical, scale-dependent problem that can be approached in a manner similar to the "infinite coastline paradox" (e.g., Mandelbrot, 1967). In general, if a more regional-scale analysis is needed, the increase of polygon order may induce an overparameterization of the model (as we have shown for

the 10-sided polygon model tested; see “Results” section), which, in turn, is contrary to good scientific practice (“Occam’s Razor” principle). Overparameterization of the rim trace shape will likely also lead to a loss of the model's physical meaning, preventing discussion of its possible connections to regional geological and tectonic features. Therefore, the irregular enneagon shape remains a sufficient solution for the AIS in the studied scenario.

Notably, seven out of the nine straight sides of the resulting “best” polygonal shape for the AIS are (quasi-)parallel to the orientation range of at least one of the prominent trends established by the analyzed lineament and field data (compare Fig. 10A with Table 2). This, along with the objective fact that a polygon adequately represents the (apparent) rim trace shape of the AIS in plan view, suggests, in itself, that these are not spurious observations. Instead, they indicate that a target with a significantly pre-structured (anisotropic) framework influenced the formation and resulting polygonal shape of the Araguainha impact structure. Otherwise, an isotropic (or isotropically behaving; see Fulmer and Roberts, 1963) target would have favored the formation of a circular impact structure (see Melosh, 1989).

Bernardes et al. (2025) recognized the influence of preexisting structures (e.g., fractures, faults) in the structural evolution of the AIS. They have suggested that regional structures related to the Paraguay Belt and the Transbrasiliano Lineament structural framework in the AIS region were the main features responsible for this structural control. Indeed, our lineament analysis (see the first part of the “Discussion” section) provides more quantitative and regional support for this interpretation. We have shown, however, that it is actually the structural trend of the Paraguay Belt (mainly N50°–70°E) in the wider NNW Paraná Basin that played the major role in influencing the first-order morphostructure of the AIS, with the Transbrasiliano Lineament trend (~N30°E) – or also their interplay – playing a secondary role. Some of the best examples of this premise are the NW and SE straight rim trace segments of the AIS, which trend N44°E and N51°E, respectively, and are somewhat parallel to the PyB and TBL structural trends or their interplay (compare Fig. 10A with Table 2). Eppler et al. (1983) demonstrated that the orientations of lunar tectonic structures are commonly parallel to the straight rim segments of polygonal impact craters in their vicinity. Following our results and observations, we propose that the AIS is the (eroded) remnant of a polygonal impact crater.

A polygonal impact crater (PIC) is a type of crater with a shape that differs from a circle in plan view due to structural control exerted by preexisting target heterogeneities (see, e.g., Öhman et al., 2010). It has been shown that the straight rim segments of PICs may form parallel (most common) or have an offset of 45° with the trend of the preexisting controlling structures (see table in Fobert et al., 2025, and references therein). They are also thought to form through two different mechanisms: one occurring during the excavation stage of cratering (e.g., Öhman, 2009), and the other during the modification stage (e.g., Schultz, 1976). Eppler et al. (1983), Öhman (2009), and Fobert et al. (2025) present more precise formulations of these two mechanisms, distinguishing them into up to four models that involve both simple and complex craters. Additionally, some PICs may have formed through a combination of both mechanisms (Eppler et al., 1983).

Our morphological and structural data (also Bernardes et al., 2025) suggest that the modification stage was likely the most critical in shaping the polygonal form of the AIS, as the downfaulted blocks of Passa Dois Group – the first-order morphostructural features that highlight the polygonal rim trace of the AIS (see Figs. 2, 4, and 9D) – were formed during this stage due to the collapse of the crater walls (see Bernardes et al., 2025). Furthermore, our modeling of the AIS (apparent) rim trace indicates that all nine rim segments of the structure can be accurately represented with straight segments (Fig. 10A). This is a relatively rare case for PICs (Öhman et al., 2010) and may imply that, prior to the impact, the Araguainha target had a somewhat optimized anisotropy relative to the impact parameters – an anisotropy which was likely created by a cohesive target material with appropriate fracture/fault spacing and penetrativity (see Fulmer and Roberts, 1963) – and which may have enhanced the resulting polygonality of the AIS.

Some might argue that, as the AIS is a somewhat eroded structure (see Lana et al., 2007; Osinski et al., 2022; Bernardes et al., 2025), its erosion could have increased the observed polygonality; however, counterintuitively, erosion usually softens a polygonal crater rim outline rather than accentuating it (Öhman et al., 2010, and references therein). Therefore, it is more likely that the pristine Araguainha impact structure would have appeared even more polygonal than it does today.

CONCLUSIONS

Different types of lineaments – magnetic, radiometric, and structural – have been studied within the Araguainha impact structure (AIS) region and across the wider NNW Paraná Basin. These lineaments provide information at various observational scales and depths. They can be linked to older tectonic features that predate the impact event and are examined in the context of their role in the formation of the AIS.

Our main findings include:

- NE-SW lineaments are the dominant structural features in the AIS region, both within and beyond the impact structure. NW-SE lineaments are also significant, but their tectonic nature remains unclear and warrants additional field data and structural analysis.
- Lineaments in the AIS region and the wider NNW Paraná Basin occur at varying depths and primarily trend N50°–70°E, reflecting the main structural orientation of the Neoproterozoic–Cambrian Paraguay Belt. Subordinate NE-SW lineaments (~N30°E) correspond to the Transbrasiliano Lineament and/or result from its interaction with the Paraguay Belt structures.
- The various lineament sets in the AIS region, which can be associated with pre-impact fractures and faults, influenced the morphological and structural evolution of the Araguainha impact structure.
- Two deep and extensive magnetic anomalies with complex geometries, outlined by NE-SW and NW-SE lineaments, occur in the northern and eastern outer AIS regions ($R \geq$~10 km). We interpret these features as granitic intrusions in the upper crust, associated with the Cambrian evolution of the Paraguay Belt.
- The central uplift of the AIS is asymmetric, having largely overprinted the preexisting lineament structural framework within about 10 km of its center. However, the preservation of a major pre-impact lineament in its southeastern sector indicates that the asymmetry developed during the formation of the central uplift.
- At the analyzed scale, the (apparent) outer rim trace shape of the Araguainha impact structure is best characterized as an irregular (asymmetric) nine-sided polygon.

- Seven of the nine sides of the irregular enneagon align closely with major lineament and field data trends in the AIS region and the wider NNW Paraná Basin. The structural trend of the Paraguay Belt played the most significant role in shaping the first-order outline morphology of the AIS.
- The Araguainha impact structure is the remnant of a polygonal crater formed by an impact on a mixed sedimentary-crystalline target exhibiting preexisting lateral anisotropy, such as fractures and faults. The modification stage of cratering likely played a key role in developing the AIS's polygonal shape.
- Our findings do not rule out the possibility that an oblique impact may have also contributed to shaping the AIS. This topic still requires further investigation.

Acknowledgments

This work is part of R. B. Bernardes' Ph.D. project in the Postgraduate Program in Geology at the Institute of Geosciences, University of Brasilia. This study was financed in part by the Coordenação de Aperfeiçoamento de Pessoal de Nível Superior – Brasil (CAPES) – Finance Code 001. The authors thank the University of Brasilia and the Institute of Geosciences for providing part of the infrastructure and conditions required to conduct and complete this research, including an Esri ArcGIS Pro academic user license and a sabbatical research leave to Bernardes. We also thank the Brazilian Nuclear Energy National Committee (CNEN) for granting permission to use the airborne geophysical data presented here for academic purposes. Manfred Gottwald and the German Aerospace Center (DLR) are thanked for providing access to the TanDEM-X digital elevation model of the Araguainha impact structure. Bernardes acknowledges financial support from a research grant from the Barringer Family Fund for Meteorite Impact Research. Bernardes is grateful to Marco Ianniruberto (IG–UnB) for his support during part of this work. Reimold and Hauser have been supported by the Brazilian National Council for Scientific and Technological Development (CNPq) through fellowship grants (Nos. 305761/2019-6 and 309878/2019-5, and 307109/2023-2, respectively). Gibson acknowledges the National Research Foundation of South Africa (Grant No. SRUG200503519568).

REFERENCES CITED

Almeida, F.F.M., Hasui, Y., Brito Neves, B.B., and Fuck, R.A., 1981, Brazilian structural provinces: An introduction: Earth-Science Reviews, v. 17, p. 1–29, doi:10.1016/0012-8252(81)90003-9.

Amaral, W.S., Kraus, R.K., Dantas, E.L., Fuck, R.A., and Pitombeira, J.P.A., 2017, Sinistral reactivation of the Transbrasiliano Lineament: Structural and geochronological evidences in the Cariré Granulite Zone, Borborema Province – NE Brazil: Journal of South American Earth Sciences, v. 79, p. 409–420, doi:10.1016/j.jsames.2017.08.022.

Barbosa, V.C.F., Silva, J.B.C., and Medeiros, W.E., 1999, Stability analysis and improvement of structural index estimation in Euler deconvolution: Geophysics, v. 64, p. 48–60, doi:10.1190/1.1444529.

Barros, G.E.B., Becker-Kerber, B., Sedorko, D., Lima, J.H.D., and Pacheco, M.L.A.F., 2021, Ichnological aspects of the Aquidauana Formation (Upper Carboniferous, Itararé Group, Brazil): An arthropod-colonized glacial setting: Palaeogeography, Palaeoclimatology, Palaeoecology, v. 578, p. 110575, doi:10.1016/j.palaeo.2021.110575.

Barrows, T.T., Magee, J., Miller, G., and Fifield, L.K., 2019, The age of Wolfe Creek meteorite crater (Kandimalal), Western Australia: Meteoritics & Planetary Science, v. 54, p. 2686–2697, doi:10.1111/maps.13378.

Beddingfield, C.B., Crane, K., Klimczak, C., and Cartwright, R., 2024, Mercury's Lobate Scarps Reveal that Polygonal Impact Craters Form on Contractional Structures: The Planetary Science Journal, v. 5, p. 52, doi:10.3847/PSJ/ad1fff.

Bernardes, R.B., Reimold, W.U., Gibson, R.L., Hauser, N., and Pavanetto, P., 2025, New insights into the geology and formation of the Araguainha impact structure, Brazil, from morphological and structural analysis: GSA Bulletin, 29 p., doi:10.1130/B38443.1.

Betts, P.G., Moore, D., Aitken, A., Blaikie, T., Jessell, M., Ailleres, L., Armit, R., McLean, M., Munukutla, R., and Chukwu, C., 2024, Geology from aeromagnetic data: Earth-Science Reviews, v. 258, p. 104958, doi:10.1016/j.earscirev.2024.104958.

Blakely, R.J., 1995, Potential Theory in Gravity and Magnetic Applications: Cambridge, Cambridge University Press, 441 p., doi:10.1017/CBO9780511549816.

Brito Neves, B.B., Fuck, R.A., Cordani, U.G., and Thomaz F°, A., 1984, Influence of basement structures on the evolution of the major sedimentary basins of Brazil: A case of tectonic heritage: Journal of Geodynamics, v. 1, p. 495–510, doi:10.1016/0264-3707(84)90021-8.

Brito Neves, B.B., Fuck, R.A., and Pimentel, M.M., 2014, The Brasiliano collage in South America: a review: Brazilian Journal of Geology, v. 44, p. 493–518, doi:10.5327/Z2317-4889201400030010.

Cagliari, J., Serratt, H., Cassel, M.C., Schmitz, M.D., and Chemale Jr., F., 2022, New high-precision U-Pb zircon age of the Irati Formation (Paraná Basin) and implications for the timing of the Kungurian anoxic events recorded in southern Gondwana: Gondwana Research, v. 107, p. 134–145, doi:10.1016/j.gr.2022.03.004.

Callefo, F., Arduin, D.H., Ricardi-Branco, F., Galante, D., Rodrigues, F., and Branco, F.C., 2018, The giant stromatolite field at Santa Rosa de Viterbo, Brazil (Paraná Basin) – A new paleoenvironmental overview and the consequences of the Irati Sea closure in the Permian: Journal of South American Earth Sciences, v. 84, p. 299–314, doi:10.1016/j.jsames.2018.04.008.

Caxito, F.A., Ribeiro, B.V., Alkmim, F., Deramchi, A., and Kirkland, C.L., 2025, Near-Synchronous Cambrian Evolution of the Transbrasiliano-Kandi-4°50′ Shear Zone in South America and Africa: Terra Nova, 9 p., doi:10.1111/ter.70017.

Collins, G.S., Wünnemann, K., Artemieva, N., and Pierazzo, E., 2012, Numerical Modelling of Impact Processes, *in* Impact Cratering: Processes and Products: Oxford, Wiley-Blackwell, p. 254–270, doi:10.1002/9781118447307.ch17.

Cordani, U.G., Brito Neves, B.B., Fuck, R., Porto, R., Thomaz Filho, A., and Cunha, F.M.B., 1984, Estudo preliminar de integração do pré-cambriano com os eventos tectônicos das bacias sedimentares brasileiras: Ciência. Técnica. Petróleo. Seção: exploração de petróleo, v. 14, p. 1–70, https://repositorio.usp.br/item/001464085 (accessed August 2025).

Cordani, U.G., Pimentel, M.M., Araújo, C.E.G.D., Basei, M.A.S., Fuck, R.A., and Girardi, V.A.V., 2013a, Was there an Ediacaran Clymene Ocean in central South America? American Journal of Science, v. 313, p. 517–539, doi:10.2475/06.2013.01.

Cordani, U.G., Pimentel, M.M., Araújo, C.E.G.D., and Fuck, R.A., 2013b, The significance of the Transbrasiliano-Kandi tectonic corridor for the amalgamation of West Gondwana: Brazilian Journal of Geology, v. 43, p. 583–597, doi:10.5327/Z2317-48892013000300012.

Cordani, U.G., Ramos, V.A., Fraga, L.M., Cegarra, M., Delgado, I., Souza, K.G., Gomes, F.E.M., and Schobbenhaus, C., 2016, Tectonic Map of South America, Second edition: CCGM/CGMW (Commission of the Geological Map of the World), scale 1:5,000,000, 12 p., doi:10.14682/2016TEMSA.

CPRM (Companhia de Pesquisa de Recursos Minerais), 1972, Levantamento gama-espectrométrico e magnetométrico na área do Projeto Alto Garças nos estados de Goiás e Mato Grosso: CPRM Technical Report 384–5, 76 p., http://rigeo.sgb.gov.br/handle/doc/4320 (accessed October 2025).

Crameri, F., 2018, Scientific colour maps, doi:10.5281/zenodo.1243862.

Crósta, A.P., Reimold, W.U., Vasconcelos, M.A.R., Hauser, N., Oliveira, G.J.G., Maziviero, M.V., and Góes, A.M., 2019, Impact cratering: The South American record – Part 1: Geochemistry, v. 79, p. 1–61, doi:10.1016/j.chemer.2018.06.001.

Curto, J.B., Vidotti, R.M., Blakely, R.J., and Fuck, R.A., 2015, Crustal framework of the northwest Paraná Basin, Brazil: Insights from joint modeling of magnetic and gravity data: Tectonophysics, v. 655, p. 58–72, doi:10.1016/j.tecto.2015.05.011.

Curto, J.B., Vidotti, R.M., Fuck, R.A., Blakely, R.J., Alvarenga, C.J.S., and Dantas, E.L., 2014, The tectonic evolution of the Transbrasiliano Lineament in northern Paraná Basin, Brazil, as inferred from aeromagnetic data: Journal of Geophysical Research: Solid Earth, v. 119, p. 1544–1562, doi:10.1002/2013JB010593.

Dalat de Sousa, E.M., Vidotti, R.M., Ruiz, A.S., and Motta, J.G., 2024, Reactivation and propagation of the transbrasiliano strike-slip system in Tocantins province, central Brazil: From Ediacaran to Cretaceous: Journal of South American Earth Sciences, v. 146, p. 105081, doi:10.1016/j.jsames.2024.105081.

Dentith, M., and Mudge, S.T., 2014, Geophysics for the Mineral Exploration Geoscientist: Cambridge, Cambridge University Press, 454 p., doi:10.1017/CBO9781139024358.

Elbeshausen, D., Wünnemann, K., and Collins, G.S., 2013, The transition from circular to elliptical impact craters: Journal of Geophysical Research: Planets, v. 118, p. 2295–2309, doi:10.1002/2013JE004477.

von Engelhardt, W., Matthäi, S.K., and Walzebuck, J., 1992, Araguainha impact crater, Brazil. I. The interior part of the uplift: Meteoritics, v. 27, p. 442–457, doi:10.1111/j.1945-5100.1992.tb00226.x.

Eppler, D.T., Ehrlich, R., Nummedal, D., and Schultz, P.H., 1983, Sources of shape variation in lunar impact craters: Fourier shape analysis: Geological Society of America Bulletin, v. 94, p. 274–291, doi:10.1130/0016-7606(1983)94<274:SOSVIL>2.0.CO;2.

Erickson, T.M., Timms, N.E., Kirkland, C.L., Tohver, E., Cavosie, A.J., Pearce, M.A., and Reddy, S.M., 2017, Shocked monazite chronometry: integrating microstructural and in situ isotopic age data for determining precise impact ages: Contributions to Mineralogy and Petrology, v. 172, p. 11, doi:10.1007/s00410-017-1328-2.

Fobert, M.-A., Spray, J.G., and Singhroy, V., 2025, An Integrated Remote Sensing Lineament Investigation of the Manicouagan Region, Canada: Implications for Planetary Cratering Processes: Journal of Geophysical Research: Planets, v. 130, p. e2025JE008982, doi:10.1029/2025JE008982.

Frugis, G.L., Campos Neto, M.C., Westin, A., and Fanning, C.M., 2024, New perspectives on the tectonic evolution of the eastern Paraguay Belt revealed through zircon U-Pb-Hf-O systematics of the inner units: Precambrian Research, v. 411, p. 107529, doi:10.1016/j.precamres.2024.107529.

Fulmer, C.V., and Roberts, W.A., 1963, Rock induration and crater shape: Icarus, v. 2, p. 452–465, doi:10.1016/0019-1035(63)90073-3.

Ganade de Araujo, C.E., Weinberg, R.F., and Cordani, U.G., 2014, Extruding the Borborema Province (NE-Brazil): a two-stage Neoproterozoic collision process: Terra Nova, v. 26, p. 157–168, doi:10.1111/ter.12084.

Gault, D.E., and Wedekind, J.A., 1978, Experimental studies of oblique impact, *in* Proceedings of the 9th Lunar and Planetary Science Conference, Houston, Texas, Lunar and Planetary Institute, p. 3843–3875, https://ui.adsabs.harvard.edu/abs/1978LPSC....9.3843G (accessed September 2025).

Gesicki, A.L.D., Riccomini, C., and Boggiani, P.C., 2002, Ice flow direction during late Paleozoic glaciation in western Paraná Basin, Brazil: Journal of South American Earth Sciences, v. 14, p. 933–939, doi:10.1016/S0895-9811(01)00076-1.

Gomes, A.S., and Vasconcelos, P.M., 2021, Geochronology of the Paraná-Etendeka large igneous province: Earth-Science Reviews, v. 220, p. 103716, doi:10.1016/j.earscirev.2021.103716.

Gottwald, M., Kenkmann, T., and Reimold, W.U., 2020, Terrestrial Impact Structures: The TanDEM-X Atlas: Munich, Verlag Dr. Friedrich Pfeil, 608 p.

Grohmann, C.H., and Campanha, G.A., 2010, OpenStereo: Open Source, Cross-Platform Software for Structural Geology Analysis, *in* American Geophysical Union Fall Meeting 2010, p. IN31C-06, https://ui.adsabs.harvard.edu/abs/2010AGUFMIN31C..06G (accessed October 2025).

Hauser, N., Reimold, W.U., Cavosie, A.J., Crósta, A.P., Schwarz, W.H., Trieloff, M., Souza, C.S.M., Pereira, L.A., Rodrigues, E.N., and Brown, M., 2019, Linking shock textures revealed by BSE, CL, and EBSD with U-Pb data (LA-ICP-MS and SIMS) from zircon from the Araguainha impact structure, Brazil: Meteoritics & Planetary Science, v. 54, p. 2286–2311, doi:10.1111/maps.13371.

Holz, M., França, A.B., Souza, P.A., Iannuzzi, R., and Rohn, R., 2010, A stratigraphic chart of the Late Carboniferous/Permian succession of the eastern border of the Paraná Basin, Brazil, South America: Journal of South American Earth Sciences, v. 29, p. 381–399, doi:10.1016/j.jsames.2009.04.004.

Horn, B.L.D., Oliveira, A.A., Simões, M.S., Besser, M.L., and Araújo, L.L., 2022, Mapa geológico da Bacia do Paraná: SGB (Serviço Geológico do Brasil)/CPRM (Companhia de Pesquisa de Recursos Minerais), Projeto Geologia e Potencial Mineral da Bacia do Paraná, scale 1:1,000,000, http://rigeo.sgb.gov.br/handle/doc/23037 (accessed November 2024).

Kenkmann, T., Collins, G.S., and Wünnemann, K., 2012, The Modification Stage of Crater Formation, *in* Impact Cratering: Processes and Products: Oxford, Wiley-Blackwell, p. 60–75, doi:10.1002/9781118447307.ch5.

Killeen, P.G., Mwenifumbo, C.J., and Ford, K.L., 2015, 11.14 - Tools and Techniques: Radiometric Methods, *in* Schubert, G., ed., Treatise on Geophysics (Second Edition), Oxford, Elsevier, p. 447–524, doi:10.1016/B978-0-444-53802-4.00209-8.

Kumar, P.S., and Kring, D.A., 2008, Impact fracturing and structural modification of sedimentary rocks at Meteor Crater, Arizona: Journal of Geophysical Research: Planets, v. 113, p. E09009, doi:10.1029/2008JE003115.

Lacerda Filho, J.V., Abreu Filho, W., Valente, C.R., Oliveira, C.C., and Albuquerque, M.C., 2004, Geologia e recursos minerais do estado de Mato Grosso: CPRM (Companhia de Pesquisa de Recursos Minerais); SICME-MT (Secretaria de Estado de Indústria, Comércio, Minas e Energia do Estado de Mato Grosso), Programa Integração, Atualização e Difusão de Dados da Geologia do Brasil technical report, 235 p., http://rigeo.sgb.gov.br/handle/doc/4871 (accessed November 2024).

Lana, C., Souza Filho, C.R., Marangoni, Y.R., Yokoyama, E., Trindade, R.I.F., Tohver, E., and Reimold, W.U., 2007, Insights into the morphology, geometry, and post-impact erosion of the Araguainha peak-ring structure, central Brazil: Geological Society of America Bulletin, v. 119, p. 1135–1150, doi:10.1130/B26142.1.

Lana, C., Souza Filho, C.R., Marangoni, Y.R., Yokoyama, E., Trindade, R.I.F., Tohver, E., and Reimold, W.U., 2008, Structural evolution of the 40 km wide Araguainha impact structure, central Brazil: Meteoritics & Planetary Science, v. 43, p. 701–716, doi:10.1111/j.1945-5100.2008.tb00679.x.

Leite, E.P., Lambert, J., Vasconcelos, M.A.R., Crósta, A.P., and Batezelli, A., 2022, Gamma-ray spectrometry of the Araguainha impact structure, Brazil: Additional insights into element mobilization due to hydrothermal alteration: Anais da Academia Brasileira de Ciências, v. 94, p. e20210182, doi:https://doi.org/10.1590/0001-3765202220210182.

Li, X., 2003, On the use of different methods for estimating magnetic depth: The Leading Edge, v. 22, p. 1090–1099, doi:10.1190/1.1634912.

Li, X., 2006, Understanding 3D analytic signal amplitude: Geophysics, v. 71, p. L13–L16, doi:10.1190/1.2184367.

Li, Y., and Nabighian, M., 2015, 11.11 - Tools and Techniques: Magnetic Methods of Exploration – Principles and Algorithms, *in* Schubert, G., ed., Treatise on Geophysics (Second Edition), Oxford, Elsevier, p. 335–391, doi:10.1016/B978-0-444-53802-4.00196-2.

Lima, M.V.A.G., Gonçalves, I.G., Soares, J.E.P., and Stephenson, R.A., 2024, Moho depth model of South America from a machine learning approach: Journal of South American Earth Sciences, v. 147, p. 105115, doi:10.1016/j.jsames.2024.105115.

Macleod, I.N., Vieira, S., and Chaves, A.C., 1993, Analytic Signal and Reduction-to-the-Pole in the Interpretation of Total Magnetic Field Data at Low Magnetic Latitudes, *in* Proceedings of the 3rd International Congress of the Brazilian Geophysical Society, Houten, Netherlands, European Association of Geoscientists & Engineers, p. cp-324-00158, doi:10.3997/2214-4609-pdb.324.830.

Mandelbrot, B., 1967, How Long Is the Coast of Britain? Statistical Self-Similarity and Fractional Dimension: Science, v. 156, p. 636–638, doi:10.1126/science.156.3775.636.

Manzano, J.C., Godoy, A.M., and Araújo, L.M.B., 2008, Contexto tectônico dos granitóides neoproterozóicos da faixa de dobramentos Paraguai, MS e MT: Geosciences = Geociências, v. 27, p. 493–507, https://www.periodicos.rc.biblioteca.unesp.br/index.php/geociencias/article/view/3374 (accessed October 2025).

Masero, W., Fischer, G., and Schnegg, P.-A., 1997, Electrical conductivity and crustal deformation from magnetotelluric results in the region of the Araguainha impact, Brazil: Physics of the Earth and Planetary Interiors, v. 101, p. 271–289, doi:10.1016/S0031-9201(96)03267-0.

Melosh, H.J., 1989, Impact Cratering: A Geologic Process: New York, Oxford University Press, Oxford monographs on geology and geophysics 11, 245 p.

Milani, E.J., Melo, J.H.G., Souza, P.A., Fernandes, L.A., and França, A.B., 2007, Bacia do Paraná: Boletim de Geociências da Petrobras, v. 15, p. 265–287.

Miyazaki, M.R., Leite, E.P., Vasconcelos, M.A.R., Wünnemann, K., and Crósta, A.P., 2021, Bouguer anomaly inversion and hydrocode modeling of the central uplift of the Araguainha impact structure: Anais da Academia Brasileira de Ciências, v. 93, p. e20210081, doi:10.1590/0001-3765202120210081.

Montibeller, C.C., Navarro, G.R.B., Zanardo, A., Rohn, R., Roveri, C.D., Rocha, R.R., and Conceição, F.T., 2020, Geochemistry of siltstones from the Permian Corumbataí Formation from the Paraná Basin (State of São Paulo, Brazil): Insights of provenance, tectonic and climatic settings: Journal of South American Earth Sciences, v. 102, p. 102582, doi:10.1016/j.jsames.2020.102582.

Moraes, L.G., Corrêa, R.T., Silva, A.B., and Matos, D.R., 2021, Investigação magnetométrica do lineamento Azimute 125°: CPRM (Companhia de Pesquisa de Recursos Minerais) Technical Report, http://rigeo.sgb.gov.br/handle/doc/22455 (accessed September 2025).

Moraes Rocha, L.G., Pires, A.C.B., Carmelo, A.C., and Araújo Filho, J.O., 2014, Geophysical characterization of the Azimuth 125° lineament with aeromagnetic data: Contributions to the geology of central Brazil: Precambrian Research, v. 249, p. 273–287, doi:10.1016/j.precamres.2014.05.005.

Niang, C.A.B., Baratoux, D., Diallo, D.P., Rochette, P., Jessell, M.W., Reimold, W.U., Bouley, S., Vanderhaeghe, O., Faye, G., and Lambert, P., 2021, Systematic survey of K, Th, and U signatures in airborne radiometric data from Australian meteorite impact structures: Possible causes of circular features and implications, *in* Reimold, W.U. and Koeberl, C., eds., Large Meteorite Impacts and Planetary Evolution VI, Boulder, Geological Society of America, Geological Society of America Special Paper 550, p. 373–405, doi:10.1130/2021.2550(15).

Öhman, T., 2009, The structural control of polygonal impact craters [Ph.D. thesis]: University of Oulu, 403 p., https://www.oulu.fi/resterr/jutut/A28_Ohman2.pdf (accessed October 2025).

Öhman, T., Aittola, M., Korteniemi, J., Kostama, V.-P., and Raitala, J., 2010, Polygonal impact craters in the solar system: Observations and implications, *in* Gibson, R.L. and Reimold, W.U., eds., Large Meteorite Impacts and Planetary Evolution IV, Boulder, Geological Society of America, Geological Society of America Special Paper 465, p. 51–65, doi:10.1130/2010.2465(04).

O'Leary, D.W., Friedman, J.D., and Pohn, H.A., 1976, Lineament, linear, lineation: Some proposed new standards for old terms: GSA Bulletin, v. 87, p. 1463–1469, doi:10.1130/0016-7606(1976)87<1463:LLLSPN>2.0.CO;2.

Osinski, G.R., Grieve, R.A.F., Ferrière, L., Losiak, A., Pickersgill, A.E., Cavosie, A.J., Hibbard, S.M., Hill, P.J.A., Bermudez, J.J., Marion, C.L., Newman, J.D., and Simpson, S.L., 2022, Impact Earth: A review of the terrestrial impact record: Earth-Science Reviews, v. 232, p. 104112, doi:10.1016/j.earscirev.2022.104112.

Pimentel, M.M., and Fuck, R.A., 1992, Neoproterozoic crustal accretion in central Brazil: Geology, v. 20, p. 375–379, doi:10.1130/0091-7613(1992)020<0375:NCAICB>2.3.CO;2.

Pimentel, M.M., Fuck, R.A., and Alvarenga, C.J., 1996, Post-Brasiliano (Pan-African) high-K granitic magmatism in Central Brazil: the role of late Precambrian-early Palaeozoic extension: Precambrian Research, v. 80, p. 217–238, doi:10.1016/S0301-9268(96)00016-2.

Pinto, M.L., and Vidotti, R.M., 2019, Tectonic framework of the Paraná basin unveiled from gravity and magnetic data: Journal of South American Earth Sciences, v. 90, p. 216–232, doi:10.1016/j.jsames.2018.12.006.

Poelchau, M.H., Kenkmann, T., and Kring, D.A., 2009, Rim uplift and crater shape in Meteor Crater: Effects of target heterogeneities and trajectory obliquity: Journal of Geophysical Research: Planets, v. 114, p. E01006, doi:10.1029/2008JE003235.

Reid, A.B., Allsop, J.M., Granser, H., Millett, A.J., and Somerton, I.W., 1990, Magnetic interpretation in three dimensions using Euler deconvolution: Geophysics, v. 55, p. 80–91, doi:10.1190/1.1442774.

Robbins, S.J., and Riggs, J.D., 2023, What Is a Polygonal Impact Crater? A Proposed Framework Toward Quantifying Crater Shapes: Earth and Space Science, v. 10, p. e2023EA002863, doi:10.1029/2023EA002863.

Schobbenhaus, C., Gonçalves, J.H., Santos, J.O.S., Abram, M.B., Neto, R.L., Matos, G.M.M., Vidotti, R.M., Ramos, M.A.B., and Jesus, J.D.A., 2004, eds., Carta Geológica do Brasil ao Milionésimo, Sistema de Informações Geográficas—SIG: CPRM (Companhia de Pesquisa de Recursos Minerais), Geological Map, scale 1:1,000,000, 41 CD-ROMs.

Schobbenhaus, C., Ribeiro, C.L., Oliva, L.A., Takanohashi, J.T., Lindenmayer, A.G., Vasconcelos, J.C., and Orlandi, V., 1975, Carta Geológica do Brasil ao Milionésimo, Folha Goiás (SC-22): Departamento Nacional de Produção Mineral, map text, p. 99–113.

Schultz, P.H., 1976, Moon Morphology: Interpretations Based on Lunar Orbiter Photography: Austin, University of Texas Press, 626 p.

Schwarz, G., 1978, Estimating the Dimension of a Model: The Annals of Statistics, v. 6, p. 461–464, doi:10.1214/aos/1176344136.

Silva, D., Lana, C., and Souza Filho, C.R., 2016, Petrographic and geochemical characterization of the granitic rocks of the Araguainha impact crater, Brazil: Meteoritics & Planetary Science, v. 51, p. 443–467, doi:10.1111/maps.12601.

Silva, A.B., Pires de Lima, R., and La Marca, K., 2023, Decomposing and recovering airborne radiometric data through principal component analysis applied on flight-line data: An alternative to reduce noise: Interpretation, v. 11, p. T523–T535, doi:10.1190/INT-2022-0110.1.

Souza, C.S.M., Hauser, N., Reimold, W.U., Bernardes, R.B., Vieira, L.C., Guimarães, E.M., and Gottwald, M., 2024, Araguainha impact structure, Brazil: New insights into the geology of the central uplift: Meteoritics & Planetary Science, v. 59, p. 2577–2607, doi:10.1111/maps.14236.

Taylor, M.J., Smettem, K., Pracilio, G., and Verboom, W., 2002, Relationships Between Soil Properties and High-Resolution Radiometrics, Central Eastern Wheatbelt, Western Australia: Exploration Geophysics, v. 33, p. 95–102, doi:10.1071/EG02095.

Theilen-Willige, B., 1981, The Araguainha impact structure/Central Brazil: Revista Brasileira de Geociências, v. 11, p. 91–97, doi:10.25249/0375-7536.19819197.

Thomé Filho, J.J., Crósta, A.P., and Paula, T.L.F., 2012, Geoparque Astroblema de Araguainha - Ponte Branca (GO/MT): proposta, *in* Schobbenhaus, C. and Silva, C.R., eds., Geoparques do Brasil: propostas, Rio de Janeiro, CPRM (Companhia de Pesquisa de Recursos Minerais), v. 1, p. 151–182.

Tohver, E., Lana, C., Cawood, P.A., Fletcher, I.R., Jourdan, F., Sherlock, S., Rasmussen, B., Trindade, R.I.F., Yokoyama, E., Souza Filho, C.R., and Marangoni, Y., 2012, Geochronological constraints on the age of a Permo–Triassic impact event: U–Pb and $^{40}Ar/^{39}Ar$ results for the 40 km Araguainha structure of central Brazil: Geochimica et Cosmochimica Acta, v. 86, p. 214–227, doi:10.1016/j.gca.2012.03.005.

UnB-IG (Universidade de Brasília–Instituto de Geociências), 2012, Araguainha Project – Final coursework mapping project by the geology graduating class of 2012: Universidade de Brasília, Instituto de Geociências, unpublished report [in Portuguese].

Vasconcelos, M.A.R., 2007, Caracterização geofísica da estrutura de impacto de Araguainha, MT/GO [Master's thesis]: Universidade de São Paulo, 157 p., https://doi.org/10.11606/D.14.2007.tde-17052007-105856 (accessed October 2025).

Warren, L.V., Assine, M.L., Simões, M.G., Riccomini, C., and Anelli, L.E., 2015, A Formação Serra Alta, Permiano, no centro-leste do Estado de São Paulo, Bacia do Paraná, Brasil: Brazilian Journal of Geology, v. 45, p. 109–126, doi:10.1590/23174889201500010008.

Zalán, P.V., 2004, A evolução fanerozóica das bacias sedimentares brasileiras, *in* Mantesso Neto, V., Bartorelli, A., Carneiro, C.D.R., and Brito Neves, B.B., eds., Geologia do Continente Sul-Americano: Evolução da obra de Fernando Flávio Marques de Almeida, São Paulo, Beca, p. 595–612.

Zalán, P.V., Wolff, S., Astolfi, M.A.M., Vieira, I.S., Conceição, J.C.J., Appi, V.T., Neto, E.V.S., Cerqueira, J.R., and Marques, A., 1990, The Paraná Basin, Brazil, *in* Leighton, M.W., Kolata, D.R., Oltz, D.F., Eidel, J.J., and Coury, A.B., eds., Interior Cratonic Basins, Tulsa, American Association of Petroleum Geologists Memoir, v. 51, p. 681–708, doi:10.1306/M51530C34.

Zanardo, A., Montibeller, C.C., Navarro, G.R.B., Moreno, M.M.T., Rocha, R.R., Roveri, C.D., and Azzi, A.A., 2016, Formação Corumbataí na região de Rio Claro/SP: Petrografia e implicações genéticas: Geosciences = Geociências, v. 35, p. 322–345.

SUPPORTING INFORMATION

CHAPTER 5 – RESEARCH ARTICLE 2: *Bernardes et al. (Submitted) – Araguainha Dome, Brazil: A polygonal impact structure due to a complex pre-impact regional structural framework*

CONTENTS (see following pages)

REFERENCES CITED IN THIS SUPPORTING INFORMATION

Bernardes, R.B., Reimold, W.U., Gibson, R.L., Hauser, N., and Pavanetto, P., 2025, New insights into the geology and formation of the Araguainha impact structure, Brazil, from morphological and structural analysis: GSA Bulletin, 29 p., doi:10.1130/B38443.1.

Robbins, S.J., and Riggs, J.D., 2023, What Is a Polygonal Impact Crater? A Proposed Framework Toward Quantifying Crater Shapes: Earth and Space Science, v. 10, p. e2023EA002863, doi:10.1029/2023EA002863.

Figure S1

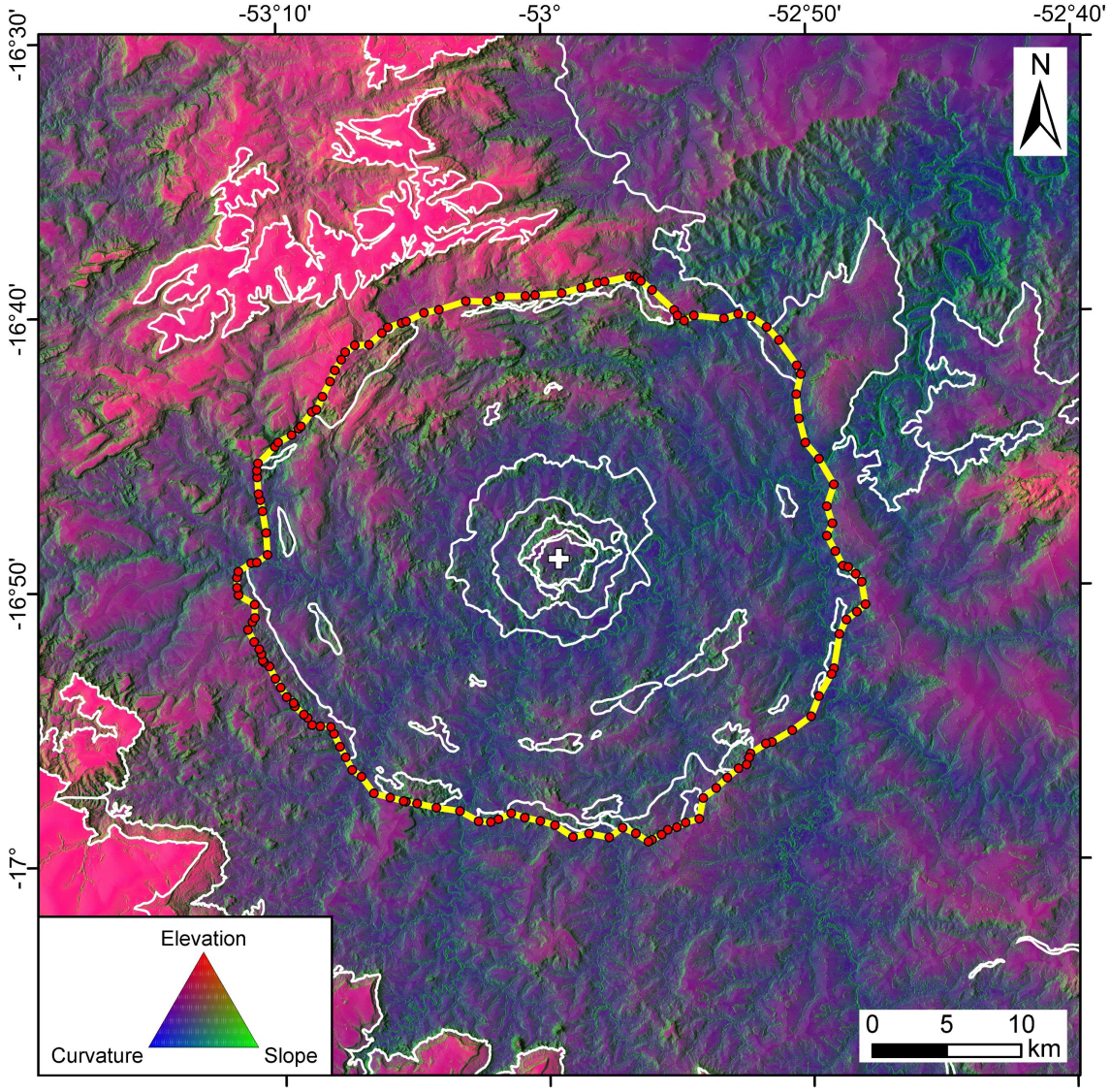

False-color composite image of processed TanDEM-X digital elevation model (DEM) data for the Araguainha impact structure (AIS) and its surroundings (courtesy of Manfred Gottwald, formerly of the German Aerospace Center – DLR). It is overlaid with a partially transparent, multidirectional hill-shaded image of the same DEM, with a 5:1 vertical exaggeration to highlight relief features. This map depicts the same area as Figs. 2, 3, and 4. The false-color composite image color map legend: red channel = elevation (the DEM itself), green channel = DEM slope, and blue channel = DEM curvature. White contours outline the mapped geological units (see Fig. 2; after Bernardes et al., 2025). The yellow contour marks the extracted (apparent) rim trace of the AIS. Red dots indicate the 141 vertex nodes that define this rim trace. For details, see the "Materials and Methods" section of the article. Map coordinate system: WGS84.

Panel S1

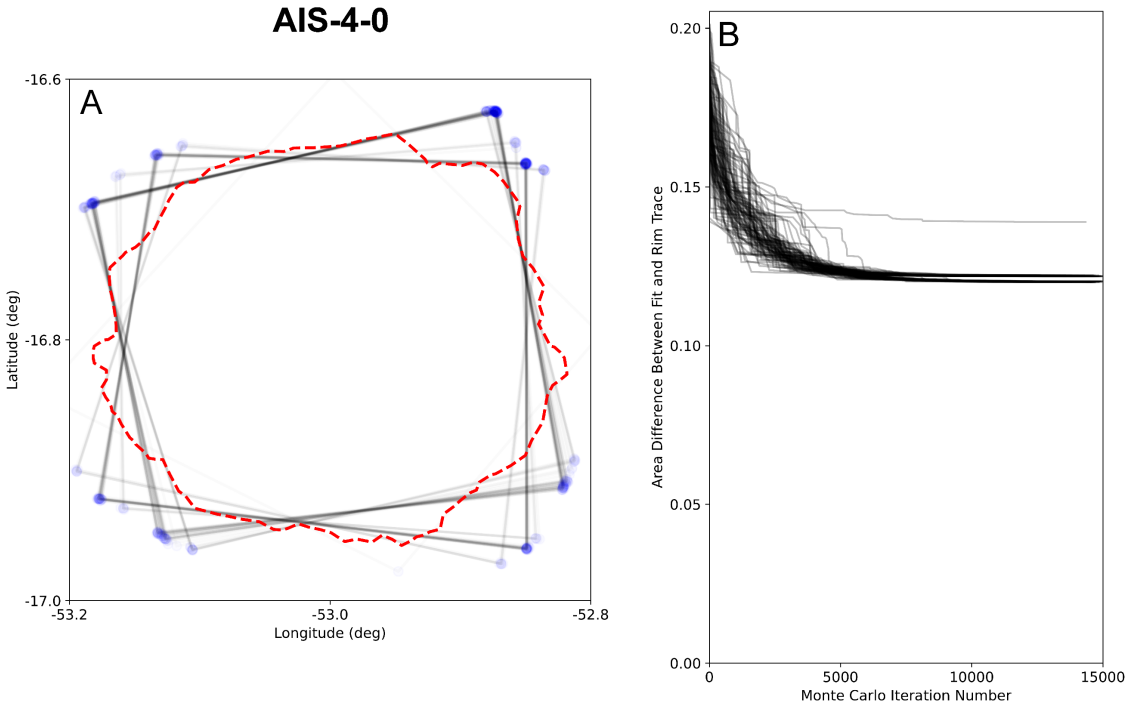
AIS-4-0
A
B
-16.6
-16.8
-17.0
-53.2
-53.0
-52.8
Latitude (deg)
Longitude (deg)
0.20
0.15
0.10
0.05
0.00
0
5000
10000
15000
Area Difference Between Fit and Rim Trace
Monte Carlo Iteration Number

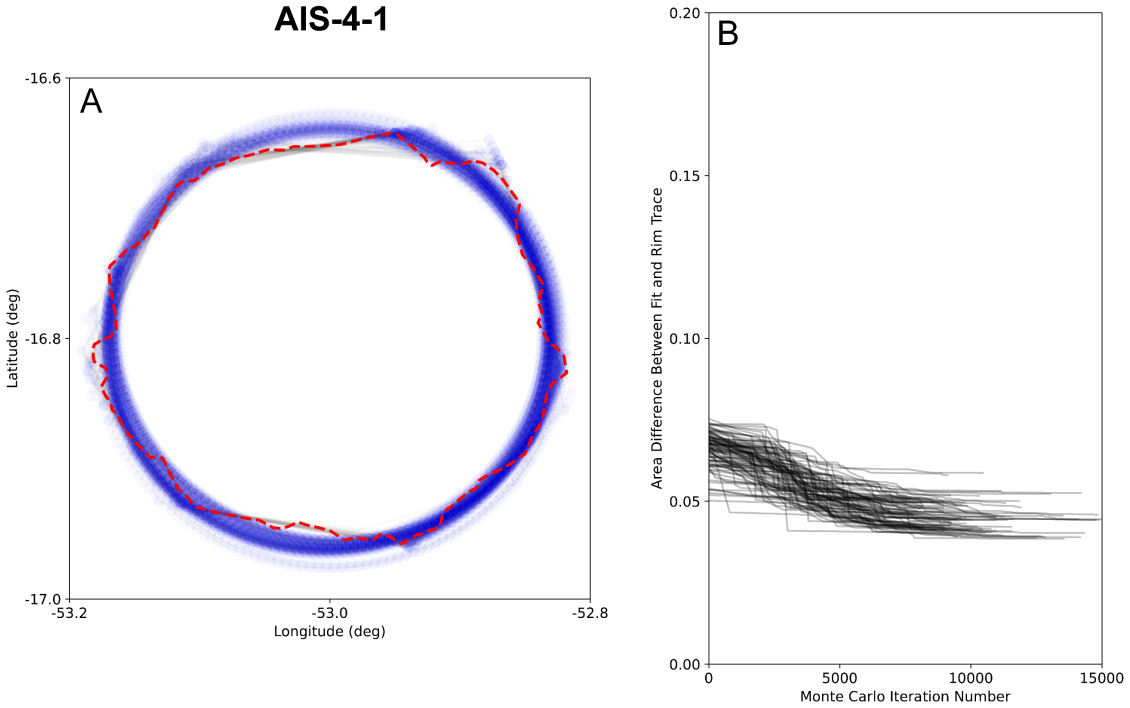
AIS-4-1
A
B
-16.6
-16.8
-17.0
-53.2
-53.0
-52.8
Latitude (deg)
Longitude (deg)
0.20
0.15
0.10
0.05
0.00
0
5000
10000
15000
Area Difference Between Fit and Rim Trace
Monte Carlo Iteration Number

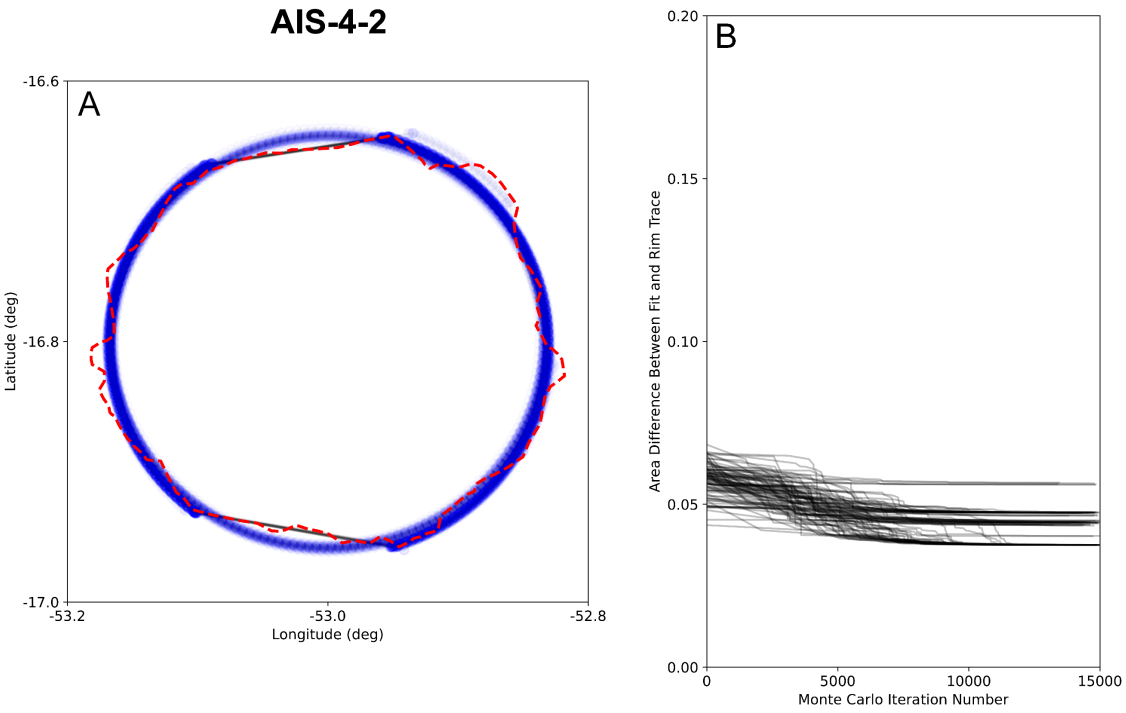
AIS-4-2
A
B
-16.6
-16.8
-17.0
-53.2
-53.0
-52.8
Latitude (deg)
Longitude (deg)
0.20
0.15
0.10
0.05
0.00
0
5000
10000
15000
Area Difference Between Fit and Rim Trace
Monte Carlo Iteration Number

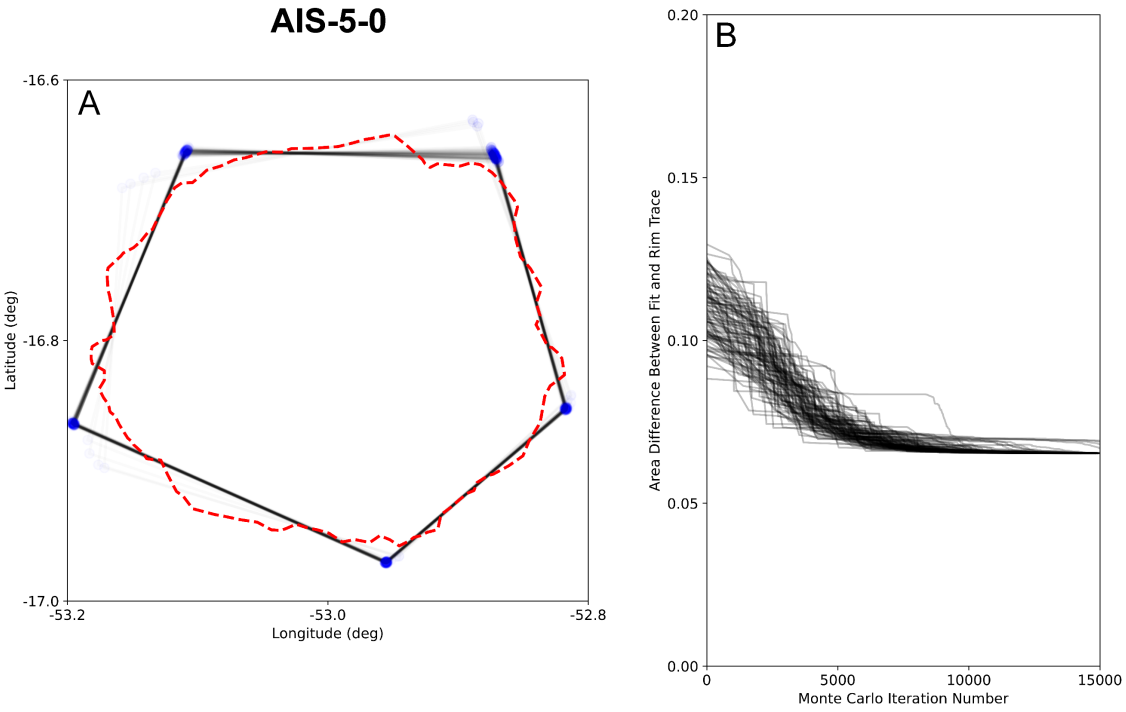
AIS-5-0
A
B
-16.6
-16.8
-17.0
-53.2
-53.0
-52.8
Latitude (deg)
Longitude (deg)
0.20
0.15
0.10
0.05
0.00
0
5000
10000
15000
Area Difference Between Fit and Rim Trace
Monte Carlo Iteration Number

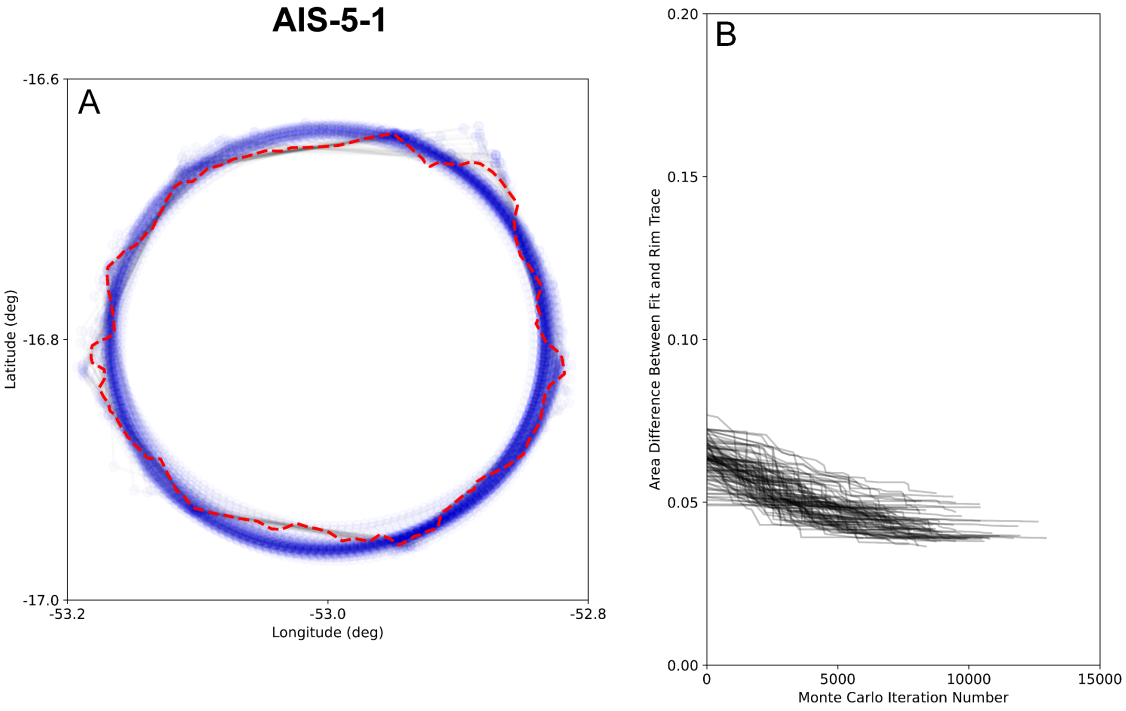
AIS-5-1
A
B
-16.6
-16.8
-17.0
-53.2
-53.0
-52.8
Latitude (deg)
Longitude (deg)
0.20
0.15
0.10
0.05
0.00
0
5000
10000
15000
Area Difference Between Fit and Rim Trace
Monte Carlo Iteration Number

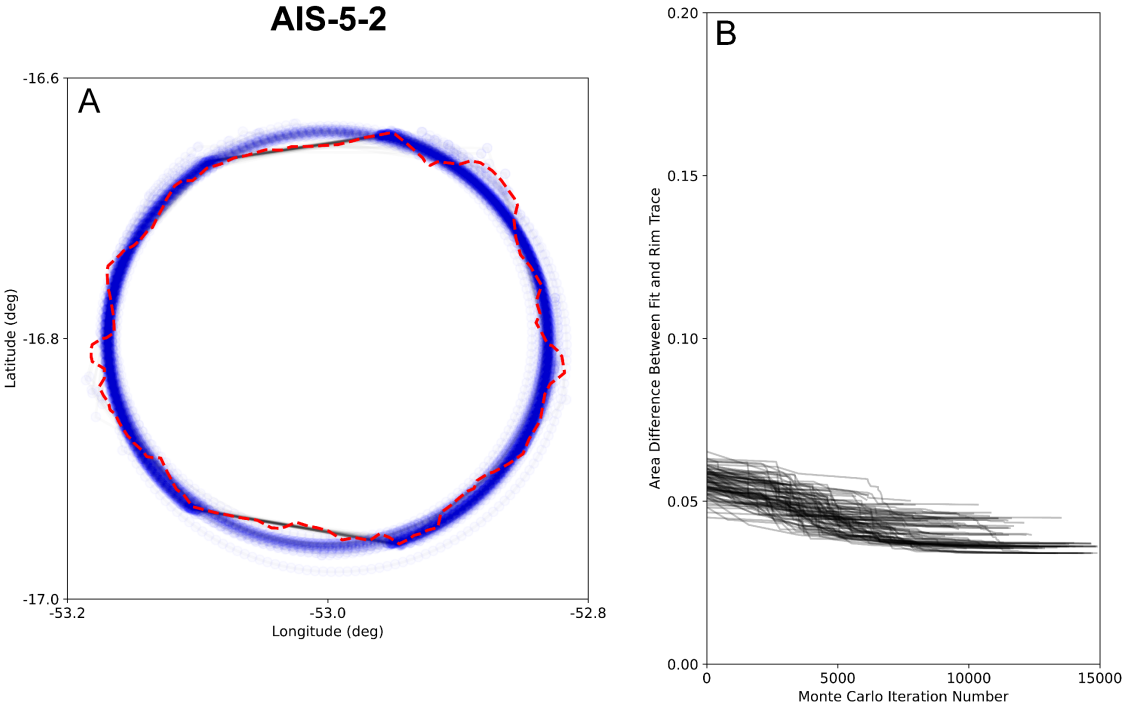
AIS-5-2
A
B
-16.6
-16.8
-17.0
-53.2
-53.0
-52.8
Latitude (deg)
Longitude (deg)
0.20
0.15
0.10
0.05
0.00
0
5000
10000
15000
Area Difference Between Fit and Rim Trace
Monte Carlo Iteration Number

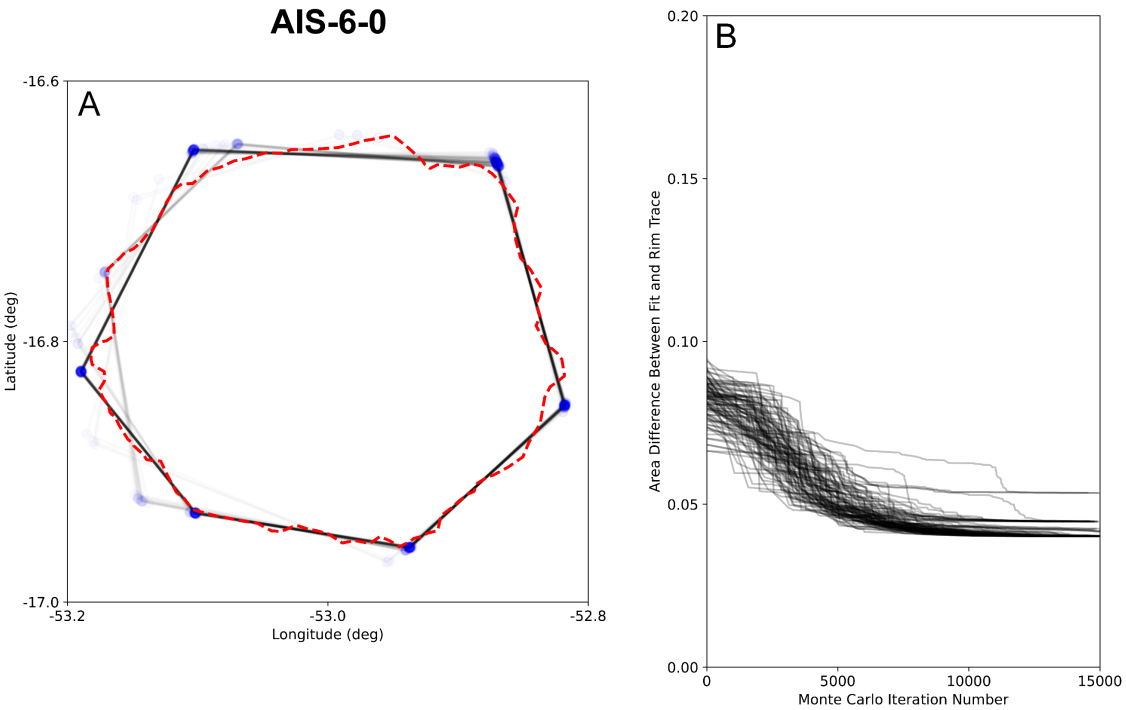
AIS-6-0
A
B
-16.6
-16.8
-17.0
-53.2
-53.0
-52.8
Latitude (deg)
Longitude (deg)
0.20
0.15
0.10
0.05
0.00
0
5000
10000
15000
Area Difference Between Fit and Rim Trace
Monte Carlo Iteration Number

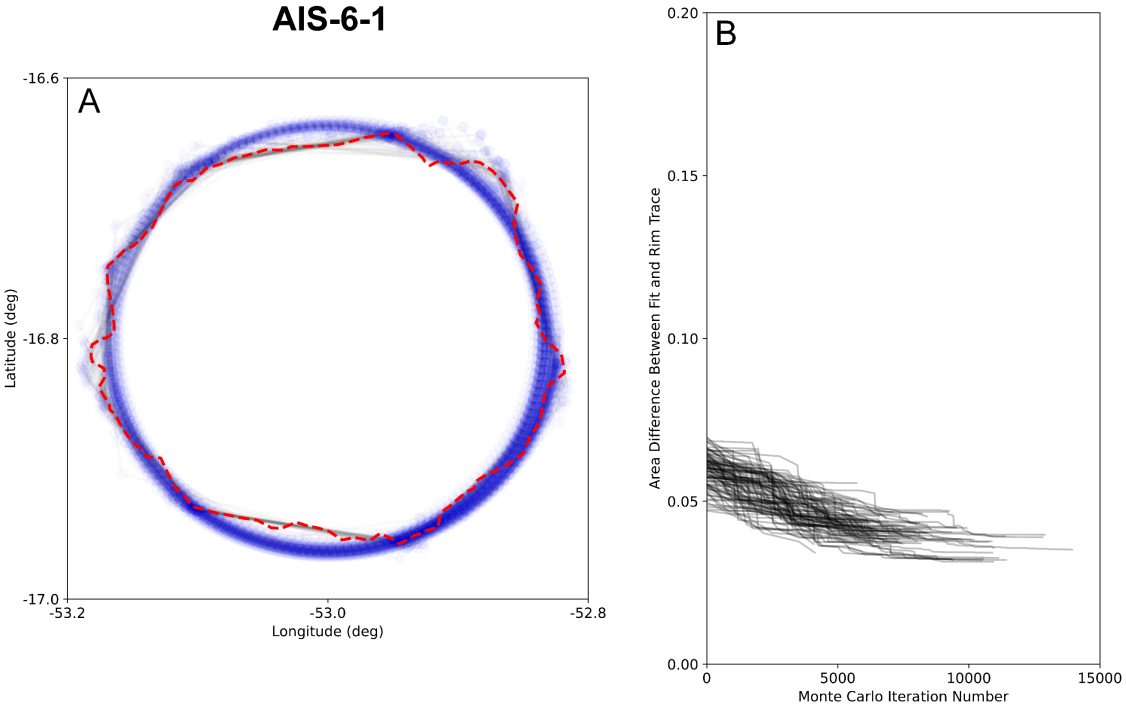
AIS-6-1
A
B
-16.6
-16.8
-17.0
-53.2
-53.0
-52.8
Latitude (deg)
Longitude (deg)
0.20
0.15
0.10
0.05
0.00
0
5000
10000
15000
Area Difference Between Fit and Rim Trace
Monte Carlo Iteration Number

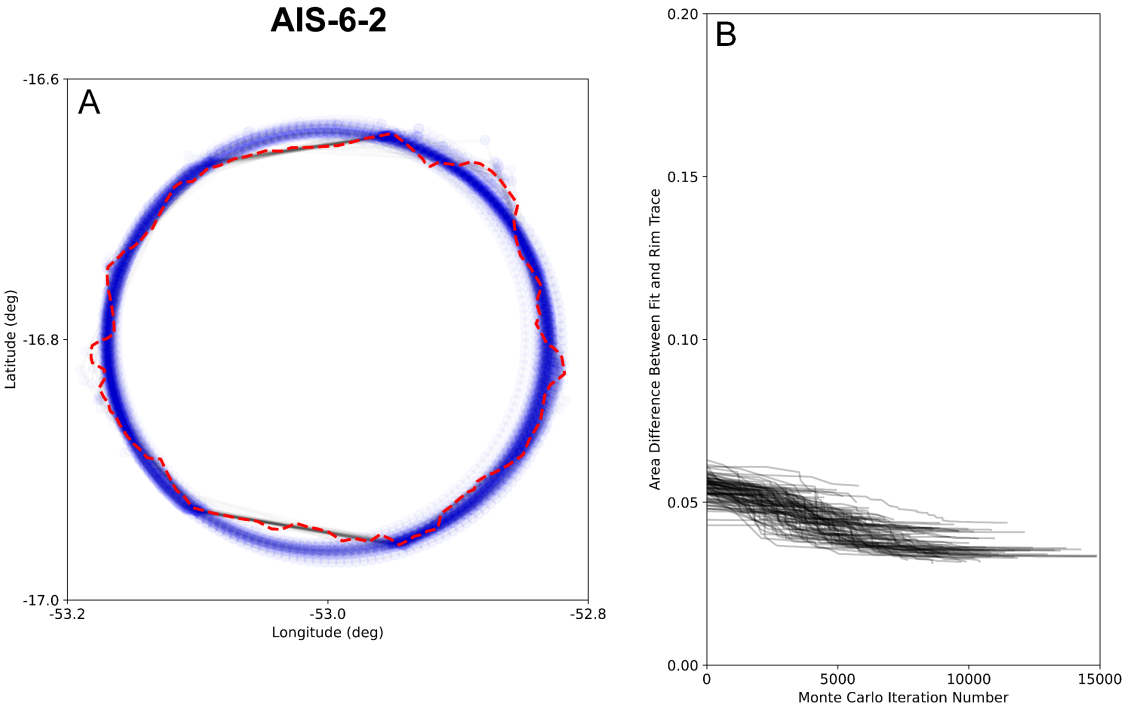
AIS-6-2
A
B
-16.6
-16.8
-17.0
-53.2
-53.0
-52.8
Latitude (deg)
Longitude (deg)
0.20
0.15
0.10
0.05
0.00
0
5000
10000
15000
Area Difference Between Fit and Rim Trace
Monte Carlo Iteration Number

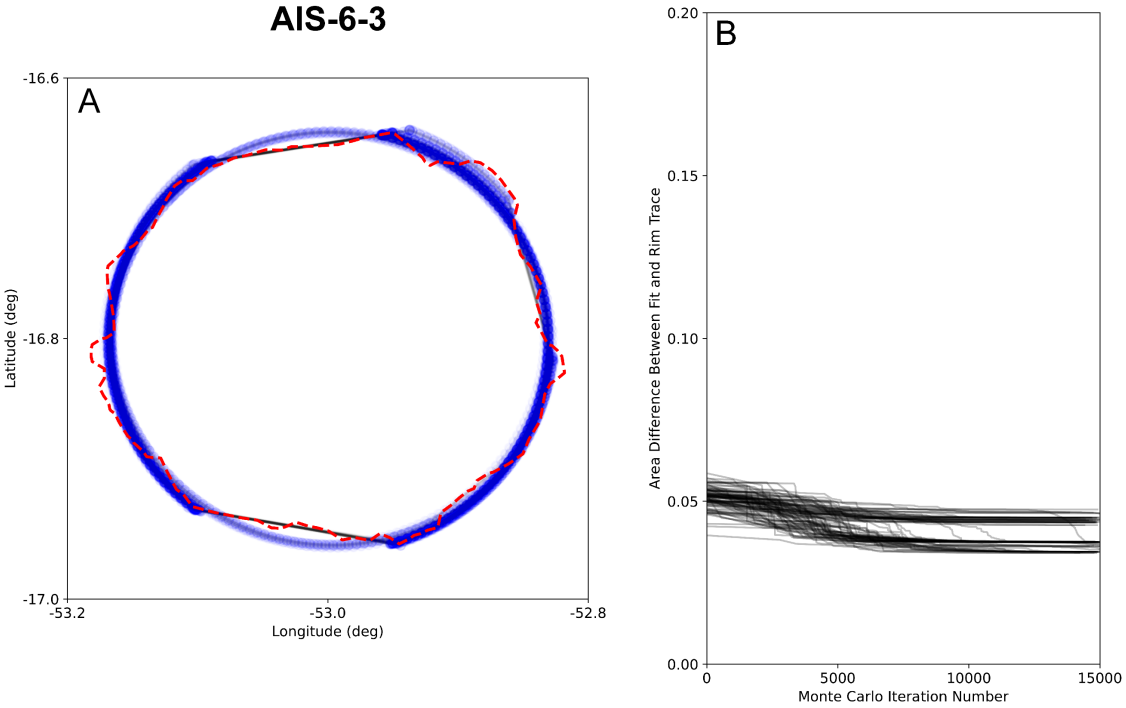
AIS-6-3
A
B
-16.6
-16.8
-17.0
-53.2
-53.0
-52.8
Latitude (deg)
Longitude (deg)
0.20
0.15
0.10
0.05
0.00
0
5000
10000
15000
Area Difference Between Fit and Rim Trace
Monte Carlo Iteration Number

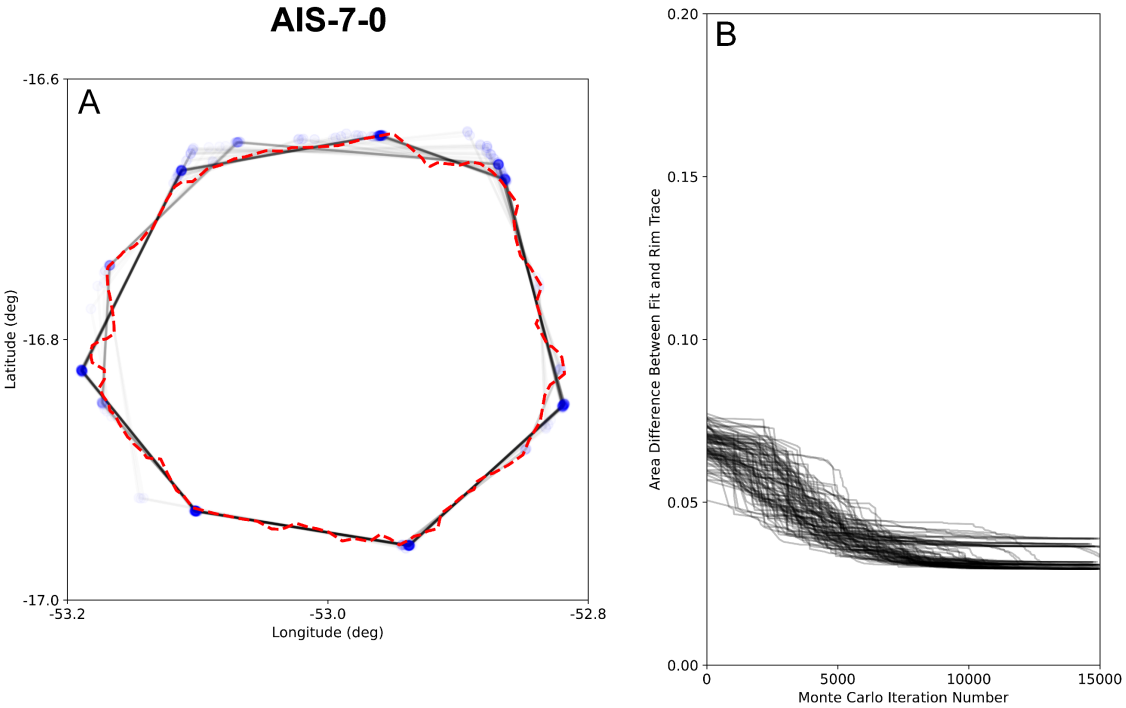
AIS-7-0
A
B
-16.6
-16.8
-17.0
-53.2
-53.0
-52.8
Latitude (deg)
Longitude (deg)
0.20
0.15
0.10
0.05
0.00
0
5000
10000
15000
Area Difference Between Fit and Rim Trace
Monte Carlo Iteration Number

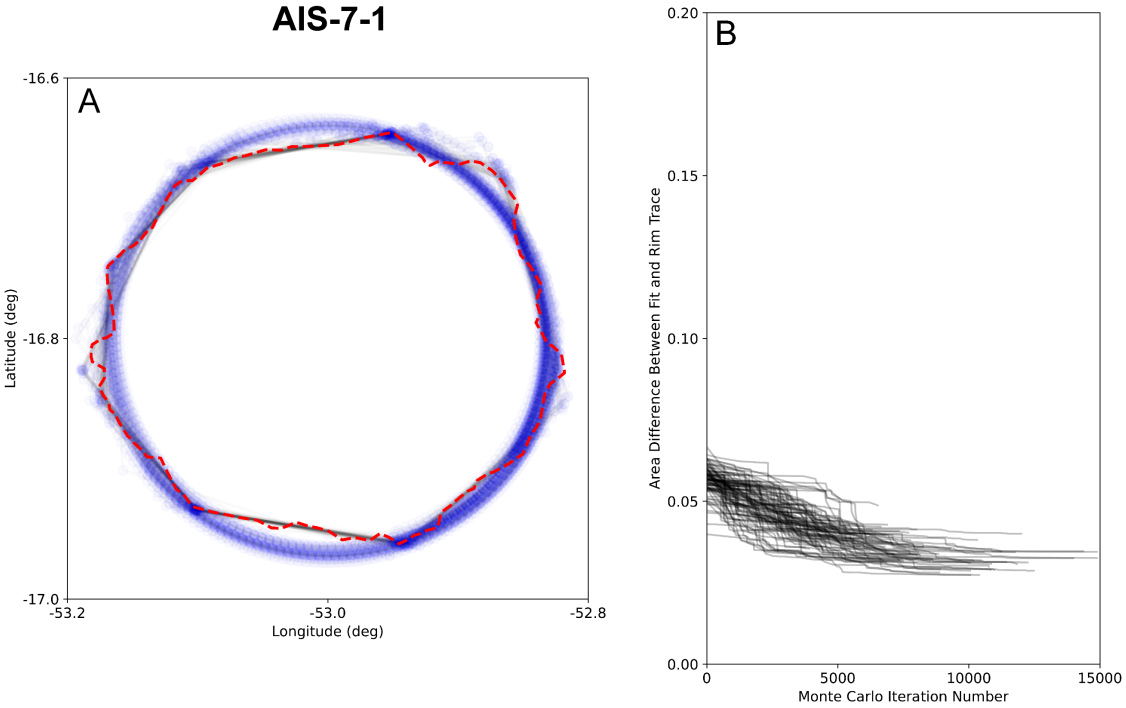
AIS-7-1
A
B
-16.6
-16.8
-17.0
-53.2
-53.0
-52.8
Latitude (deg)
Longitude (deg)
0.20
0.15
0.10
0.05
0.00
0
5000
10000
15000
Area Difference Between Fit and Rim Trace
Monte Carlo Iteration Number

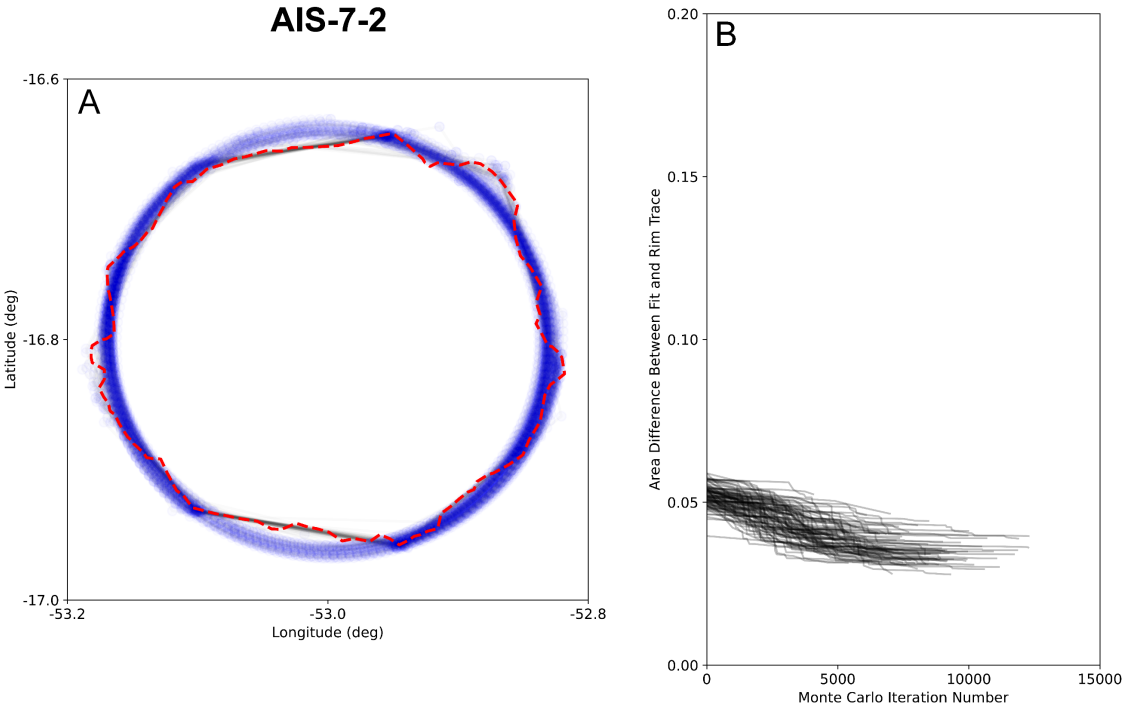
AIS-7-2
A
B
-16.6
-16.8
-17.0
-53.2
-53.0
-52.8
Latitude (deg)
Longitude (deg)
0.20
0.15
0.10
0.05
0.00
0
5000
10000
15000
Area Difference Between Fit and Rim Trace
Monte Carlo Iteration Number

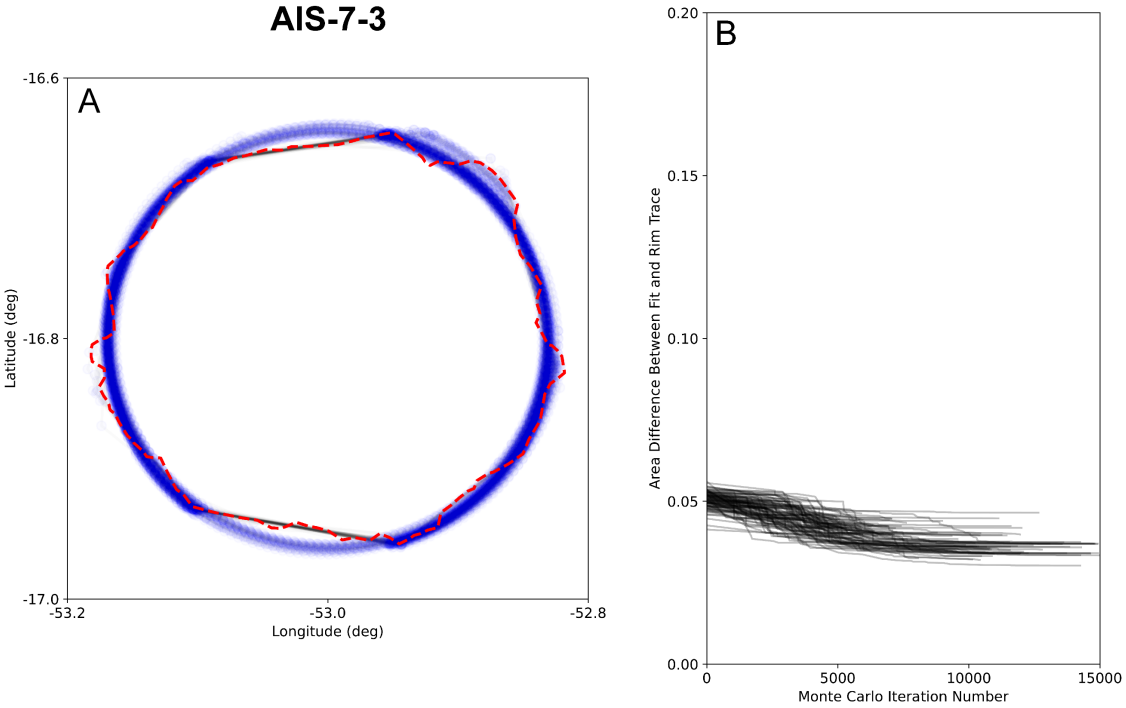
AIS-7-3
A
B
-16.6
-16.8
-17.0
-53.2
-53.0
-52.8
Latitude (deg)
Longitude (deg)
0.20
0.15
0.10
0.05
0.00
0
5000
10000
15000
Area Difference Between Fit and Rim Trace
Monte Carlo Iteration Number

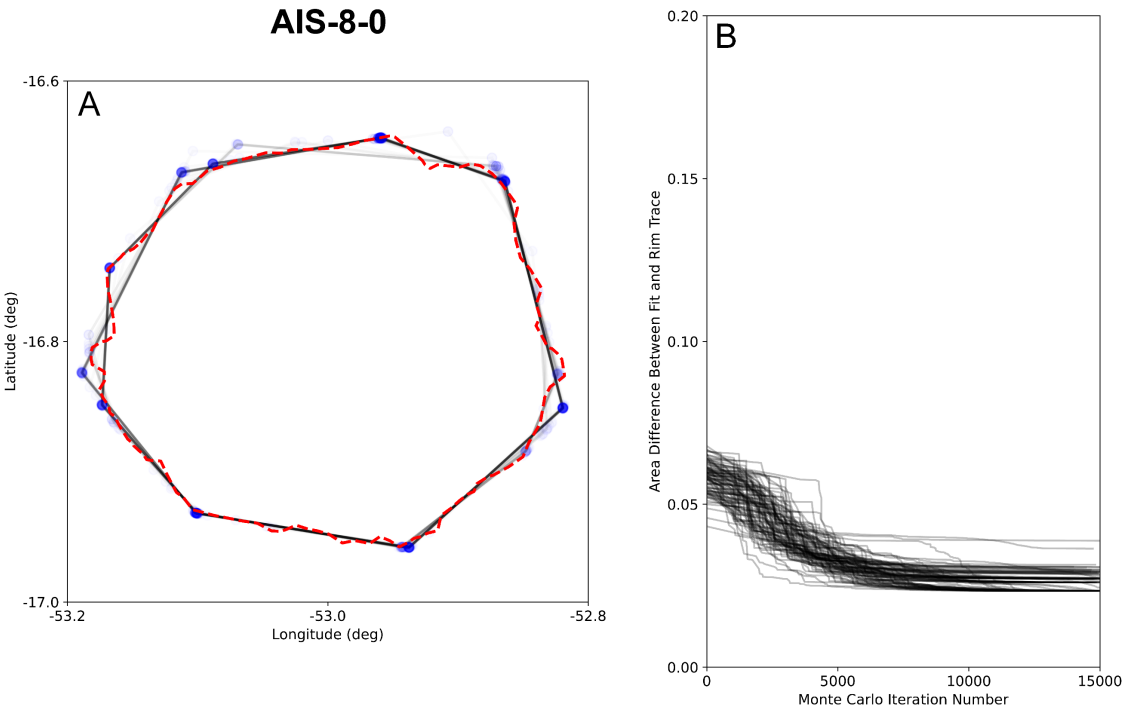
AIS-8-0
A
B
-16.6
-16.8
-17.0
-53.2
-53.0
-52.8
Latitude (deg)
Longitude (deg)
0.20
0.15
0.10
0.05
0.00
0
5000
10000
15000
Area Difference Between Fit and Rim Trace
Monte Carlo Iteration Number

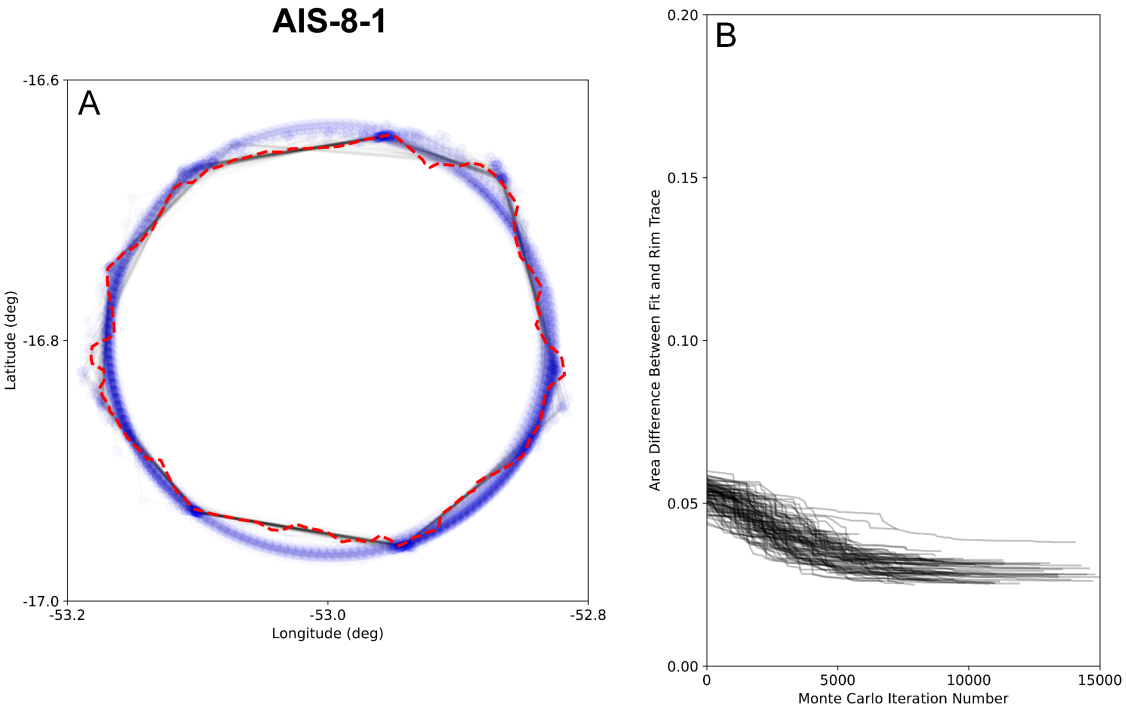
AIS-8-1
A
B
-16.6
-16.8
-17.0
-53.2
-53.0
-52.8
Latitude (deg)
Longitude (deg)
0.20
0.15
0.10
0.05
0.00
0
5000
10000
15000
Area Difference Between Fit and Rim Trace
Monte Carlo Iteration Number

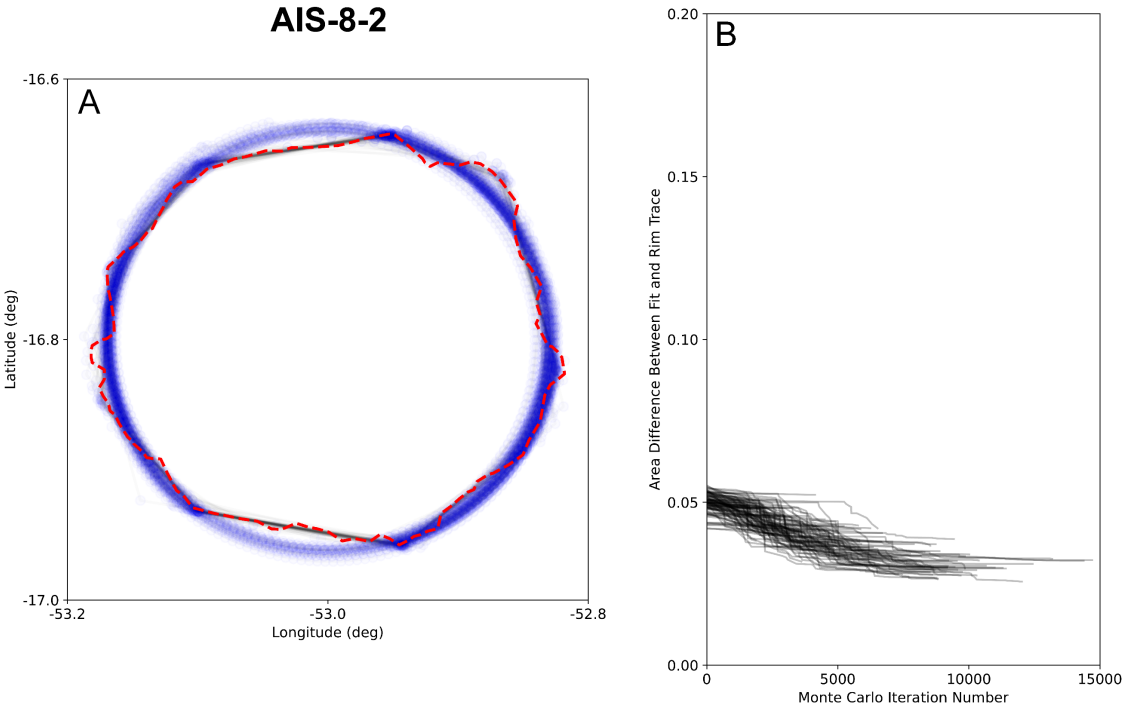
AIS-8-2
A
B
-16.6
-16.8
-17.0
-53.2
-53.0
-52.8
Latitude (deg)
Longitude (deg)
0.20
0.15
0.10
0.05
0.00
0
5000
10000
15000
Area Difference Between Fit and Rim Trace
Monte Carlo Iteration Number

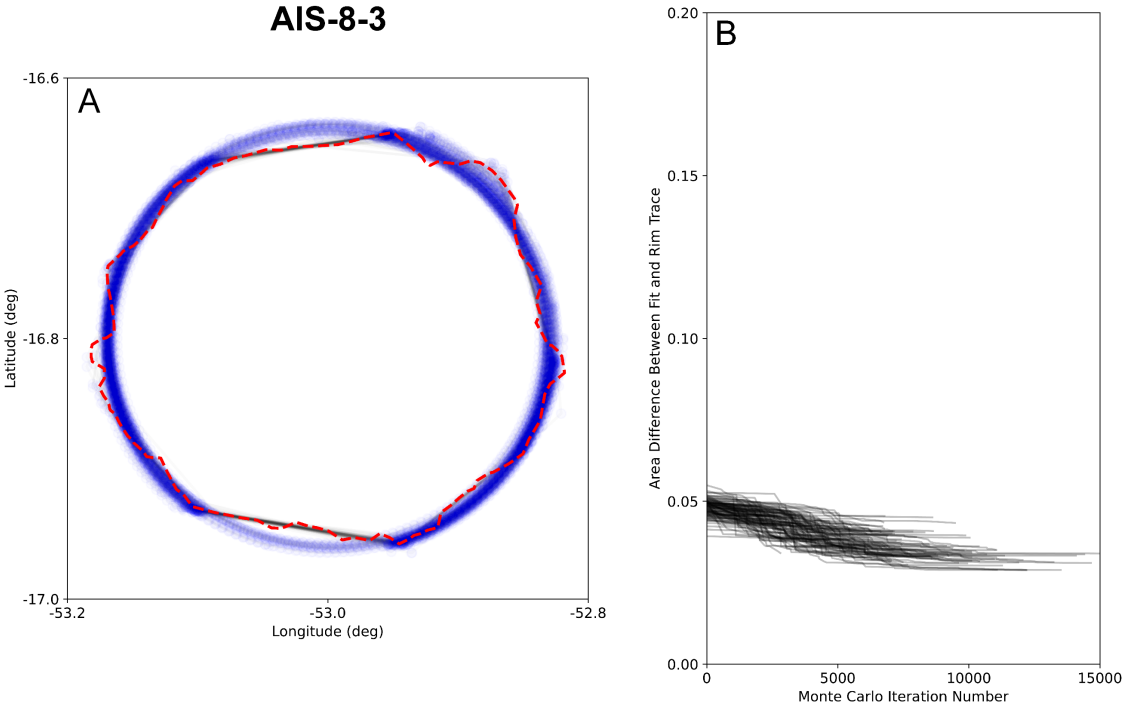
AIS-8-3
A
B
-16.6
-16.8
-17.0
-53.2
-53.0
-52.8
Latitude (deg)
Longitude (deg)
0.20
0.15
0.10
0.05
0.00
0
5000
10000
15000
Area Difference Between Fit and Rim Trace
Monte Carlo Iteration Number

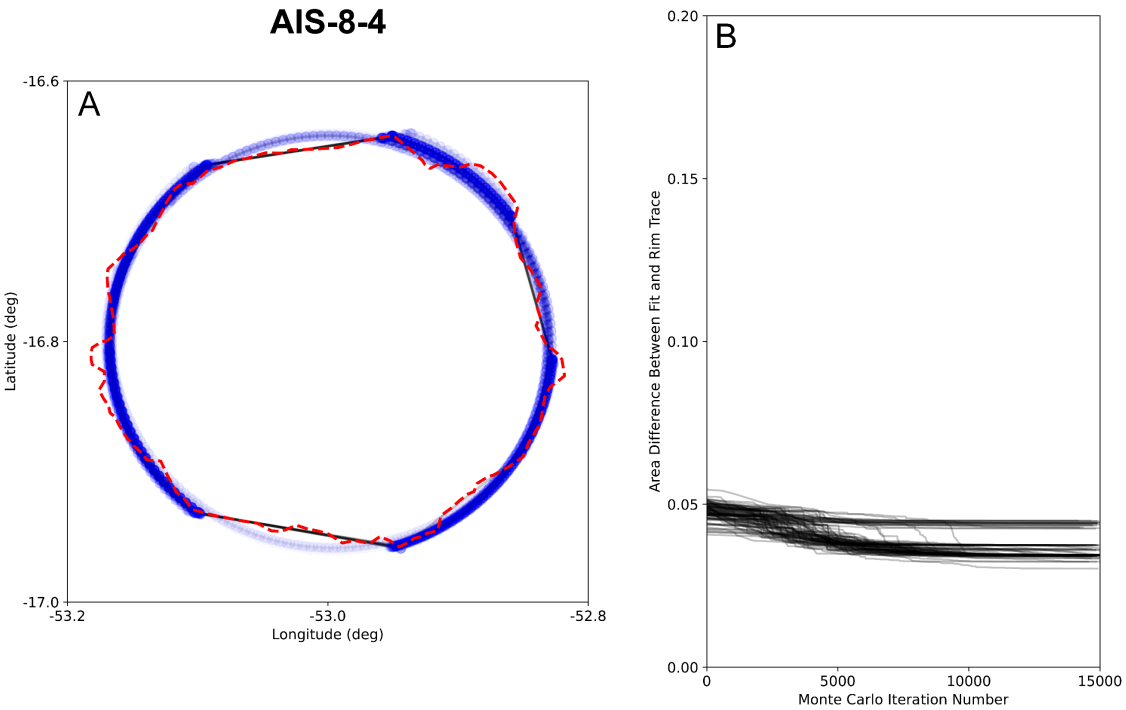
AIS-8-4
A
B
-16.6
-16.8
-17.0
-53.2
-53.0
-52.8
Latitude (deg)
Longitude (deg)
0.20
0.15
0.10
0.05
0.00
0
5000
10000
15000
Area Difference Between Fit and Rim Trace
Monte Carlo Iteration Number

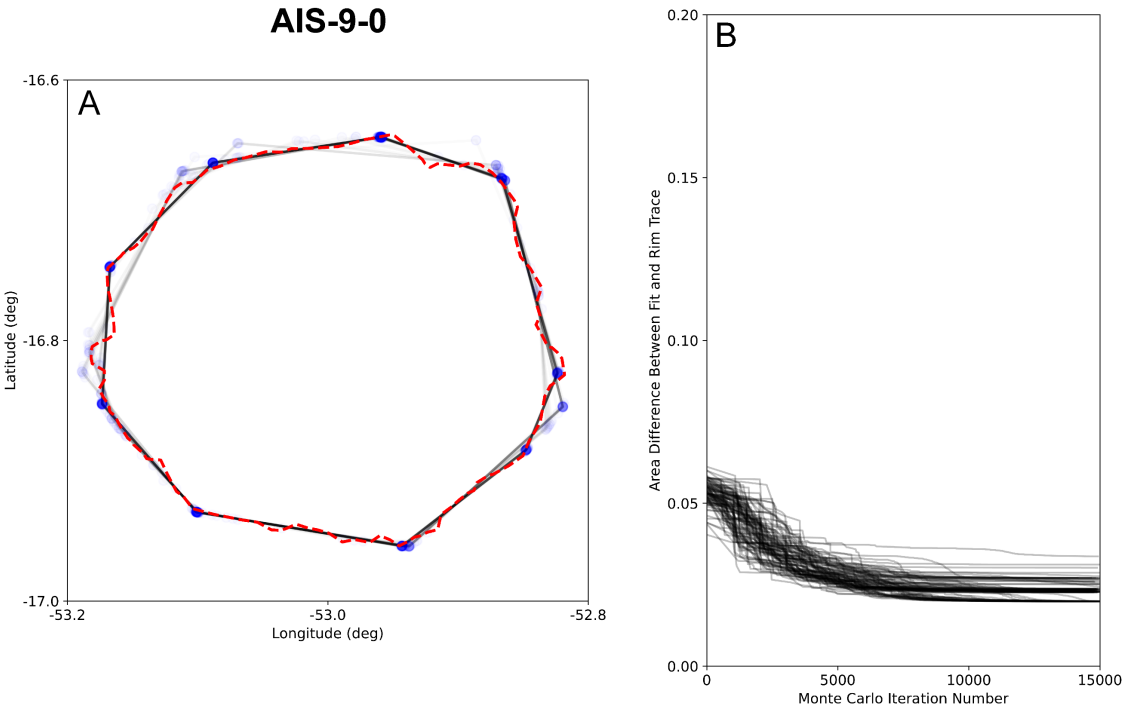
AIS-9-0
A
B
-16.6
-16.8
-17.0
-53.2
-53.0
-52.8
Latitude (deg)
Longitude (deg)
0.20
0.15
0.10
0.05
0.00
0
5000
10000
15000
Area Difference Between Fit and Rim Trace
Monte Carlo Iteration Number

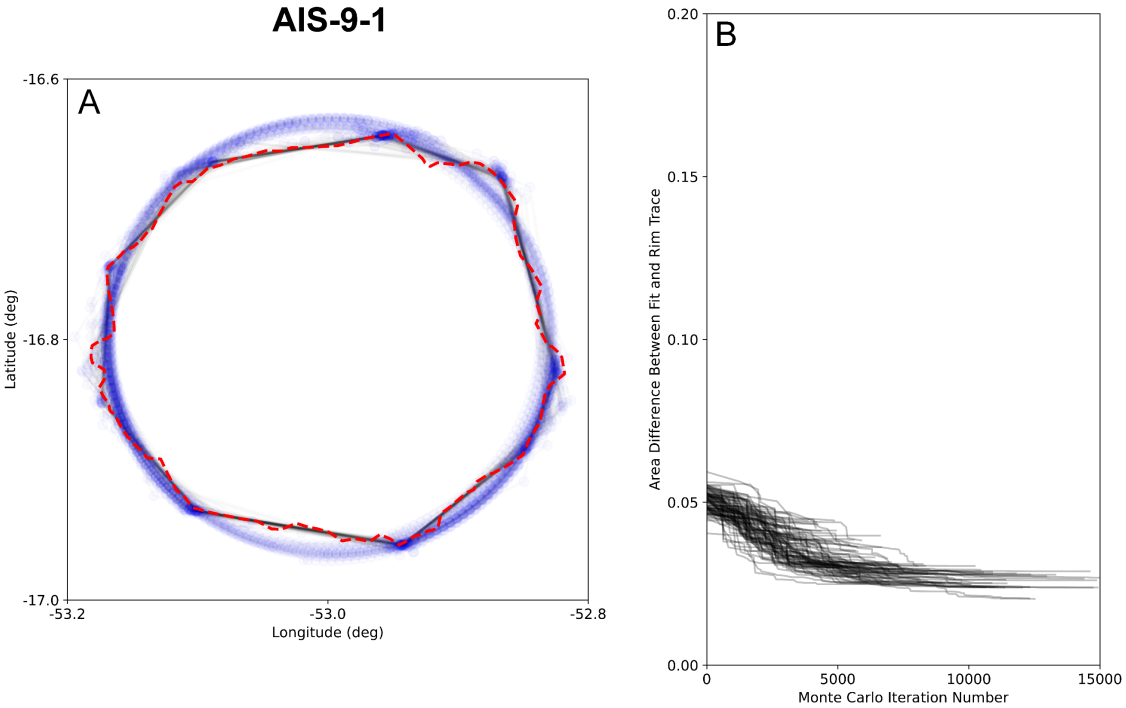
AIS-9-1
A
B
-16.6
-16.8
-17.0
Latitude (deg)
-53.2
-53.0
-52.8
Longitude (deg)
0.20
0.15
0.10
0.05
0.00
Area Difference Between Fit and Rim Trace
0
5000
10000
15000
Monte Carlo Iteration Number

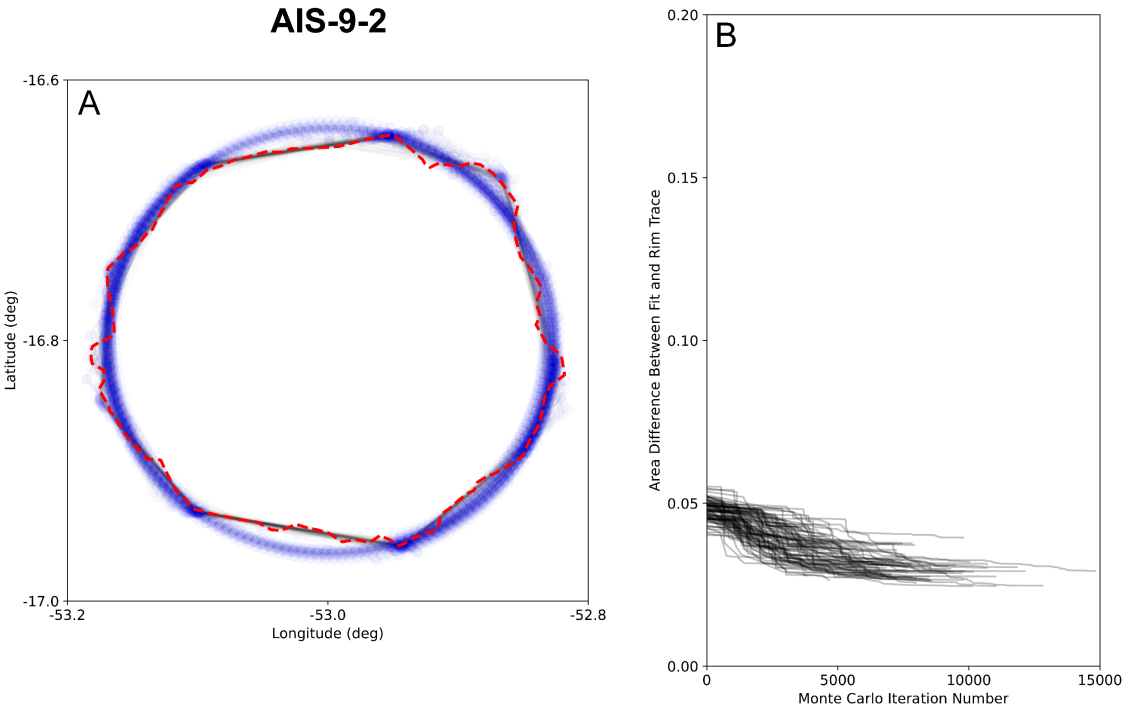
AIS-9-2
A
B
-16.6
-16.8
-17.0
Latitude (deg)
-53.2
-53.0
-52.8
Longitude (deg)
0.20
0.15
0.10
0.05
0.00
Area Difference Between Fit and Rim Trace
0
5000
10000
15000
Monte Carlo Iteration Number

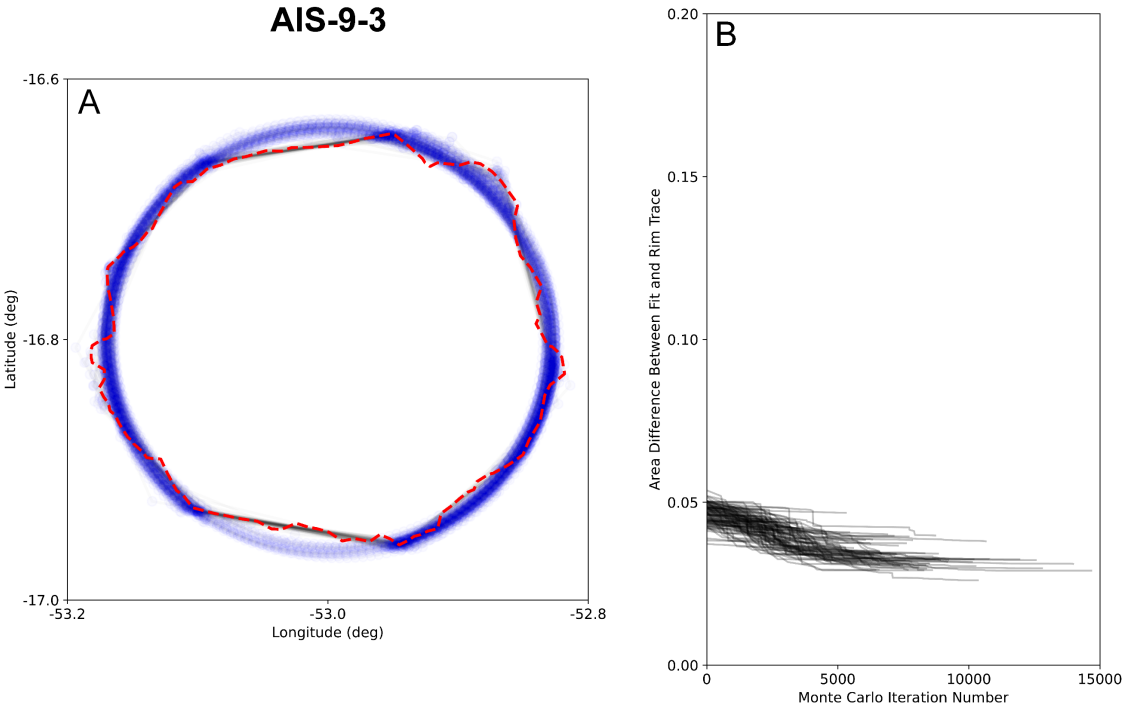
AIS-9-3
A
B
-16.6
-16.8
-17.0
-53.2
-53.0
-52.8
Latitude (deg)
Longitude (deg)
0.20
0.15
0.10
0.05
0.00
0
5000
10000
15000
Area Difference Between Fit and Rim Trace
Monte Carlo Iteration Number

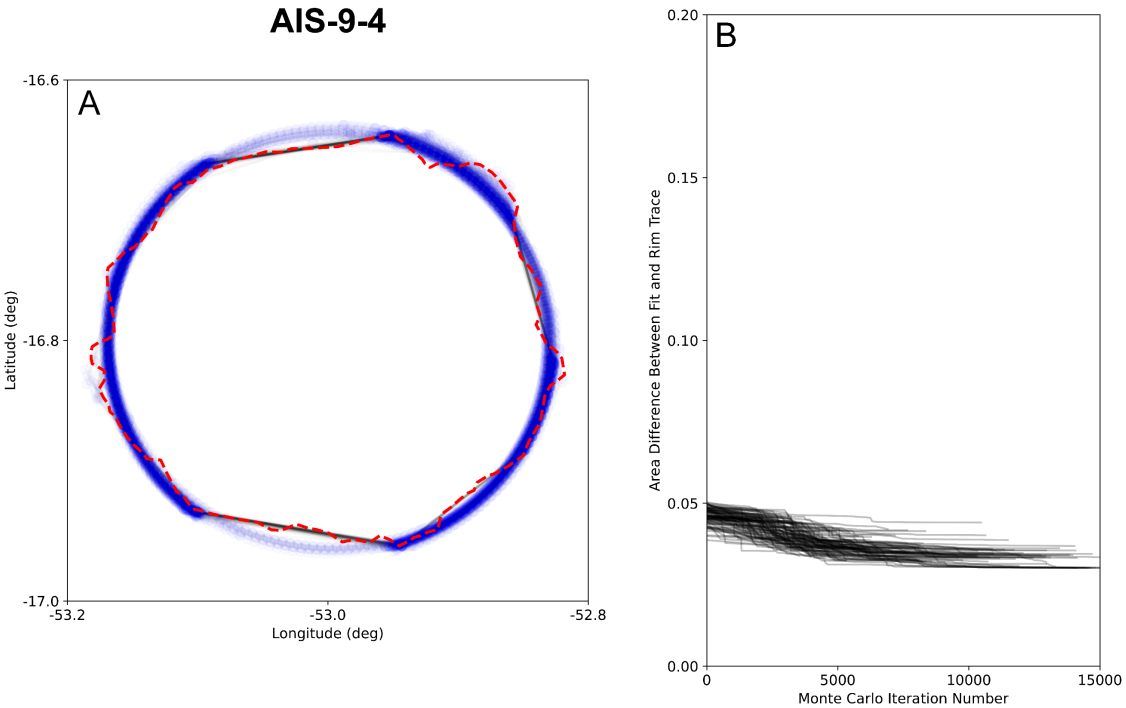
AIS-9-4
A
B
-16.6
-16.8
-17.0
-53.2
-53.0
-52.8
Latitude (deg)
Longitude (deg)
0.20
0.15
0.10
0.05
0.00
0
5000
10000
15000
Area Difference Between Fit and Rim Trace
Monte Carlo Iteration Number

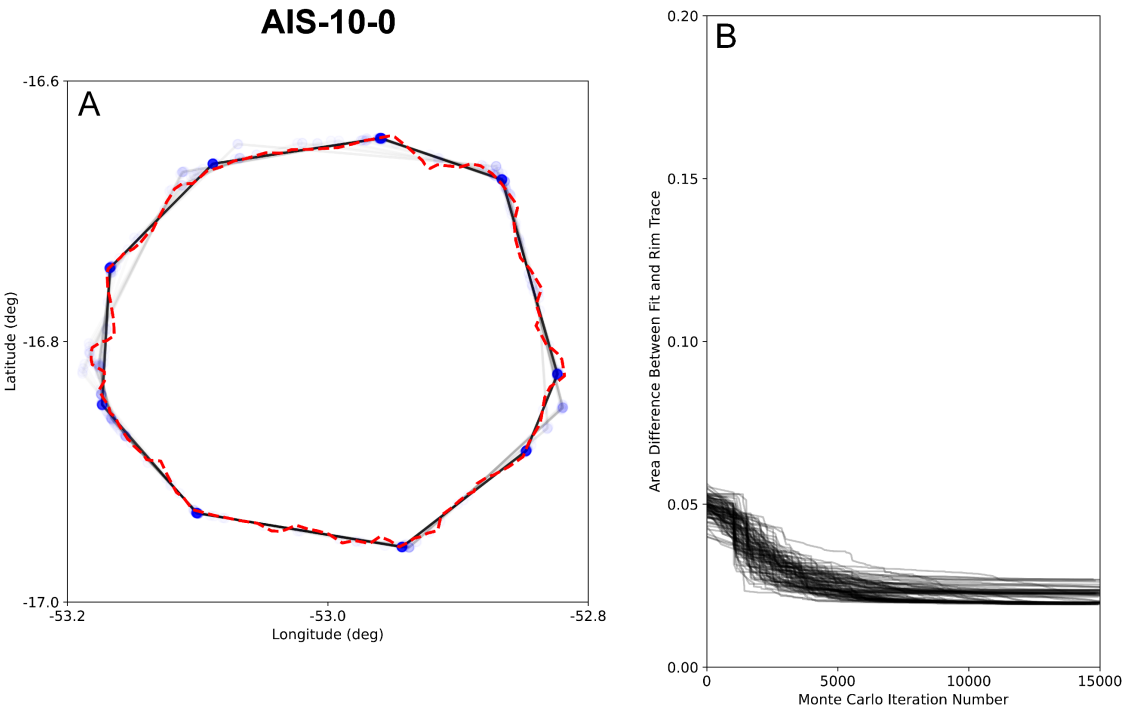
AIS-10-0
A
B
-16.6
-16.8
-17.0
-53.2
-53.0
-52.8
Latitude (deg)
Longitude (deg)
0.20
0.15
0.10
0.05
0.00
0
5000
10000
15000
Area Difference Between Fit and Rim Trace
Monte Carlo Iteration Number

CHAPTER 6

SOME INSIGHTS INTO HOW THE CENTRAL UPLIFT OF THE AIS FORMED

CHAPTER 6 – SOME INSIGHTS INTO HOW THE CENTRAL UPLIFT OF THE AIS FORMED

Various studies using different approaches, such as geological-structural investigation (e.g., von Engelhardt et al., 1992; Lana et al., 2008; Hippertt et al., 2014; Souza et al., 2024) or geophysical and numerical modeling methods (e.g., Tong et al., 2010; Yokoyama et al., 2012; Miyazaki et al., 2021; Leite et al., 2022), have advanced our understanding of the constitution, formation, and collapse of the central uplift of the Araguainha impact structure (AIS). For example, the most recent numerical model of the AIS by Miyazaki et al. (2021) suggests that the sedimentary collar rocks (Furnas and Ponta Grossa formations) were uplifted along with the granitic core by about 2 km. Tong et al.'s (2010) study supports the idea that, right after the collapse of the central uplift, there was a resurgence of impact melt and breccias over the central uplift of the AIS, near the collar-core boundary, which was controlled by the complex crater floor topography related to the mixed (crystalline-sedimentary) Araguainha target. In addition, the work of Souza et al. (2024) indicates that granite clasts are minor constituents in the polymict impact breccia, suggesting that, although uplifted, the Araguainha granite did not contribute substantially to the formation of the impact breccias of the AIS (see also Chapter 4).

However, some questions related to the evolution of the central uplift remain unanswered, such as whether the central uplift of the AIS formed and collapsed as a single, coherent mass or as multiple, incoherent masses, and which weakening mechanism operated most prominently during its evolution. This chapter discusses current knowledge and gaps in our understanding of the first-order evolution of the central uplift of the AIS, mainly focusing on its core and the possible weakening mechanisms that may have influenced this evolution.

The central uplift of a complex crater begins to form as the excavation stage ends and the predominantly gravity-controlled modification stage of cratering commences (Melosh, 1989; see also Chapter 2 of this thesis for an introduction). During this stage, the cavity floor begins to rise, creating an inward- and upward-directed material flow within the transient cavity, leading to an uplifted rock volume spatially related to the crater's center (see Kenkmann et al., 2012). This central uplift eventually becomes gravitationally unstable and collapses under its own weight, causing a downward- and

outward-directed flow of material over the inwardly collapsing crater wall volume (see, e.g., Ivanov, 2005; Dörfler and Kenkmann, 2020).

Whilst the above scenario sufficiently describes the first-order evolution of central uplifts, especially those formed in homogeneous (isotropic) targets, differences from this symmetric, gross hydrodynamic pattern may occur and are thought to be linked to various conditions and mechanisms, such as impact energy and angle, target composition and rheology, pre-existing target structure (Kenkmann et al., 2012) and, in the case of the formation of very large impact structures, the important, but often disregarded, geothermal gradient (see Ivanov, 2024). Among the proposed temporary weakening mechanisms that may control the evolution of central uplifts are *frictional heating* (e.g., Dence et al., 1977), *thermal softening* (O'Keefe and Ahrens, 1993, 1999), *dynamic fault weakening* (Senft and Stewart, 2009), and the much-debated *acoustic fluidization* (Melosh, 1979) – which will be discussed below.

Frictional heating is a weakening mechanism that involves the lubrication of fault movement and the injection of melt produced by shear heating in the central uplifts of large impact structures (Dence et al., 1977). *Thermal softening* alters the target's temperature distribution, reducing its strength due to impact-induced shock heating (O'Keefe and Ahrens, 1999). *Dynamic fault weakening*, in turn, involves large displacements at high slip velocities of a network of impact-generated faults along which lubrication by friction-melted material occurs, and the orientation of which may control crater collapse (Senft and Stewart, 2009).

Acoustic fluidization is considered a mechanism originally proposed to qualitatively explain certain impact-related phenomena, such as crater slumping and central peak formation (see Melosh, 1979; Melosh and Ivanov, 1999; Ivanov, 2005; Rajšić et al., 2024). The core idea of acoustic fluidization involves the temporary relief of static overburden pressure in parts of the rock volume through the influence of sufficiently strong acoustic waves (Melosh, 1979). It is worth noting, however, that a better understanding and modeling of this theoretical mechanism and its effects on the evolution of impact craters, especially of central uplifts, are still strongly debated (see Melosh, 1979; Melosh, 1989; Melosh and Ivanov, 1999; Hay et al., 2024), especially with respect to its duration (i.e., can it extend into the modification stage) and whether the affected rocks retain any distinctive evidence of its operation (more on that below).

Among these four weakening mechanisms, and based on the available evidence, three do not appear to have significantly influenced the central uplift evolution of the Araguainha impact structure:

(1) Frictional heating: As Yokoyama et al. (2012) discussed, the central uplift of the AIS indeed contains quenched melt in some fractures. However, these authors argue that the quantity of melt-bearing fractures is probably too small to have caused significant bulk weakening of the central uplift during the modification stage. The geological-structural mapping and profiling conducted along the northern core of the central uplift of the AIS in the current study also support this observation, indicating that melt-bearing fractures/faults are not ubiquitous features. Instead, polymict lithic (i.e., non-melt-bearing) impact breccia likely represents the most common and voluminous impactite, also within some fractures, in this section of the Araguainha central uplift (see Fig. 10 in Chapter 4). On the other hand, it is possible that some melt-bearing fractures/faults and melt pods were likely even more prominent in the uppermost, now-eroded part of the core of the central uplift of the AIS. However, this should be tested using numerical models of the AIS specifically designed to address this hypothesis.

(2) Thermal softening: This weakening mechanism is probably only effective in the collapse of very large impact craters (>200 km), where shock heating might be strong enough and affects a large rock volume (see Melosh and Ivanov, 1999).

(3) Dynamic fault weakening: Although the central uplift of the Araguainha impact structure does host fractures and faults, observations and results presented in Chapter 4 reveal that these structures are complexly and heterogeneously distributed across the different sections of the central uplift, such as the collar and core (more on that below), with the granitic core not displaying a prominent, macroscopic fracture/fault network (see Chapter 4; see also Yokoyama et al., 2012). Additionally, distinguishing preexisting from impact-induced fractures and faults, and their displacement history, is particularly challenging, especially in the granitic-(meta)sedimentary basement core of the AIS, which lacks suitable markers (see Chapter 4). Furthermore, as discussed above, melt-bearing fractures and faults are widely distributed but rarely localized in large numbers within the central uplift of the AIS. Lastly, the dynamic fault weakening mechanism has been numerically tested only for the collapse of impact craters around 100 km in diameter (see Senft and Stewart, 2009); thus, its applicability to structures the size of the AIS (~40 km in diameter) remains uncertain. The remaining weakening

mechanism – acoustic fluidization – is currently the only one explicitly invoked to explain the development of the AIS's central uplift (see discussion below).

Regarding the central uplift of the AIS, results from previous works have advanced our understanding of the deformational evolution of the Furnas Formation sedimentary collar (see Lana et al., 2008; Hippertt et al., 2014; see also chapters 4 and 5 of this thesis). However, little attention has been paid to the granitic-(meta)sedimentary basement core in this context. Currently, there are two proposals for the deformational style of the (granitic) core of the AIS. The first suggests that the Araguainha granite was uplifted as a uniform plastic body, based on the observation that the granite lacks conspicuous fracture systems (see von Engelhardt et al., 1992). However, these authors do not discuss any weakening mechanism that could account for such rheological behavior. The second proposed style was described by Yokoyama et al. (2012), who explained the orientation of the magnetic fabric (foliation and lineation) in the granitic core as resulting from the collapse flow of the central uplift. According to these authors, microstructural deformation progressed – in time and space – from widespread brittle fracturing, mostly at the outer parts of the granitic core, to discrete shear bands (cataclasis) at the center of the AIS. From that, Yokoyama et al. (2012) proposed that acoustic fluidization was the primary weakening mechanism operating at multiple scales within the core of the central uplift of the AIS, and causing first-order (macroscopic) apparent plastic deformation through cataclastic flow of the Araguainha granite.

The observations and results of the current study (see below; also chapters 4 and 5) provide a basis for discussing deformation during the uplift and subsequent collapse of the central part of the Araguainha impact structure. First, meso- and macroscopic brittle(-ductile) deformation structures (e.g., fractures, faults, shear bands) are observed in all sections of the central uplift; however, they are heterogeneously distributed within the different lithological units and sections present in the central uplift. These structures are more prominent in the (inner) sedimentary collar (e.g., Furnas Formation; see also Lana et al., 2008; Hippertt et al., 2014) than in the granitic-(meta)sedimentary basement core of the central uplift. Moreover, within the core itself, these deformation structures are more commonly observed in the (meta)sedimentary basement rocks than in the granitic core (see Fig. 10 in Chapter 4).

These findings are in line with von Engelhardt et al.'s (1992) observation of a lack of pronounced, widespread meso- and macroscopic fractures and faults throughout the

Araguainha granite (see Chapter 4; see also Yokoyama et al., 2012); however, most observations of the current study on the Araguainha granite were conducted on its fine-to-medium-grained phase, in some new exposures in the northern core region of the central uplift (see also Souza et al., 2024). There, this granitic phase occurs in limited exposures only, where it generally lacks significant – or even pervasive – fracture and fault systems (see Fig. 10 in Chapter 4). Nonetheless, it must be cautioned that all these observations of the Araguainha granite discussed so far may be biased by a lack of high-density and spatially well-distributed observation points, as it is difficult to find continuous granite exposures in the center of the AIS that would allow a representative observation of mesoscopic to macroscopic fracture and fault systems. Nonetheless, at the current observational level and in a scenario where mostly spatially limited, well-separated exposures provide the main outcrop situation, it appears that deformation is generally unevenly (asymmetrically) distributed throughout the central uplift of the AIS, especially in its granitic core. This, in turn, may be related to a structurally asymmetric development of the central uplift (see chapters 4 and 5).

Second, the geological-structural observations and results of this study (see Chapter 4) imply the occurrence of detachment interfaces between lithological units with different rheological behaviors within the AIS – most notably in the units of the central uplift, such as the Furnas Formation collar/granitic-(meta)sedimentary basement core contact, which represents the most prominently contrasting rheological interface in the central uplift. As discussed in Chapter 4, the presence of this detachment at the collar-core contact would allow contrasting types of deformation in each of the two central uplift subsections, i.e., the formation of the sedimentary collar would be dominated by inward-directed folding and imbrication (faulting), lateral constriction, and rotation of the strata (see also Lana et al., 2008). In contrast, the granitic core would have responded more independently and coherently, at least on a bulk, first-order scale. However, it is essential to emphasize that distinguishing deformation features (e.g., fractures, faults, shear bands) that are pre-impact in nature from those formed during the uplift or collapse of the central uplift, or even in some cases, from features that have been activated during both events (uplift and collapse), is an extremely challenging task (see chapters 4 and 5 for more detailed discussions).

Nonetheless, so far, and considering the overall discussion presented above, for a first-order model, the scenario proposed by von Engelhardt et al. (1992), in which the

central Araguainha granite rose as a "uniform plastic mass," seems plausible. This scenario, however, does not preclude the existence of localized deformation fabrics within the Araguainha granite, such as the concentrically arranged magnetic fabric described by Yokoyama et al. (2012) along the border of the granite with the (meta)sedimentary basement rocks (although these were not observed or tested in this work). Also, it does not preclude that, at a micro-scale, a brittle or brittle(-ductile) weakening mechanism – even of the nature of some kind of acoustic fluidization mechanism – may have influenced the large-scale, apparent ductile deformation of the (granitic) core of the central uplift of the Araguainha impact structure, as suggested by Yokoyama et al. (2012). It is worth noting that although fractured Araguainha granite occurs in the core of the AIS, the impact-related damage within it may be largely focused on the grain scale, which has been attributed to shock deformation (i.e., intragrain microdeformation; see Silva et al., 2016), rather than to central uplift evolution during the modification stage. Therefore, the two proposed deformational and uplift styles of the granitic core of the AIS (i.e., that of von Engelhardt et al., 1992; and Yokoyama et al., 2012; see above) could, in principle, be reconciled into a single hypothesis.

Considering the reconciled hypothesis, some significant open questions remain, such as (1) whether this acoustic fluidization weakening mechanism operated across the entire central uplift, including its collar, or if the possible detachment between the collar and core sections restricted its occurrence to the core of the central uplift; (2) whether acoustic fluidization also played a role during the outward-directed collapse of the central uplift at the end of the modification stage or if it was limited to its initial formation phase (i.e., the uplift process itself); and (3) whether post-impact thermal effects potentially destroyed evidence related to acoustic fluidization.

A main issue with acoustic fluidization, however, is that although it has been successfully applied numerically to replicate various morphological and structural features on a range of rocky and planetary bodies, including Earth and the Moon (see e.g., Hay et al., 2024; Rajšić et al., 2024, and references therein), there is still insufficient direct evidence (observations) for its duration and precise operating mechanism (see Dörfler and Kenkmann, 2020; Rajšić et al., 2024, and references therein). In particular, it has been questioned why pervasive micro-/mesodeformation that would conceivably result from this "flow mechanism" in rocks of the inner parts of central uplifts has not been detected. Although various authors have considered that fracturing at the several millimeter to

centimeter scale – or the widespread formation of veinlets and pods of pseudotachylitic breccia – as possible products of acoustic fluidization (e.g., Lana et al. 2003; Reimold and Gibson, 1996; Gibson and Reimold, 2008; for the case of the Vredefort impact structure in South Africa), it may be significant that the Archean gneisses in the core of the Vredefort central uplift do not appear to have been significantly modified by the impact process at the grain scale. There, pseudotachylitic breccia veins and pods are ubiquitous, but they have been predominantly formed within the framework of earlier fabrics (see Reimold and Gibson, 1996; Gibson and Reimold, 2008, and references therein).

Ultimately, it is clear that more fieldwork, numerical modeling, and scaled-analog modeling (e.g., Dörfler and Kenkmann, 2020) studies are needed to better grasp the prevailing weakening mechanism(s). The main contribution of the current study on the central uplift of the Araguainha impact structure is to emphasize its structural complexity, especially of its core and inner collar (see also Chapter 4). A viable integrated first-order hypothesis has been tentatively proposed to reconcile acoustic fluidization with the available structural observations of the Araguainha central uplift. In addition, this chapter raises some new questions for future work. Further progress in understanding the evolution of the central uplift of the AIS could be achieved through more detailed structural field mapping and mineral-scale analysis of the collar-core contact and of the granitic-(meta)sedimentary basement core itself.

CHAPTER 7

DID AN OBLIQUE IMPACT CREATE THE AIS?

CHAPTER 7 – DID AN OBLIQUE IMPACT CREATE THE AIS?

Although most impacts occur at an oblique angle of incidence, with 45° being the most probable impact angle to the target surface (Shoemaker, 1961), the morphological and structural outcomes of an oblique impact – including impact direction and angle – are not readily resolved without detailed morphological and structural analysis (see Kenkmann et al., 2014), as crater shapes generally remain essentially circular for impact angles >10°–15° (Gault and Wedekind, 1978; Bottke et al., 2000). Key features that can help identify an oblique impact, such as the first-order shape of the ejecta deposits or the orientation of deformation structures in the ring syncline and central uplift (Kenkmann et al., 2014, and references therein), may have been eroded or could still be hidden by overlying impact-generated materials, such as impact melt rock and breccia. For terrestrial impact structures, which are often eroded, morphological criteria are of limited use in studying oblique impacts, whereas structural criteria offer more reliable insights (Kenkmann et al., 2014). Furthermore, the size, morphology, and structural characteristics of an oblique impact can differ significantly, depending on factors like impact direction, angle, velocity, impactor size, and the properties of both the impactor and the target (see, e.g., Kenkmann et al., 2014; Davison and Collins, 2022; Fobert et al., 2025, and references therein).

Therefore, despite the oblique impact hypothesis for the AIS being an important topic of discussion, it is one of the most difficult to analyze and resolve. Based on available morphological and structural observations at the AIS, I briefly explore some possible scenarios for its formation via oblique impact.

Although it provides a reasonable first-order appraisal of the apparent diameter of the AIS, the depicted 40-km-diameter circle (see Fig. 2 of Chapter 5) reveals that the apparent rim of the AIS is actually irregular (polygonal; see Chapter 5) and somewhat elliptical. In this context, the Araguainha impact structure is less elongated along its northern and southern sides, resulting in apparent center-to-outer-rim radial distances as low as ~17.5 km. These radial distances translate to apparent diameters of less than 40 km based on these sectors. Interestingly, in these same sectors, the rim trace analysis also more commonly roughly matched straight segments in the models that included arc segments (see Panel S1 of the Supporting Information of Chapter 5). Conversely, the AIS is slightly more elongated along the approximate WNW-ESE direction, with an apparent diameter of a few kilometers exceeding 40 km (see Fig. 2 of Chapter 5).

Based on these first-order morphological observations, the overall apparent rim trace of the AIS roughly resembles a “shield badge” shape, with an axis of symmetry nearly aligned along the WNW-ESE direction and with a “badge tip” pointing toward WNW (280°–290° azimuth) (see Fig. 2 of Chapter 5). This overall shape is significantly controlled by the pre-impact structural framework of the target region (see Chapter 5). Furthermore, considering this somewhat elliptical rim outline of the AIS, two main axial directions of interest can be highlighted: (1) the more elongated WNW-ESE direction; and (2) the NNE-SSW direction, which is perpendicular to – and slightly shorter than – the former.

Notably, within the central uplift, the WNW-ESE direction is also visually prominent, as it defines the more elongated orientation of this feature, especially of the core and the Furnas Formation collar (compare Figs. 2 and 4 of Chapter 5). Furthermore, this direction appears to separate two contrasting radiometric (and also structural; see Chapter 4) domains in the outer collar of the AIS. This framework is evident in the Ponta Grossa Formation, as shown in both the geological map (Fig. 2 of Chapter 5) and the radiometric total count map (Fig. 4 of Chapter 5). In both maps, it is evident that the northern portion of the Ponta Grossa Formation collar is wider, whereas its southern counterpart has a comparatively smaller apparent width (nearly half as wide).

One could argue that this morphological difference results from erosion caused by the Araguaia River, which may have removed the Ponta Grossa Formation in southern sectors. However, the geological map (Fig. 2 of Chapter 5) indicates that the river primarily cuts through the relatively younger Aquidauana Formation (see stratigraphic column; Fig. 2 of Chapter 4) along the southern and eastern central uplift regions. Since there are no overturned strata in the SW collar of the central uplift (see Chapter 4), this likely indicates that the Ponta Grossa Formation remains below the Aquidauana Formation in the same southern region where the Ponta Grossa Formation collar appears narrower. These observations imply that the morphological difference in collar width between the northern and southern parts of the Ponta Grossa Formation is structural and likely related to impact. I propose that this difference results from the sector-dependent collapse of the central uplift (see Chapter 4). If this analysis is considered in isolation, it would favor a southern uprange direction. This uprange direction could have generated greater momentum downrange, causing an outward destabilization of the northern portion

of the outer collar – including the Ponta Grossa Formation – during the collapse of the central uplift.

Furthermore, numerical modeling (Elbeshausen et al., 2013) and physical analog experiments (e.g., Gault and Wedekind, 1978) show that at shallow impact angles – approximately <20° relative to the target surface – the longer axis of an elliptical crater tends to align parallel to the impact trajectory. If that were the case for the AIS, the impact trajectory would be restricted to the WNW-ESE direction. However, this scenario does not align with the field structural observations presented and discussed in Chapter 4, which demonstrate a sector-dependent collapse of the central uplift of the AIS. Whereas the SW sector has minor collapse-related structures, more prominent features, such as overturned beds and outward-verging folds, are consistently observed in the ENE collar sector of the central uplift. Combining these observations with the discussion of the first-order morphological differences of the Ponta Grossa Formation outer collar (see the previous paragraph) indicates that a trajectory along the WNW-ESE direction is unlikely for the Araguainha impactor.

The experiments by Gault and Wedekind (1978) demonstrate that, for strength-controlled targets, impact angles between 15° and 30° can produce elliptical craters with the long axis of the ellipse perpendicular to the impact trajectory. Fobert et al. (2025) suggested that this scenario may apply to the ~85-km-diameter Manicouagan complex impact structure in Canada. This condition would also support the NNE-SSW impact trajectory for the AIS, as this direction is perpendicular to the relatively longer elliptical axis of the structure (see Figs. 2 and 4 of Chapter 5). However, as Fobert et al. (2025) also point out, further studies are needed to better understand this unusual type of oblique impact effect. Nevertheless, it seems that the somewhat elliptical shape of the AIS was considerably more influenced by the preexisting framework of the target area (see chapters 4 and 5) than by oblique impact alone.

Another morphological indicator we can analyze to obtain insights into oblique impacts is the offset of the central uplift relative to the geometric center of the impact structure (e.g., Schultz and Anderson, 1996). However, some recent studies have challenged the validity of this approach (e.g., Goeritz et al., 2009). Fobert et al. (2025) showed that the central uplift of the Manicouagan impact structure is offset by ~5 km to the northeast, which they defined as the uprange direction of an oblique impact. In the case of the AIS, the maps indicate no clearly noticeable offset of the central uplift (see

Figs. 2 and 4 of Chapter 5). This may suggest that if the Araguainha impact event was indeed oblique, it probably did not have a particularly shallow angle of impact – i.e., it was likely not less than 15°.

In summary, the full constraints and outcomes regarding an oblique impact for the Araguainha impact structure remain unresolved. The discussion presented here suggests that the AIS shape was likely more influenced by the target's pre-impact anisotropy – as discussed in Chapter 5 – rather than solely by a prominent oblique impact. Additionally, the full extent and influence of erosional effects on the AIS still require further clarification. However, assuming the Araguainha impactor's trajectory was oblique, I tentatively propose that the impact angle was not extremely shallow (i.e., it was >15°) and possibly with an uprange direction in the present-day southern region (perhaps from the SSW direction). Nonetheless, a more comprehensive evaluation of the oblique impact hypothesis definitely calls for more in-depth fieldwork in structural geology and numerical modeling.

CHAPTER 8

SYNTHESIS AND FINAL REMARKS

CHAPTER 8 – SYNTHESIS AND FINAL REMARKS

The main goals of this project were to update the geological map and expand the structural inventory of the Araguainha impact structure (AIS), using both fieldwork and remote sensing data. This mapping effort arrived just in time, coinciding with recent roadworks within and around the AIS, and helped preserve the newly exposed geological record of the impact structure before it was irreversibly altered by anthropogenic activity and the rapid tropical weathering typical of Central-West Brazil.

Emphasis was placed on understanding the highly complex deformation structures within the central uplift and the outer rim region. The new data provide a basis for addressing several unresolved questions about the formation and morphology of the AIS – e.g., its apparent diameter and shape, the size of its central uplift, the deformation styles in its different morphostructural sections and impact cratering stages, the nature and role of the pre-impact paleoenvironment and target, and the possibility that it results from an oblique impact.

The main contributions of the new geological map of the AIS and its surroundings include a more accurate depiction of the distribution, sizes, and shapes of the Passa Dois Group Blocks (PDGBs), as well as the units within the central uplift, compared to previous maps (e.g., Lana et al., 2008; UnB-IG, 2012; Souza et al., 2024). Moreover, the new map emphasizes the presence of various concentric, tangential, radial, or oblique (relative to the AIS center) structural lineaments throughout the impact structure and its vicinity.

The project successfully addressed the fundamental question regarding the remaining diameter of the eroded structure, reaffirming that the widely accepted apparent diameter of ~40 km for the AIS is accurate. This study also determined that post-impact, loss of diameter due to erosion of the AIS has been relatively minor, estimating no more than a 1% loss of the apparent diameter of the structure since its formation, equivalent to a diameter loss of 290–400 meters. These findings provide a crucial constraint for all subsequent interpretations of the crater's shape and formation processes.

Major achievements of the geological-structural mapping endeavor also include: (1) an updated first-order, morphostructural compartmentalization of the different sections of the AIS (i.e., outer rim region, intermediate section, and central uplift), with evidence of the central uplift extending up to ~10 km in radial distance from the center of the structure; (2) a detailed characterization of the structural framework within these

different sections of the AIS and beyond; and (3) the discussion of the rheological state of the Passa Dois Group sediments/rocks just before the Araguainha impact event.

The investigation into the nature of the deformation within the AIS revealed a complex interplay between impact-driven processes and the rheological properties of the target rocks. Most of the observed structural features are associated with the end of the excavation stage and the subsequent modification stage of the impact event. This includes the formation of the PDGBs and the development and collapse of an asymmetric central uplift. A key finding is that continuous, large-scale concentric anticlines in the outer ring basin are not supported by this work. Instead of a folding model for the outer domains of the AIS, this study proposes a model involving large, tilted, and rotated fault-bounded blocks, with the strain likely accommodated along detachment surfaces between units of different rheologies. The analysis of the PDGBs further supports this perspective, identifying them in the outer rim region of the AIS as complex slump features resulting from the gravitational collapse of the transient crater rim. Moreover, a marine impact target is not needed to explain the deformation observed in the Passa Dois Group, the uppermost unit of the target stratigraphy.

Deformation within the AIS was strongly influenced by preexisting tectonic fabrics, primarily associated with the Paraguay Belt and, to a lesser extent, the Transbrasiliano Lineament. These pre-impact fracture and fault systems created significant anisotropy in the target crust. Instead of a centro-symmetrical structure, the AIS – and its central uplift – are regarded here as fundamentally asymmetric. Asymmetry is evident in the sector-dependent collapse of the central uplift and in the changing orientation and vergence of structural features at various sectors and radial distances from the center of the structure.

Another outcome of this work supports a scenario in which the morphostructural asymmetry of the AIS is a direct consequence of the preexisting anisotropy of the target, rather than solely stemming from an oblique impact. However, the latter cannot be dismissed and requires further investigation. Assuming the Araguainha impactor's trajectory was oblique, structural data from the central uplift and remote sensing observations suggest that the impact angle was not extremely shallow (i.e., it was >15°). The morphostructural differences between the northern and southern parts of the Ponta Grossa Formation collar in the outer central uplift may indicate the impact direction, with the uprange direction likely in the current southern region, possibly in the SSW direction.

The analysis of magnetic, radiometric, and structural lineaments within and outside the impact structure has led to the novel conclusion that the Araguainha impact structure is the eroded remnant of a polygonal impact crater. At the analyzed scale, the (apparent) outer rim trace of the AIS is best described as an irregular, asymmetric enneagon (a nine-sided polygon), with the orientation of its sides strongly influenced by the preexisting regional structural trends. This finding is a significant contribution, as it places the AIS among an increasing number of terrestrial and planetary impact structures recognized to have polygonal shapes, a morphology now understood to be a common outcome of impacts into structurally anisotropic targets.

In summary, this project has successfully achieved its main goals (see Chapter 1). It has delivered an improved geological map, expanded the structural inventory, and advanced the understanding of the morphostructure of the Araguainha impact structure. This research not only answers its initial questions but also sheds light on new aspects of the intricate processes involved in the formation of large, complex impact structures in heterogeneous targets, especially highlighting the importance of anisotropic features, such as layering and/or fractures and faults. Moreover, this study has provided strong evidence for the critical role of pre-impact target structures in shaping the final morphostructure of the AIS, including its notable asymmetry and plan-view polygonal shape.

This work leaves a legacy of new questions and opportunities for future research in the Araguainha impact structure, such as conducting a more detailed analysis of the PDGBs across all sectors and a comprehensive investigation of the central uplift collar-core contact, the megablock zone in the “Serra da Arnica” (Furnas Formation) region, as well as the Ponta Grossa Formation outer collar, to better understand the formation, collapse, and resulting asymmetry of the central uplift. Finally, a definitive assessment of the oblique impact hypothesis – and its key parameters – will require more extensive (azimuthally comprehensive) geological-structural fieldwork, along with advanced numerical modeling, especially of 3-D anisotropic targets.

REFERENCES

Alvarez, L.W., Alvarez, W., Asaro, F., and Michel, H.V., 1980, Extraterrestrial Cause for the Cretaceous-Tertiary Extinction: Science, v. 208, p. 1095–1108, doi:10.1126/science.208.4448.1095.

Baker, D.M.H., Head, J.W., Collins, G.S., and Potter, R.W.K., 2016, The formation of peak-ring basins: Working hypotheses and path forward in using observations to constrain models of impact-basin formation: Icarus, v. 273, p. 146–163, doi:10.1016/j.icarus.2015.11.033.

Bottke, W.F., Love, S.G., Tytell, D., and Glotch, T., 2000, Interpreting the Elliptical Crater Populations on Mars, Venus, and the Moon: Icarus, v. 145, p. 108–121, doi:10.1006/icar.1999.6323.

Brenner, A.R., Cavosie, A.J., Palma-Gomez, J., Li, J., Lee, S.-A.K., and Fu, R.R., 2025, Geology and Mars analog potential of the <2.7-billion-year-old Miralga impact structure, North Pole Dome, Pilbara Craton, Australia: Science Advances, v. 11, p. eadu5379, doi:10.1126/sciadv.adu5379.

Cintala, M.J., and Grieve, R.A.F., 1998, Scaling impact melting and crater dimensions: Implications for the lunar cratering record: Meteoritics & Planetary Science, v. 33, p. 889–912, doi:10.1111/j.1945-5100.1998.tb01695.x.

CPRM (Companhia de Pesquisa de Recursos Minerais), 1972, Levantamento gama-espectrométrico e magnetométrico na área do Projeto Alto Garças nos estados de Goiás e Mato Grosso: CPRM Technical Report 384–5, 76 p., http://rigeo.sgb.gov.br/handle/doc/4320 (accessed October 2025).

Crósta, A.P., Gaspar, J.C., and Cândia, M.Â.F., 1981, Feições de metamorfismo de impacto no Domo de Araguainha: Revista Brasileira de Geociências, v. 11, p. 139–146.

Crósta, A.P., Reimold, W.U., Vasconcelos, M.A.R., Hauser, N., Oliveira, G.J.G., Maziviero, M.V., and Góes, A.M., 2019, Impact cratering: The South American record – Part 1: Geochemistry, v. 79, p. 1–61, doi:10.1016/j.chemer.2018.06.001.

Davison, T.M., and Collins, G.S., 2022, Complex Crater Formation by Oblique Impacts on the Earth and Moon: Geophysical Research Letters, v. 49, p. e2022GL101117, doi:10.1029/2022GL101117.

Dence, M.R., 1972, The Nature and Significance of Terrestrial Impact Structures, *in* Proceedings of the 24th International Geological Congress, Montréal, Canada, International Union of Geological Sciences, p. 77–89.

Dence, M.R., Grieve, R.A.F., and Robertson, P.B., 1977, Terrestrial impact structures: Principal characteristics and energy considerations, *in* Roddy, D.J., Pepin, R.O., and Merrill, R.B., eds., Impact and Explosion Cratering: Planetary and Terrestrial Implications, Flagstaff, Arizona, New York: Pergamon Press, Inc., p. 247–275.

Deutsch, A., Buhl, D., and Langenhorst, F., 1992, On the significance of crater ages: New ages for Dellen (Sweden) and Araguainha (Brazil): Tectonophysics, v. 216, p. 205–218, doi:10.1016/0040-1951(92)90167-5.

Dietz, R.S., and French, B.M., 1973, Two Probable Astroblemes in Brazil: Nature, v. 244, p. 561–562, doi:10.1038/244561a0.

Dörfler, M.A., and Kenkmann, T., 2020, Central uplift collapse in acoustically fluidized granular targets: Insights from analog modeling: Meteoritics & Planetary Science, v. 55, p. 441–456, doi:10.1111/maps.13442.

Elbeshausen, D., Wünnemann, K., and Collins, G.S., 2013, The transition from circular to elliptical impact craters: Journal of Geophysical Research: Planets, v. 118, p. 2295–2309, doi:10.1002/2013JE004477.

von Engelhardt, W., Matthäi, S.K., and Walzebuck, J., 1992, Araguainha impact crater, Brazil. I. The interior part of the uplift: Meteoritics, v. 27, p. 442–457, doi:10.1111/j.1945-5100.1992.tb00226.x.

Erickson, T.M., Timms, N.E., Kirkland, C.L., Tohver, E., Cavosie, A.J., Pearce, M.A., and Reddy, S.M., 2017, Shocked monazite chronometry: integrating microstructural and in situ isotopic age data for determining precise impact ages: Contributions to Mineralogy and Petrology, v. 172, p. 11, doi:10.1007/s00410-017-1328-2.

Fobert, M.-A., Spray, J.G., and Singhroy, V., 2025, An Integrated Remote Sensing Lineament Investigation of the Manicouagan Region, Canada: Implications for Planetary Cratering Processes: Journal of Geophysical Research: Planets, v. 130, p. e2025JE008982, doi:10.1029/2025JE008982.

French, B.M., 1998, Traces of Catastrophe: A Handbook of Shock-Metamorphic Effects in Terrestrial Meteorite Impact Structures: Houston, Lunar and Planetary Institute, LPI Contribution 954, 120 p.

Gault, D.E., and Wedekind, J.A., 1978, Experimental studies of oblique impact, *in* Proceedings of the 9th Lunar and Planetary Science Conference, Houston, Texas, Lunar and Planetary Institute, p. 3843–3875, https://ui.adsabs.harvard.edu/abs/1978LPSC....9.3843G (accessed September 2025).

Gibson, R.L., and Reimold, W.U., 2008, Geology of the Vredefort impact structure: A guide to sites of interest: Pretoria, Council for Geoscience, South African Council for Geoscience Memoir 97, 181 p.

Goeritz, M., Kenkmann, T., Wünnemann, K., and van Gasselt, S., 2009, Asymmetric Structure of Lunar Impact Craters Due to Oblique Impacts?, *in* Proceedings of the Lunar and Planetary Science Conference, The Woodlands, Texas, Lunar and Planetary Institute, p. ID. 2096, https://ui.adsabs.harvard.edu/abs/2009LPI....40.2096G (accessed September 2025).

Gottwald, M., Kenkmann, T., and Reimold, W.U., 2020, Terrestrial Impact Structures: The TanDEM-X Atlas: Munich, Verlag Dr. Friedrich Pfeil, 608 p.

Grieve, R.A.F., and Pilkington, M., 1996, The signature of terrestrial impacts: AGSO Journal of Australian Geology & Geophysics, v. 16, p. 399–420, http://ecat.ga.gov.au:8080/geonetwork/srv/api/records/fae9173a-718b-71e4-e044-00144fdd4fa6 (accessed September 2025).

Grieve, R.A.F., Robertson, P.B., and Dence, M.R., 1981, Constraints on the formation of ring impact structures, based on terrestrial data., *in* Schultz, P.H. and Merrill, R.B., eds., Proceedings of the Lunar and Planetary Science Conference, New York, Pergamon Press, Multi-ring Basins: Formation and Evolution, v. 12A, p. 37–57, https://ui.adsabs.harvard.edu/abs/1981mrbf.conf...37G (accessed September 2025).

Hammerschmidt, K., and von Engelhardt, W., 1995, 40Ar/39Ar dating of the Araguainha impact structure, Mato Grosso, Brazil: Meteoritics, v. 30, p. 227–233, https://onlinelibrary.wiley.com/doi/10.1111/j.1945-5100.1995.tb01116.x (accessed September 2025).

Hartmann, W.K., and Wood, C.A., 1971, Moon: Origin and evolution of multi-ring basins: The moon, v. 3, p. 3–78, doi:10.1007/BF00620390.

Hauser, N., Reimold, W.U., Cavosie, A.J., Crósta, A.P., Schwarz, W.H., Trieloff, M., Souza, C.S.M., Pereira, L.A., Rodrigues, E.N., and Brown, M., 2019, Linking shock textures revealed by BSE, CL, and EBSD with U-Pb data (LA-ICP-MS and SIMS) from zircon from the Araguainha impact structure, Brazil: Meteoritics & Planetary Science, v. 54, p. 2286–2311, doi:10.1111/maps.13371.

Hauser, N., Reimold, W.U., Souza, C.S.M., and Crósta, A.P., 2021, The Araguainha Dome, Brazil: After 40 years of investigation - Quo Vadis?, *in* Anais do 50° Congresso Brasileiro de Geologia, Brasília, DF, Sociedade Brasileira de Geologia, v. 2, p. 384–384.

Hay, H.C.F.C., Collins, G.S., Davison, T.M., Rajšić, A., and Johnson, B.C., 2024, Complex Crater Collapse: A Comparison of the Block and Melosh Acoustic Fluidization Models of Transient Target Weakening: Journal of Geophysical Research: Planets, v. 129, p. e2024JE008544, doi:10.1029/2024JE008544.

Hergarten, S., and Kenkmann, T., 2015, The number of impact craters on Earth: Any room for further discoveries? Earth and Planetary Science Letters, v. 425, p. 187–192, doi:10.1016/j.epsl.2015.06.009.

Hippertt, J.P., Lana, C., Weinberg, R.F., Tohver, E., Schmieder, M., Scholz, R., Gonçalves, L., and Hippertt, J.F., 2014, Liquefaction of sedimentary rocks during impact crater development: Earth and Planetary Science Letters, v. 408, p. 285–295, doi:10.1016/j.epsl.2014.09.045.

Ivanov, B.A., 2005, Numerical Modeling of the Largest Terrestrial Meteorite Craters: Solar System Research, v. 39, p. 381–409, doi:10.1007/s11208-005-0051-0.

Ivanov, B.A., 2024, Impact Craters on Earth with a Diameter of More than 200 km: Numerical Modeling: Solar System Research, v. 58, p. 509–525, doi:10.1134/S0038094624700370.

Jahn, A., and Riller, U., 2009, A 3D model of first-order structural elements of the Vredefort Dome, South Africa — Importance for understanding central uplift formation of large impact structures: Tectonophysics, v. 478, p. 221–229, doi:10.1016/j.tecto.2009.08.007.

Jovane, L., Yokoyama, E., Seda, T., Burmester, R.F., Trindade, R.I.F., and Housen, B.A., 2011, Rock magnetism of hematitic “bombs” from the Araguainha impact structure, Brazil: Geochemistry, Geophysics, Geosystems, v. 12, p. Q12Z34, doi:10.1029/2011GC003758.

Kenkmann, T., 2021, The terrestrial impact crater record: A statistical analysis of morphologies, structures, ages, lithologies, and more: Meteoritics & Planetary Science, v. 56, p. 1024–1070, doi:10.1111/maps.13657.

Kenkmann, T., Collins, G.S., and Wünnemann, K., 2012, The Modification Stage of Crater Formation, *in* Impact Cratering: Processes and Products: Oxford, Wiley-Blackwell, p. 60–75, doi:10.1002/9781118447307.ch5.

Kenkmann, T., and von Dalwigk, I., 2000, Radial transpression ridges: A new structural feature of complex impact craters: Meteoritics & Planetary Science, v. 35, p. 1189–1201, doi:10.1111/j.1945-5100.2000.tb01508.x.

Kenkmann, T., Poelchau, M.H., and Wulf, G., 2014, Structural geology of impact craters: Journal of Structural Geology, v. 62, p. 156–182, doi:10.1016/j.jsg.2014.01.015.

Kring, D.A., 2017, Guidebook to the Geology of Barringer Meteorite Crater, Arizona (a.k.a. Meteor Crater): Lunar and Planetary Institute, LPI Contribution 2040, 272 p., https://www.lpi.usra.edu/publications/books/barringer_crater_guidebook/ (accessed August 2023).

Kurta, A.T., Wünnemann, K., and Kenkmann, T., 2009, Morphometry and Structure of Eroded Complex Impact Craters: A Parameter Study Using Hydrocode Modeling, *in* Proceedings of the Lunar and Planetary Science Conference, The Woodlands, Texas, Lunar and Planetary Institute, p. ID. 1948, https://ui.adsabs.harvard.edu/abs/2009LPI....40.1948K (accessed September 2025).

Lambert, P., and Reimold, W.U., 2023, Terrestrial impact sites as field analogs for planetary exploration: Frontiers in Astronomy and Space Sciences, v. 10, doi:10.3389/fspas.2023.1186173.

Lana, C., Gibson, R.L., and Reimold, W.U., 2003, Impact tectonics in the core of the Vredefort dome, South Africa: Implications for central uplift formation in very large impact structures: Meteoritics & Planetary Science, v. 38, p. 1093–1107, doi:10.1111/j.1945-5100.2003.tb00300.x.

Lana, C., Romano, R., Reimold, U., and Hippertt, J., 2006, Collapse of large complex impact craters: Implications from the Araguainha impact structure, central Brazil: Geology, v. 34, p. 9, doi:10.1130/G21952.1.

Lana, C., Souza Filho, C.R., Marangoni, Y.R., Yokoyama, E., Trindade, R.I.F., Tohver, E., and Reimold, W.U., 2007, Insights into the morphology, geometry, and post-impact erosion of the Araguainha peak-ring structure, central Brazil: Geological Society of America Bulletin, v. 119, p. 1135–1150, doi:10.1130/B26142.1.

Lana, C., Souza Filho, C.R., Marangoni, Y.R., Yokoyama, E., Trindade, R.I.F., Tohver, E., and Reimold, W.U., 2008, Structural evolution of the 40 km wide Araguainha impact structure, central Brazil: Meteoritics & Planetary Science, v. 43, p. 701–716, doi:10.1111/j.1945-5100.2008.tb00679.x.

Leite, E.P., Lambert, J., Vasconcelos, M.A.R., Crósta, A.P., and Batezelli, A., 2022, Gamma-ray spectrometry of the Araguainha impact structure, Brazil: Additional insights into element mobilization due to hydrothermal alteration: Anais da Academia Brasileira de Ciências, v. 94, p. e20210182, doi:https://doi.org/10.1590/0001-3765202220210182.

Machado, R., Lana, C., Stevens, G., Souza Filho, C.R., Reimold, W.U., and McDonald, I., 2009, Generation, mobilization and crystallization of impact-induced alkali-rich melts in granitic target rocks: Evidence from the Araguainha impact structure, central Brazil: Geochimica et Cosmochimica Acta, v. 73, p. 7183–7201, doi:10.1016/j.gca.2009.08.029.

Manzi, S., Gibson, R.L., and Tshibubudze, A., 2021, Dynamics of collapse of an impact central uplift: Evidence from folds and faults in the collar of the Vredefort Dome, South Africa, *in* Reimold, W.U. and Koeberl, C., eds., Large Meteorite Impacts and Planetary Evolution VI, Boulder, Geological Society of America, Geological Society of America Special Paper 550, p. 585–606, https://pubs.geoscienceworld.org/gsa/books/edited-volume/2312/chapter/130246383/Dynamics-of-collapse-of-an-impact-central-uplift (accessed September 2025).

Masero, W., Fischer, G., and Schnegg, P.-A., 1997, Electrical conductivity and crustal deformation from magnetotelluric results in the region of the Araguainha impact, Brazil: Physics of the Earth and Planetary Interiors, v. 101, p. 271–289, doi:10.1016/S0031-9201(96)03267-0.

Masero, W., Schnegg, P.-A., and Fontes, S.L., 1994, A magnetotelluric investigation of the Araguainha impact structure in Mato Grosso-Goiás, central Brazil: Geophysical Journal International, v. 116, p. 366–376, doi:10.1111/j.1365-246X.1994.tb01803.x.

Melosh, H.J., 1979, Acoustic fluidization: A new geologic process?: Journal of Geophysical Research: Solid Earth, v. 84, p. 7513–7520, doi:10.1029/JB084iB13p07513.

Melosh, H.J., 1989, Impact Cratering: A Geologic Process: New York, Oxford University Press, Oxford monographs on geology and geophysics 11, 245 p.

Melosh, H.J., and Ivanov, B.A., 1999, Impact crater collapse: Annual Review of Earth and Planetary Sciences, v. 27, p. 385–415, doi:10.1146/annurev.earth.27.1.385.

Miyazaki, M.R., Leite, E.P., Vasconcelos, M.A.R., Wünnemann, K., and Crósta, A.P., 2021, Bouguer anomaly inversion and hydrocode modeling of the central uplift of the Araguainha impact structure: Anais da Academia Brasileira de Ciências, v. 93, p. e20210081, doi:10.1590/0001-3765202120210081.

Morgan, J.V. et al., 2016, The formation of peak rings in large impact craters: Science, v. 354, p. 878–882, doi:10.1126/science.aah6561.

Northfleet, A.A., Medeiros, R.A., and Mühlmann, H., 1969, Reavaliação dos dados geológicos da Bacia do Paraná: Boletim Técnico da Petrobras, v. 12, p. 291–346.

O'Keefe, J.D., and Ahrens, T.J., 1993, Planetary cratering mechanics: Journal of Geophysical Research: Planets, v. 98, p. 17011–17028, doi:10.1029/93JE01330.

O'Keefe, J.D., and Ahrens, T.J., 1999, Complex craters: Relationship of stratigraphy and rings to impact conditions: Journal of Geophysical Research: Planets, v. 104, p. 27091–27104, doi:10.1029/1998JE000596.

Osinski, G.R., Grieve, R.A.F., Ferrière, L., Losiak, A., Pickersgill, A.E., Cavosie, A.J., Hibbard, S.M., Hill, P.J.A., Bermudez, J.J., Marion, C.L., Newman, J.D., and Simpson, S.L., 2022, Impact Earth: A review of the terrestrial impact record: Earth-Science Reviews, v. 232, p. 104112, doi:10.1016/j.earscirev.2022.104112.

Osinski, G.R., 2012, Processes and Products of Impact Cratering: Glossary and Definitions, *in* Impact Cratering: Processes and Products: Oxford, Wiley-Blackwell, p. 306–309, doi:10.1002/9781118447307.ch20.

Osinski, G.R., and Ferrière, L., 2016, Shatter cones: (Mis)understood? Science Advances, v. 2, p. e1600616, doi:10.1126/sciadv.1600616.

Osinski, G.R., and Pierazzo, E., eds., 2012, Impact Cratering: Processes and Products: Oxford, Wiley-Blackwell, 336 p.

Osinski, G.R., Silber, E.A., Clayton, J., Grieve, R.A.F., Hansen, K., Johnson, C.L., Kalynn, J., and Tornabene, L.L., 2019, Transitional impact craters on the Moon: Insight into the effect of target lithology on the impact cratering process: Meteoritics & Planetary Science, v. 54, p. 573–591, doi:10.1111/maps.13226.

Osinski, G.R., and Spray, J.G., 2005, Tectonics of complex crater formation as revealed by the Haughton impact structure, Devon Island, Canadian High Arctic: Meteoritics & Planetary Science, v. 40, p. 1813–1834, doi:10.1111/j.1945-5100.2005.tb00148.x.

Pike, R.J., 1980, Control of crater morphology by gravity and target type: Mars, Earth, Moon.: Lunar and Planetary Science Conference Proceedings, v. 3, p. 2159–2189, https://ui.adsabs.harvard.edu/abs/1980LPSC...11.2159P (accessed September 2025).

Poelchau, M.H., Kenkmann, T., and Kring, D.A., 2009, Rim uplift and crater shape in Meteor Crater: Effects of target heterogeneities and trajectory obliquity: Journal of Geophysical Research: Planets, v. 114, p. E01006, doi:10.1029/2008JE003235.

Rajšić, A., Johnson, B.C., Collins, G.S., and Hay, H.C.F.C., 2024, Using the Melosh Model of Acoustic Fluidization to Simulate Impact Crater Collapse on the Earth and Moon: Journal of Geophysical Research: Planets, v. 129, p. e2024JE008562, doi:10.1029/2024JE008562.

Reimold, W.U., and Gibson, R.L., 1996, Geology and evolution of the Vredefort impact structure, South Africa: Journal of African Earth Sciences, v. 23, p. 125–162, doi:10.1016/S0899-5362(96)00059-0.

Reimold, W.U., and Koeberl, C., 2014, Impact structures in Africa: A review: Journal of African Earth Sciences, v. 93, p. 57–175, doi:10.1016/j.jafrearsci.2014.01.008.

Schmieder, M., and Kring, D.A., 2020, Earth's Impact Events Through Geologic Time: A List of Recommended Ages for Terrestrial Impact Structures and Deposits: Astrobiology, doi:10.1089/ast.2019.2085.

Schnegg, P.-A., and Fontes, S.L., 2002, Feasibility study of the geoelectric structure of the Araguainha impact, Brazil: Earth, Planets and Space, v. 54, p. 597–606, doi:10.1186/BF03353048.

Schulte, P. et al., 2010, The Chicxulub Asteroid Impact and Mass Extinction at the Cretaceous-Paleogene Boundary: Science, doi:10.1126/science.1177265.

Schultz, P.H., and Anderson, R.R., 1996, Asymmetry of the Manson impact structure: Evidence for impact angle and direction, *in* Koeberl, C. and Anderson, R.R., eds., The Manson impact structure, Iowa; anatomy of an impact crater, Geological Society of America, p. 0, doi:10.1130/0-8137-2302-7.397.

Senft, L.E., and Stewart, S.T., 2009, Dynamic fault weakening and the formation of large impact craters: Earth and Planetary Science Letters, v. 287, p. 471–482, doi:10.1016/j.epsl.2009.08.033.

Shoemaker, E.M., 1961, Interpretation of Lunar Craters, *in* Kopal, Z., ed., Physics and Astronomy of the Moon, Academic Press, p. 283–359, doi:10.1016/B978-1-4832-3240-9.50012-2.

Silva, D., Lana, C., and Souza Filho, C.R., 2016, Petrographic and geochemical characterization of the granitic rocks of the Araguainha impact crater, Brazil: Meteoritics & Planetary Science, v. 51, p. 443–467, doi:10.1111/maps.12601.

Silveira Filho, N.C., and Ribeiro, C.L., 1971, Informações geológicas preliminares sobre a estrutura vulcânica de Araguainha, Mato Grosso: Departamento Nacional de Produção Mineral, DNPM Internal Report, 50 p.

Souza, C.S.M., Hauser, N., Reimold, W.U., Bernardes, R.B., Vieira, L.C., Guimarães, E.M., and Gottwald, M., 2024, Araguainha impact structure, Brazil: New insights into the geology of the central uplift: Meteoritics & Planetary Science, v. 59, p. 2577–2607, doi:10.1111/maps.14236.

Spudis, P.D., 1993, The Geology of Multi-Ring Impact Basins: The Moon and Other Planets: Cambridge, Cambridge University Press, Cambridge Planetary Science Old, 263 p., doi:10.1017/CBO9780511564581.

Theilen-Willige, B., 1981, The Araguainha impact structure/Central Brazil: Revista Brasileira de Geociências, v. 11, p. 91–97, doi:10.25249/0375-7536.19819197.

Tohver, E., Lana, C., Cawood, P.A., Fletcher, I.R., Jourdan, F., Sherlock, S., Rasmussen, B., Trindade, R.I.F., Yokoyama, E., Souza Filho, C.R., and Marangoni, Y., 2012, Geochronological constraints on the age of a Permo–Triassic impact event: U–Pb and $^{40}Ar/^{39}Ar$ results for the 40 km Araguainha structure of central Brazil: Geochimica et Cosmochimica Acta, v. 86, p. 214–227, doi:10.1016/j.gca.2012.03.005.

Tohver, E., Schmieder, M., Lana, C., Mendes, P.S.T., Jourdan, F., Warren, L., and Riccomini, C., 2018, End-Permian impactogenic earthquake and tsunami deposits in the intracratonic Paraná Basin of Brazil: GSA Bulletin, v. 130, p. 1099–1120, doi:10.1130/B31626.1.

Tong, C.H., Lana, C., Marangoni, Y.R., and Elis, V.R., 2010, Geoelectric evidence for centripetal resurge of impact melt and breccias over central uplift of Araguainha impact structure: Geology, v. 38, p. 91–94, doi:10.1130/G30459.1.

Turtle, E.P., Pierazzo, E., Collins, G.S., Osinski, G.R., Melosh, H.J., Morgan, J.V., and Reimold, W.U., 2005, Impact structures: What does crater diameter mean?, *in* Kenkmann, T., Hörz, F., and Deutsch, A., eds., Large Meteorite Impacts III, Geological Society of America, Special Paper 384, p. 1–24, doi:10.1130/0-8137-2384-1.1.

UnB-IG (Universidade de Brasília–Instituto de Geociências), 2012, Araguainha Project – Final coursework mapping project by the geology graduating class of 2012: Universidade de Brasília, Instituto de Geociências, Unpublished Report.

Vasconcelos, M.A.R., 2007, Caracterização geofísica da estrutura de impacto de Araguainha, MT/GO [Master's thesis]: Universidade de São Paulo, 157 p., https://doi.org/10.11606/D.14.2007.tde-17052007-105856 (accessed October 2025).

Wieland, F., Gibson, R.L., and Reimold, W.U., 2005, Structural analysis of the collar of the Vredefort Dome, South Africa—Significance for impact-related deformation and central uplift formation: Meteoritics & Planetary Science, v. 40, p. 1537–1554, doi:10.1111/j.1945-5100.2005.tb00416.x.

Yokoyama, E., Trindade, R.I.F., Lana, C., Souza Filho, C.R., Baratoux, D., Marangoni, Y.R., and Tohver, E., 2012, Magnetic fabric of Araguainha complex impact structure (Central Brazil): Implications for deformation mechanisms and central uplift formation: Earth and Planetary Science Letters, v. 331–332, p. 347–359, doi:10.1016/j.epsl.2012.01.005.